2007

Electrodeposition of multilayered nanostructures for giant magnetoresistance and thermoelectric applications

Despina Davis
Louisiana State University and Agricultural and Mechanical College

ELECTRODEPOSITION OF MULTILAYERED NANOSTRUCTURES
FOR
GIANT MAGNETORESISTANCE AND THERMOELECTRIC APPLICATIONS

A Dissertation

Submitted to the Graduate Faculty of the
Louisiana State University and
Agricultural and Mechanical College
in partial fulfillment of the
requirements for the degree of
Doctor of Philosophy

in

The Interdepartmental Program in Engineering Science

By
Despina Davis
B.S., Texas Tech University, 2002
M. S., Louisiana State University 2004
May, 2007

to my advisor,

Dr. Elizabeth Podlaha-Murphy

ACKNOWLEDGEMENTS

TABLE OF CONTENTS

LIST OF TABLES

LIST OF FIGURES

ABSTRACT

The electrodeposition of novel materials such as multilayer nanotubes for giant magneto resistance (GMR) applications and bismuth telluride nanotubes for thermoelectric applications are presented in this dissertation. The motivation for the multilayer electrodeposition is the investigation of giant magnetoresistance (GMR), a change in the material resistance in an applied magnetic field as a consequence of antiferromagnetic coupling. The nanowire high aspect ratio geometry allows the measurement of GMR with the current applied perpendicular to the plane (CPP) of the multilayers, which has been theoretically identified as being larger than the GMR in the (CIP) configuration (current in plane of multilayers). The current perpendicular to the plane giant magneto-resistance (CPP)-(GMR) effect makes multilayered nanowires of huge interest as magnetic sensor materials.

Electrodeposition is the most efficient method for fabricating magnetic nanowires. In addition to the cost-effectiveness, electrodeposition is one of the few methods that can overcome the geometrical restrictions of inserting metals into very deep nanometric recesses, making it the favored method for nanowire and nanotube fabrication. In this dissertation, the quaternary CoNiFeCu alloy system was investigated in order to electrodeposit multilayered nanowires/nanotubes for GMR effect. Electrodeposited multilayer CoNiFeCu/Cu nanowires and nanotubes were fabricated by pulsed applied electric potential and their giant magnetoresistance (GMR) behavior characterized. The effect of electrolyte concentration on the GMR was investigated. The $FeSO_4$, $CoSO_4$ and $NiSO_4$ concentrations were varied to optimize the GMR and the saturation field of the multilayered nanowires. Nanolayer thicknesses were controlled and varied for commercially viable GMR results. Furthermore, the influence of electrolyte temperature on nanotube formation and the resulting GMR was explored.

Micro fluidic magnetic nanoparticles sensors based on CoNiFeCu/Cu GMR nanowires were fabricated for the first time. The test results show that the sensors are highly sensitive to small nanoparticle concentrations.

Employing the potentiostatic electrodeposition, nanotubes of bismuth-telluride (Bi_2Te_3) were obtained. The electrolyte concentration was varied and affected the nanotube formation and the resulting Seebeck coefficients.

CHAPTER I. INTRODUCTION

1.1 Introduction

The growing need for high performance data storage media and sensing devices demands the development of innovative magnetic materials. As more information is packed into smaller volumes and all devices become smaller, nanotechnology tackles the critical limit that dealing with the quantum properties of matter. Nanofabrication refers to the ability to fabricate with nanometric scale precision structures having unique electronic properties that can be tailored by manipulating size, shape and composition. Currently there is tremendous interest for fabrication of nanostructured magnetic materials due to their unusual properties, which makes them interesting for applications in ultra-high-density magnetic recording and sensors.

Electrodeposition also known as electroplating is one of the most efficient methods for fabricating metallic nanostructures. In addition to the cost-effectiveness, electrodeposition can overcome the geometric restrictions of inserting metals into deep nanometric grooves. For metal alloy fabrication the electrodeposition method eliminates the need of handling extremely different high vapor pressures as required by CVD techniques.

A great deal of research interest is in the electrodeposition of iron-group metals because these cobalt-nickel-iron alloys possess superior soft magnetic properties that are needed in computer data recording and storage. Iron-group alloys are attractive materials for fabricating micromachined magnetic devices due to their favorable soft magnetic properties. For instance permalloy ($Ni_{80}Fe_{20}$) and orthonol ($Ni_{50}Fe_{50}$) are preferred due to their small coercivity, low anisotropy and practically no magnetostriction. Sensor and actuator applications need such magnetic materials that have low hysteresis (soft magnetic materials). A good soft magnetic material should have a large saturation magnetization to obtain a wide range of operation and a

high permeability to achieve high magnetization even under a low applied field. For higher frequency applications, soft magnetic materials with higher resistivities are needed to reduce eddy current losses. (Parky and Allen, 1998)

In the last decade data storage capacity increased exponentially while decreasing the size of the magnetic grains that make up data bits, therefore increasing the recording densities. However, by shrinking the magnetic grains the read heads have to be even more sensitive to very small magnetic changes. The discovery of giant magnetoresistance (GMR) makes possible the reading of very high density hard drives which brought about a recent revolution in disk storage technology.

Manufactured materials that show GMR are used for perpendicular magnetic recording and magnetic field sensors. These magnetic materials are good candidates for computer disk drives, audio-video tape heads, magnetometers, compass systems, etc.

Currently, most magnetic drives read stored data using GMR-based heads. Based on its orientation, the small magnetic field of each particle on the disk affects the electrical resistance of the read head. When the magnetic layers of the head sense a magnetic moment signifying "1" the spins are aligned, and when it senses a "0" the spins are anti-ferromagnetically coupled. In one position the electrical resistance is high, since the magnetic moments are not aligned, allowing only a small current to pass through the read head. On the other hand, the magnetic moment signifying "1" decreases the electrical resistance, letting a high current pass though the head. The shifting strengths of an electrical signal, as a result of changes in electrical resistance, allow the GMR read head to copy stored data to a computer. The GMR effect can also be used for position detection devices of objects that have permanent imprinted magnetization patterns. Robotics and assembly lines use position sensors that sense a change in a magnetic field due to

the movement of a magnetized object. GMR integrated fluidic sensors can be used to detect bio-molecules and also provide a vehicle for the placement, detection and study of biomolecular interactions, in particular those with DNA. Other biological applications include magnetically assisted separations, high sensitivity biosensors and biochips for protein and DNA screening. GMR sensors possess higher sensitivity, better signal-to-noise ratios, and exhibit less mechanical wear since they could be considered contactless sensors.

The giant magnetoresistance (GMR) property is described as a change in the material electrical resistance when an external magnetic field is introduced. This giant magnetoresistance effect is observed when ferromagnetic elements are layered with nonmagnetic elements like chromium or copper. The GMR theory proposed by Baibich *et al.* (Baibich, 1988) showed that an applied magnetic field changes the spin alignment of the ferromagnetic layer from antiparallel to parallel, resulting in a decrease of material resistance. GMR showing multilayered nanostructures are composed of alternating ferromagnetic and nonmagnetic nano-size layers.

Improving the GMR property could be achieved by testing the addition of different elements in the magnetic alloy layer. Andricacos and Robertson (1998) showed that cobalt would increase the saturation magnetization while the copper addition could decrease the coercivity while improving corrosion resistance. The combination of cobalt and iron would yield a zero magnetostrictive alloy with a large saturation moment (Liao, 1987) Osaka *et al.* (2000) studied the relation between composition and magnetic properties of FeCoNi ternary alloys and found that soft magnetic materials with low coercivity had high cobalt content and fine grains.

Sputtering techniques showed high GMR values for thin film FeCoNi alloy layered with Cu. Jimbo *et al.* (1994) used the magnetron sputtering technique for layer deposition and found the CoNiFe/Cu thin film GMR to be very sensitive at low magnetic fields 16 % GMR at 50 Oe.

This GMR property can be further improved by fabrication of 3D nano-layered nanostructures with large aspect ratios. These high surface area nanostructures are almost impossible to produce by vacuum techniques. Template electroplating has been widely used to make nanowires. The extreme shape anisotropy of nanowires permit the measurement of a special configuration GMR called current-perpendicular-to-plane (CPP-GMR). In thin film multilayers, only one kind of GMR measurement is possible and that is the current-in-plane (CIP-GMR) configuration. The mechanism behind the CIP-GMR is limited by the layer thickness, which has to be very small, comparable to the electron mean free path in order to exhibit GMR. The CPP-GMR is limited by another characteristic length called the electron spin diffusion length, which is several times larger than the electron mean free path. It was predicted that, since the CPP-GMR is governed by a larger electron travel length, it would yield a larger resistance drop compared to the CIP-GMR that is limited by the small electron mean free path. Dubois *et al.* (1997) showed that the electrodeposited multilayer nanowires exhibited larger GMR than the same electrodeposited thin films.

After the discovery of GMR in 1988 by Baibich, multilayered films for GMR purposes were only achieved using expensive vacuum sputtering techniques, molecular beam epitaxy and melt spinning methods. These vapor deposition techniques showed large GMR values (70 % at room temperature and 130 % at 4.2 K) in thin Co/Cu multilayer films, Parkin [Parkin, 1995]. As a less costly fabrication alternative, in the past ten years the electrodeposition process has been shown to produce thin films exhibiting GMR. Ross [Ross, 1994] reviewed electrodeposition as an alternative technique for making multilayer films, and pointed out that electrochemical methods permit the manipulation of mechanical properties and orientation dependent properties. However, in comparison with thin films obtained by vapor techniques, electrodeposited films

showed lower GMR values. The reviewer mentioned that non-discrete layering, rough interfaces and heterogeneous growth could contribute to the lower values of GMR obtained by electrodeposition.

However, electrodeposition finds a niche in assembling nanometric size structures in complex geometries and recessed areas, as with nanowires and nanotubes. Vapor deposition techniques are of little value when it comes to inserting metals into very deep recesses, such as nanoporous membranes. Electrodeposition is the easiest and most practical way of obtaining nanowires, by inserting metals in porous membranes.

As the size of nano-magnets becomes comparable to characteristic magnetic length scales, the magnetic behavior is strongly affected. In the case of the ultra high density magnetic storage the bit lateral size needs to be as small as possible, but when the bit volume gets too small its magnetization changes reaching the super-paramagnetic limit. That is an undesirable state because the energy needed to switch the bit magnetization is less than the thermal energy [L.W. Wang, 2002]. A promising way to achieve the small lateral size, with relatively large volume and high magnetic transition energy is the nanowire geometry.

1.2 Research Goal

In this study, we focus on the electrodeposition a particular category CoNi(Fe)/Cu of magnetic multilayered nanowires. Nanowires are structures of enormous surface area and aspect ratios (length to diameter), which confer upon them unique properties. Furthermore, due to the nanowire unique geometry, the GMR property can be measured in a perpendicular mode (CPP), which has been proven to show larger changes in electrical resistance with magnetic fields than the in-plane (CIP-GMR) [Pratt, 1991].

To the best of my knowledge, our lab is the first to examine the combined Co-Ni-Fe-Cu system of nanowires for GMR effect (Huang, 2004). Therefore, the present work focuses on the quaternary CoNiFeCu/Cu electrodeposition in the form of multilayered nanowires and tubes using different pore size polycarbonate (PC) and aluminum oxide (AAO) membranes.

The reason behind the choice of elements is the fact that Co-rich FeCoNi alloys are good candidates as soft magnetic materials and layering this magnetic alloy with copper could increase the materials resistivity, which can eliminate the contact effects and avoid eddy current interference. Our goal was to use a single electrolyte and to adjust the plating conditions in order to tailor the deposit composition, structure and properties.

Magnetic properties of obtained nanowires were tested and related to changes in the electrodeposition operating conditions, such as applied potential and electrolyte composition. Moreover, this work shows how the electrolyte concentration and temperature affected the wires GMR. Microfluidic sensors using CoNi(Fe)/Cu nanowires GMR were fabricated and tested with different magnetic nanoparticles and ferrofluids.

CHAPTER II. LITERATURE SURVEY

2.1 GMR Background

The discovery of giant magnetoresistance (GMR) in 1988 by Baibich *et al.* (Baibich, 1988) marked the beginning of an intense research topic in multilayered magnetic alloys and currently most computer read heads are using GMR materials. GMR is defined as a change of the solid-state resistance due to the magnetic field. Correctly the % GMR should be defined as 100*[(R (in magnetic field) –R (no magnetic field))/ R (no magnetic field))]. In this case, since R(H) = $R_{saturation}$, the GMR is bounded between 0-100 % and it does not exceed 100 %. The study proposed by Baibich *et al.* showed that an applied magnetic field changes the spin alignment of the ferromagnetic layer from antiparallel to parallel, resulting in a decrease of material resistance. Baibich *et al.* observed this GMR phenomena on a superlattice of Fe (30Å)/Cr (9Å) deposited by molecular beam epitaxy. The antiferromagnetic (AF) coupling of the two adjacent Fe layers was the reason behind the GMR. When there is no magnetic field applied, the adjacent separated ferromagnetic Fe layers sense each other and naturally anti-ferromagnetically (orient their electron spins in opposite direction). When an electric current is passed through the layers with opposite spin, the current carriers (electrons) will need to switch their spin when they pass through different oriented Fe layers and this additional energy of spin re-orientation increases the resistance. However, when the multilayers are placed in an external magnetic field, the spins in Fe magnetic layers are forced in the same direction, and the passed electric current would not have to spin flip in each encountered magnetic layer, consequently the material becomes less resistive for the passage of electric current. According to Mott (Mott, 1964) electrical current is comprised of two distinct conduction channels, the spin-up and spin-down s-p electrons, and the conductivity is different in the two spin channels. When a

perpendicular current is applied to a magnetic layer, the electrons with spin parallel to the magnetized layer (majority carriers) will be scattered less than the electrons with spin antiparallel to the magnetization layer (minority carriers). In the case of no applied magnetic field shown in Figure 2.1 schematic, the majority carriers are strongly scattered in every other magnetic layer, and the minority carriers are strongly scattered in alternating magnetic layers, therefore both carriers encounter higher net resistance. When a magnetic field is applied to this configuration, the electrons in all the ferromagnetic layers will orientate such that the majority carriers are not strongly scattered in any of the magnetic layers. The minority carriers are still scattered in all of the magnetic layers, but the net effect of this rearrangement is a lower resistance to the current passing through the multilayered material.
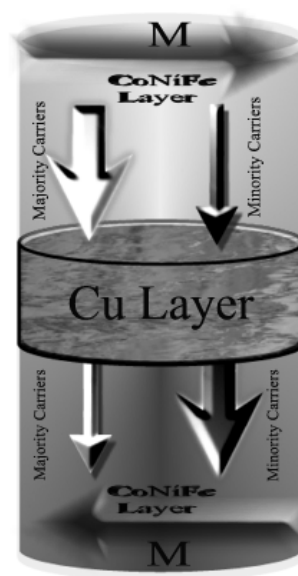
Figure 2.1 Antiferromagnetically coupled layers in no magnetic field: majority carriers become minority carriers in the adjacent magnetic layer → increased electrical resistance

Furthermore, the majority and minority electrons have different interface reflection coefficients, making the spin transport along the interfaces act as a torque on the magnetization. This torque aligns the magnetization according to the reflection coefficients.

Initially, physical methods such as sputtering, molecular beam epitaxy and chemical vapor deposition were the only methods to attempt fabrication of GMR multilayers. Focusing on thin film magnetic layers sandwiched with non-magnetic layers, Parkin [Parkin, 1995] reviewed the magnetoresistance dependence in layered structures. The reviewer emphasized the layered materials requirements to be used for magnetic data storage applications: magnetic stability against increased temperatures, no electromigration at high current density usage and minimal environmental corrosion. A decrease in GMR was observed when the alternating magnetic layers were not completely antiferromagnetically coupled, due to larger layer sizes or non-discrete layers. 70 % room temperature GMR was reported for Co/Cu thin films obtained by magnetron sputtering and 220 % GMR at 1.5 K. It is important to note that the definition of GMR varies between different authors. If the GMR is defined as $100*[(R(0)-R)/R_{sat}]$, where $R(0)$ is the resistance at zero magnetic field and R_{sat} is the saturation resistance, then when $R = R_{sat}$ it is possible that the GMR value goes over 100 %, an inflated GMR.

Ross [Ross, 1994] also reviewed magnetic thin films but focused on the electrodeposition process as an affordable alternative method of obtaining multilayer thin films. The electrodeposition advantages include the ability to tailor the deposit composition and crystallographic structure. Ross also pointed out that electrolyte composition, pH, agitation and current regime affect the multilayer fabrication process. The reviewer, called attention to the 18 % GMR at room temperature observed in the CoNiCu/Cu electrodeposited thin films. Aside from bath composition and deposition conditions, Ross mentioned that additives and the substrate choice seem to have an effect on the crystal nucleation and epitaxial growth. In thin films, the GMR is measured with the electric current in plane of the multilayers, the so-called (CIP) configuration. The characteristic length is the feature that controls the GMR effect, and it

differs in the two configurations, CIP and CPP (current perpendicular to the plane of layers). Valet and Fert (Valet, 1993) derived an expression which relates the electron mean free path (λ) to the spin diffusion length (L). Since the electron mean free path (λ) in CIP is about ~2 nm, the layer thicknesses in the CIP mode is critical. On the other hand, in CPP configuration, the larger spin diffusion length (~ 20 nm) allows for larger layer thickness and theoretically larger GMR. Experimentally it is difficult to measure CPP-GMR in thin films due to their very small resistance, but arrays of nanowires make this configuration readily accessible. The CPP configuration is conducive for tall and narrow geometries such as nanowires.

2.2 Magnetic Nanowires Electrodeposition

Not only does electrochemical deposition show promising results for multilayers fabrication, but it also has the capability to deposit metal onto curved and recessed areas, e.g. nanowires geometries.

2.2.1 Multilayered Nanowires

Piraux *et al.* (Piraux, 1994) was the first to take advantage of the multilayer nanowire geometry. They studied the Co/Cu system electrodeposited in polycarbonate membranes (PC) (40 nm pore diameter and 10 μm pore length), and reported the CPP-GMR to be 15 % at room temperature for (10 nm Co/10 nm Cu) layers.

Concurrently, Blondel *et al.* (Blondel, 1994) looked at the Co/Cu and FeNi/Cu multilayers electrodeposited in nanowires. Blondel *et al.* also measured CPP-GMR at room temperature, and obtained a slightly higher GMR (14 %) for the Co/Cu system than for the FeNi/Cu system (10 %). Using PC membranes (80 nm pore diameter and 6 μm pore length), Blondel *et al.* tested different layer thicknesses and found that a larger GMR was shown for layers less than 10 nm.

Liu *et al.* (Liu, 1995) retested the Co/Cu system for layers in nanowires, and found 11 % CPP-GMR at room temperature, and 22 % CPP-GMR at 5 K. Testing two different kinds of polycarbonate membranes (30 nm pore diameter/ 6 μm pore length, 400 nm pore diameter /10 μm pore length), Liu *et al.* utilized coulometric potential control electrodeposition as the method for fabricating nanowires. In the different CIP and CPP GMR measurements, they found that the nanowire CIP-GMR was temperature independent, while the CPP-GMR was especially sensitive to temperature. Testing different Cu layer thicknesses ranging from 8 to 400 Å, they observed that the GMR effect becomes insignificant for Cu layer thicknesses exceeding the spin-flip diffusion length. For Cu layer thicknesses of (0.8 nm), the CPP-GMR was reported to be 22 % at low temperatures. The GMR as a function of Cu layer thicknesses showed two separate peaks, but no clear values were given. Liu *et al.* concluded that the CPP-GMR effect in nanowires was due to the layered arrangement combined with an extra interfacial resistance. Furthermore, the smaller diameter wires showed significant boundary scattering that could explain the larger observed GMR.

Blondel *et al.* (Blondel, 1995) also studied the CPP-GMR in electrodeposited multilayered nanowires, using polycarbonate membranes (80 nm pore diameter/ 6 μm pore length). Blondel *et al.* sandwiched CoNi/Cu using a square pulsed potentiostatic technique, and obtained very smooth and flat layers. For equal magnetic and nonmagnetic layer thicknesses, the measured CPP-GMR was 20 % at room temperature. Both the nonmagnetic impurity level and the strict interface control were presented as key factors in maximizing the GMR property.

Wang *et al.* (Wang, 1996) prepared Ni/Cu multilayered nanowires using polycarbonate membranes (80 nm pore diameter/ 8 um pore length) as templates. Employing a potentiostatic pulsed scheme, Wang *et al.* observed the multilayers displaying a concave growth. A

disagreement between the pore diameter and the wire diameter was observed, which was explained as wire expansion during electrodeposition. Wang *et al.* also reported that the bilayer thickness increased as the wire grew when a potentiostatic pulsed scheme was used.

To obtain pure layer nanowires, Blondel *et al.* (Blondel, 1997) implemented a dual bath technique electrodeposition, and then compared the results with the ones obtained from the single bath deposition. Analyzing the Co/Cu system and keeping both magnetic and nonmagnetic layer thicknesses the same, Blondel *et al.* reported 8 % GMR for 10 nm layers using the dual bath technique. On the other hand, Blondel *et al.* reported 22 % GMR for 8 nm layers obtained from the single bath electrodeposition. As a consequence, Blondel *et al.* concluded that the impurity of Cu in the Co layer, inherent in the single bath, was not the determining factor for the GMR effect.

Dubois *et al.* (Dubois, 1999) compared the NiFe/Cu system with the Co/Cu system for the CPP-GMR effect in PC membranes. At 77 K, the 10 nm Co/ 5 nm Cu multilayered nanowires showed 30 % GMR, and the 12 nm $Ni_{80}Fe_{20}$ / 4 nm Cu had 65 % GMR. At an even lower temperature (4.2 K), Dubois *et al.* saw an increase of the CPP-GMR to 78 % for the NiFe/Cu multilayers. They did not report room temperature GMR.

Simultaneously, both Schwarzacher *et al.* (Schwarzacher, 1997) and Heydon *et al.* (Heydon, 1997) researched a more complex combination of elements and were able to obtain multilayered CoNiCu/Cu nanowires in polycarbonate membranes. Schwarzacher *et al.* reported a maximum GMR of 22 % at room temperature for CoNiCu (50 Å)/ Cu (40 Å) multilayered nanowires in 80 nm pore diameter membrane. In the same study Schwarzacher *et al.* hypothesized that adding Ni to the bath reduced Co dissolution during the Cu deposition. In a later study, Huang and Podlaha (Huang, 2004) showed that Co dissolution during Cu deposition

could exaggerate the compositional gradient at the interface, making the layers less discrete. Even for thicker layers (5 nm CoNiCu/3.5 nm Cu) Heydon *et al.* showed 20 % GMR at room temperature. When the Cu layer decreased (2.4 nm CoNiCu/3.5 nm Cu) the GMR increased to 22 % at room temperature.

Comparing a typical multilayer arrangement $Ni_{80}Fe_{20}$ (12 nm)/Cu (4 nm) and a trilayered layer arrangement $Ni_{80}Fe_{20}$ (3 nm)/Cu (10 nm)/ $Ni_{80}Fe_{20}$ (3 nm) separated by 90 nm long Cu fragments, Piraux *et al.* (Piraux, 1997) observed a decrease in magnetic saturation fields for the trilayered nanowires obtained in aluminum oxide templates. At low temperature (4.2 K) and high magnetic fields (9 T), 80 % CPP-GMR was obtained for the typical multilayered NiFe/Cu system, while a 19 % CIP-GMR, at low saturation fields, was observed for the trilayered nanowires. When the same GMR measurements were performed at room temperature, the MR decreased to a third (~ 26 %) of the low-temperature GMR value.

Evans *et al.* (Evans, 2000) investigated the electrodeposition of CoNiCu/Cu multilayers in 20 nm pore diameter aluminum oxide templates. Using potentiostatic charge control to control layer thicknesses, they reported 55 % room temperature GMR and 115 % low temperature GMR, for sub-nanometric layer sizes CoNiCu (54 Å)/Cu (21 Å). Evans *et al.* concluded that the GMR observed in the AAO membranes was 2.5 times larger than the GMR obtained for a comparable system deposited in PC membranes. Their study also showed that sample annealing over 500 °C would reduce the GMR effect due to interdiffusion and recrystallization phenomena.

Schwarzacher *et al.* (Schwarzacher, 2000) used 20 nm diameter pore AAO templates for electroplating multilayered nanowires. They pointed out that AAO pore size specification was an order of magnitude smaller than the observed pore diameter (200 nm). Using galvanostatic

electrodeposition, Schwarzacher *et al.* achieved 60 % room temperature GMR for CoNiCu (5nm)/Cu (3nm) multilayered nanowires, although their result has not been reproduced.

Garcia *et al.* (Garcia, 2002) showed that multilayered wires of extreme magnetic layer thickness, such as Co (170 nm)/Cu (10nm) and Co (25 nm)/Cu (190 nm) exhibited inconsistent magnetic states, having transverse and oblique magnetic domains.

2.2.2 Alloy Nanowires

Schwarzacher *et al.* (Schwarzacher, 1999) prepared heterogeneous CoCu nanowires in AAO templates (20 nm diameter) by galvanostatic electrodeposition. The researchers showed that, for heterogeneous nanowires, the coercivity decreased with annealing temperature and pressure, due to phase separation that generated larger Co-rich particle size.

Fedosyuk *et al.* (Fedosyuk, 1999) also researched heterogeneous CoCu alloy nanowires grown in AAO membranes of 20 nm pore diameter. The alloy nanowires showed room temperature GMR of less than 1 %, which slightly increased after annealing. In their study, Fedosyuk *et al.* remarked that the GMR shape changed drastically when the field was applied perpendicular or parallel to the wire axis. The magnetic behavior dependence on the field direction demonstrated that the wires exhibit magnetic anisotropy. Furthermore, it was concluded that nanowire geometry greatly influenced magnetic properties. Fedosyuk *et al.* also commented on the AAO membrane temperature resistance compared to PC membranes, but they pointed out the difficulty of AAO nanowires examination due to the more complicated membrane dissolution.

Blythe *et al.* (Blythe, 2000) further investigated heterogeneous $Co_{20}Cu_{80}$ alloy grown by galvanostatic electrodeposition in the shape of nanowires, using two different sizes AAO membranes: 200 nm and 20 nm pore diameters. Their publication mentioned that heterogeneous

nanowire alloys showed GMR at room temperature, but they do not provide any values. Blythe *et al.* concluded that there was a non-uniform distribution of large and very fine magnetic clusters along the deposited alloy nanowire, which led to high anisotropy in the demagnetizing field. Also, Blythe *et al.* mentioned that the high-ratio magnetic nanowires showed a broader range of magnetic clusters compared to a thin film of similar composition.

Zhu *et al.* (Zhu, 2001) studied the effect of applied magnetic field during CoNi alloy nanowire electrodeposition in AAO templates (200 nm pore diameter). Their examination showed that the perpendicular applied magnetic field during electrodeposition not only reduced the (BH) saturation fields, but also enhanced squareness. In a different study, Zhu *et al.* looked at magnetic properties of FeNi nanowires with very high aspect ratios (>1000). The FeNi nanowires were electroplated in self-prepared AAO of highly ordered pores (43 nm pore diameters and 60 nm distance between pores). Enhanced coercivity of 769 Oe and 70 % remanent magnetization was observed when the magnetic field was applied parallel to the wires.

Wang *et al.* (Wang, 2001) analyzed the structure and magnetic anisotropy of compositionally modulated FeNi alloy nanowires electrodeposited in AAO. Using XRD and Mossbauer spectroscopy, the obtained wires (16 nm diameter and 4 μm length) showed a polycrystalline structure along the (110) direction. The Fe component proved to have magnetic moments parallel to the wires in contrast to bulk Fe that had the (100) direction as the easy magnetization axis. The authors stated that the change in the preferred magnetization axis was due to the large shape anisotropy. Moreover, Wang *et al.* confirmed that the Ni component showed a disordered placement along the wires.

Pena *et al.* (Pena, 2001) researched the electrodeposition of multi-material (conductor-semiconductor) nanowires, such as Au-CdSe-Ni-Au, Au-Ni-CdSe-Ni-Au, Au-CdTe-Au, and Au-

CdTe-Ag-Au, using 200 nm pore diameter AAO commercial templates. The conductive and semiconductive elements were electrodeposited from separate baths; Au, Ni, Ag under galvanostatic control, while the semiconductors (Cd, Te, Se) were electrodeposited by cyclic voltammetry at a high scanning rate (750 mV/s) with a deposition rate of 2 A/scan. Pena *et al.* showed the ability to incorporate semiconductor portions along metallic wires, and investigated the respective changes in the electrical properties.

Wang *et al.* (Wang, 2002) used an in-house prepared AAO membranes (60 nm pore diameter) to electrodeposit CoAg alloy nanowires and studied the annealing effect on magnetic properties. The coercivity was larger for the parallel magnetic measurements, and it also increased with increasing annealing temperature, due the isolation of single Co magnetic domains. A maximum parallel field coercivity of 183 Oe was reached at a critical maximum annealing temperature of 400 °C, after which the coercivity decreased sharply with temperature due to Co particle contraction. The perpendicular magnetic measurements showed much smaller coercivity values, and it did not improve with annealing temperature. Wang *et al.* concluded that CoAg alloy nanowires showed anisotropic coercivity that could be optimized with an appropriate annealing temperature.

Qin *et al.* (Qin, 2002) investigated the annealing effect on coercivity and squareness of CoNi alloy nanowires electrodeposited in self-made high pore density AAO (20 nm pore diameter). Qin *et al.* observed that the crystalline difference of CoNi alloy grains from the bulk Co contributed a great deal to the magnetic behavior. The squareness was improved for high concentrations of Ni (>50 %) in the alloy. The parallel field coercivity saw a maximum of 950 Oe for low Ni content (>10 %), and decreased with higher Ni content. Qin *et al.* concluded that the annealing treatment lowered the coercivity values but increased squareness.

Wang *et al.* (Wang, 2002) revised the structural profile and magnetic behavior of $Ni_{50}Cu_{50}$ alloy nanowires electrodeposited in high aspect ratio AAO (50 nm diameter/ 50 μm length). Parallel magnetic anisotropy was observed. The author pointed out that the Ni atoms in the NiCu alloy wires did not show a proportional, structured placement pattern because the wire electrodeposition was not at steady state.

Khan and Petrikowski (Khan, 2002) investigated the Co and CoFe alloy nanowires electrodeposited in AAO, and compared the wire magnetic properties to the thin film alloy of similar composition. High aspect ratio CoFe nanowires (18 nm pore diameter and 3 μm length) were obtained, and were compared to the 1-2 μm thin films electrodeposited on Cu substrate from the same electrolyte. The $Co_{90}Fe_{10}$ alloy nanowires held the highest parallel coercivity (2275 Oe) followed by the Co only nanowires that showed a smaller coercivity (1188 Oe). Conversely, the Co only thin film had a larger perpendicular coercivity (288 Oe) than the $Co_{90}Fe_{10}$ thin film (187 Oe), while all the nanowire cases had significantly higher coercivity compared to the thin films. A latter study, (Khan and Petrikowski, 2002) showed that parallel magnetic anisotropy, coercivity and squareness decreased drastically with increasing pore diameters ($Hc_{Co90Fe10}$ = 2275 Oe (18 nm pore diameter) and $Hc_{Co90Fe10}$ = 723 Oe (78 nm pore diameter)).

In a different study, Fodor *et al.* (Fodor, 2002) researched compositionally modulated CoFe alloy nanowires in AAO. They observed that at low Fe concentration in the alloy (< 10%), the cobalt crystalline arrangement changed from HCP to FCC, while at higher concentrations of Fe (>15%) the cobalt crystalline arrangement switched to a BCC structure. The largest observed coercivity (2150 Oe) was measured for a $Co_{45}Fe_{55}$ alloy, which had no crystal anisotropy (BCC arrangement). Fodor *et al.* mentioned the significant magnetostatic interactions between wires,

17

which could be explained by dipolar stray fields opposing each other and reducing the field necessary to reverse magnetization.

Ross *et al.* (Ross, 2002) reviewed alloy nanowires obtained by a combination of interface lithography and electrodeposition. The electrodeposition takes place inside a porous polymer layer (57-180 nm pore diameters) set on a silicon wafer coated with gold. After electrodeposition, cylindrical geometries (300 nm tall) were obtained after the template removal. Magnetic Force Microscopy (MFM) proved that small diameter structures showed high remnant magnetization, vital for information readback processes. In contrast, the large diameter wires showed low remanence. Ross *et al.* pointed out that magnetostatic interactions between wires controlled the magnetic behavior of highly packed arrays, which generated instantaneous demagnetization. Ross *et al.* concluded that larger coercivity values, which were needed to avoid instantaneous demagnetization, were obtained for single domain structures observed only in small diameters wires.

Sellmyer *et al.* (Sellmyer, 2001) summarized in review the influence of electrolyte additives on the coercivity and squareness ratios of alloy nanowires. They showed that coercivity increased linearly with increasing Fe content in Ni-Fe alloy nanowires. In the same review, Sellmyer *et al.* mentioned that the addition of Cu and phosphorous to the Fe nanowires decreased their coercivity under 1000 Oe.

Very recently, Bai and Hu (Bai, 2003) reported making FeCo and FeCoNi alloy nanowires by cyclic voltammetry and pulse reverse electrodeposition. Surprisingly, Bai and Hu did not use any porous membrane for electrodeposition. Bai and Hu explained that the anodic cyclic voltammetry guided the formation of nanowires on a flat Cu plate. Furthermore, adding Ni to the electrolyte showed an increase in the wire diameter.

2.2.3 Elemental Nanowires

Ounadjela *et al.* (Ounadjela, 1997) studied the magnetic properties of Co nanowires electrodeposited in polymer membranes (PC) of various pore sizes and observed strong magneto-crystalline anisotropy perpendicular to the wire axis. Ounadjela *et al.* also pointed out that in small diameter nanowires, Co acts as a single domain structure with the easy axis parallel to the nanowire axis.

Piraux *et al.* (Piraux, 1997) realized a comparative study of ferromagnetic Co, Ni, Fe nanowires grown by electrodeposition in polycarbonate membranes of various pore diameters, ranging from 30 to 500 nm. Using low porosity membranes for low dipolar interactions, the researchers observed that all Co, Ni and Fe nanowires exhibited an increase in coercivity as the pore diameter decreases. However, for Co and Ni nanowires, the remanent magnetization decreased with pore diameter, which suggests that wires split into domains when the pores were large. In the case of Co only nanowires, the shape anisotropy competed with the crystal anisotropy, which led to a specific magnetic behavior. Piraux *et al.* concluded that Ni and Fe nanowire magnetic properties were governed by the shape anisotropy.

Schwanbeck and Schmidt (Schwanbeck, 2000), using both porous aluminum templates and polycarbonate membranes, tested different electrolytes and examined the influence on magnetic properties of Co nanowires. Initially, in the non-steady-state fraction of the electrodeposition, galvanostatic control was employed until the voltage reached a constant value at which time the potential was controlled. The authors observed that the growth of nanowires inside the membrane stopped if some of the nanowires reached the surface. The boric acid (pH 3.7) bath yielded the least coercive nanowires in comparison to the propionic acid (pH 6.7) and maleic acid (pH 6.8) baths. The nanowires obtained in AAO membranes of 200 nm pore

diameter showed similar magnetic results in both perpendicular and in-plane measurements. The nanowires grown in PC membrane (100 nm pore diameter) showed higher coercivity for the in-plane measurements compared to the perpendicular to the wire axis measurements.

Interested in data recording materials, Ge *et al.* (Ge, 2000) studied the perpendicular magnetic anisotropy of high-density surface distribution Co nanowires electrodeposited in polycarbonate membranes. Using 400 nm pore diameter membranes, Ge *et al.* applied a magnetic field during the potentiostatic electrodeposition of the nanowires, and different results were obtained when the electrodeposition magnetic field was perpendicular or parallel to the membrane plane. Significant differences in the crystalline structures were observed as a function of magnetic field direction. When the magnetic field applied during the electrodeposition was perpendicular to the membrane, the magnetic anisotropy was enhanced. Furthermore, the perpendicular magnetic field led to a larger coercivity and improved squareness due to a preferred growth direction of the Co crystal under magnetic field influence. Ge *et al.* showed that the Co particles deposited in the pores would have random crystallographic orientation without an applied magnetic field that would force the cobalt grain axis along the applied magnetic field, resulting in a stronger structure.

Garcia *et al.* (Garcia, 1999) investigated the electrodeposition and magnetic behavior of Co nanowires arrays in AAO templates (200 nm pore diameters). From the hysteresis loops (BH), Garcia *et al.* concluded that even though the Co nanowires arrays showed magnetic anisotropy with the easy axis parallel to the wires, the coercivity was a minimum in that direction. In their study, Garcia *et al.* demonstrated that the decrease in coercivity was due to the magnetic interactions between the nanowires.

Thurn-Albrecht *et al.* (Thurn-Albrecht, 2000) showed a different method of making nanowires by electrodeposition into self-assembled copolymer templates. Starting with self-assembled diameter diblock copolymers of polystyrene and polymethylmethacrylate (PMMA), after annealing, applied electric field, and deep ultraviolet exposure, the resulting polymer film contained 14 nm diameter pores inside which Co and Cu nanowires were successfully electrodeposited. Magnetic properties of the obtained Co nanowires showed that array regularity had a tremendous effect on the coercivity. According to their study, highly irregular arrays showed accidental spin switching, so-called recording media noise. Thurn-Albrecht *et al.* concluded that the self-assembled copolymer method could overcome the nanowires' disorder observed in PC membranes that led to decreased coercivity.

Valizadeh *et al.* (Valizadeh, 2001) investigated the concentration distribution of Co during the electrodeposition of Co nanowires into PC membranes (250 nm pore diameter and 20 μm length). During wire growth, Valizadeh *et al.* could identify two separate electrodeposition regions: at the bottom of the membrane (short time) and almost filled pores. Valizadeh *et al.* determined that, for short times, the limiting current was given by Cottrell's expression ($i_{lim} \sim t^{-1/2}$), and the Co diffusion coefficient was calculated to be $D_{Co} = 2.5 \times 10^{-5} cm^2/s$. At longer times, a steady state diffusion controlled current, obtained by the overlapping of the individual nanowires diffusion zones, was given by a different expression ($i_{lim} \sim 1/(r+L)$). Investigation of the magnetic properties of Co nanowires showed improved coercivity values compared to bulk Co, with a preferred magnetic field parallel to the wires axis. Valizadeh *et al.* concluded that for large diameter wires, multi-magnetic domains were present when there was no exterior magnetic field applied.

Almawlawi *et al.* (Almawlawi, 1991) fabricated Fe nanowires by AC electrolysis deposition into self-prepared AAO templates of different diameters, ranging from 20 to 180 nm. For the magnetic characterization of the Fe nanowires, Almawlawi *et al.* concluded that nanowire coercivity strongly depended on the wire aspect ratio and less on the membrane pore density. Furthermore, Almawlawi *et al.* pointed out that Fe nanowire coercivity showed no anisotropy, being only a function of the aspect ratio.

Vila *et al.* (Vila, 2002) were the first to investigate the magnetoresistance (MR) and magnetic transport behavior of isolated Co nanowires. After being electrodeposited in PC (60 nm diameter pore) membrane, the Co wires were removed from the membrane and Electron Beam Lithography (EBL) was used to make contacts along individual wires. EBL gave the capability to obtain information on different segments along the same wire. From the AMR (Anisotropic Magneto Resistance) measurements of a single Co nanowire, Vila *et al.* concluded that the remanent magnetization did not depend on the direction of the applied field. Moreover the remanent magnetization was much different along the same wire, which could explain the vanishing magnetoresistance problems and resistance jumps observed when the measurements cover an array of micron long wires.

Garcia *et al.* (Garcia, 2002) reviewed the MFM (magnetic force microscopy) studies done on nanowires, and emphasized that Co nanowires, 35 nm in diameter, revealed single magnetic domains. Larger diameter wires showed multiple magnetic domains, which caused magnetic disorder. In their study they emphasized the use of nanowires as MFM probes.

In a recent review, Sellmyer *et al.* (Sellmyer, 2001) analyzed transition metal arrays of nanowires electrodeposited in self-assembled aluminum oxide membranes. They concluded that porous aluminum oxide templates, obtained by electrochemical anodization of aluminium in

acidic electrolytes, were excellent mediums for nanowires electrodeposition due to high pore density, uniform pore distribution and high aspect ratios. Sellmyer *et al.* showed that large aspect ratio Co, Ni and Fe nanowires showed magnetization anisotropy, having an easy magnetization axis along the wires axis and 0.9 remanence ratios. The maximum coercivity was shown by Fe nanowires (3000 Oe), followed by Co nanowires (2600 Oe) and lastly by Ni nanowires (950 Oe). In their review, Sellmyer *et al.* highlighted the crucial effect of wire imperfections that led to a curling behavior, controlling the nanowire coercivity and magnetic viscosity. Using a magnetic model simulation, Sellmyer *et al.* also showed that the demagnetizing field could be attributed the wire interactions.

CHAPTER III. NANOWIRES ELECTRODEPOSITION

Arrays of nanowires were electrodeposited by filling up the porous template that served as the cathode in the electrochemical set-up. A 3D substrate schematic is shown in Figure 3.1 (a). Two types of commercially available porous membranes or substrates, polycarbonate (PC) Millipore Isopore™ and aluminum oxide (AAO) Whatman Anodisc were used to deposit nanowires. The polycarbonate membrane fabrication involves a nuclear track etch process, which arises from a bombardment of the polycarbonate film with high-energy particles which produce the paths which later are etched in different chemical baths. This etching process determines the size of the pores. Typical available pore sizes range from 20 nm to 14 μm and a thickness of 6 μm. Figure 3.1 (b) shows a SEM picture of a commercial PC membrane, with a reported pore size of 800 nm. Although the pores seem to have similar diameters, the pore placement is random. In addition, a common problem with PC membranes is frequent pore fusion, but the internal stress in the plated metal nanowires is low due to the polymer elasticity. Anopore Aluminum Oxide (AAO) membranes were also employed as templates for nanowire electrodeposition. AAO filter preparation involves an anodic potential applied to aluminum foil in an acidic environment.
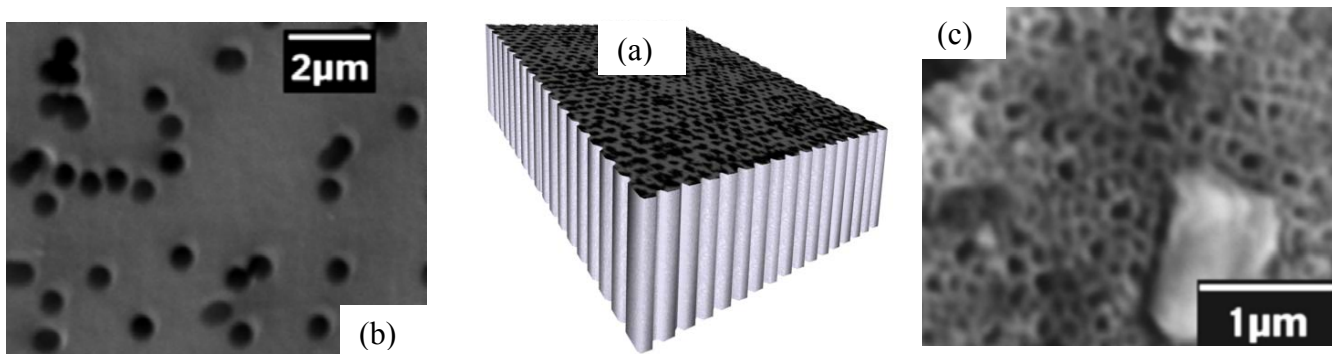
Figure 3.1 Membranes (a) 3D schematic (b) SEM of polycarbonate (c) SEM of AAO

Under electrochemical control, the membrane pores could be controlled. Figure 3.1 (c) shows a SEM picture of a commercial AAO membrane, with a reported pore size of 200 nm and 60 μm in length. Commercially available Anopore AAO membranes having 20 and 200 nm pore diameters were used in our experiments. The membrane serving as the cathode was fixed inside a stationary polyetheretherketone (PEEK) holder exposing a square area of 2.25 cm^2 of the membrane. At the cathode the metal reduction takes place and metal deposits according to:

$$M^{n+} + n\ e^- \rightarrow M(s)$$
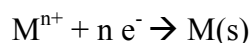
The electrodeposition occurs when an electric current passes though an ionic solution (electrolyte) Figure 3.2 illustrates the three-electrode cell set-up used in this study. A platinum mesh was used as the anode (or counter electrode).
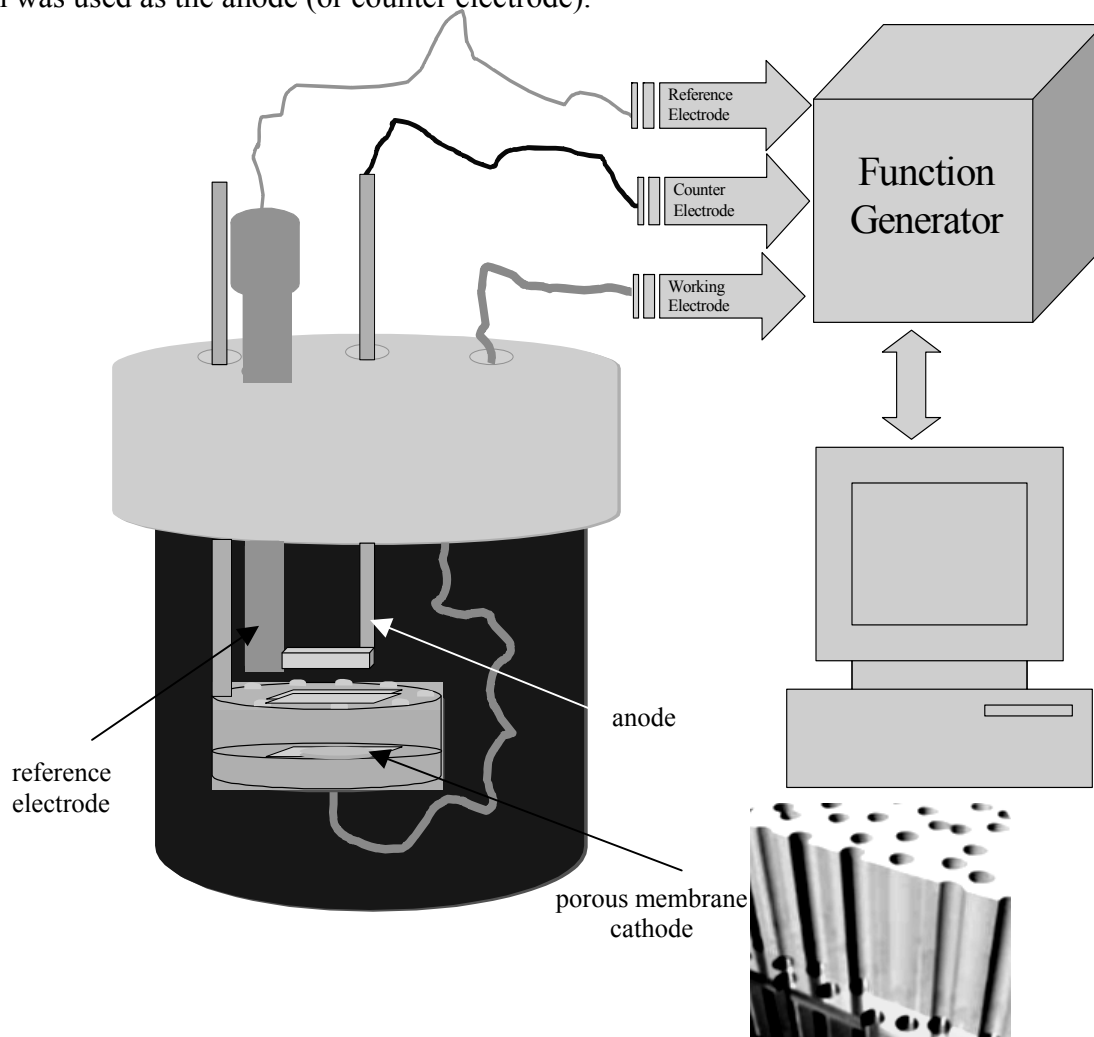
Figure 3.2 Electrochemical set-up

A saturated calomel electrode (SCE) functioned as the potential reference. Since the membrane is not conductive by nature it was sputtered with gold on one side for electrical contact.

Different electrolyte recipes and plating schemes were investigated for the nanowire deposition. Both constant potential plating and pulsed potential plating were carried out with a computer controlled Solatron function generator (model SI 1287). Electrolyte polarization studies, cyclic voltammetry at different sweep rates and impedance measurements were also carried out using the Solatron (model SI 1255B).

The electrodeposition process is stopped when the wires reached the top of the membrane, which is indicated by a sudden increase in the plating current. The typical behavior of nanowire growth is shown in the Figure 3.3 that displays the three different stages of the nanowire growth process. During the first stage of wire growth in the membrane the metal is getting deposited inside the pores while the reduction current takes on a value of 13 mA/cm^2 and the wires growth proceeds in the pores until they fill up completely the membrane and reach the top of the membrane. Beyond this point if the deposition continues the current rapidly increases since the effective electrode area increases. For instance Figure 3.3 shows the actual current response when CoNiCu alloy nanowires were plated inside AAO membrane using -1.9 V vs. SCE as the controlled potential. Mushroom like hemispherical caps form on top of the wires if the deposition continues after the pores fill up like in the 3rd stage of deposition shown in Figure 3.3. The current arrives at a semi-steady state when the nanowires reach the top of the membrane, after 10000 s. Between 5000 and 10000 s, the wires have reached the top of the membrane. The area of the metal deposition is increasing so the current is also increasing. Below 5000 s, the all the metal deposit is going inside the membrane.
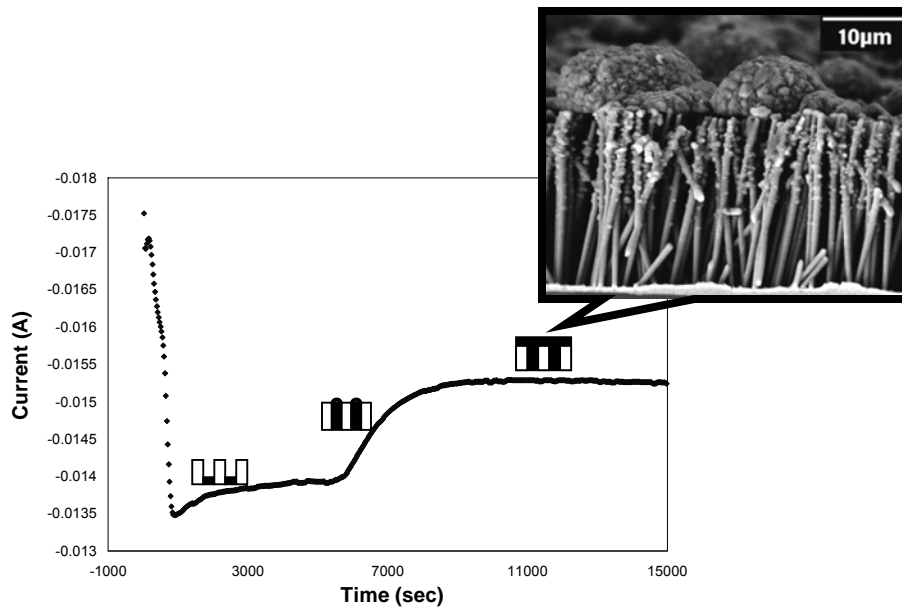
Figure 3.3 Current response for CoNiCu nanowires deposition at –1.9 V in AAO 20 nm pores

Figure 3.4 shows the general schematic of nanowire electrodeposition inside porous membranes.

empty membrane sputtered with Au on the bottom

Electrodeposition

electrodeposited membrane - pores filled with metal

PC dissolved in CH_2Cl_2
AAO dissolved in NaOH

dissolved membrane – nanowires
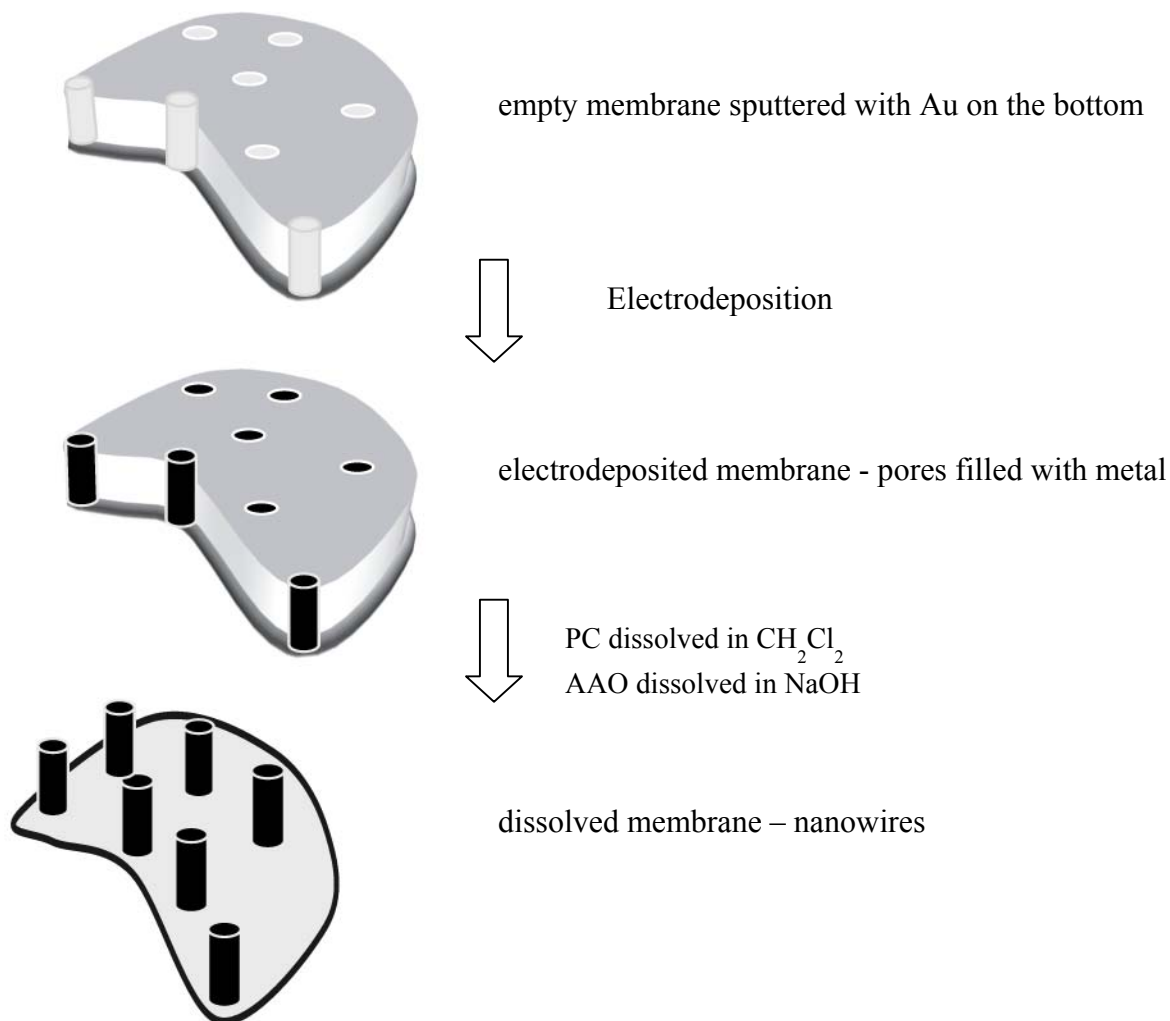
Figure 3. 4 Template electrodeposition schematic

Two main kinds of electrodeposition techniques were employed in making nanowires: (1) constant potential control was used for making elemental and alloy nanowires and (2) pulsed potential for making alternating layers of Cu and CoNi(Fe) alloy. The schematic shown in Figure 3.5 displays the basic concept behind depositing alloy or layered nanowires. Figure 3.5 (a) illustrates the constant potential electrodeposition method used making elemental (Cu) or alloy nanowires. Multilayered nanowires were obtained by stepping the potential between the Cu reduction potential (-0.4 V) and the CoNiFe alloy potential, as shown in Figure 3.5 (b). Layer
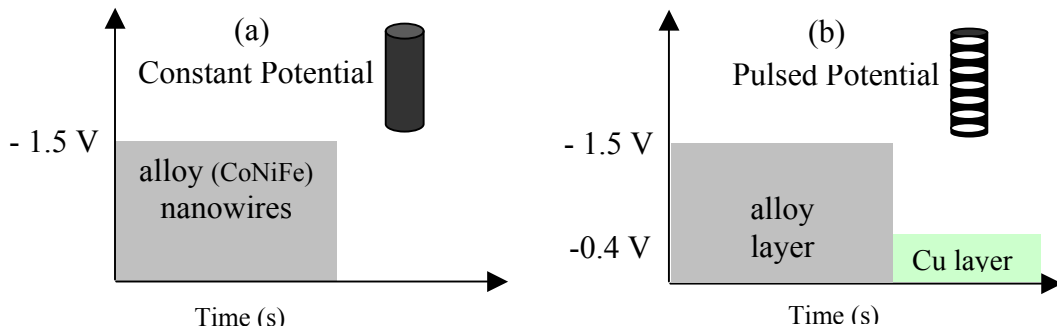
Figure 3.5 Electrodeposition techniques for making nanowires
(a) constant potential for alloy or elemental nanowires (b) pulsed potential for multilayered nanowires

thicknesses could be controlled strictly by changing the layer deposition time. For a typical 20 μm-thick AAO membrane, the number of bilayers required depended on the thickness of the layer sizes. For example, approximately 2400 bilayers were needed to reach the top of the membrane when the Cu reduction potential was -0.4 V for 20 s and the alloy conditions were -1.5 V for 1 s. The potential selection for the Cu layer and alloy layer was based on my previous MS work.

In order to release the nanowires for further investigation, the polycarbonate membranes were soaked in dichloromethane, and the aluminum oxide filter were exposed to 1M NaOH solution for 1h. After dissolving the membrane, the arrays of nanowires were imaged using

Scanning Electron Microscope (SEM-JEOL JSM-840 operated at 20 kV) and Transmission Electron Microscope (TEM JEM-100CX operated at 100 kV). The SEM technique scans the specimen with a focused beam of electrons and produce secondary electrons that are detected and converted into an image. TEM examination involves passing the electron beam through the sample and can obtain a higher magnification than the SEM technique. The electrons' very short wavelength makes it possible to obtain high resolution. The SEM was used to inspect arrays of nanowires, while the TEM was utilized to examine nanowire layers and nanotube formation.

Figure 3.6 shows electron microscope images of different types of nanowires. Figure 3.6 (a) shows a low magnification SEM image of CoNiFeCu alloy nanowires obtained in 50 nm pore PC membranes. In this micrograph the wires were held together by the Au sputtered side of the membrane since the membrane was only partially removed. Figure 3.6 (b) shows a SEM image of elemental Cu nanowires obtained in 20 nm pore AAO membranes after dissolving the membrane using 1M NaOH. Figure 3.6 (c) shows a TEM image of CoNiFeCu alloy nanowires obtained in 50 nm pore PC membranes when the membrane was completely removed. These CoNiFeCu alloy nanowires were 150 nm in diameter and about 5-micrometer in length. Figure 3.6 (d) shows a SEM image of CoNiFeCu alloy nanowires when the AAO membrane was completely removed and the wires lay disorientated on the SEM Cu tape. Figure 3.6 (e) shows multilayer nanowires from a colloidal suspension obtained after completely dissolving the polycarbonate membrane and collecting the wires on carbon grids. When making multilayers, the CoNiFeCu alloy layer potential was controlled at -1.9 V for a period of 20 s. The TEM micrograph shows that for 20 s of deposition at –1.9 V the alloy layers came out to be 200 nm thick. The lighter layers are pure Cu deposited using a potential of -0.5 V for 200 s, yielding 20 nm thick Cu layers. The TEM micrograph also shows that the layer thickness changed along the

wires, being smaller at the bottom and gradually increasing towards the top of the membrane. This change in layer thickness along the wires could be caused by changes in the diffusion layer thickness.

Compositional analysis of the nanowire arrays was obtained using Energy Dispersive Spectroscopy (SEM-EDS) and X-Ray Fluorescence (XRF KEVEX Omicron). SEM-EDS provides a qualitative composition analysis, which uses a stream of high-energy electrons to knock off inner shell electrons. On contact, electrons from a higher energy level lose energy filling in the vacancies left. The energy conservation principle dictates photon creation. The released photon energy will be equal to the difference of the two exchanged energy levels. Since these energy levels are unique for an atom type, the released photon will be characteristic of the type of atom from which it was emitted. Therefore, from the released photon energy, the sample composition is determined. SEM-EDS analyses a spot size of about 1μm.
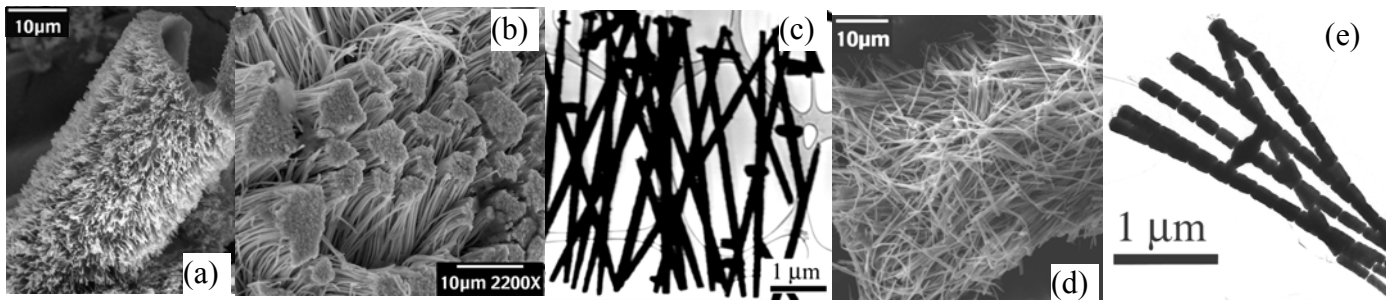
Figure 3.6 Electron microscope images of electrodeposited nanowires (a) SEM of CoNiFeCu alloy nanowires in PC (b) SEM of Cu nanowires in AAO (c) TEM of alloy CoNiFeCu nanowires in PC (d) SEM of CoNiFe alloy nanowires in AAO (e) TEM of multilayered CoNiFe/Cu nanowires in PC

XRF was employed to obtain the quantitative average composition analysis of the nanowire array. The XRF analysis is based on a primary x-ray tube that emits characteristic x-rays of known energy. The specific instrument used in our lab contains a Rh tube. An electron can be ejected from its atomic orbital by the absorption of a light wave (photon) of sufficient energy. Any elements in the sample having excitation energy below that of the primary beam

energy will be fluoresced. The particular wavelength of fluorescent light emitted is related to the number of photons per unit time, (peak intensity or count rate) and to the amount of the specific element in the sample. Therefore, by determining the energy of the X-ray peaks and by calculating the count rate of the various elemental, it is possible to quantitatively measure the concentration of these elements in the sample.

The magnetic properties, such as Giant Magnetoresistance (GMR) were investigated with PPMS (Quantum Design Physical Property Measurement System 6000) using an electric current ranging between 0.1-1 mA and a magnetic field in between −1 T to 1 T. In the GMR set-up, the magnetic field was set perpendicular to the electric current passing through the nanowires, the magnetic field being parallel to the layers. Most measurements were performed at room temperature.
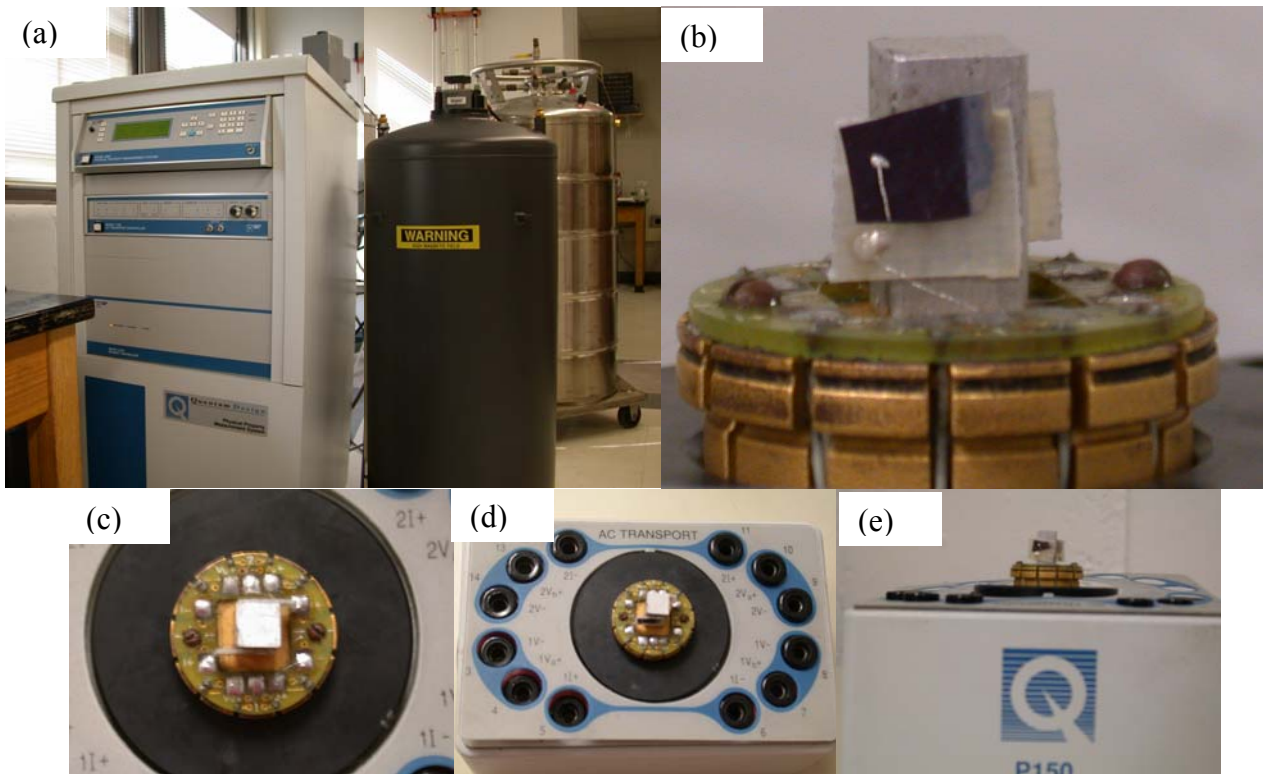
Figure 3.7 GMR measurements (a) PPMS (b) Pt. contact on membrane containing nanowires (c) mounted samples on the puck –top view (left) (d) zoomed out puck with samples (e) side view puck with sample

The highest obtained GMR was re-measured at 100 K. The multilayered nanowires showed fairly large electrical resistance, depending on the number of wires connected in parallel. Figure 3.7 shows photographs of the PPMS, the GMR set-up and GMR measurement contacts. Selected GMR samples were annealed in a pure H_2 flowing environment. The annealing temperature was set to 300 ^{o}C. The temperature was ramped at 2°C per minute and the sample was soaked at 300 ^{o}C under continuous H_2 flow for 3 hours. The heating was shut off and the sample allowed to cool to room temperature still under H_2 flow. The quartz boat containing the GMR samples, was placed in the middle of the furnace to avoid temperature gradients. Before pure H_2 flow was started the chamber was purged with He gas at room temperature to remove any traces of air.

CHAPTER IV MULTILAYERED NANOWIRES

To the best of my knowledge, our lab is the first to examine the combined Co-Ni-Fe-Cu system in nanowires and nanotubes for GMR effect (Huang, 2004, Davis 2006). Therefore, the present work focuses on this quaternary CoNiFeCu/Cu electrodeposition in the form of multilayered nanowires and the investigation of magnetic properties.

4.1 Electrodeposition

Multilayered nanowires were electrodeposited using a double potentiostatic scheme, stepping between a higher negative CoNiFe potential and the more noble Cu deposition potential. All experiments were carried out with a Solatron 1255 B/1287 potentiostat/function generator. The overpotential was controlled versus a saturated calomel reference electrode (SCE). The open circuit potential (OCP) was $\pm$ 0.05 V vs. SCE.

Since Cu can be easily reduced, the concentration of Cu in the electrolyte was kept low, in order to have Cu deposition under mass transport control, while all the other elements (Co-Ni-Fe) would be deposited under kinetic control. The iron group alloy deposition is also called anomalous codeposition, since the least noble element (Fe) tends to deposit before the Ni and Co, even thought these elements have a more noble reduction potentials than Fe. To limit the preferential Fe deposition, Co and Ni concentrations in the electrolyte were larger than the Fe concentration. The main electrolyte for CoNiFeCu/Cu nanowire deposition was composed of $CoSO_4$ (50 mM), $NiSO_4$ (18 mM), $FeSO_4$ (0.5 mM), $CuSO_4$ (1 mM), potassium tartrate (20 mM) and sulfamic acid (10 mM).

In my MS thesis work the CoNiFeCu electrolyte was characterized and optimized for the electrodeposition of nanowires. Polarization curves of the electrolyte were performed using an empty PC membrane as the cathode. From studying the influence of electrolyte agitation

(mixing) in the form of N_2 bubbling, it was concluded that when mixing was induced the Cu limiting current would increase immensely which would translate in a larger Cu content into the ferromagnetic layer, which would in turn damage the GMR.

Figure 4.1 shows a polarization curve of the CoNiFeCu electrolyte, using a potential sweep rate of 5 mV/s. Impedance measurements were performed and the ohmic drop was accounted for. The Cu limiting current was revealed to be 1.1 mA, while the CoNiFe alloy limiting current was observed to be 24.5 mA. From the polarization curve, the Cu deposition potential was noted to be between -0.25 V and -0.6 V, while the alloy deposition potential was in the more negative range between -1.2 V to -3 V.
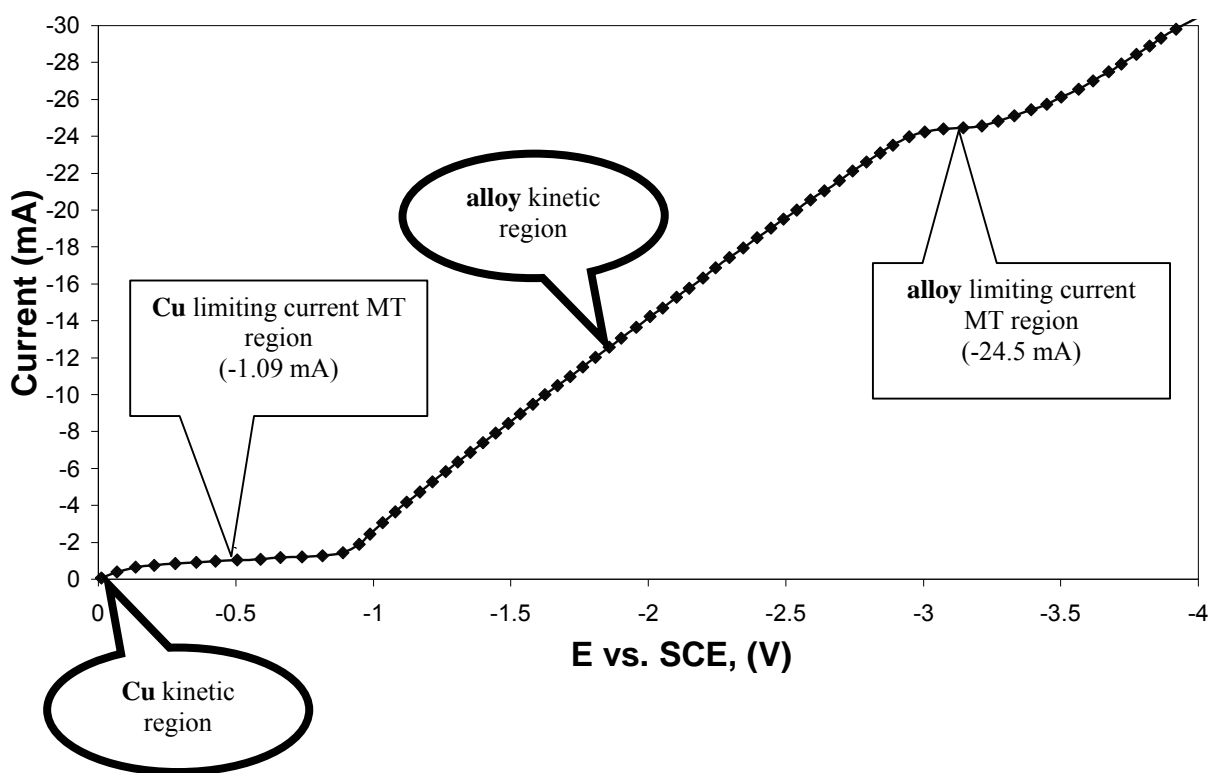
Figure 4.1   CoNiFeCu electrolyte polarization curve

In my previous work Co, Ni, Fe and Cu individual partial currents as a function of potential were calculated using Faradays law. The partial current densities are shown in Figure 4.2. It is important to note although Fe was kept in much smaller quantities in the electrolyte its

limiting current was comparable to the Ni limiting current, confirming the anomalous codeposition behavior of CoNiFe.
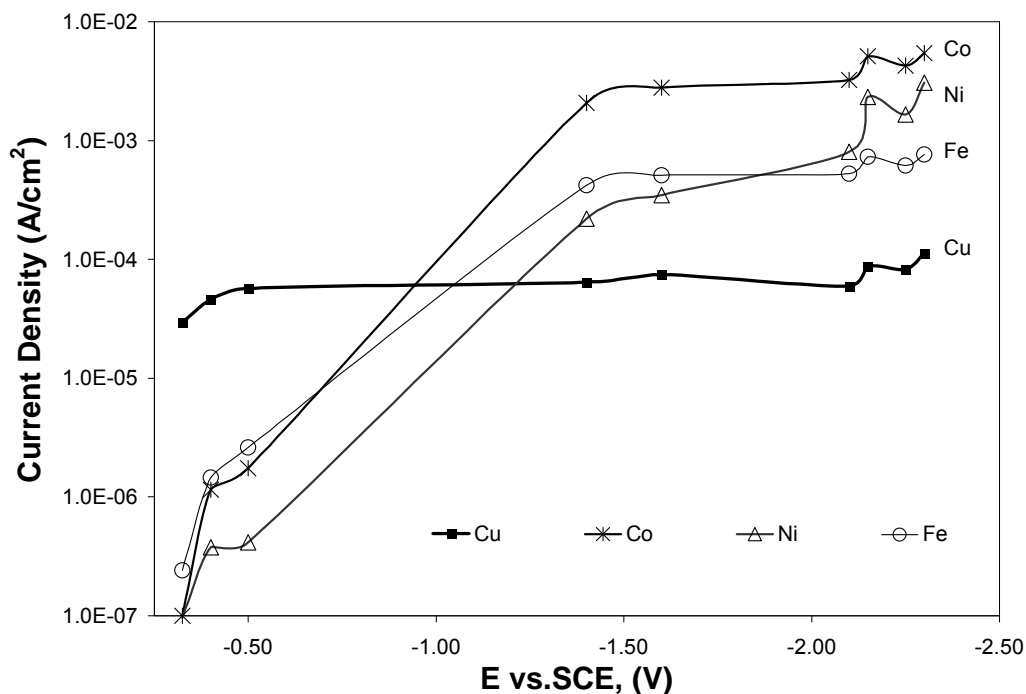
Figure 4.2   Partial currents of Co, Ni, Fe and Cu

To determine the optimal conditions at which pure Cu or alloy of CoNiFe would deposit, several constant potential depositions were performed and from the XRF composition analysis it was concluded that 98 wt. % Cu was deposited at -0.325 V and minimal Cu (1 wt.%) was deposited at –2.4 V.

A series of alloy nanowire deposition experiments were performed using different constant potentials. Judging from the current behavior as a function of potential during nanowires deposition it was concluded that the nanowire deposition was not a steady state process. When the pores were empty the current dropped suddenly and reached a semi-steady state when the wires were growing. The current gradually increased with the filling of the pores and reached a second semi-steady state when the wires reached the top of the membrane. When

the wires reached the top of the membrane the deposition area became constant and the resulting current was constant. Given the membrane thickness, it was possible to calculate the time it would take to fill up the pores with nanowires. For a constant potential of −1.9 V vs. SCE it only took 700 s for the nanowires to reach the top of the membrane (6-micron deep pores). However during Cu deposition the current density was lower compared wit the alloy nanowire case, therefore the time to fill up the pores was much larger (5000 seconds). It was concluded that the long transient region at the start of the deposition was due to changes in the Cu concentration gradient.

Multilayers of pure Cu sandwiched with magnetic CoNiFeCu alloy layers were deposited into the membrane pores using a double potentiostatic pulsing scheme show in Figure 4.3. Stepping between the CoNiFe and Cu deposition potentials, alternating alloy and Cu layers was achieved from the same electrolyte. Faraday's law was used to calculate the time to electrodeposit nanometric size layers. A detailed MathCAD calculation for determining the electrodeposition time and the bilayers number is included in the Appendix. When making the multilayered it is important to notice that the alloy layer would also contain traces of Cu. Switching from the CoNiFe potential (-1.9 V) to the more noble Cu potential (−0.4 V), the current transitions though an anodic (positive) region until it settles down to the Cu deposition current (-0.001 A). The anodic current will dissolve some of the Co rich layer previously deposited. To ensure that the anodic current would not dissolve the entire CoNiFe layer, different alloy deposition times were investigated. In essence, charge deposition, which equals to the applied current times the deposition time, was monitored so that the portion of anodic Cu current would be negligible compared to the alloy deposition current.
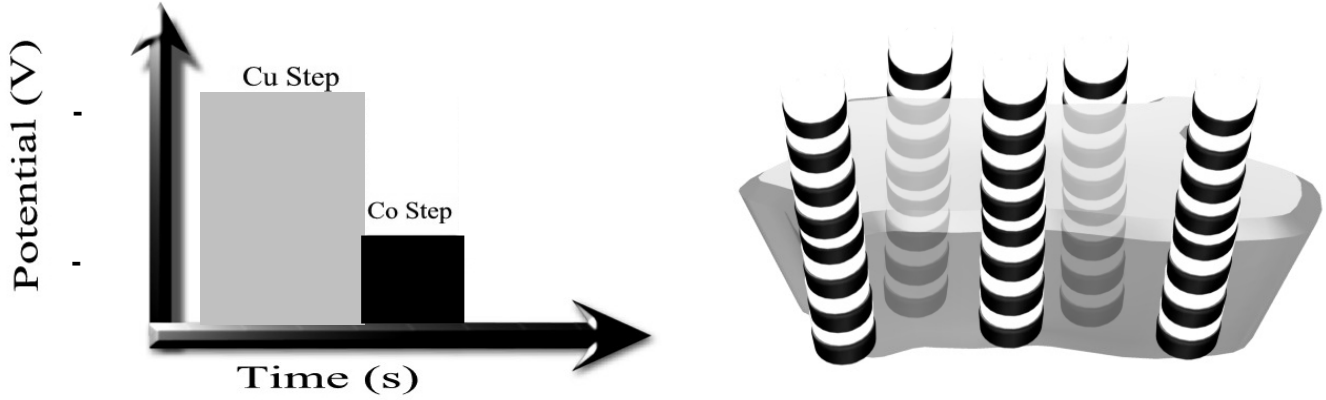
Figure 4.3 Potential pulsing scheme applied to make multilayered nanowires

The schematic shown in Figure 4.4 illustrates the partial dissolution of the alloy layer when the current becomes anodic.
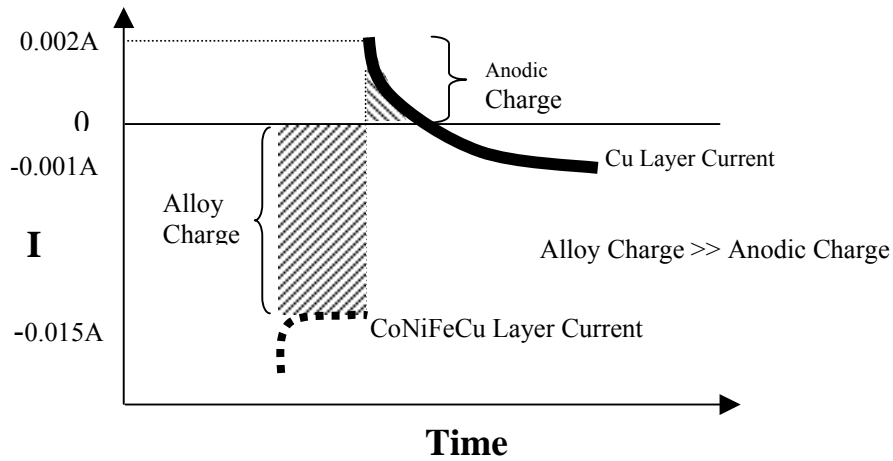
Figure 4.4 Potentiostatic pulsing charge control

In my previous MS work I electrodeposited CoNi/Cu multilayered nanowires and examined them using TEM. One of the samples that turned out to have good magnetic properties was electrodeposited using the following potentiostatic pulse plating parameters: CoNiCu alloy layer (–1.9 V vs. SCE for a period of 1 s)/ Cu layer (–0.325 V vs. SCE for a period of 15 s). After the 2400 bi-layers of alloy/Cu layers, the deposition was stopped and the membrane was dissolved in order to examine the nanowires with the TEM. From the examined micrograph the

alloy layers were 10 nm thick and the Cu layers were 8 nm thick. From the TEM micrograph and knowing the electrodeposition times the Cu current efficiency was determined to be 70 %, while the CoNi current efficiency was calculated to be 35 %.

4.2 CoNiFe/Cu Multilayered Nanowires GMR Results

Due to their intrinsic geometry, multilayered nanowires favor the study of perpendicular magneto-transport phenomena, CPP-GMR. The experimental set-up for magnetic measurements is shown below in Figure 4.5.   Under no magnetic field, the nanowires antiferromagnetic-coupled multilayers show a certain resistance, which decreases when the nanowire sample is placed in a magnetic field.
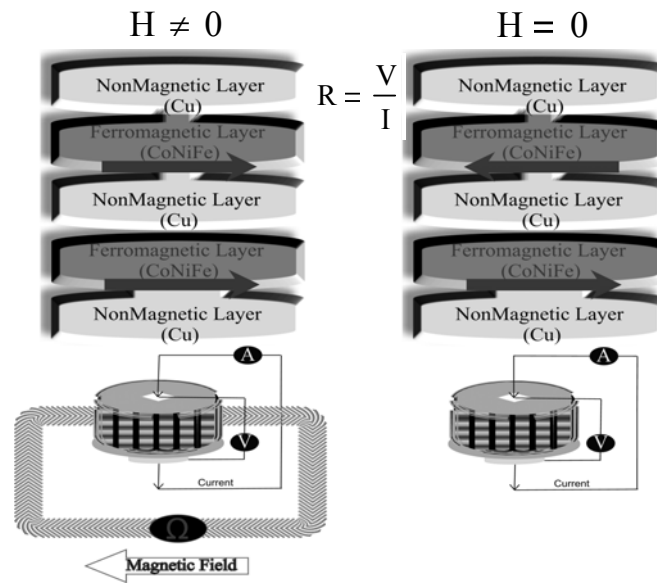
$$R_{H \neq 0} < R_{H=0}$$

Figure 4.5 Nanowires CPP-GMR measurement

The electron spins of adjacent magnetic layers align under a certain magnetic field allowing the majority carriers to travel less scattered along the wires. Minimizing electron scattering across the layers, the magnetic field promotes electron travel, therefore decreasing electrical resistance.

For GMR measurements multilayered nanowires of CoNi/Cu and CoNiFeCu/Cu were fabricated in 60 μm thick commercially available anodized aluminum oxide membranes (Whatman, Anodisc 25). The pore size used was 0.02 μm. Electrodeposition was carried out under potentiostatic pulsing without agitation using a base electrolyte composed of 50 mM $CoSO_4$, 18 mM $NiSO_4$, 1 mM $FeSO_4$, 1 mM $CuSO_4$, 20 mM Na-K tartrate, 10 mM sulfamic acid and 10 mM boric acid. The concentrations of $CoSO_4$, $NiSO_4$ and $FeSO_4$ were varied for GMR investigation.   The electrolyte had an equilibrium pH of 4, and was not adjusted. To keep the layers flat, a Cu bottom was first deposited followed my 2400 bilayers that would not complete the nanowires growth.
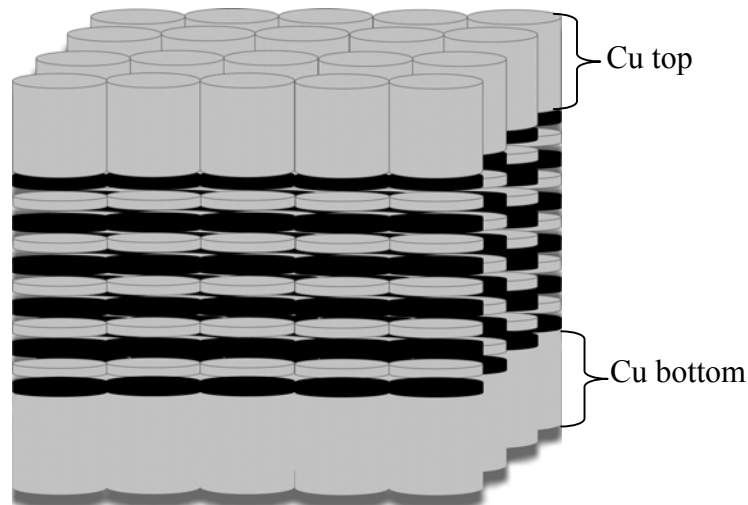
Figure 4.6 Multilayered nanowires with Cu top/bottom

Before the nanowires reached the top of the membrane, the multilayers were stopped and a Cu top was deposited to insure the final growth of the nanowires. Figure 4.6 shows a sketch of the multilayers placed in between the Cu top and bottom. The orientation of the magnetic field was parallel to the nanowire layers and perpendicular to the current passing through the nanostructures. All magnetic measurements were performed at room temperature.

4.2.1 The Effect of Electrodeposition Potential on GMR

In my MS work I determined and optimized the Cu layer thickness, which was one of the most important parameters in obtaining GMR. For a given potential the Cu deposition time was tested and optimized to yield the highest GMR. At room temperature the GMR showed a maximum of 15% for a Cu layer deposited for 17 s. When the Cu layer thickness was slightly increased by a longer deposition time (20 seconds), the GMR decreased drastically to 5 %. The GMR also decreased to 8% when the Cu layer was thinner (15 seconds deposition). It was concluded that a thicker spacer, represented by the nonmagnetic Cu layer, would make it harder for the magnetic CoNi alternating layers to sense each other and spin-couple, damaging the GMR effect. When the Cu spacer is too thin, the GMR effect would also suffer either due to non-discrete layering or from a lower number of coupled layers.

The alloy layer thickness was also important in obtaining GMR. In this study we investigated the optimal alloy deposition potential and time. To find the optimal alloy deposition time, the Cu layer was kept constant at (-0.325 V for 20 s). The alloy layer deposition potential was set to (-1.5 V) and the deposition time was varied between 0.5 and 2 s. Figure 4.7 shows the effect of the alloy layer deposition time on the GMR. The maximum resistance drop of 16 % was observed when the alloy layer was controlled at (-1.5 V for 1 s). When the CoNi layer time was halved to 0.5 s, the GMR decreased drastically to 6 %. When the magnetic alloy layer is too thin, the GMR effect decreased due to non-discrete layering and smaller magnetic layer reorientation. When the alloy layer time was doubled to 2 s the GMR decreased even more to 4 %. A thicker magnetic layer would lead to individual domain forming within the ferromagnetic layer and more difficult spin-coupling effect therefore damaging the GMR. Figure 4.8 shows a TEM picture of the CoNi/Cu sample that showed the highest GMR. The light layer is the non-

magnetic Cu layer that was deposited for 20 s and its thickness can be observed to be 9 nm. The darker layer is the magnetic alloy that was deposited for 1 s showing. The magnetic layer had a thickness of 6 nm.
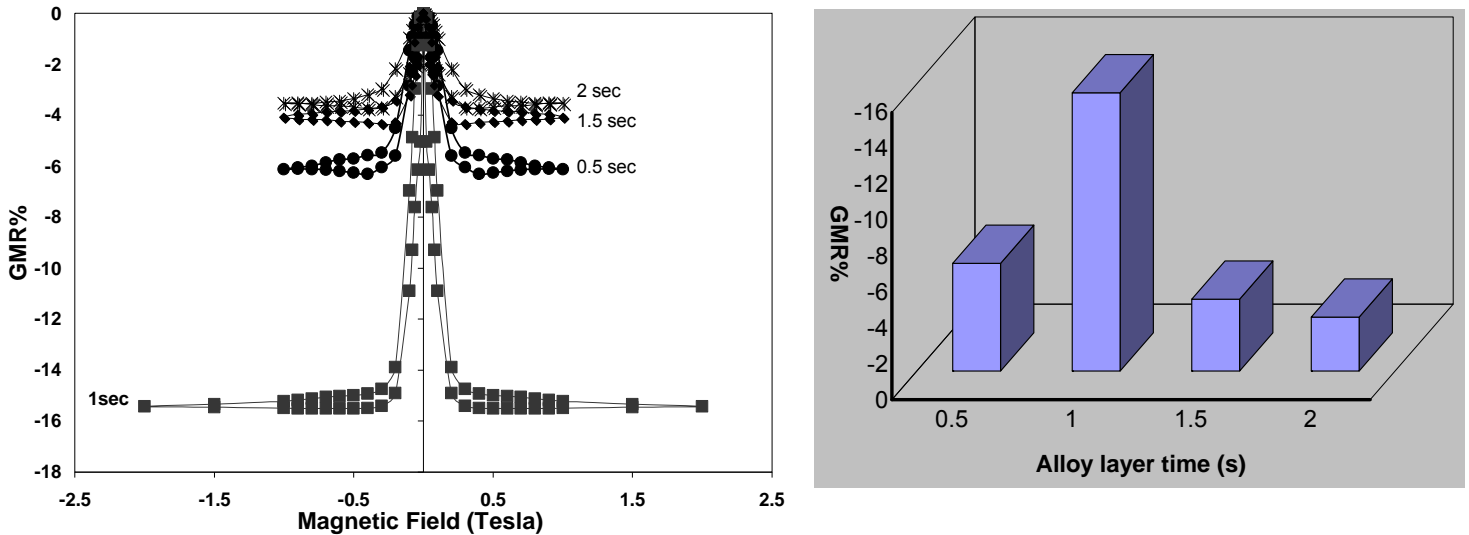
Figure 4.7 Alloy layer deposition time influence on CoNi/Cu nanowire GMR
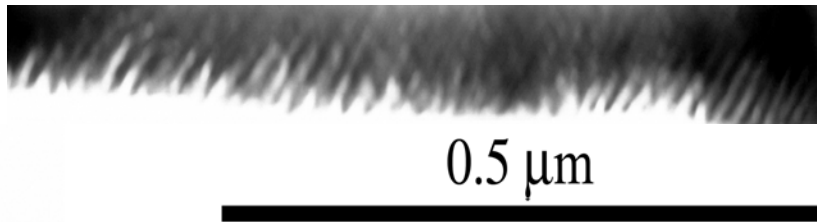
Figure 4.8 TEM of CoNi/Cu Nanowires
Cu layer: (-0.325 V for 20 s)/CoNi layer (-1.5 V for 1 s)

When Fe was introduced into the electrolyte the next parameter to be optimized to obtain larger GMR values was the alloy deposition potential. Table 4.1 summarizes the electrolyte composition and deposition conditions. Figure 4.9 shows the effect of alloy deposition potential on GMR. The Cu layer was deposited at (-0.4 V for 20 s) while the alloy layer potential was varied between (-1.4 and -2 V). The alloy deposition time was set for 1 s. The GMR decreased

at higher overpotentials. The highest GMR (20 % at 0.2 Tesla) was obtained at the lowest alloy deposition potential of (-1.4 V). This is the largest GMR value recorded in the CoNiFe/Cu system in both thin films and nanowires obtained by electrodeposition.

Table 4. 1 CoNiFeCu electrolyte

Electrolyte (mM)		Cu Layer Potential (V)	Cu Layer Time (s)	Alloy Layer Potential (V)	Alloy Layer Time (s)
$CoSO_4$	50				
$NiSO_4$	25				
$FeSO_4$	0.5	-0.4	20	varied	1
$CuSO_4$	1				
Na-K Tartrate	27				
Sulfamic Acid	10				

Figure 4.10 shows a TEM picture of the multilayered nanowires that had the highest GMR. The multilayers are clear and evident especially on the wire edges. The dark inside region depicting the middle of the wire is typical for wire formation in contrast to the tube formation that has a light, see-through inside. The light layer is Cu and it was measured to be 4.15 ± 0.7 nm of standard deviation. The dark layer is the alloy CoNiFe and it was measured to be 5.57 ± 0.4 nm of standard deviation. These layer thicknesses are consistent with what is expected using Faraday's law calculation.

4.2.2 Electrolyte Concentration Effect on GMR

Figure 4.11 (a) shows the effect of Fe concentration when the electrolyte concentration of $CoSO_4$ was constant at 50 mM. Different amounts of $FeSO_4$ were added to the CoNiCu electrolyte and multilayered CoNiFe/Cu nanowires were deposited. The Cu layer was deposited at -0.4 V for 20 s and the alloy layer was reduced at -1.5 V for 1 s. In Figure 4.11 (a), it was observed that the GMR decreased at higher concentration of $FeSO_4$ and affected the saturation magnetization field. The saturation magnetization field was reduced to 0.06 Tesla when the Fe concentration was 2.5 mM. Concentrations greater than 2.5 mM $FeSO_4$ increased the saturation

magnetization field. Electrolyte polarization curves for different amounts of Fe are shown in Figure 4.11 (b). The total current increased significantly with more Fe added to the electrolyte. Since the deposition time and potential were constant, the alloy layer thickness increased with the addition of Fe.
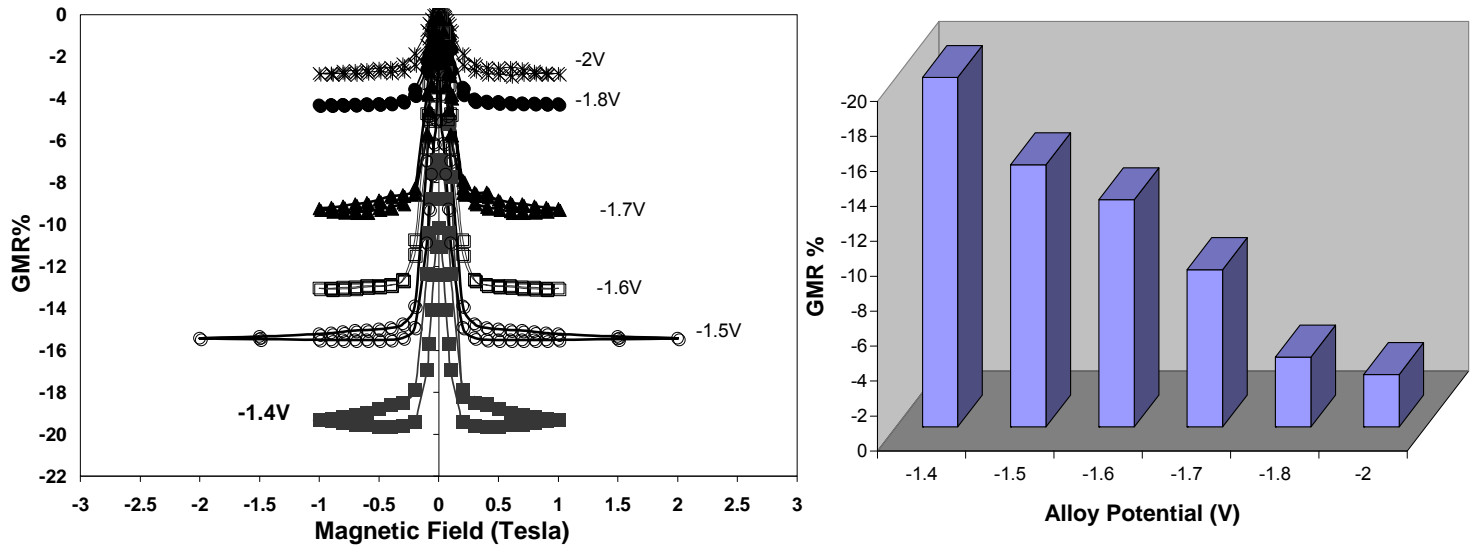
Figure 4.9 CPP-GMR % in CoNiFeCu /Cu as a function of alloy layer potential
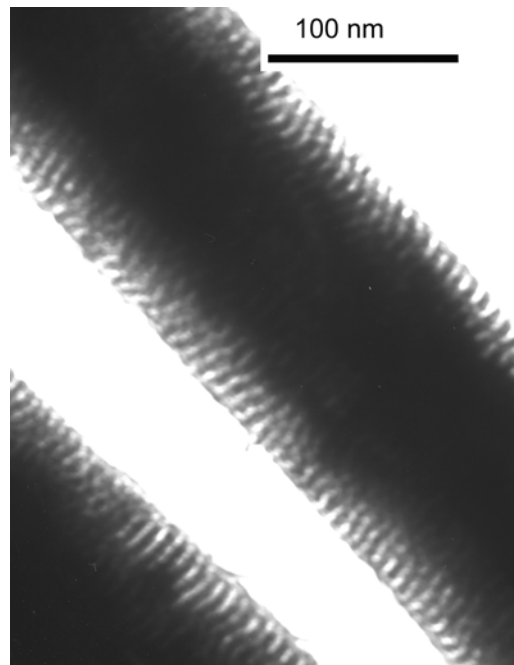
Figure 4.10 TEM of multilayered CoNiFe/Cu nanowires with highest GMR
(-0.4 V for 20 s)/(-1.4 V for 1 s)

Figure 4.11 (c) shows a TEM picture of the nanowires deposited from the 1mM FeSO4 electrolyte. The Cu layer is observed to be 10.5 nm while the alloy layer was 8 nm.
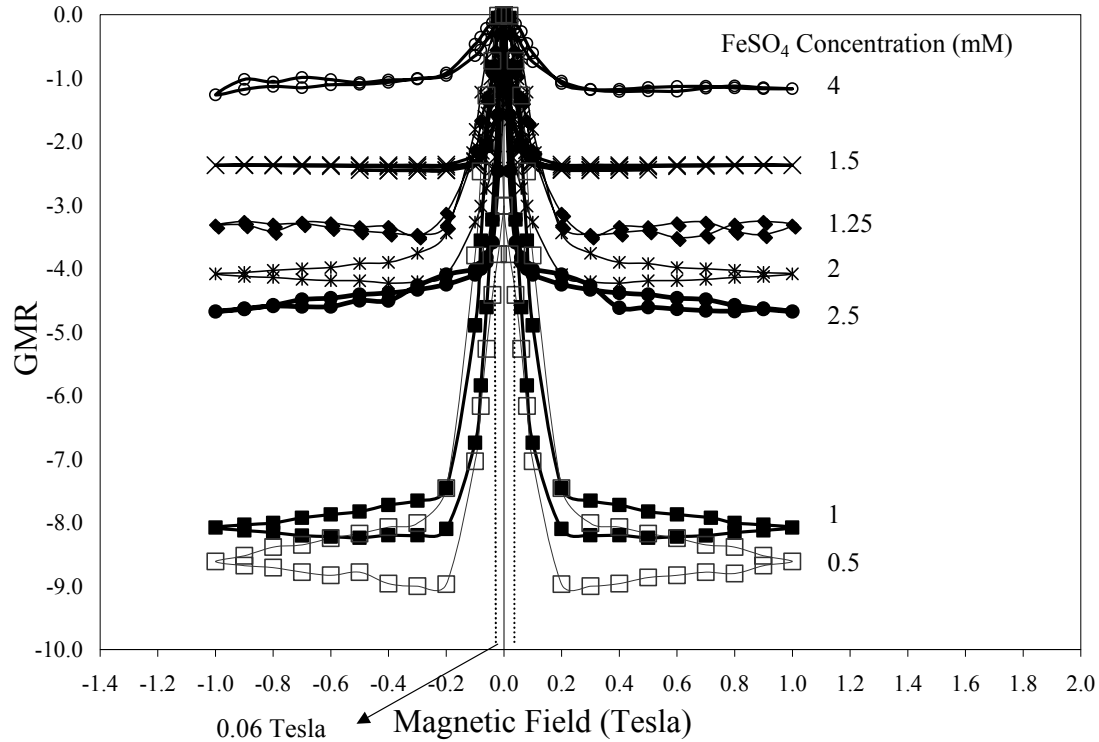
Figure 4.11 (a) CoNiFe/Cu nanowires GMR (different $FeSO_4$ concentrations)
(-0.4 V for 20 s)/(-1.5 V for 1 s)

Electrolyte composition influenced GMR by affecting the alloy layer composition and thickness. The XRF compositional analysis in Table 4-2 shows that when more $FeSO_4$ was added to the electrolyte, more Fe was found in the deposit. Furthermore, with the addition of $FeSO_4$ to the electrolyte the GMR tended to decrease, although the saturation magnetization field was improved. A large amount of $FeSO_4$ (4 mM) had no favorable qualities. The last column in Table 4-2 shows the relative Fe concentration in the deposit (the ration of Fe wt. % to the other components). The Fe to CoNiCu ratio increases with the increased $FeSO_4$ in the electrolyte and agrees with the anomalous codeposition theory.
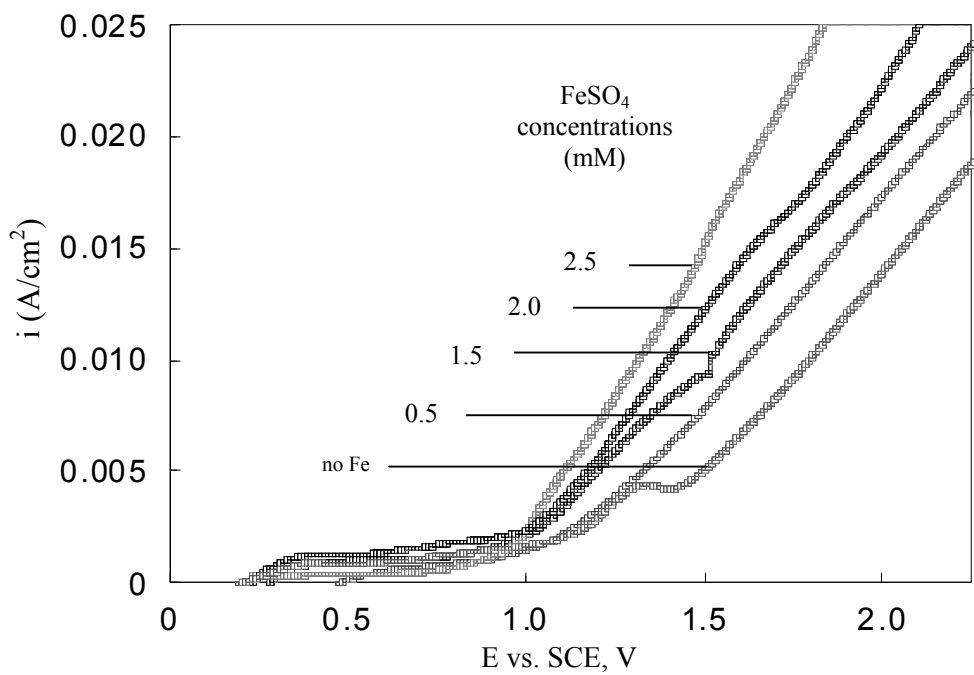
Figure 4.11 (b) CoNiFeCu polarization curves (different $FeSO_4$ concentrations), 25 mV/s
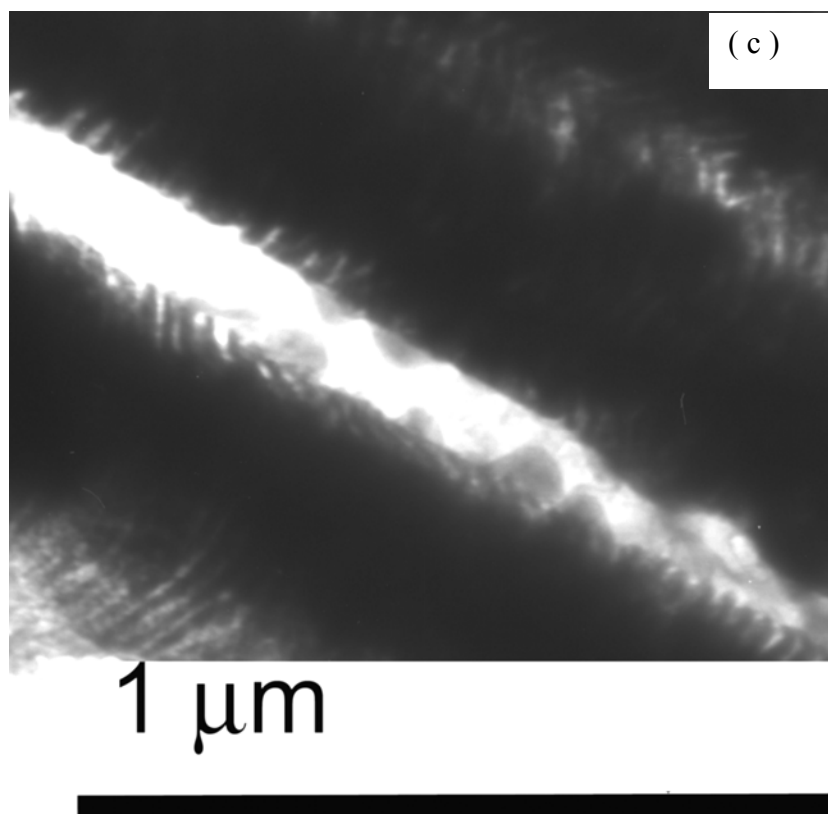
Figure 4.11 (c) TEM of CoNiFe/Cu nanowires from the 1 mM $FeSO_4$ electrolyte

Table 4-2 XRF Composition analysis of CoNiFe/Cu nanowires
(different amounts of FeSO₄)

FeSO₄ (mM)	Composition wt. %				(Fe$_{CoNiCu}$)%
	Fe	Ni	Co	Cu	
0.5	1.26	5.37	19.53	73.82	1.591
1	1.46	3.52	36.27	58.71	2.346
1.5	2.56	6.22	16.3	74.39	3.176
2	2.835	5.91	14.6	76.51	3.44
2.5	3.71	5.72	18.01	72.54	4.741
4	7	5.007	15.67	72.31	9.054

Figure 4.12 shows the influence of different amounts of $CoSO_4$ in the electrolyte without $FeSO_4$. The Cu layer was deposited at -0.4 V for 20 s and the CoNi alloy layer was deposited at -1.9 V for 1 s. Figure 4.12 (a) shows the effect of Co concentration on the nanowire GMR. Higher GMR (15 %) was recorded for low Co concentration (50 mM). The GMR decreased for higher concentration of $CoSO_4$. The saturation magnetization field was slightly reduced at higher $CoSO_4$ concentrations. Electrolyte polarization curves for different amounts of Co are shown in Figure 4.12 (b). Since the total current density increased slightly in the region where the magnetic alloy layer was deposited, with more Co added to the electrolyte, the alloy layer thickness may also slightly increase with the addition of Co in the deposit. With the addition of $CoSO_4$ the GMR also tended to decrease. The largest CoNi/Cu GMR value observed (15 %) occurred at a larger saturation field, compared to the case with Fe in the deposit, CoNiFe/Cu (2.5 mM $FeSO_4$).

Figure 4.13 shows the effect of Ni concentration in the CoNiFeCu/Cu nanowires GMR. Different amounts of $NiSO_4$ were added to the CoNi(Fe)Cu electrolyte and multilayered CoNi(Fe)/Cu nanowires were deposited. The Ni concentration was varied between 25 and 57 mM. The concentration of $CoSO_4$ was 50 mM. The Cu layer was deposited at (-0.4 V for 20 s)

and the alloy layer was reduced at (-1.5 V for 1 s).   Table 4-3 summarizes the electrolyte composition and deposition conditions.
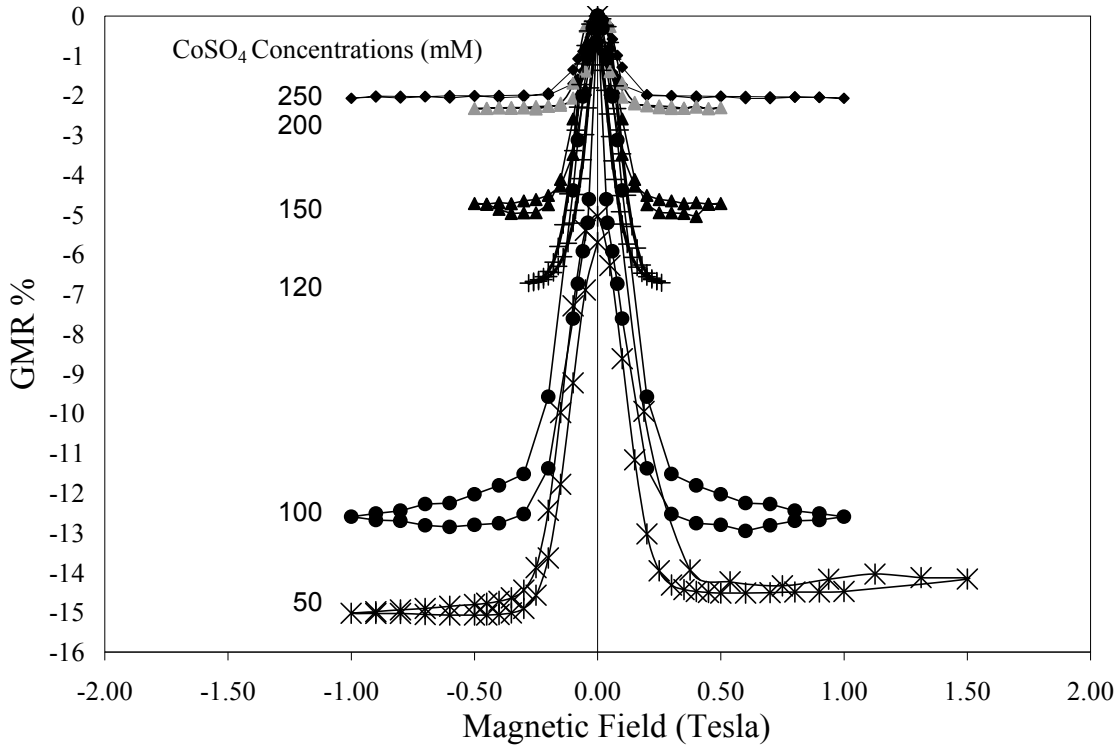
Figure 4.12 (a) CoNi/Cu nanowires GMR for different $CoSO_4$ concentrations
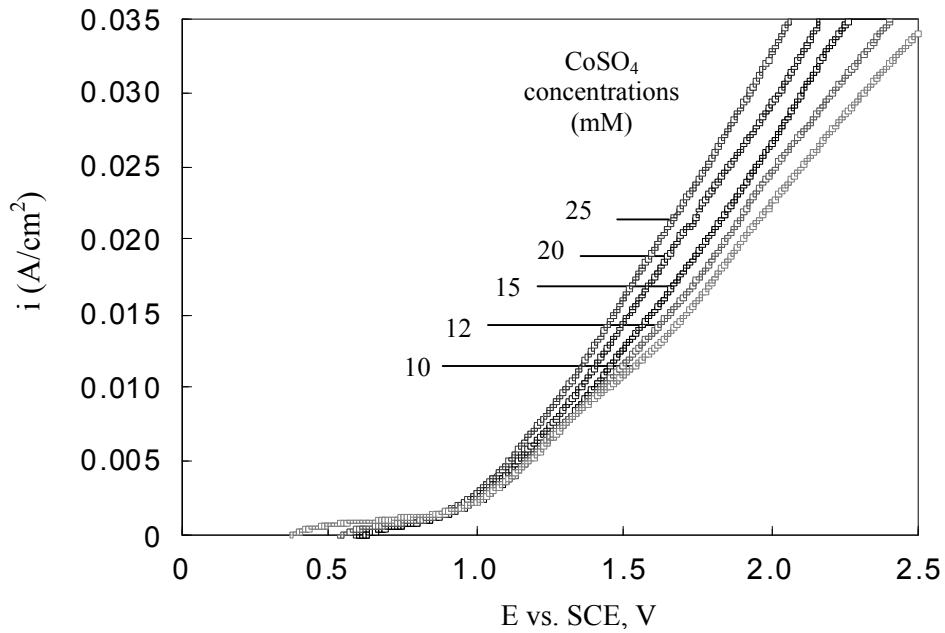
Figure 4. 12 (b) CoNiCu polarization curves (different $CoSO_4$), 25mV/s
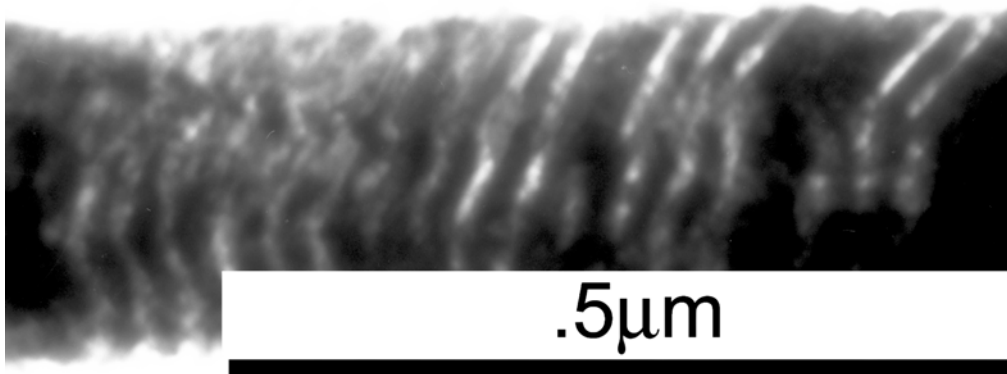
Figure 4.12 (c) TEM of CoNi/Cu nanowires from the 50 mM CoSO$_4$ electrolyte

Table 4-3 CoNiFe/Cu electrolyte and deposition conditions

Electrolyte (mM)		Cu Layer Potential (V)	Cu Layer Time (s)	Alloy Layer Potential (V)	Alloy Layer Time (s)
CoSO$_4$	50				
NiSO$_4$	varied				
FeSO$_4$	0.5	-0.4	20	-1.5	1
CuSO$_4$	1				
Na-K Tartrate	27				
Sulfamic Acid	10				

Figure 4.13 (a) the GMR increased at higher concentration of NiSO$_4$. Figure 4.13 (b) shows polarization curves of the electrolyte when more NiSO$_4$ was added and it could be observed that the total current increased significantly with more Ni added to the electrolyte. Since the deposition time and potential were constant, the alloy layer thickness increased with the addition of Ni. Figure 4.13 (c) shows that magnetic saturation field slightly decreased at higher Ni concentrations.

Ni concentration effect was then tested in the CoNiCu system. Figure 4.14 shows the effect of Ni concentration in the CoNiCu/Cu nanowires GMR. Different amounts of NiSO$_4$ were added to the CoNi(Fe)Cu electrolyte and multilayered CoNi(Fe)/Cu nanowires were deposited. The Ni concentration was varied between 12 and 100 mM. The concentration of CoSO$_4$ was 50 mM. The Cu layer was deposited at (-0.4 V for 20 s) and the alloy layer was reduced at (-1.9 V for 1 s). Table 4.4 summarizes the electrolyte composition and deposition conditions.

48
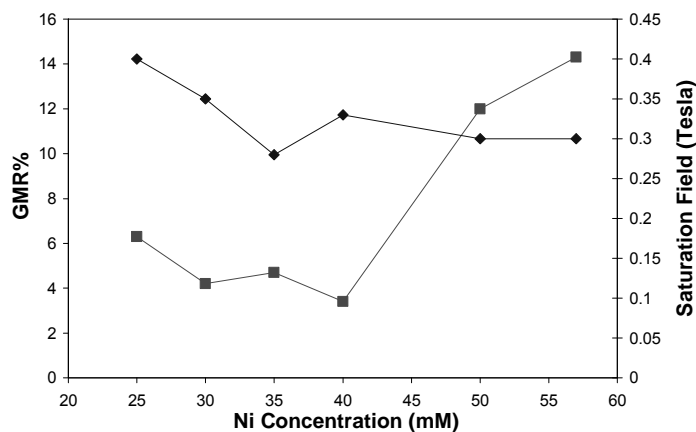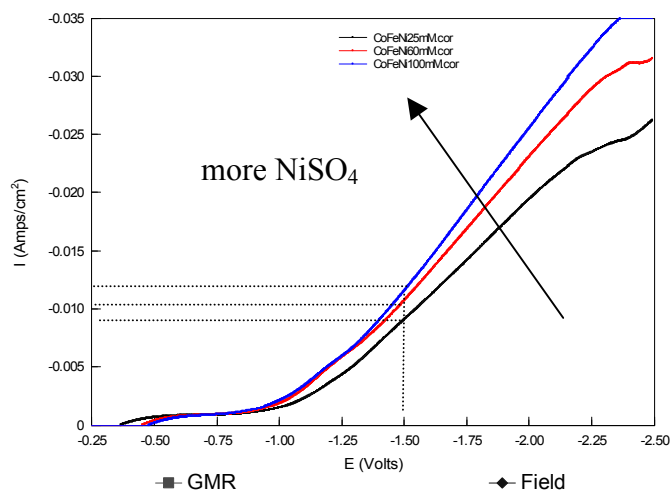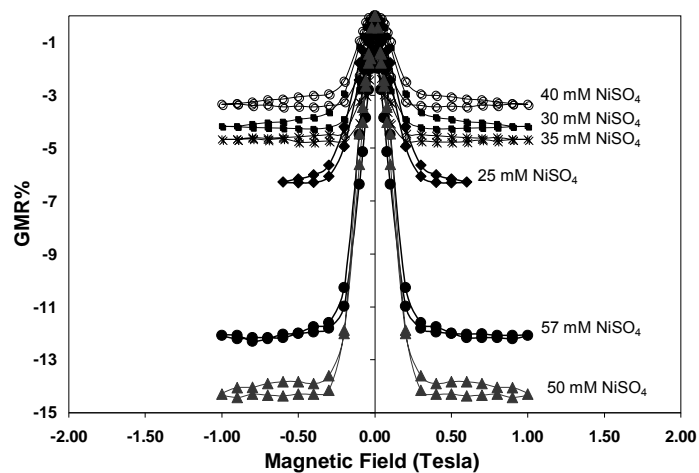
Figure 4.13 Effect of NiSO4 in CoNiFe/Cu nanowires
(a) GMR function of NiSO4 added, (b) polarization curves, (c) saturation field variation

Table 4-4 CoNi/Cu electrolyte and deposition conditions

Electrolyte (mM)		Cu Layer Potential (V)	Cu Layer Time (s)	Alloy Layer Potential (V)	Alloy Layer Time (s)
CoSO₄	50				
NiSO₄	varied				
FeSO₄	0	-0.4	20	-1.9	1
CuSO₄	1				
Na-K Tartrate	27				
Sulfamic Acid	10				

In Figure 4.14 (a) the GMR decreased at higher concentration of $NiSO_4$. Figure 4.14 (b) shows polarization curves of the electrolyte when more $NiSO_4$ was added and it could be observed that the total current did not change with more Ni added to the electrolyte. Since the deposition time and potential were constant, the alloy layer thickness remained the same with the addition of Ni. Figure 4.14 (c) shows that the magnetic saturation field increased at higher Ni concentrations. When comparing the $NiSO_4$ addition to the CoNiFeCu and the CoNiCu systems, an opposed behavior in the GMR could be identified. In CoNiFe the GMR increased at higher concentration of $NiSO_4$ while in CoNiCu the GMR decreased at higher Ni. In the case without Fe the total current remained constant with more Ni added to the electrolyte, while in the case of CoNiFeCu the total current changed significantly with more Ni added.

4.3 GMR Results Discussion

Antiferromagnetic coupling can be induced in nanometric multilayered structures for magnetic GMR sensor applications. Layering a cobalt-rich alloy with copper can increase the resistivity of the high moment, low coercivity CoNiFe alloy layers which would minimize the presence of eddy currents during sensing. The GMR property is closely affected by the discreteness of the layer interfaces. Therefore controlling the interface composition gradient controls the GMR. When the nanolayers are deposited during potential pulses the nanowire growth process under non-steady-state conditions and the current transient deposition behavior becomes very important. Moreover, since the electrolyte used contained diffusion-limited elements (Cu, Fe and Ni) the layer interfaces were even more affected by the non-steady state deposition. Even as a steady state process, the electrodeposition of CoNiFeCu is considered an anomalous phenomenon because it is characterized by the preferential deposition of the less noble metal (Fe). This anomalous codeposition phenomenon is well known in the

50

electrodeposition of iron group elements. In a binary system of FeNi the deposition rate of Ni, which is the more noble element in the system, is inhibited.
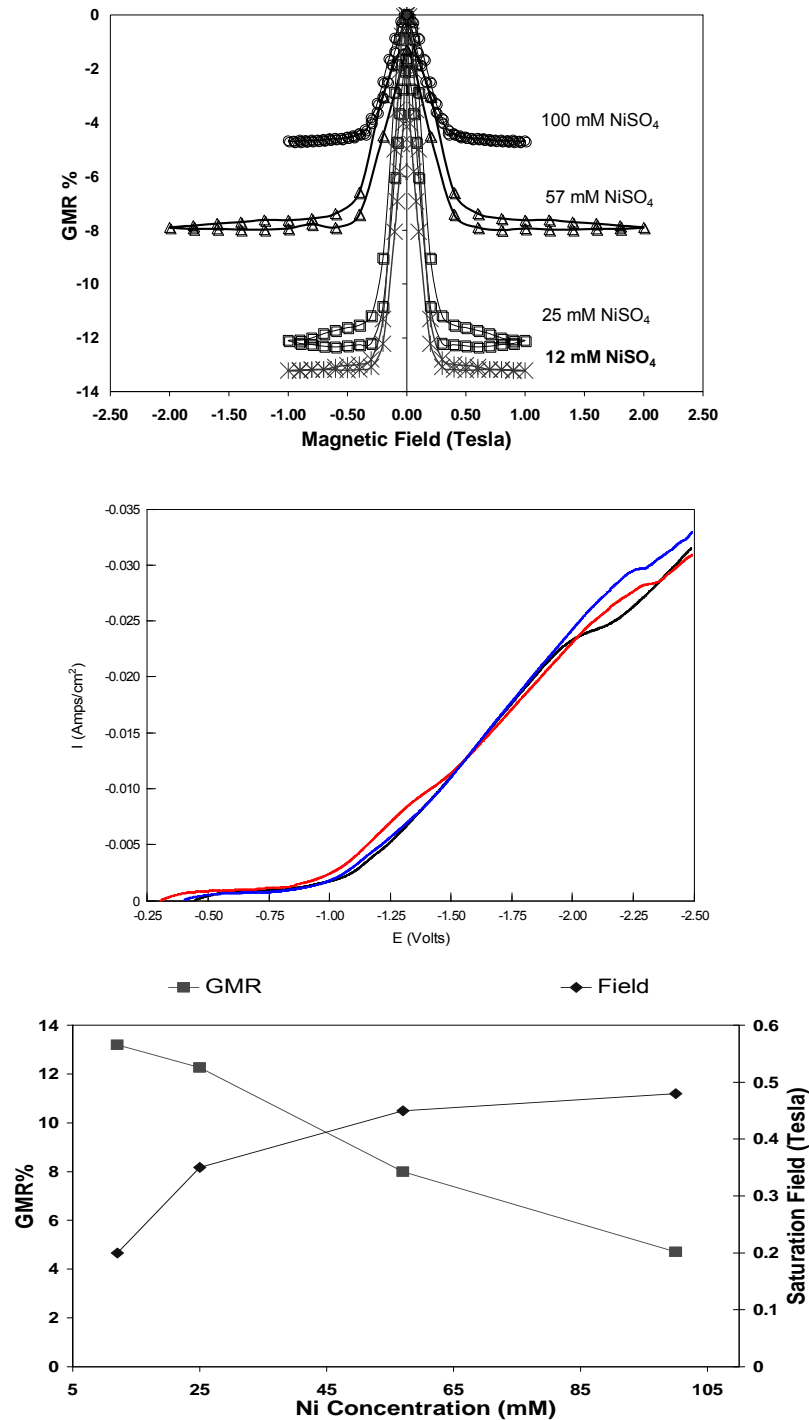
Figure 4.14 Effect of NiSO4 in CoNi/Cu nanowires
(a) GMR function of NiSO4 added, (b) CoNiCu polarization curves (c) GMR and saturation field variation function of NiSO$_4$ concentrations

The same behavior is also observed for tertiary systems of iron-group elements. Furthermore, it has been observed that the deposition rate of the less noble element in the system could be enhanced during the codeposition process. Previous studies in our lab (Zhuang and Podlaha, 2003, Huang and Podlaha, 2004) modeled the CoNiFeCu electrodeposition behavior taking into consideration the transient effects, describing how the adsorbed species accumulate during deposition and also the competitive interactions.

For this quaternary system, the three iron-group elements exhibit anomalous codeposition behavior that is further complicated by the non-steady pulsed plating of nanometric layers in deep nanosize pores. Therefore, there is also a composition profile along the pore length.

4.4 GMR Application: Microfluidic Sensing Devices

The main objective for these GMR integrated fluidic sensors is to detect bio-molecules and also to provide a vehicle for the placement, detection and study of biomolecular interactions, in particular those with DNA. Other biological applications include magnetically assisted separations, high sensitivity biosensors and biochips for protein and DNA screening. Advantages of using GMR sensors are that it can be placed on a single chip along with the needed electrical circuitry, it is compact and sensitive to small magnetic fields. As an example, vapor deposited GMR sensors proved to be sensitive to extremely small magnetic fields and are now employed in the hard disk drive-read head system present within every personal computer. State-of-the-art read heads can detect a 20 nm x 500 nm bits on a magnetized surface with great reliability and at extremely high speed. (Tondra, 2000) Consequently, a wide range of bio-technological applications, including miniaturized biochip devices are foreseen. The GMR sensor integration in microfluidic devices is in its incipient phase and there is room for much research and improvement.

4.4.1 Background

One of the pioneers in the GMR sensor integration is Tondra *et al*. (Tondra, 2000) who studied the detection of commercially available superparamagnetic nanospheres in a micro-size device. Their group employed thin film GMR sensors. The results showed that the lower detection limit is set by the lithographical feature size. Also they pointed out that increased sensitivity of these detectors can be achieved by making the GMR sensor as small as the objects being detected and by positioning the sensor very close (100 nm) to the magnetic particles. They concluded that the GMR sensor could detect a single superparamagnetic particle (500 nm in diameter) if the sensor was about the same size as the bead, and the bead surface is about 0.2 bead radii away from the surface of the sensor. Positioning of the beads with respect to the GMR sensor was very important for the detection process.

Another research group interested in biotechnological applications, Graham *et al*. (Graham, 2002) used spin valve GMR sensors for the detection of a single magnetic microsphere. Two kinds of commercially available superparamagnetic particles (400 nm dextran iron oxide, 2 μm polymer encapsulated iron oxide) with biomolecules immobilized on the surface were detected using a GMR spin valve (5 %). The unique part of this study was the construction of on-chip current line structures to control the movement of magnetically labeled biomolecules. A higher signal of 1.2 mV was obtained for the detection of the 400 nm nanoparticles due to the higher density of labels that can accumulate on the sensor surface, but the disadvantage of using the nanoparticles was their tendency to cluster in an external field. On the other hand, the microspheres were easier to control and detect even as single labels. The typical noise level was 10 mV, which was rather high compared to the signal strength.

Utilizing the GMR spin valve as the sensor element, Pekas *et al.* (Pekas, 2004) was able to monitor magnetic pico-droplets in an integrated microfluidic system. The device combined three sets of spin valve sensors on a silicon-based platform. The GMR pieces were centered directly under a microfluidic channel (13 mm wide and 18 mm deep) that was lithographically defined. The device was sputter-coated with a 300 nm silicon nitride layer which was oxygen-plasma etched along with a polydimethylsiloxane (PDMS) lid. The lid, built by micromolding contained the channels. The device was mounted between the poles of a miniature electro-magnet in order to apply an external magnetic field. They utilized two immiscible flowing liquids inside perpendicular channels. One of the liquids was a commercially available ferrofluid (aqueous suspension of 10 nm magnetite particles, Ferrotec EMG 507) and the other liquid was oil. When the two immiscible liquids encountered each other at the channel crossing they formed alternating droplets. The droplets sizes were controlled by the difference in the flow rates of the two liquids. Their microdevice was able to control the formation of pico-liter-size droplets of ferrofluid and to sense these ferrofluid droplets in a continuous-flow mode.

Recently, Millen *et al.* (Millen, 2005) reported the fabrication of a GMR-based sensor for the detection of immunosorbent assays (immunological interaction between surface-bound mouse IgG and r-mouse IgG coated on superparamagnetic particles). In their sensor design, first they capture an antibody surface right above the GMR piece and then the magnetic nanoparticles (MNP) were coupled to the target antigen. The change in resistance showed the presence of the MNP-labeled antigen. They examined the GMR response as a function of the concentration of the antibody-labeled MNP. They used a commercial available GMR chip made of alternating layers of Ta, NiFeCo alloy and Cu. One of the most important observations was that the change in the GMR response was strongly dependent on the MNP solution concentration. They

concluded that the GMR response was much larger for the higher concentration of MNPs. These literature results demonstrate the potential of GMR sensors for multiple applications for homeland security agencies such as early detection of various and diseases.

4.4.2 Experimental

The development of a microfluidic sensor presented here is distinguished from other bio-GMR sensors by the use of nanowires, replacing the thin film GMR element in an effort to provide a more sensitive response at a low cost for nanoparticulate detection. CoNiFeCu/Cu nanowires used in the sensors were fabricated using commercially available AAO templates with the manufacturer- specified pore diameter and length of 20 nm and 60 μm, respectively. The template acted as the working electrode and to make the template conductive for electrodeposition Au was sputtered on one side of the template. The electrolyte for CoNiFeCu/Cu nanowire deposition was composed of 50 mM CoSO4, 18 mM NiSO4, 0.5 mM FeSO4, 1 mM CuSO4, 20 mM sodium potassium tartrate, 10 mM sulfamic acid at a pH of 4. The potential was controlled vs. a saturated calomel reference electrode. The multilayered nanowire deposition was carried out using a double potentiostatic scheme, stepping between a higher negative overpotential of −1.5 for CoNiFeCu alloy deposition and -0.4 V for Cu deposition. Figure 4.15 (a) shows a TEM micrograph of the layer-by-layer structure of CoNiFeCu/Cu multilayered nanowires. TEM analysis was carried out using JEOL-100CX by dissolving the nanowire sample in 1 M NaOH. The nanowire array CPP–GMR measurements were carried out with PPMS (Quantum Design Physical Property Measurement System 6000). All measurements were performed at room temperature. Figure 4.15 (b) shows GMR plot for the nanowires used here in the fabrication of microfluidic sensors.

(a)

(b)
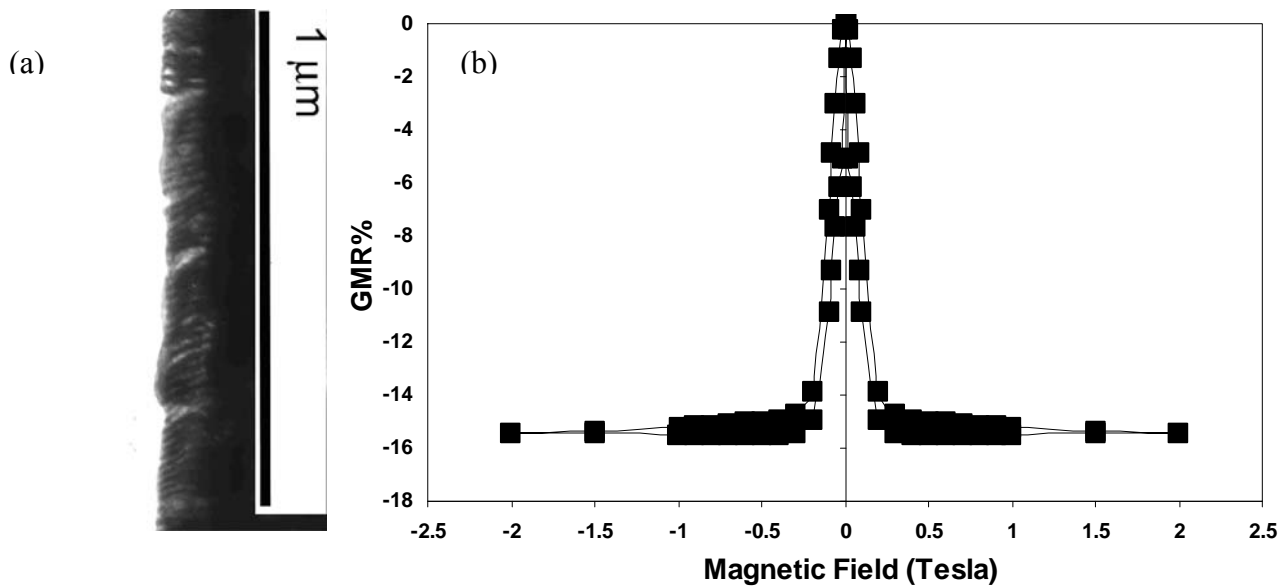
Figure 4.15 CoNiFeCu/Cu multilayered nanowires deposited in 20 nm AAO
(a) TEM micrograph (b) GMR plot

The microfluidic sensor was fabricated by molding PDMS into a micro-channel using a pattern created on a silicon wafer by UV lithography. Dr. Podlaha at MIT created a silicon/SU-8 "master" that was used for molding the micron-size channels into PDMS. Figure 4.16 shows a schematic of the silicon master and the PDMS replica.

Microfluidic nano-particle sensors based on multilayered GMR nanowires were fabricated following the fabrication scheme presented in Figure 4.17. A GMR nanowire array with platinum wires connected to the two ends of the array was placed adjacent to a pattern created on a silicon wafer with SU-8 resist by UV lithography.
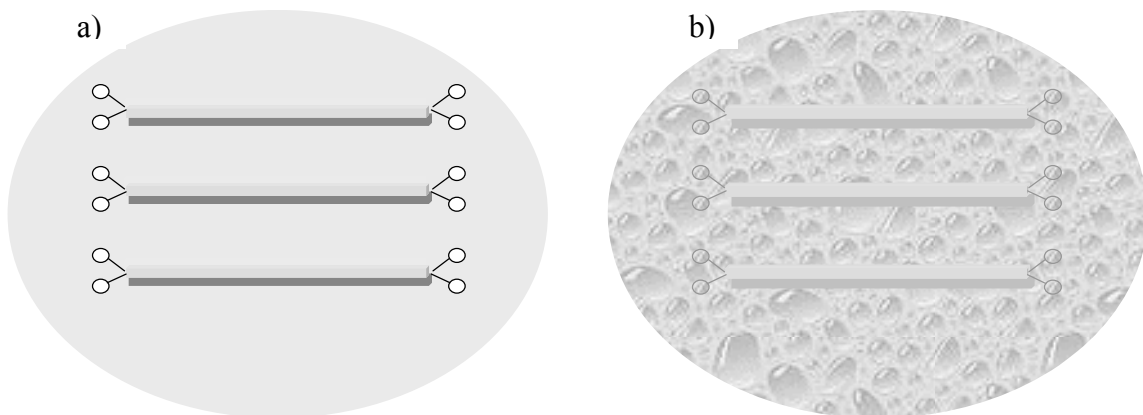
Figure 4.16 Silicon wafer master and PDMS replica
a) silicon wafer   b) PDMS replica

56
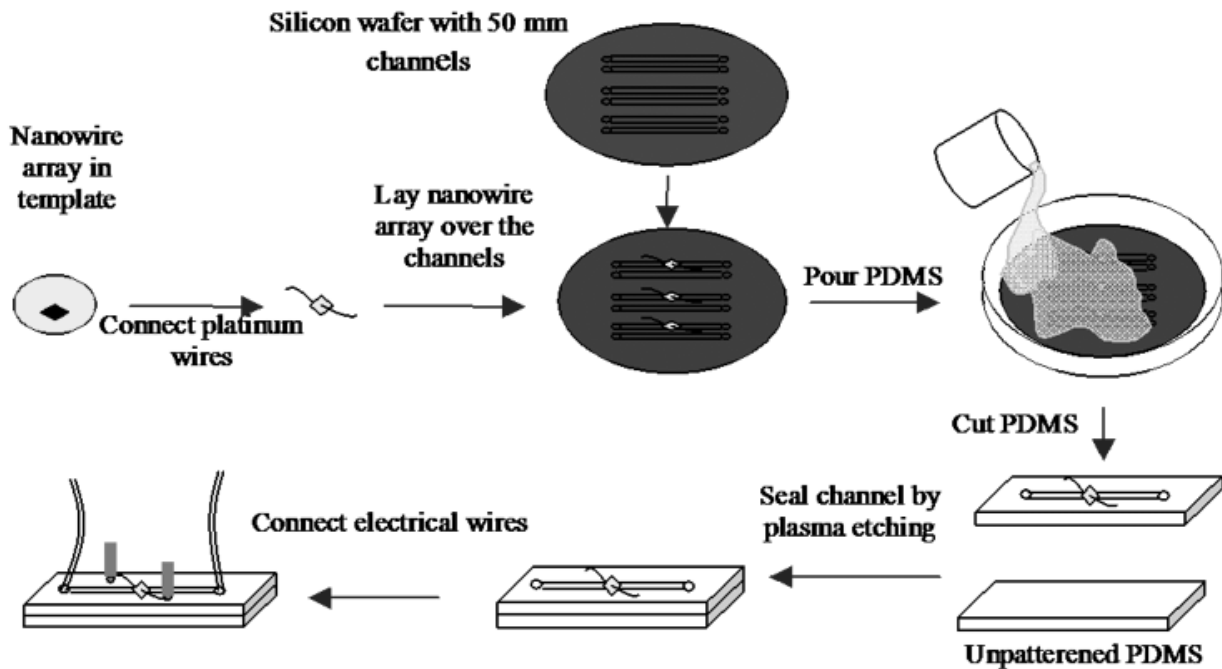
Figure 4.17 Schematic outline of microfluidic sensor fabrication process

Platinum wires serve as the current collectors along the two ends of the nanowire array. The microchannel of 100-µm width by 100-µm depth was created by the conventional PDMS "stamping" of the pattern. An unpatterened PDMS block is used to seal the micro-channel by oxygen plasma etching. Flow tubes are connected at the two ends of the micro-channel and electrical contacts are soldered on the two platinum contact wires connected to the two faces of the nanowire template. Figure 4.18 shows the assembled microfluidic sensor. Figure 4.18 (a) shows a schematic of the GMR sensor and Figure 4.18 (b) shows an actual picture of the microfluidic sensors fabricated in our lab. The sensor testing was based on a change in resistance of the multilayered nanowire array when placed in proximity of magnetic nanoparticles.
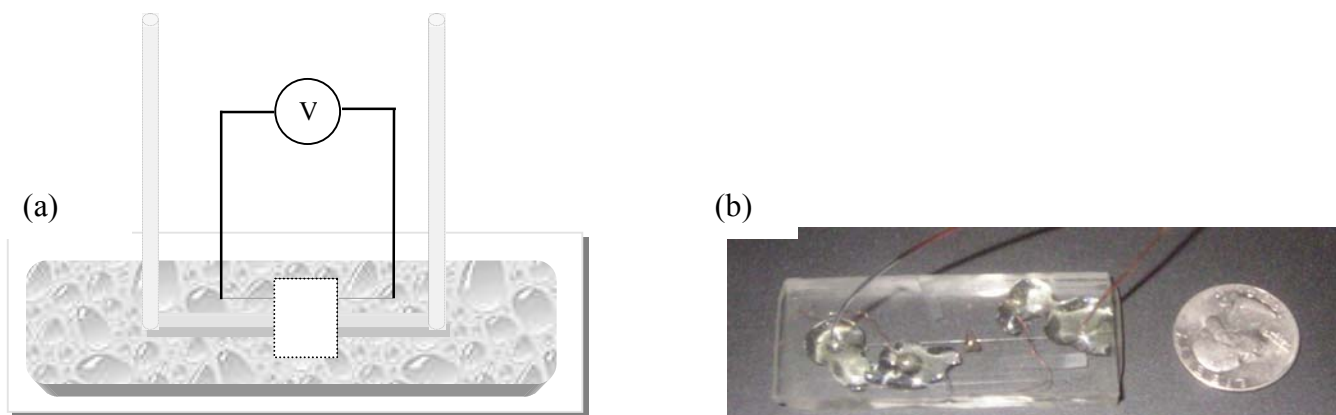
Figure 4.18 GMR microfluidic sensor (a) schematics (b) actual photo

An aqueous suspension of 10 nm magnetite particles EMG 507 commercially available from Ferrotec Corporation was used for testing. The ferrofluid is a stable colloidal suspension of sub-domain magnetic nano particles in a liquid carrier, which in thi case was water. These commercial available particles were coated with a stabilizing surfactant, which prevents particle agglomeration in a strong magnetic field.

Ferrofluids are commonly used in the study of magnetic domain, in magnetic tapes, in hard drives and magnetic heads. The EMG series used in this experiment was chosen because it offered a simple and cost-effective testing of the microfluidic sensor. The nanoparticles obtained from the supplier are in an aqueous dispersion with a concentration of 0.4 to 1.1 volume %. Since the nanoparticles are superparamagnetic at room temperature, a pulsed magnetic field was introduced with the help of an electromagnet in order to align the nanoparticles. Care was taken, however, to control the magnitude of the external magnetic field so that superparamagnetic particles are well aligned and still, the GMR nanowires are not saturated by the external magnetic field. A Solatron 1287 potentiostat was used to measure the change in resistance of the sensor.

Figure 4.19 shows the experimental set-up of testing of the GMR microfluidic sensors. An in-house made electromagnet was placed above the sensor's channel. The external magnetic field was pulsed using a potentiostat and the pulsing ferrofluid illustrates the electromagnet behavior. Voltage changes during particle flow were recorded and monitored using a second function generator connected to the sensor. All processes were computer controlled.

electromagnet

ferrofluid pulsing
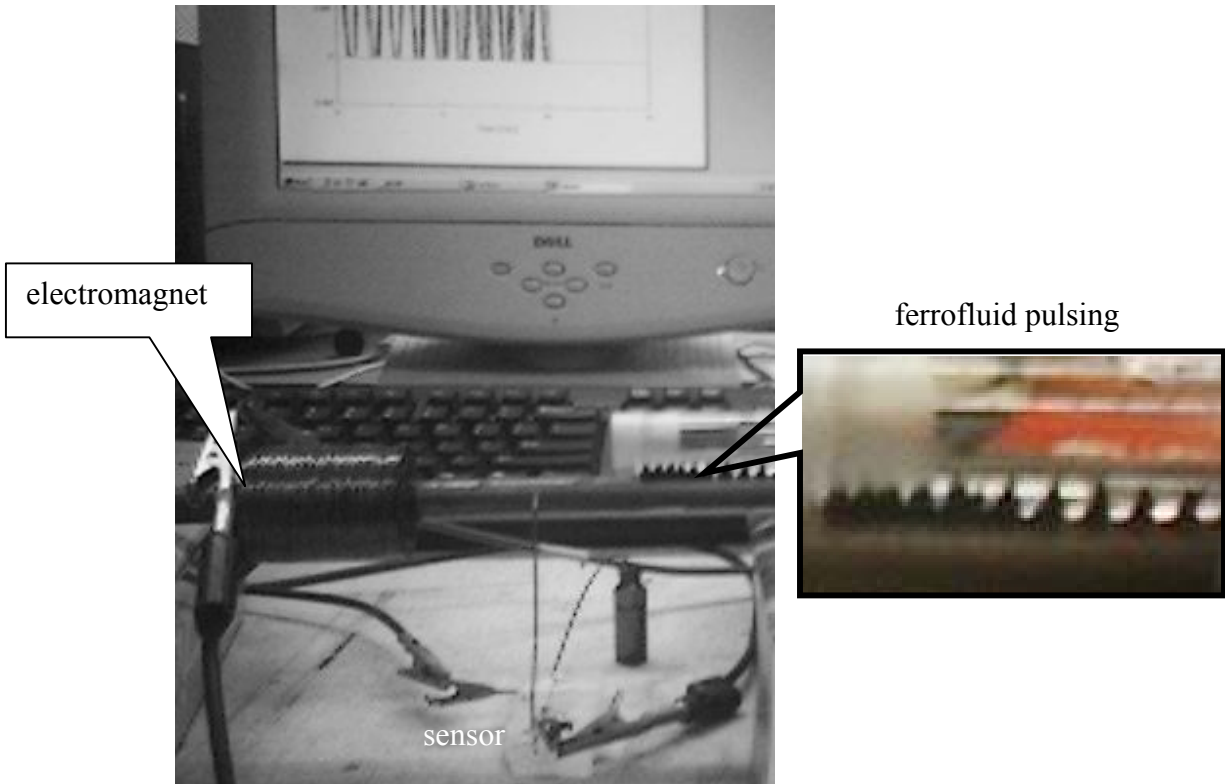
sensor

Figure 4.19 Sensor testing using an external pulsing electromagnet

Figure 4.20 shows the change in resistance of the sensor when water and nanoparticles are alternatively passed through the sensor. The nanoparticle used in this experiment had a concentration of 0.4-1.1 volume % based on the information provided by the supplier. In order to measure the resistance of the sensor, a pulsed current was made to flow across the sensor and the corresponding potential across the two ends of the sensor was monitored. The use of pulsed current as compared to direct current helps to minimize the heating up of the contacts thus

minimizing the noise and increasing the reproducibility of the sensor. The resistance of the

sensor during the water flow was 6.86 ohms which dropped down to 6.64 ohm as shown in

Figure 4.20. An average GMR of 3.09 % was observed under these conditions.

Upon dilution of the nanoparticles the observed GMR of the sensor decreased. Figure

4.21 shows the change in resistance of the sensor in presence of the nanoparticles diluted to 60%

of its original concentration. The GMR value observed for 60% diluted particles was 1.18% as
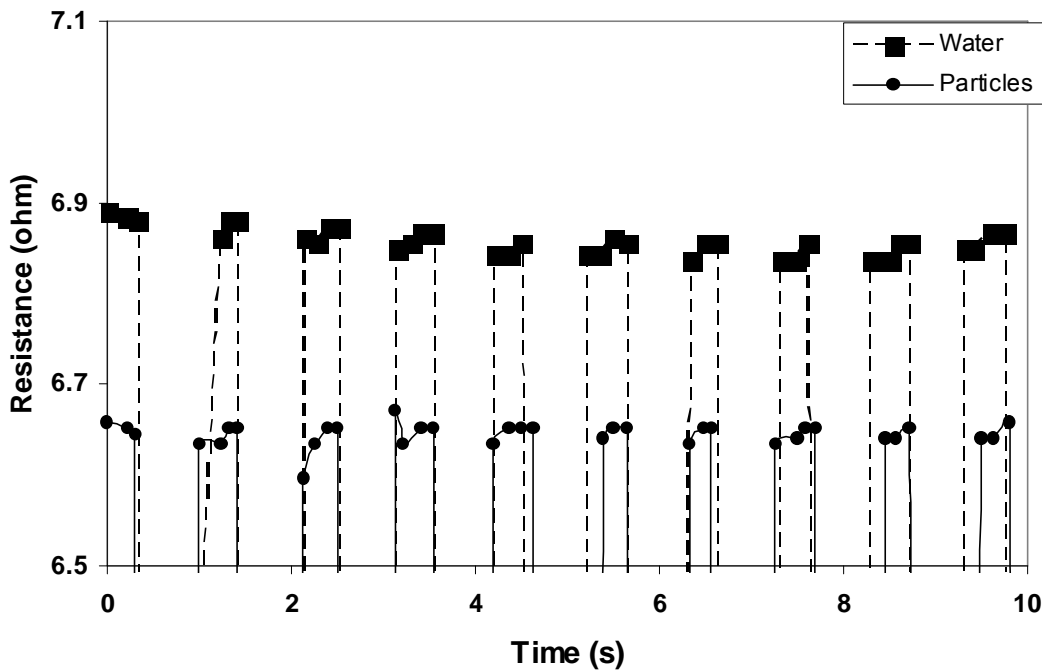
Figure 4.20 Sensor test results for undiluted nanoparticles concentration

compared to 3.09% for undiluted particles. The response of the sensor, however, is still quite

uniform and the reproducibility of the data is very good as can be seen from the response for a

number of current pulses through the sensor. The results presented in Figure 4.20 and Figure

4.21 was measured using two different sensors which are obvious from the difference in water-

flow-resistance in the two figures. Although the initial resistances of the sensors are quite

different, the change in resistance of the GMR seems to be unaffected by the initial resistance of

the sensors. In order to test the sensitivity of the sensor down to very low concentration of nanoparticles, a calibration curve was developed.
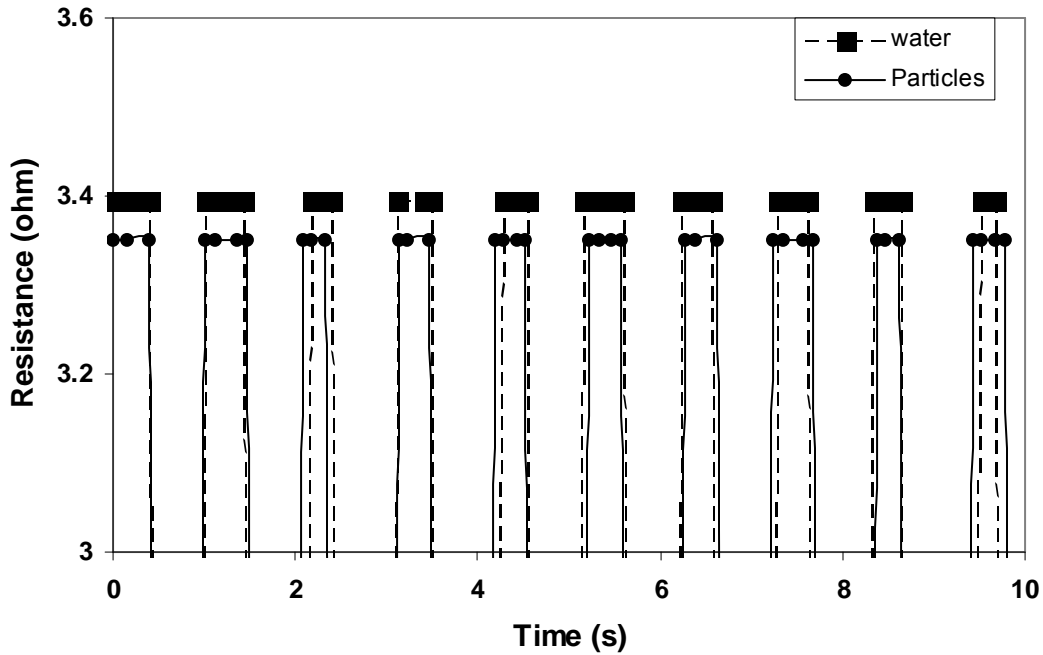
Figure 4.21 Sensor test result for 60 vol.% nanoparticles concentration

The GMR values for different dilution of nano-particle were measured and a calibration curve was plotted as shown in Figure 4.22. The calibration curve is a straight line showing a drop in resistance with a decrease in concentration of the particles. The error bars represent the spread of data in GMR measurement using the sensors.

4.5 Conclusions

Electrodeposited multilayered CoNiFeCu/Cu nanowires were fabricated with pulsed applied potential and their giant magnetoresistance (GMR) behavior characterized. The effect of electrolyte concentration on the GMR was investigated. The $FeSO_4$, $CoSO_4$ and $NiSO_4$ concentrations were varied.
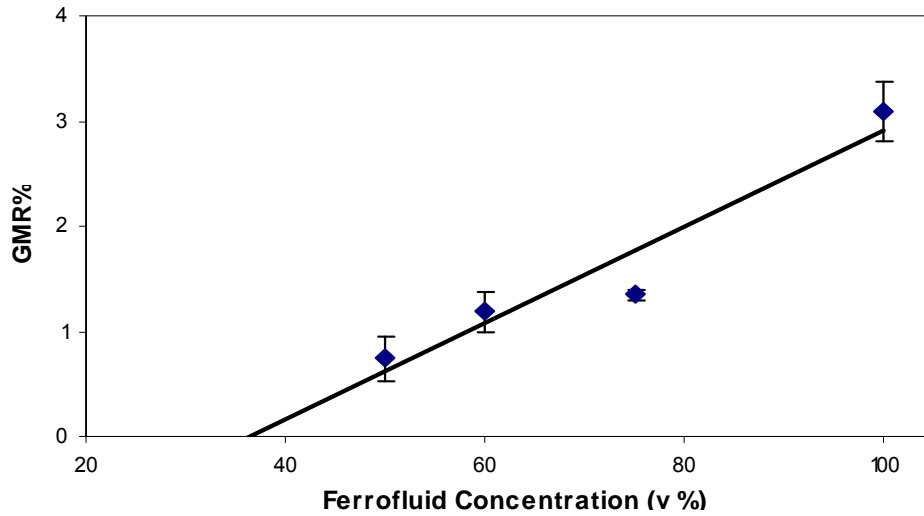
Figure 4.22 Sensor calibration curve

Electrolyte composition influenced GMR by affecting the alloy layer composition and thickness. With the addition of $FeSO_4$ the GMR tended to decrease, although the saturation magnetization field was improved. A large amount of $FeSO_4$ (4 mM) had no favorable qualities. With the addition of $CoSO_4$ the GMR also tended to decrease. The largest CoNiFe/Cu GMR value observed (20 %) at room temperature.

In the CoNiFe/Cu nanowires case, the GMR increased at higher concentration of $NiSO_4$, while the polarization curves showed that the alloy layer thickness increased with the addition of Ni. Therefore the CoNiFe/Cu GMR increased for larger alloy layers. The result was totally opposite when no Fe was present in the electrolyte. In the CoNi/Cu nanowires the GMR decreased at higher concentration of $NiSO_4$, while the polarization curves showed that the alloy layer thickness remained the same with the addition of Ni. Therefore the addition of more Ni in the CoNiCu layer decreased the GMR. The GMR of CoNiFe/Cu nanowires decreased at high overpotentials. The highest room temperature GMR (20 % at 0.2 Tesla) was obtained at the lowest alloy deposition potential. This is the largest GMR value recorded in the CoNiFe/Cu system in both thin films and nanowires obtained by electrodeposition.

Microfluidic nano-particle sensors based on GMR nanowires were fabricated for the first time. The fabrication process involves stamping of a micro-channel pattern in PDMS and sealing the channel with oxygen plasma etching. The sensors testing results show a high signal to noise ratio and good reproducibility.

The microfluidic sensor project was carried on in collaboration with Dr. Mishra, N. McBride and V. George from the Chemical Engineering department at LSU.

CHAPTER V ELECTRODEPOSITION OF NANOTUBES FOR GMR

Metallic nanotubes are alternative nano-structures with inherently larger resistance and surface area. There are two kinds of nanotubes that are investigated in this study: elemental or alloy nanotubes and multilayered nanotubes, which are a new addition to the nanostructures pallet. Multilayered nanotubes are of particular interest because they allow CPP GMR measurement. Even though there are a variety of methods to fabricate inorganic nanotubes, only electrodeposition has the potential to control the chemical composition of the tube in a modulated fashion. Figure 5.1 shows a schematic of the two types of nanotubes array: (a) alloy nanotubes and (b) multilayered nanotubes formed by electrodeposition in a porous membrane substrate.
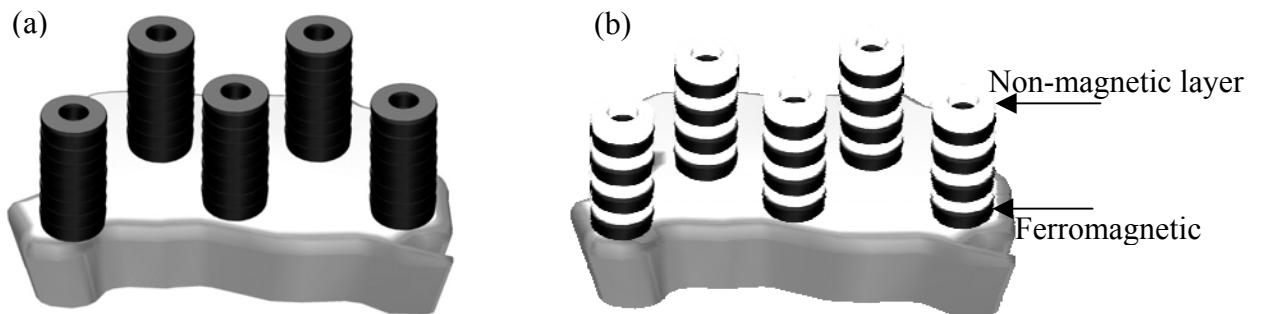
Figure 5.1 Nanotubes schematic (a) alloy (b) multilayered

In this chapter the electrodeposition conditions of elemental Cu nanotubes, alloy CoNiCu nanotubes and multilayered nanotubes are examined. After determining the conditions under which alloy and elemental nanotubes are obtained, multilayered nanotube conditions are explored for GMR. The magnetoresistance at room temperature and high sensitivity to small magnetic fields make the multilayered nanotubes fabricated by electrodeposition an attractive and cost efficient material for their potential use in magnetic sensing applications.

In the past decade, electrodeposition inside nanoporous membranes has been proven to

be a feasible method for obtaining nanometric size wires. However, nanotubes electrodeposited inside porous membranes have not yet been fully explored. Nanometric, magnetic tubes may be of interest for both advanced catalytic and sensory materials, as well as magnetic field sources for nanoelectromechanical devices. (Sui, 2004) In addition, corrosion resistant nanotubes, such as NiCoCu materials, may be possible materials as transport vessels for nanoparticles (Vankrunkelsven, 2004), bioseparations (Hou, 2004) and components of novel core-shell cable alloys (Yoo, 2004). Some of the other methods for obtaining tubes include template anodization (Lee, 2005), membrane doping (Vertesy, 2004) and carbon nanotubes doping (Jia, 2005) Gold tubular-like shapes were reported by Kautek, *et al.* (Kautek, 1995) in a study of Au nanowire electrodeposition. When the back of the membrane pores was not fully sealed by an initial sputtering step, nanowires were not formed and short tubular-like structures were observed. In addition, short 1 μm nanotubes were observed by Vaidyanathan *et al*. (Vaidyanathan, 2003) in the underpotential deposition of In_2Se_3 semiconductors. Martin's group demonstrated more robust Au nanotubes in polycarbonate and alumina templates by electroless deposition (Martin, 1994, 2001). They were also successful in using a sol-gel method for the deposition of silica nanotubes (Miller, 2001), test tubes (Gasparc, 2004), a wide variety of semiconductor oxides (Lakshmi, 1997) and polypyrrole (Yamada, 2004) inside alumina templates.

Electrodeposition has been employed to obtain elemental metal nanotubes such as Au (Kautek, 1995, Vidu, 2004, Lee, 2005, Mu, 2004, Yoo, 2004), Pt, (Mu, 2004, Yoo, 2004), Ni (Bao, 2001, Wu, 2005) and Cu. (Wang, 2004, Davis and Podlaha, 2005). Wang *et al.* (Wang, 2004) showed that Cu nanotubes can be electrodeposited inside aluminum oxide membranes (AAO) from a $CuSO_4$ electrolyte using constant current deposition and they attributed the formation of the tubular structure to the Au sputtering step that partially covered the bottom of

the pores. Concurrently, Yoo and Lee (Yoo and Lee, 2004) also identified that the Au sputtering was a key factor in obtaining the tubes, and that the growth of the tube was field dependent. They used a galvanostatic electrodeposition with AAO to obtain a variety of elemental metal nanotubes at high current density and mixtures of wires and tubes at low current densities. Wu *et al*. (Wu, 2005) used n-type Si as the AAO substrate and observed nanotubes at high overpotentials, calling into question the importance of the partial pore coverage as a key component in the fabrication of nanotubes. An alternative approach to fabricate nanotubes without the risk of forming nanowires was presented by Mu *et al*. (Mu, 2004). They used a multistep approach combining template replication and potentiostatic electrodeposition to deposit into an annular region. The drawback to this technique is that several processing steps are required. Lee *et al.* (Lee, 2005) used Ag metal nanoparticles to coat the walls of AAO and inducing preferential electrodeposition of metals along the pore wall. They also demonstrated the ability to fabricate large multilayers (800 nm Ni/3000 nm Au).

5.1 Alloy and Elemental Nanotubes

Cu and CoNiCu alloyed nanotubes were electrodeposited in nanoporous templates. Both polycarbonate (PC) Millipore Isopore^{TM} membrane filters, with specified pore diameters of 800 nm and pore length of 10 μm, and Anopore Aluminum Oxide (AAO) membranes, with specified pore diameters of 200 nm and pore length of 60 μm, were used as mediums for nanotube synthesis. A layer of gold was sputtered on one side of the membrane and the sputtering time was varied to investigate the tube formation dependence on the sputtering time.

Table 5-1 summarizes the experimental conditions used for fabricating the nanostructures. All plating parameters were kept constant, -1 V deposition for 60 min, while the

gold sputtering time increased from 20, 30 to 50 min. Tubes were observed for all sputtering times ranging from 20-50 min.

Table 5-1 Nanotubes experimental conditions

Sputtering time (min)	Pore Diameter (nm)	Time Plated (min)	Solution	SEM	Wall Tickness (nm)	Potential (V)
20	800	60	CoNiCu	alloy tubes	155±35	-1
30	800	60	CoNiCu	alloy tubes	132±15.7	-1
50	800	60	CoNiCu	alloy tubes	68±26.8	-1
50	800	840	CoNiCu	Cu tubes	218±54	-0.325
10	800	150	$CuSO_4$	Cu wires	NA	-0.325
20	800	800	CoNiCu tubes $CuSO_4$ filling	core-shell wires	NA	-1 / -0.325

Figure 5.2 (a)-(c) shows SEM micrographs of the CoNiCu alloy tubes obtained from the different time sputtered membranes. A decrease in the tube wall thickness with increased sputtering time was observed. When the PC membrane was sputtered for 20 min the observed tube wall thickness averaged 155 nm with 35 nm in standard deviation. The array of tubes was also sparse. When the PC membrane sputtering time was increased to 30 min, the nanotube wall thickness averaged 132 nm with 15.7 nm standard deviation, Figure 5.2(b). The total charge passed, determined by integrating the current, was –2.75 and –2.43 C for the two Au sputtering times of 20 and 30 min, respectively. An even longer Au membrane sputtering time of 50 min resulted in a deposit with a thinner tube wall thickness of 68 nm and 26.8 nm standard deviation, and a more dense tube population. Also, when the membrane sputtering time increased, the tubes grew taller. The charge passed was –5.64 C, larger than the short Au sputtering time samples, which is consistent with a larger reactive area for the constant deposition time. A qualitative EDS

analysis in Figure 5.2(d) indicates the presence of CoNiFe and a quantitative XRF analysis found the composition to be: 48-wt % Co, 38-wt% Cu and 14-wt% Ni. As indicated in Table 5.1, Cu tubes were also obtained from the CoNiCu electrolyte at –0.325 V. For this case the electrodeposition time was increased to compensate for the lower current density and the membrane was sputtered for 50 min.
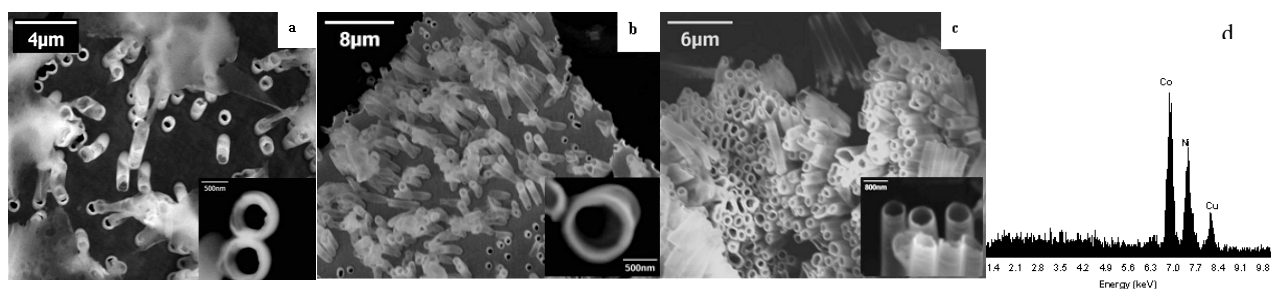
Figure 5.2 SEM Micrographs of CoNiCu nanotubes electrodeposited at constant potential of -1V for 60 min from CoNiCu electrolyte: (a) 20 (b) 30 (c) 50 min sputtering time (d) EDS spectrum

Figure 5.3 shows the SEM micrographs of the Cu nanotubes plated from the CoNiCu bath, which was expected to have an efficiency of less than 50 % due to its low electrolyte concentration. Nanotubes of approximately 5 μm length were observed, while the wall thickness averaged 218 nm. The EDS analysis in Figure 5.3 shows a deposit of pure Cu, also confirmed by XRF.

A high efficiency Cu electrolyte was used to test the role of the side reaction in the tube formation. A shortly sputtered membrane of 10 min was used. After 150 min of deposition time, Cu wires were obtained instead of tubes, Figure 5.4). The wire length was 6 μm. Chene and Landolt (1989) reported a 100% current efficiency for this concentrated Cu electrolyte used here resulting in nanowires, while Huang *et al.* (Huang, 2002, Huang and Podlaha, 2004) reported a value of 45 % for Cu deposition from a similar electrolyte used to deposit the nanotubes.
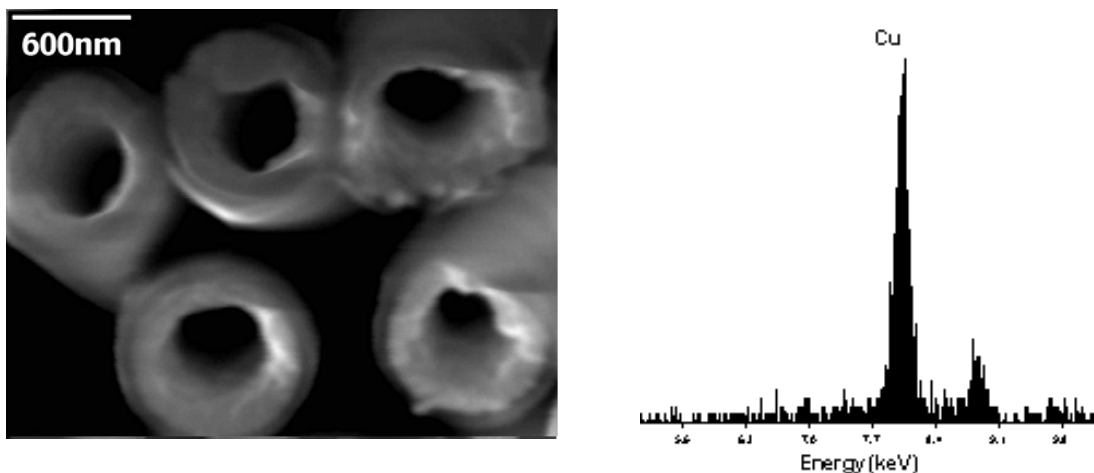
Figure 5.3 SEM micrograph of Cu nanotubes plated from the CoNiCu bath at –0.325 V and EDS spectrum

Thus, gas evolution plays a significant role in the formation of nanotubes. When there is no gas generation, as in the concentrated Cu electrolyte, nanowires were obtained instead of tubes. A suggested mechanism is that for horizontally positioned membranes, the generated H_2 finds a path from the growing electrode surface through the pore center to the pore mouth, and subsequently blocks the deposition in its path. A sketch of this electrodeposition pattern is shown below in Figure 5.4.
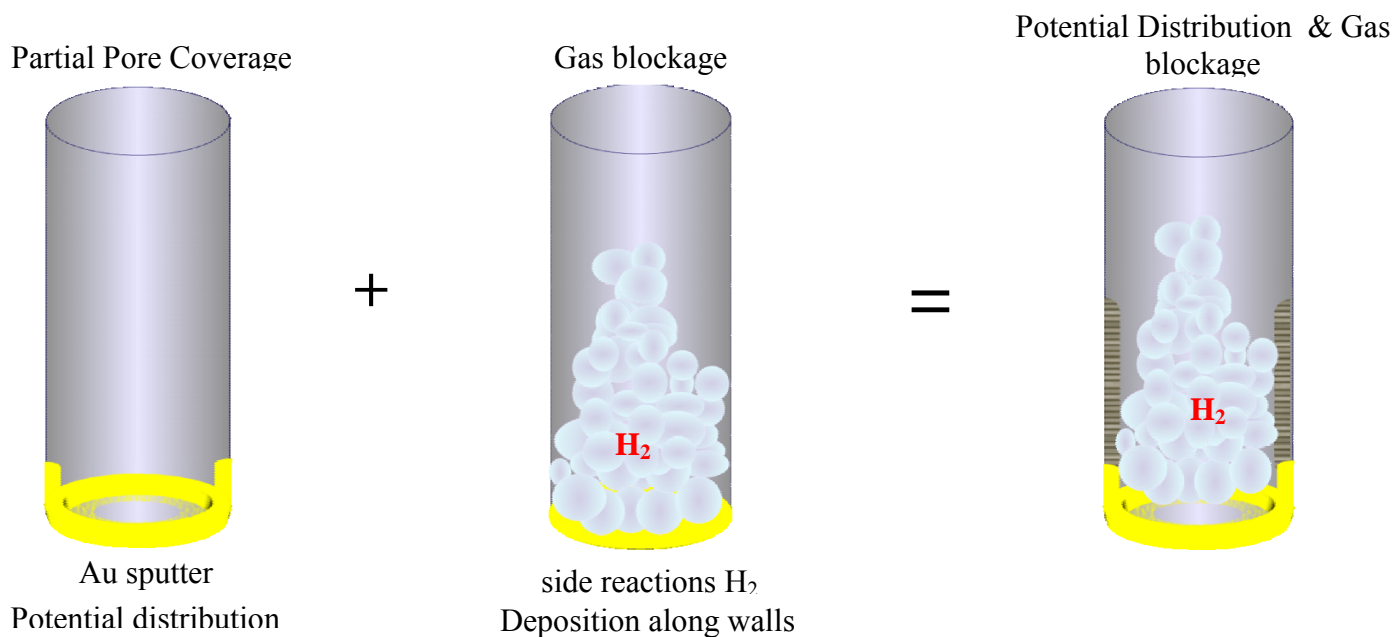
Figure 5.4 Tubes electrodeposition along the pore wall assisted by hydrogen generation

efficiency and generation of gas from the side reaction is important to the nanotube formation. Unique to electrodeposition is the ability to fabricate and control nanometric size layers. Taking

advantage of potential pulsed electrodeposition, we electrodeposited nanolayers of magnetic and nonmagnetic material in a sandwiched fashion.

5.2 Multilayered Nanotubes

The motivation for this work is the investigation of giant magnetoresistance (GMR), a change in the material resistance in an applied magnetic field as a consequence of antiferromagnetic coupling. GMR measured with current passing parallel to the multilayers (CIP) has been widely reported for vapor and electrodeposited thin films. (Ross, 1994, Parkin, 1995) The nanowire high aspect ratio geometry allows the measurement of GMR with the current applied perpendicular to the plane (CPP) of the multilayers, which has been theoretically identified as being larger than the GMR in the other configuration (CIP). (Valet and Fert, 1993) Consequently, multilayered nanowires fabricated by electrodeposition have been demonstrated in a wide array of systems including Co/Cu,(Piraux, 1994, Blondel, 1994) CoNi/Cu,(Liu, 1995, Schwarzacher, 1999) NiFe/Cu (Piraux, 1997) and CoNiFe/Cu (Huang, 2006) for sensor materials. Here, the first demonstration of electrodeposited multilayered nanotubes that exhibit GMR is presented. To demonstrate the concept, CoNiFeCu/Cu magnetic alloy layers with alternating Cu layers are deposited in a tubular fashion under pulsed potential conditions, and their CPP-GMR is characterized at room temperature.

The electrolyte for CoNiCu/Cu nanotube deposition was composed of $CoSO_4$ (50 mM), $NiSO_4$ (18 mM), $FeSO_4$ (1mM), $CuSO_4$ (1 mM), potassium tartrate (20 mM) and boric acid (10 mM), at the equilibrium pH. The overpotential was controlled versus a saturated calomel reference electrode (SCE). The open circuit potential (OCP) was -0.05 V vs. SCE. The multilayered nanotubes were electrodeposited using a double potentiostatic scheme, stepping

70

between a higher negative potential, ranging between (-1.5 V and -2 V), and Cu deposition potential (-0.4 V).

The nanotube array CPP-GMR measurements were carried out with a Quantum Design PPMS (Physical Property Measurement System 6000) using an alternative at 27 Hz ranging between 0.1-1 mA and a magnetic field between –2 Tesla to 2 Tesla. All measurements were performed at room temperature. The orientation of the magnetic field was parallel to the nanotube layers and perpendicular to the current passing through the nanostructures. The schematic shown in Figure 5.5 illustrates the CPP GMR measurement of the multilayered nanotubes.
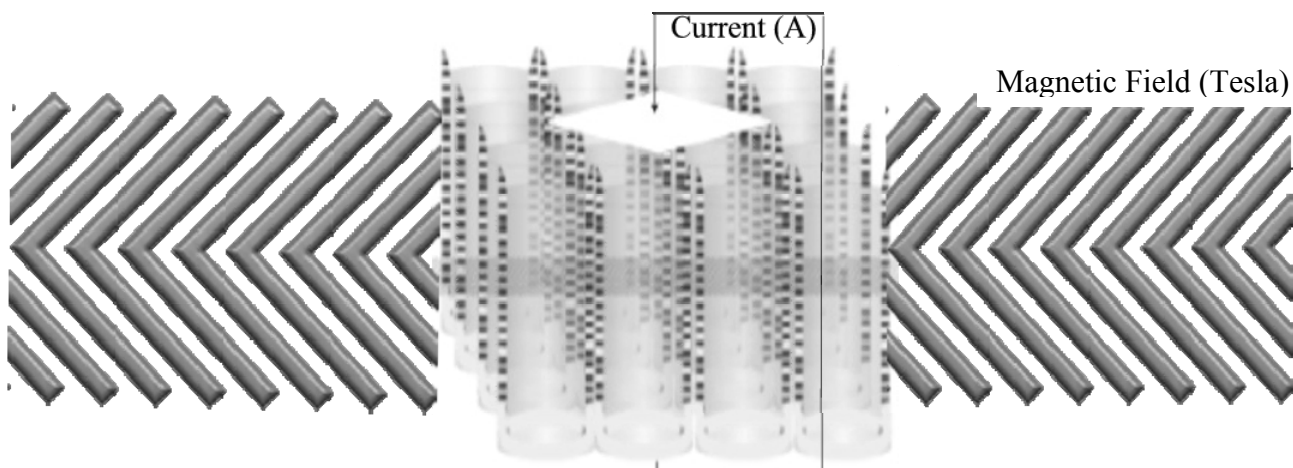
Figure 5.5 CPP-GMR measurement of multilayered nanotubes at room temperature

Multilayered CoNiCu/Cu nanotubes are shown in Figure 5.4. The CoNiCu/Cu tubes were fabricated under a potential pulse. The CoNiCu alloy layer was deposited at (-1.7 V for 1 s) and the Cu layer was reduced at (-0.4 V). The deposition time of the Cu layer was varied in the range of 50-100 s. In Figure 5.4 (a) the Cu layer was controlled at -0.4 V for 50 s and the observed wall thickness averaged 30 nm with a standard deviation of 5.5 nm. Figures 5.6 (b) show CoNiCu/Cu tubes when the Cu pulsing time was increased to 75 s and the observed wall

thickness averaged 45 nm with 8 nm of standard deviation. Increasing the Cu pulsing time to 100 s, the CoNiCu/Cu tubes wall thickness averaged 60 nm (7.5 nm standard deviation) as shown in Figure 5.6 (c). The tube wall thickness increased for longer Cu pulsing time. The tube diameter was estimated to be 315 nm with a standard deviation of 80 nm.
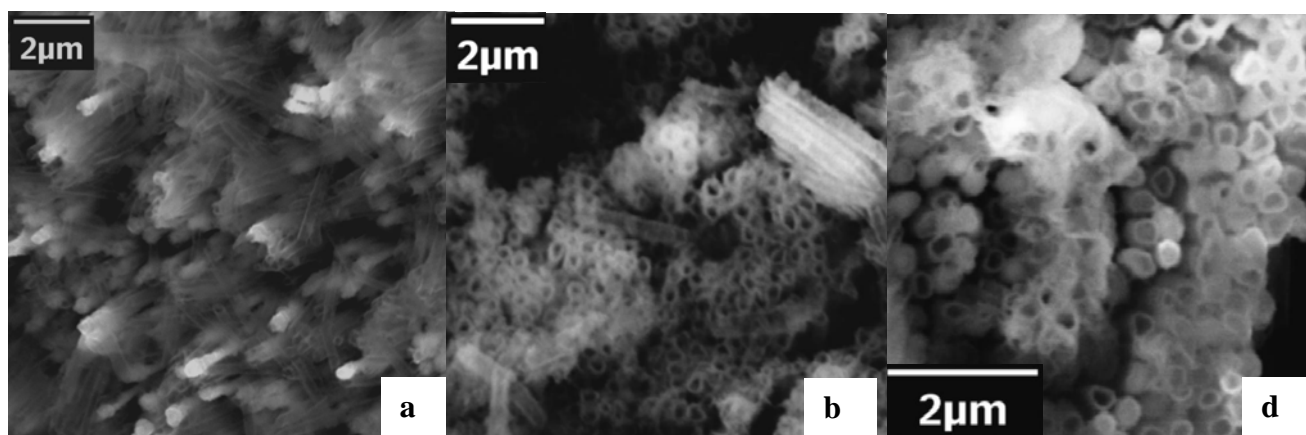
Figure 5.6 SEM micrographs of CoNiCu/Cu tubes in AAO membrane   (a) Cu layer deposited for 50 s, (b) Cu layer deposited for 75 s, (c) Cu layer deposited for 100 s

In Figure 5.7, TEM micrographs show robust, long and well-formed CoNiCu/Cu tubes fabricated by pulsed potential electrodeposition. Keeping the Cu potential constant at -0.4 V, the alloy deposition potential was varied. In Figure 5.7 (a) the CoNiCu magnetic layer was deposited at -2 V for 3 s, and the resulting wall thickness averaged 50 nm with 9 nm in standard deviation. In Figure 5.7 (b) the CoNiCu alloy layer was deposited at -1.7 V for 3 s and the observed wall thickness averaged 28 nm with 5 nm in standard deviation.   Figure 5.7 (c) shows CoNiCu/Cu tubes with the alloy layer deposited at (-1.5 V) for 3 s, while the tube walls were estimated to be 15 nm in thick (6 nm standard deviation). The wall thickness decreased when ferromagnetic layer deposition potential decreased and all the other parameters were kept constant. When the magnetic layer deposition potential was high, for instance –2 V, the deposition current was also high, and therefore thicker tubes were formed since more charge got deposited. Decreasing the

alloy deposition potential and keeping the deposition time constant decreased the amount of charge deposited and resulted in thinner tubes.
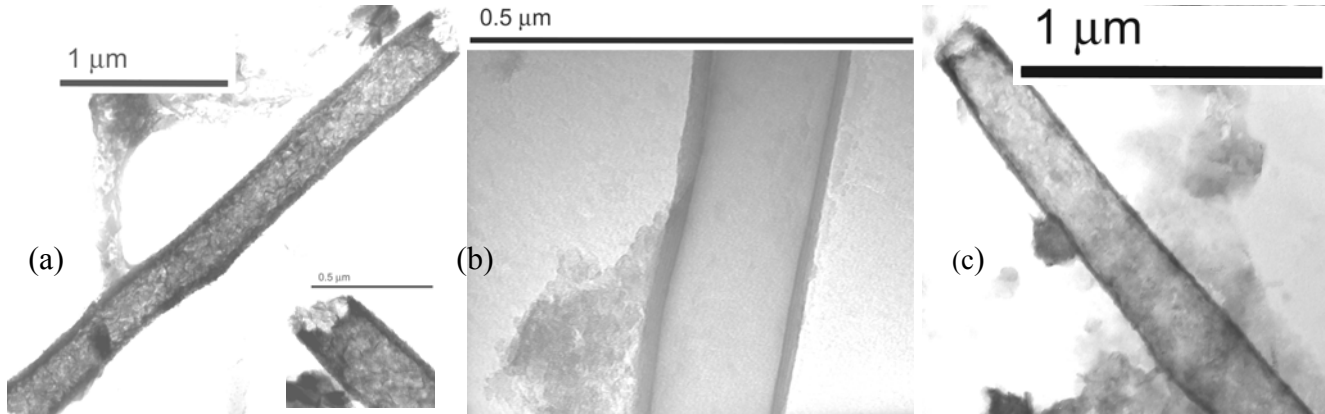
Figure 5.7 TEM micrographs of CoNiCu/Cu in AAO membrane: (a) CoNiCu (-2.0 V)/Cu (-0.4 V), (b) CoNiCu (-1.7 V)/Cu (-0.4 V), c) CoNiCu (-1.5 V)/ Cu (-0.4 V)

Even though at this magnification layers were not visible, tubular shapes were clearly marked by the darker and denser sides enclosing the lighter core regions. Figure 5.8 shows the EDS spectrum of the CoNiCu/Cu tubes deposited using the following parameters: CoNiCu (-2.0 V)/Cu (-0.4 V). The EDS analysis provides a qualitative composition analysis that confirms the presence of Co, Ni and Cu in the deposit. On the same array of tubes, XRF was used to get a quantitative composition analysis. An averaged composition of the tubes was found to be: 46.6-wt % Co, 45.9-wt% Cu and 7.5-wt% Ni.
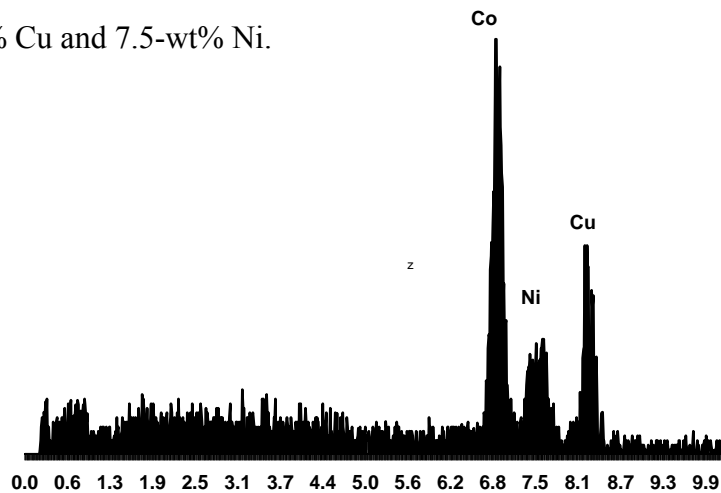
Figure 5.8 EDS spectrum of the CoNiCu/Cu tubes

The CoNi/Cu multilayered nanotubes showed GMR at room temperature and low magnetic fields (less than 0.5 Tesla). Alloy deposition potential was one of the first variables shown to have an affect on the GMR values. Figure 5.9 presents a series of GMR measurements for the CoNi/Cu nanotubes deposited at different alloy potentials, while keeping the Cu layer condition constant.

The alloy layer time was set to 3 s, while the Cu layer pulsing time was 100 s. When the tube alloy deposition potential was set to ($-$1.7 V), the observed GMR was 3 % with a magnetic saturation field of 0.25 Tesla. When, decreasing the alloy deposition potential to -1.5 V the GMR slightly increased to 3.6 % but the magnetic saturation field almost doubled (0.5 Tesla). The best GMR shape was obtained when the CoNi alloy layer was deposited at -2 V. The first scan (virgin state) GMR value was 8.7 %, although the re-measured GMR value settled to 3.5 % at a lower magnetic field of 0.2 Tesla. Although the virgin state rendered higher GMR upon the first scan, the GMR value did not drastically change for different alloy deposition potentials. However, the GMR profile reproducibility and magnetic saturation field were influenced by the alloy reduction potential.

In order to image arrays of multilayered tubes, similar conditions that shown GMR were used to deposit multilayered tubes in PC membranes that were easier to dissolve and image at the SEM. Figure 5.10 shows an array of CoNi/Cu multilayered nanotubes electrodeposited by pulsing potential between (-2 V for 3 s) and (-0.4 V for 100 s). Figure 5.11 shows both SEM and TEM micrographs of CoNiFeCu/Cu nanotubes fabricated by pulsed overpotential electrodeposition at (a) -1.6 V and (b) -2 V for the alloy layer at 3 s and with the Cu layer electrodeposited at -0.4 V for 100 s. Both figures show an array of nanotubes. The tube walls are

evident by the darker regions in the TEM micrographs. The tube walls were thicker for the larger

overpotential -2 V.
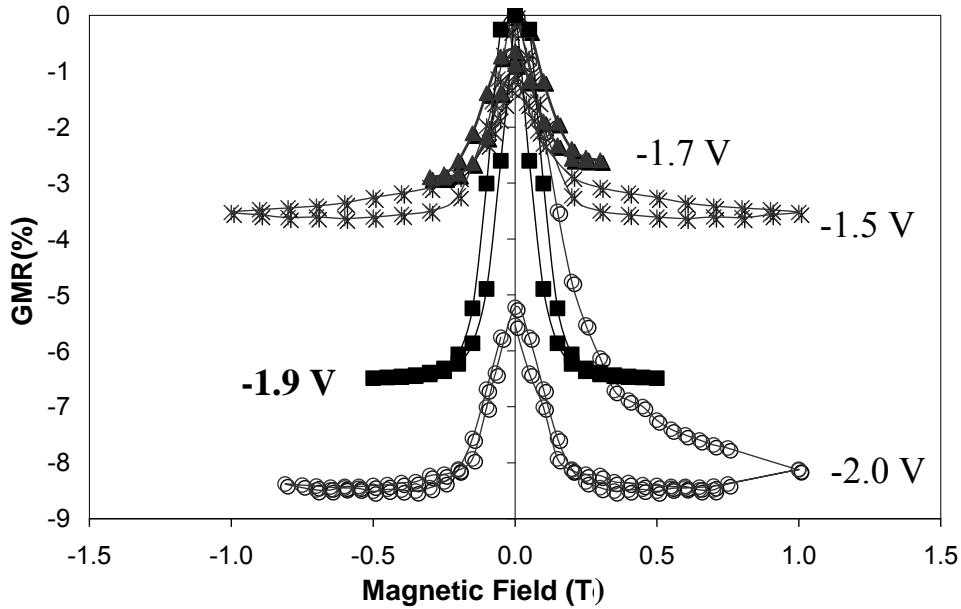
Figure 5.9 CoNiCu/Cu multilayered nanotubes GMR for different alloy deposition potentials

Figure 5.10 CoNiCu/Cu multilayered nanotubes: CoNiCu (-2 V) and Cu (-0.4 V)

Layered CoNiFeCu tubes were imaged under higher resolution TEM and analyzed by

EDS in Figure 5.12. The layers are clearly evident in Figure 5.12 (a), which shows a CoNiFe/Cu

nanotube with the alloy layers electrodeposited at -2.0 V. Guidelines have been added to

illustrate the layer orientation.
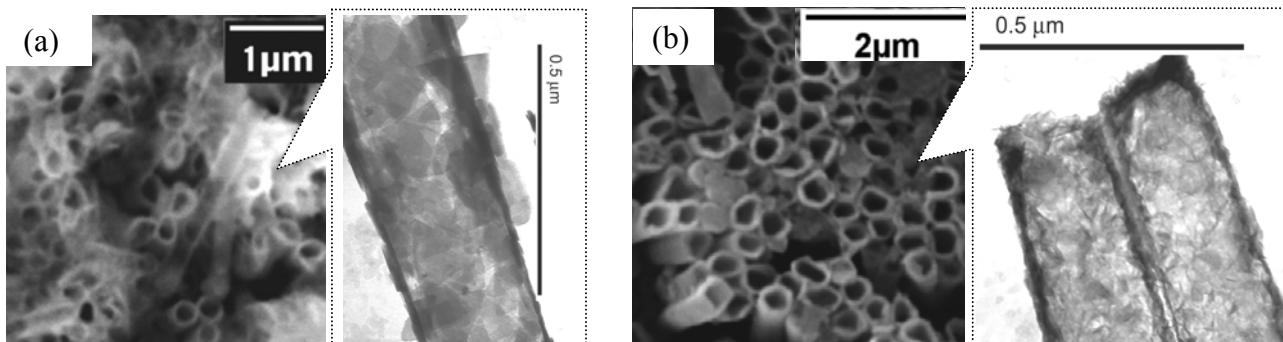
Figure 5.11 Micrographs of CoNiFeCu/Cu in AAO membrane: SEM (left), TEM (right)
(a) CoNiFe/Cu (-1.6 V)/ Cu (-0.4 V) (b) CoNiFe/Cu (-2.0 V)/Cu (-0.4 V)

The CoNiFe alloy layer was estimated to be 10 nm, and the Cu layer was 6 nm. Figure 5.12 (b)

shows an EDS spectrum of the sample. A XRF analysis provided a bulk elemental composition

of: 42.0-wt % Co, 54.4-wt % Cu, 3-wt % Cu, and 0.6-wt % Fe, consistent with the qualitative

EDS spectrum.
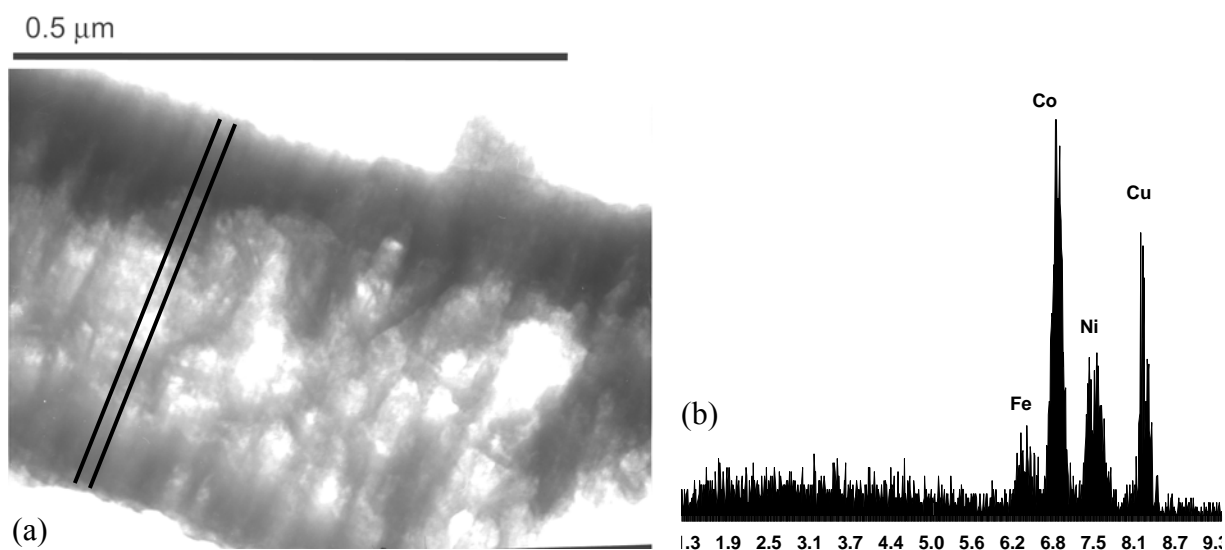
Figure 5.12 Nanolayered tubes CoNiFeCu/Cu (- 2.0 V) / Cu (-0.4 V)
a) TEM   b) EDS

The array of CoNiFeCu/Cu nanotubes exhibited GMR $= \left(\dfrac{\Delta R}{R} \right)$ at room temperature and

low magnetic fields (less than 0.5 Tesla). Figure 5.13 shows the CoNiFeCu alloy deposition

potential effect on the % GMR, when the Cu layer conditions were maintained at -0.4 V. The

alloy layer overpotential ranged from -1.7 to -2.3 V. The highest CoNiFeCu/Cu tube GMR (3.5

% at 0.2 Tesla) was observed when the alloy layer was pulsed at -1.7 V. All the GMR nanotubes

were deposited inside AAO membranes with 200 nm pores as specified by the manufacturer or

approximately 350 nm as observed at the SEM and TEM. When the overpotential decreased

from -2.0 V to -1.7 V, the GMR value increased. Compared to nanowire counterparts, the larger

inherent resistance of a nanotube or array of nanotubes is particularly of interest to sensor

development, where a high ratio of the GMR sample resistance to the contact resistance is

critical for room temperature devices.
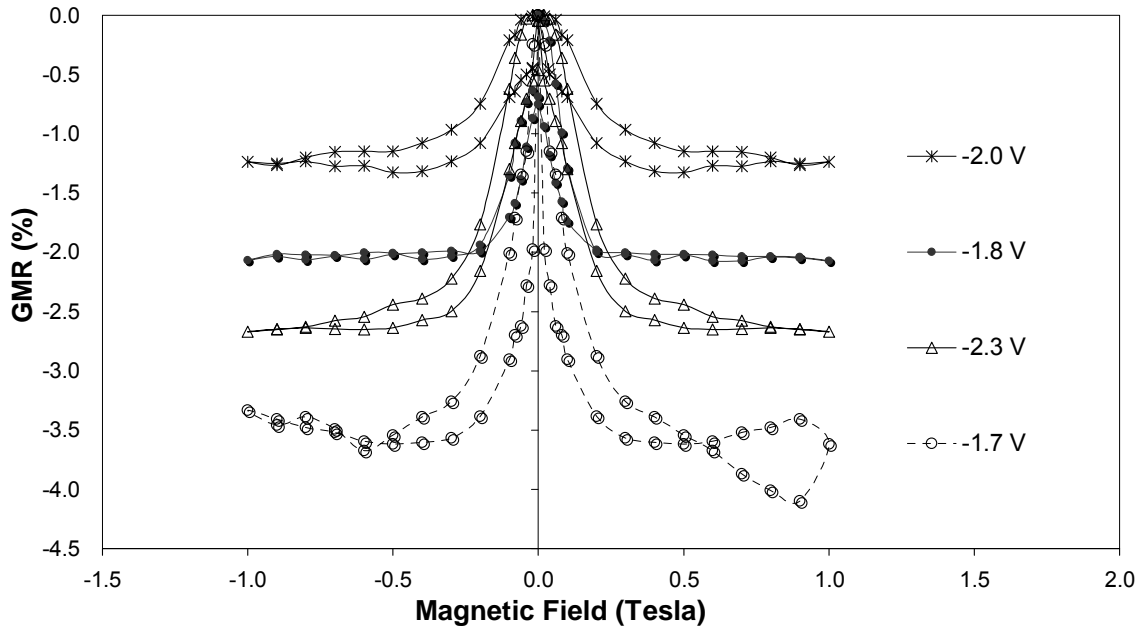
Figure 5.13 CoNiFeCu/Cu tubes GMR function of alloy layer potential
(Cu layer = -0.4 V) (room temperature measurement)

Figure 5.14 shows an example of layered tubes, with the alloy layer deposited at a higher negative potential -2.25 V, while the Cu layer was controlled at the same potential of -0.4 V. Figure 5.14 (a) shows a TEM image of a multilayered tube formed inside AAO (0.2 µm) membrane. The alloy and Cu layer deposition time was the same as in the previous example: 3 s for the alloy layer and 100 s for the Cu layer. The observed wall thickness averaged 50 nm with 9 nm in standard deviation.

Figure 5.14 (b) shows SEM images of the multilayered tubes electrodeposited inside a polycarbonate membrane having larger diameter than the AAO membrane (0.8 µm diameter). The alloy and Cu layer deposition times were doubled to 6 s for the alloy layer and 200 s for the Cu layer. The wall thickness was larger at 100 nm with a 20 nm standard deviation.
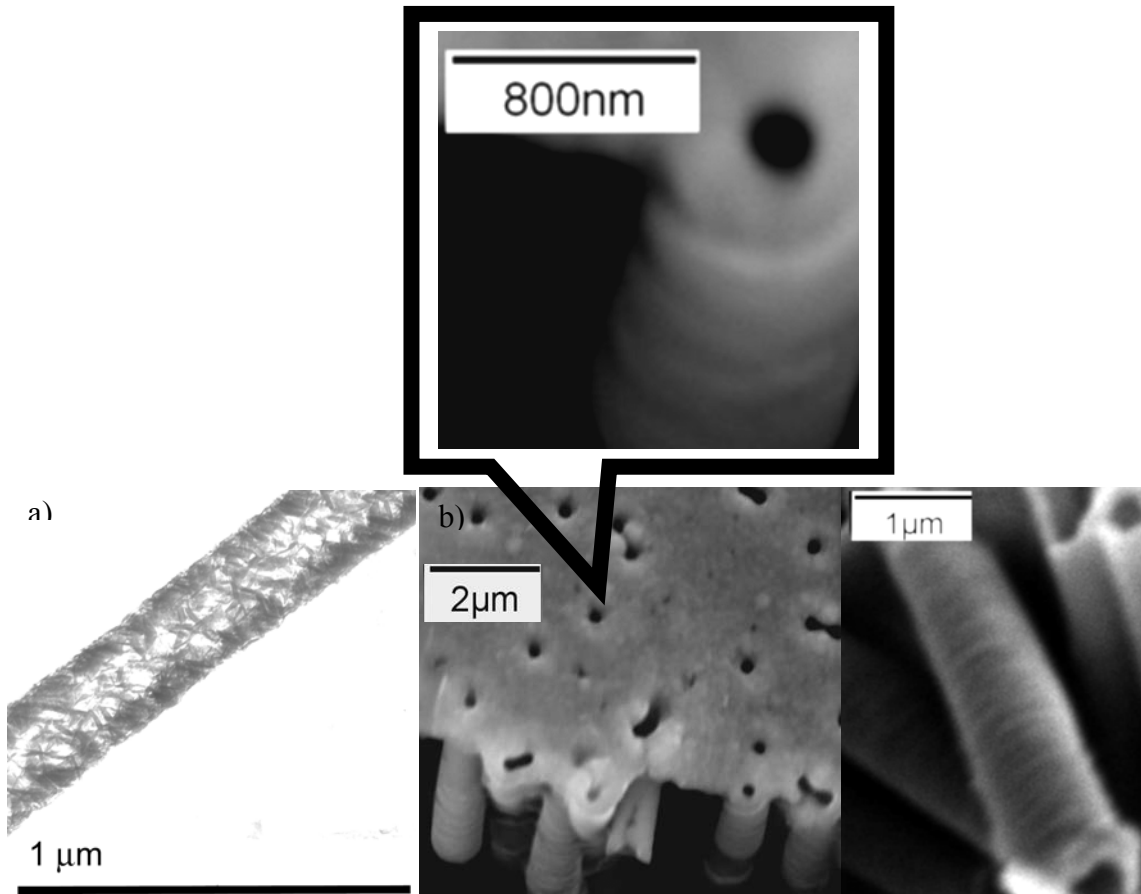
Figure 5.14 Multilayered CoNiFeCu/Cu tubes [alloy layer (- 2.25 V) / Cu layer (-0.4 V)] (a) AAO membrane tube (TEM) (b) bottom view of an array of tubes in a PC membrane, left; higher magnification of a single nanotube showing modulated, right (SEM)

The larger layers and doubled wall thickness are clearly seen in the SEM micrograph. Figure 5.15 shows how the nanotubes GMR would be influenced by the addition of Fe (+2) and Fe (+3) to the CoNi/Cu tubes. Figure 5.15 (a) shows the GMR % as a function of applied magnetic field for CoNi(Fe)Cu/Cu nanotubes electrodeposited under the following conditions: Cu layer applied potential was -0.4 V for 100 s and the alloy layer applied potential was -1.5 V for 3 s. At these potentials the addition of Fe (+2) in the CoNiCu alloy increased the tube GMR while the addition of Fe (+3) had a negative effect on the GMR.
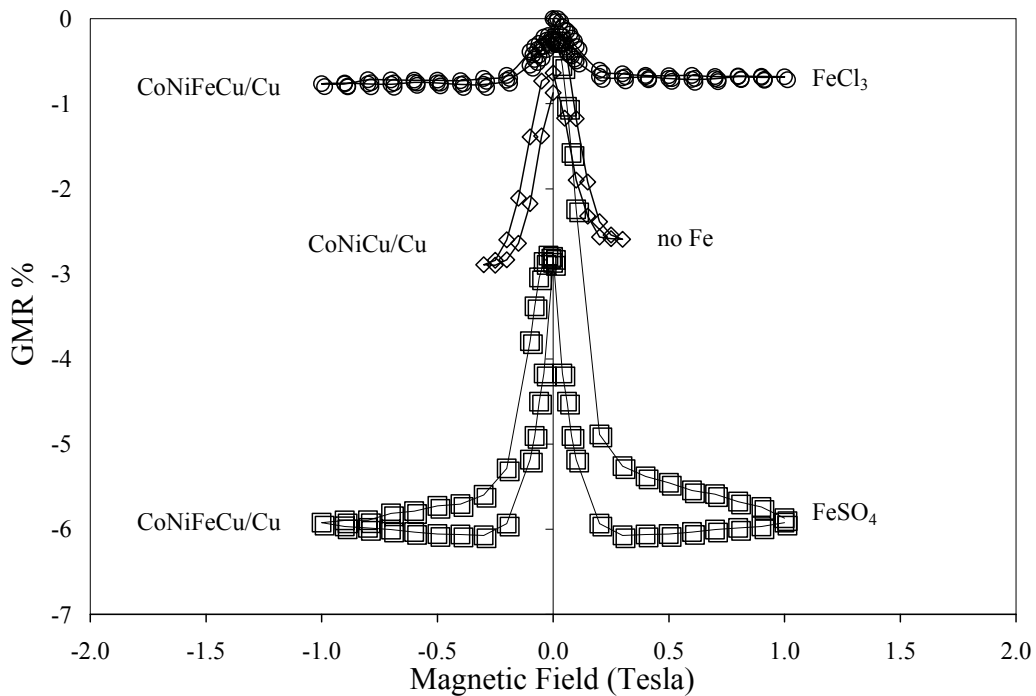
Figure 15 (a) Multilayered tubes GMR as a function of Fe oxidation state

Figure 5.15 (b) shows a SEM image of multilayered CoNiFe/Cu tubes deposited inside PC membrane (800 nm pore diameter) by pulsing potential between slightly different potentials alloy layer (-1.5 V) and Cu layer (-0.4 V). In order for the layers to be imaged at the SEM the layer thicknesses had to be increased. Therefore, the layer deposition time was doubled: the Cu layer was deposited for 200 s and the Co rich layer for 6 s.
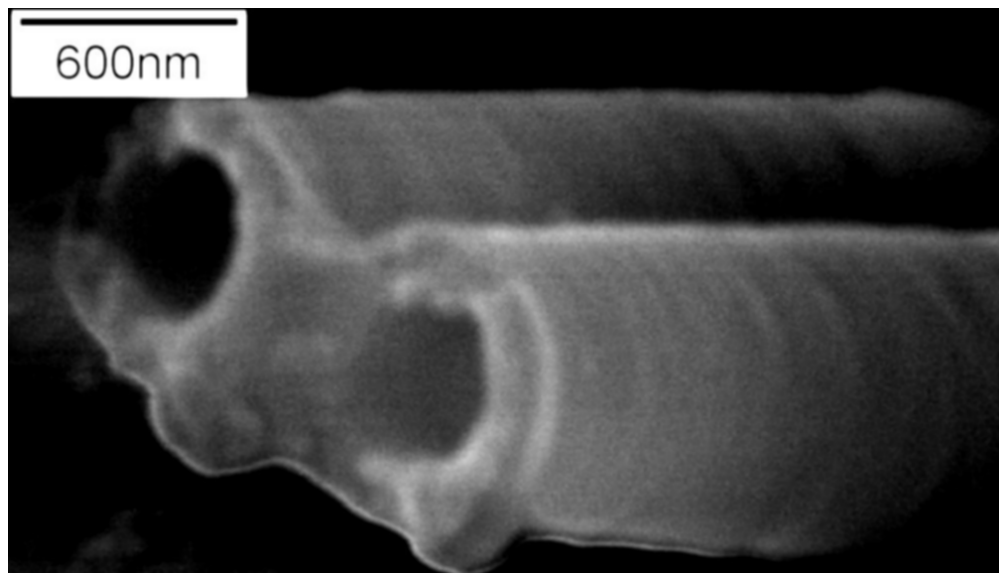
Figure 15 (b) CoNiFe(+2)/Cu multilayered tubes CoNiFe (-1.5 V) and Cu (-0.4 V) PC membrane

5.3 Parameters Affecting Nanotubes vs. Nanowires Formation

In this subsection different parameters that were believed to influence the nanotubes versus nanowires formation will be investigated. Throughout the investigation multilayers of CoNiFeCu/Cu were electrodeposited using the same potentiostatic scheme: [Cu layer (-0.4 V)/CoNiFe (-1.4 V)]. First, while keeping the electrodeposition conditions constant, different pore sizes will be tested to check if they made a difference in obtaining tubes versus wires. Secondly, the alloy layer pulsing time will be varied to investigate its effect on obtaining tubes.

5.3.1 Pore Diameter Effect

In order to examine if the pore size makes a major difference in obtaining tubes versus wires identical deposition conditions [Cu layer (-0.4 V for 20 s)/CoNiFe (-1.4 V for 1s)] were used to test pore size effect. Three different pore sizes (20 nm, 200 nm and 400 nm) were tested to see if tubes or wires would form while keeping the same deposition condition.

Using the smallest pore diameter nanowires were electrodeposited using the above mentioned pulse scheme. Figure 16 (a) shows a micrograph of the wires obtained when

80

multilayers CoNiFe/Cu were deposited inside 20 nm pores. The wire diameter averaged 198 nm

with 18.5 nm standard deviation. The Cu layer (light) averaged 3.5 nm with 2.2 nm standard

deviation and the CoNiFe layer (dark) was 6.5 nm with 2.5 nm of standard deviation. When the

membrane pore diameter was increased to 200 nm and the same pulsing scheme was employed

for electrodeposition, nanotubes were formed instead of nanowires. Figure 16 (b) shows a

micrograph of an array of CoNiFe/Cu tubes obtained when multilayers were deposited inside

200 nm pores. The tubes diameter averaged 281 nm with 36.7 nm standard deviation. Therefore,

when a larger pore diameter 200 nm was used to deposit CoNiFe/Cu multilayers, tubes were

obtained instead of wires, however distinct layers were hard to distinguished. When even larger

pore size 400 nm were used for electrodeposit multilayers nanotubes were observed.
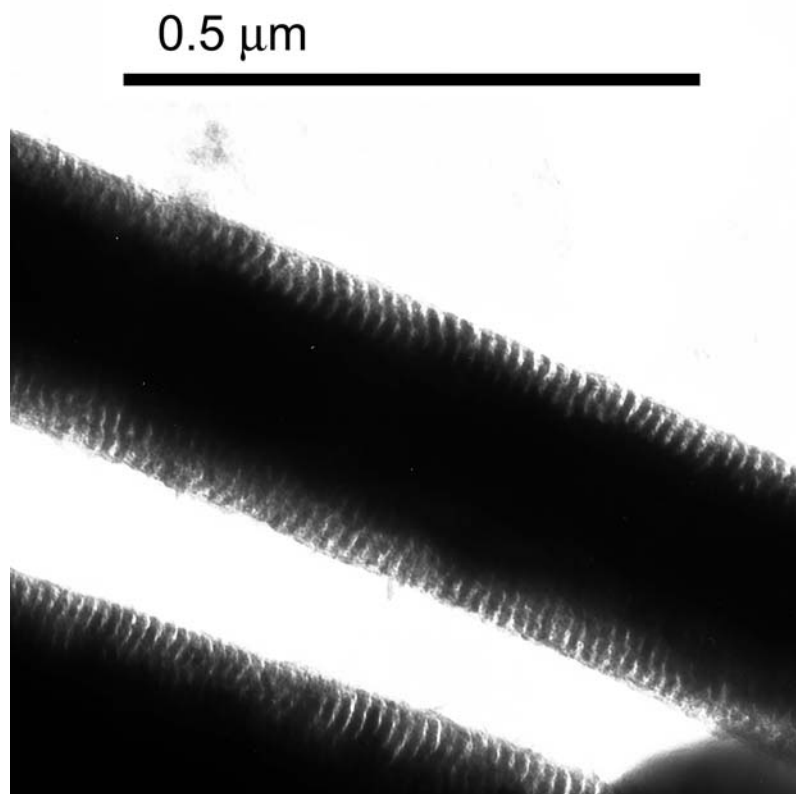
Figure 5.16 (a) TEM of CoNiFe/Cu wires electrodeposited in 20 nm pore AAO membrane

Figure 16 (c) shows an SEM of an array of CoNiFe/Cu tubes deposited using 400 nm pore membrane. The tubes diameter averaged 524 nm with 102 nm of standard deviation.
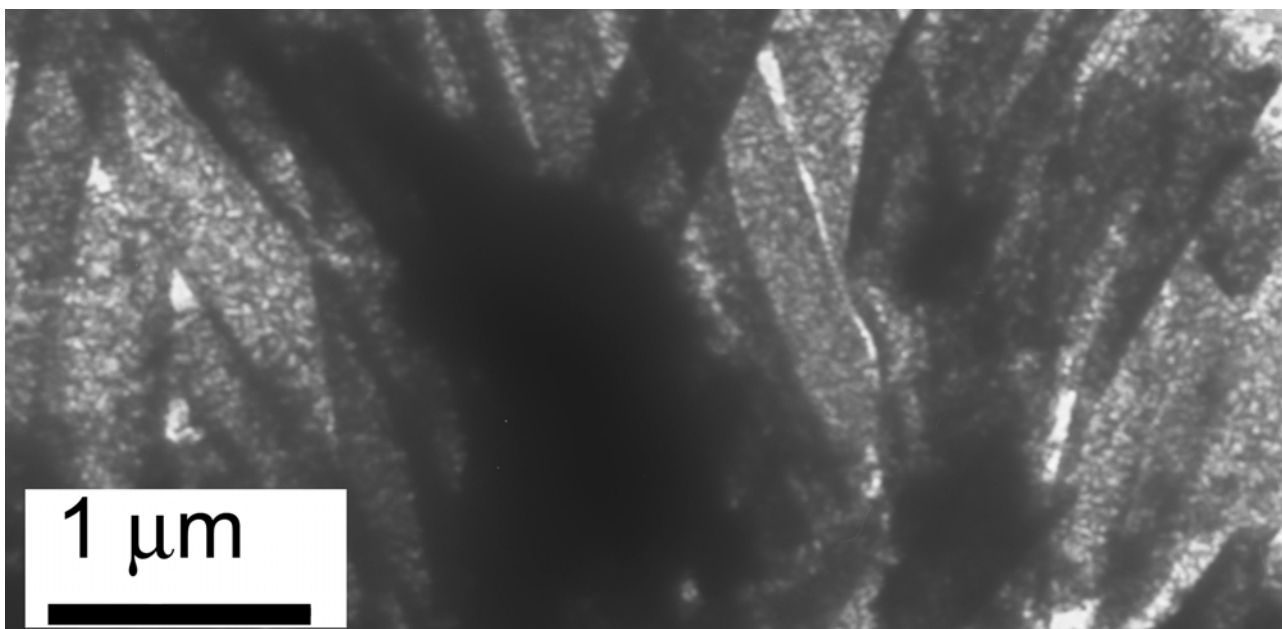
Figure 5.16 (b) TEM of CoNiFe/Cu tubes array electrodeposited in 200 nm pore AAO membrane
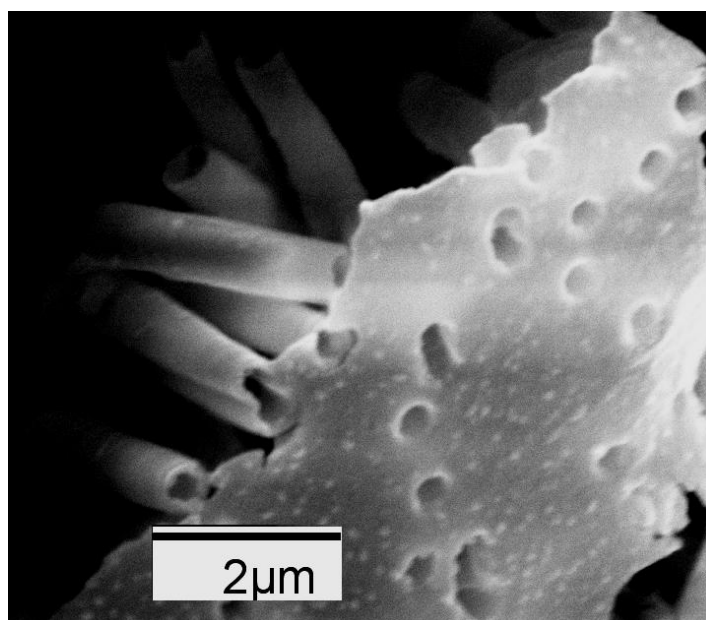
Figure 5.16 (c) SEM of CoNiFe/Cu tube array electrodeposited in 400 nm pore PC membrane

5.3.2 Alloy Layer Pulsing Time

Another parameter that influenced the wire/tube formation is the layers pulsing time. Looking at the experimental data, when the alloy pulsing time was increased the subsequent Cu layer pulse would have a longer transient time. Therefore increasing the alloy layer deposition time would increase the anodic portion of the Cu transient current, and as a result dissolving most of the alloy layer previously deposited. The schematic shown in Figure 5.17 illustrates this concept. To examine if the alloy deposition time would influence the formation of wire versus tubes, all deposition conditions were kept the same while the alloy layer deposition time was increased from 1 s to 3 s and 6 s. The Cu layer deposition time was constant at 20 s. The deposition scheme was the same as before: [Cu layer (-0.4 V for 20 s)/CoNiFe (-1.4 V for varied s)]. All experiments were executed using the smallest pore diameter membranes (20 nm). Figure 5.17 (a) shows the current transients when the alloy layer pulse at −1.4 V was the shortest, 1s. The Cu transient current shows a short (2 s) overshoot in the anodic current region during which a small portion of the alloy region would be dissolved. When the sample was examined at the TEM wires were observed and not tubes, as shown in Figure 5.18 (a). Figure 5.17 (b) shows the current transients when the alloy layer was pulsed at the same potential (−1.4 V) but the duration was increased to 3 s. The Cu transient current shows a slightly larger overshoot in the anodic current region but more importantly a longer anodic portion of 6 s during which a larger portion of the CoNiFe region was dissolved. As a result of less charge deposited, tubes were imaged at the TEM as shown in Figure 5.18 (b). Increasing the alloy pulsing time to 6 s further increased the Cu layer anodic transient current to approximately 12 s out of the 20 s total Cu deposition time. Figure 5.17 (c) shows the current transients when the alloy layer was pulsed at the same potential (−1.4 V) but the duration was increased to 6 s.
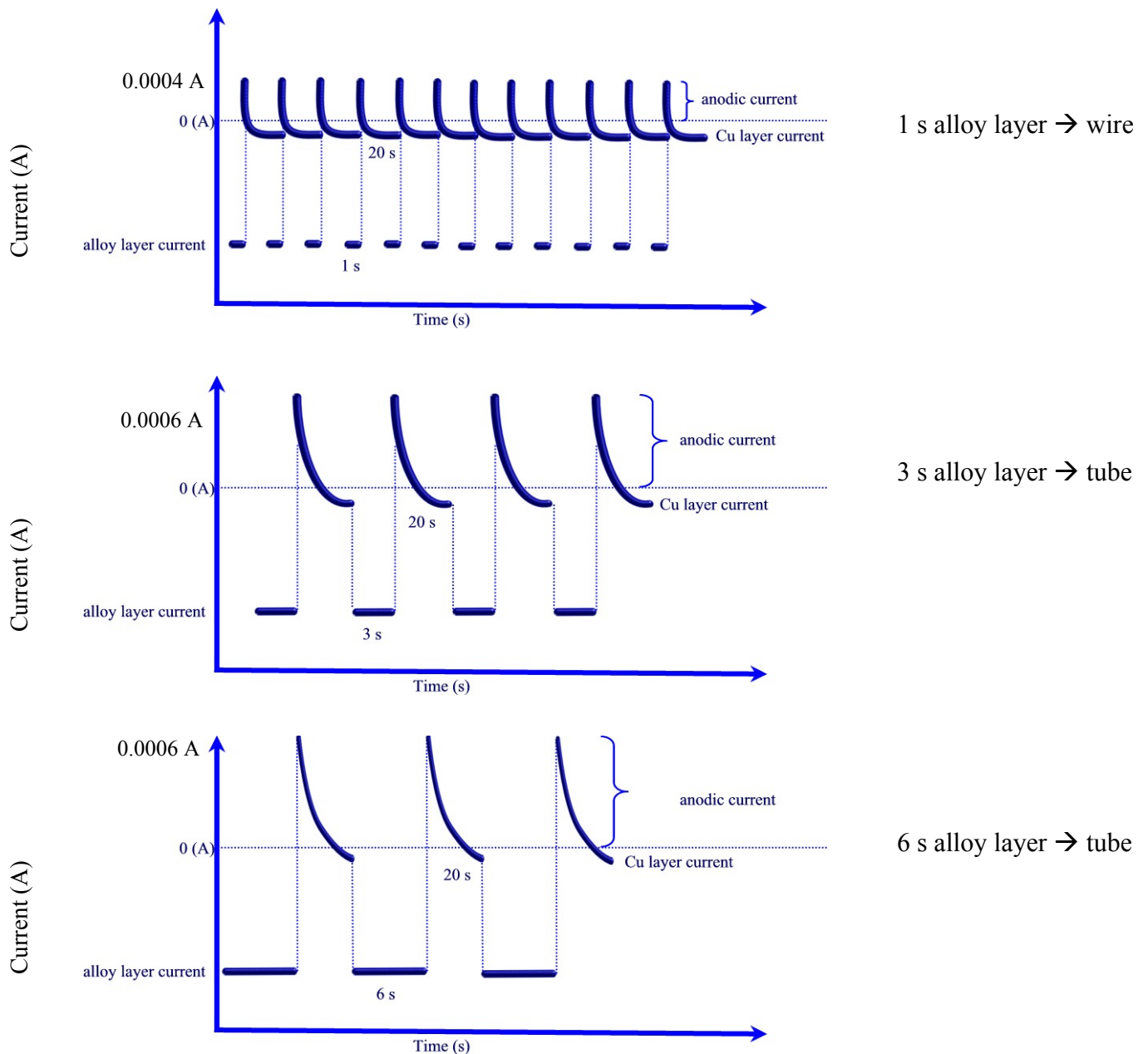
Figure 5.17 Current transients profiles during multilayered nanotube/nanowires deposition using potentiostatic control (a) 1 s alloy pulse (b) 3 s alloy pulse (c) 6 s alloy pulse

The Cu transient current shows a long (>10 s) overshoot in the anodic current region during which most of the alloy layer previously deposited would dissolve. When the sample was examined at the TEM tubes were observed as shown in Figure 5.18 (c). Figure 5.18 (a) shows a micrograph of the wires obtained when the alloy layer deposition time was 1s. The wire diameter averaged 167 nm with 13.5 nm standard deviation. The Cu layer (light) averaged 2.3

nm with 0.5 nm standard deviation and the CoNiFe layer (dark) was 3.7 nm with 1.5 nm of standard deviation. Figure 5.18 (b) shows a micrograph of a CoNiFe/Cu tubes obtained when the alloy layer time was increased to 3 s.   The tubes diameter averaged 156 nm with 22.5 nm standard deviation. Therefore, when the alloy layer was deposited for a longer time while the Cu layer was maintained the same as for the nanowires formation, tubes were formed instead of wires. Distinct layers were hard to distinguished at the TEM. Figure 5.18 (c) shows a TEM of an array of CoNiFe/Cu tubes formed by increasing the alloy deposition time to 6 s while maintaining the Cu layer time to 20 s. For this deposition scenario the layers were not visible at the TEM, however the tube formation was obvious. Cu layer pulsing time was also tested to determine if it influenced the wire/tube formation. Keeping the alloy layer the same as in the nanowire formation (-1.4 V for 1 s) the Cu layer deposition time was increased from 20 s to 100 s. From deposition data, when the Cu pulsing time was increased the Cu transient current was able to reach a semi steady state value, and the overall deposition charge increased for longer deposited Cu layers.

Figure 5.19 shows the CoNiFe/Cu nanowires obtained when the Cu layer pulsing time was varied. Figure 5.19 (a) shows the CoNiFe/Cu nanowires obtained when the Cu layer pulsing time was 20 s. The Cu layer (light layer) averaged 2.6 nm with 0.97 nm in standard deviation. Figure 5.19 (b) shows the CoNiFe/Cu nanowires obtained when the Cu layer pulsing time was 100 s. The Cu layer (light layer) averaged 15.5 nm with 3.2 nm in standard deviation. Increasing the Cu layer pulsing time did not induce the wire to tube transition, it just enlarged the wire Cu layer thickness.

To show the versatility of the multilayered tube-wire transition and manipulation, we attempted the electrodeposition of a tube inside a previously deposited tube. Figure 5.20 shows an SEM of a tube-in-tube configuration obtained in a two-step electrodeposition process.

Figure 5.18 (a) TEM of CoNiFe/Cu wires (1 s alloy layer pulse)
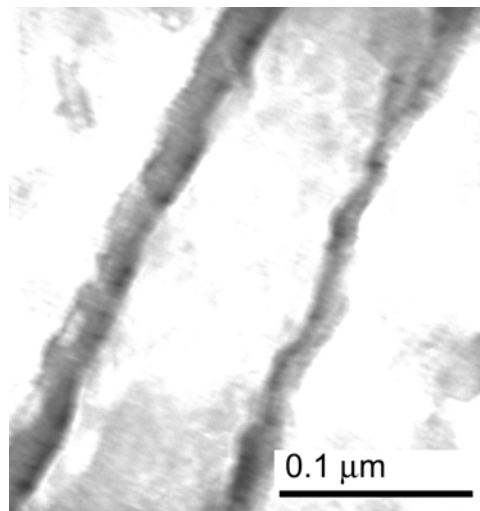
Figure 5.18 (b) TEM of CoNiFe/Cu tubes (3 s alloy layer pulse)
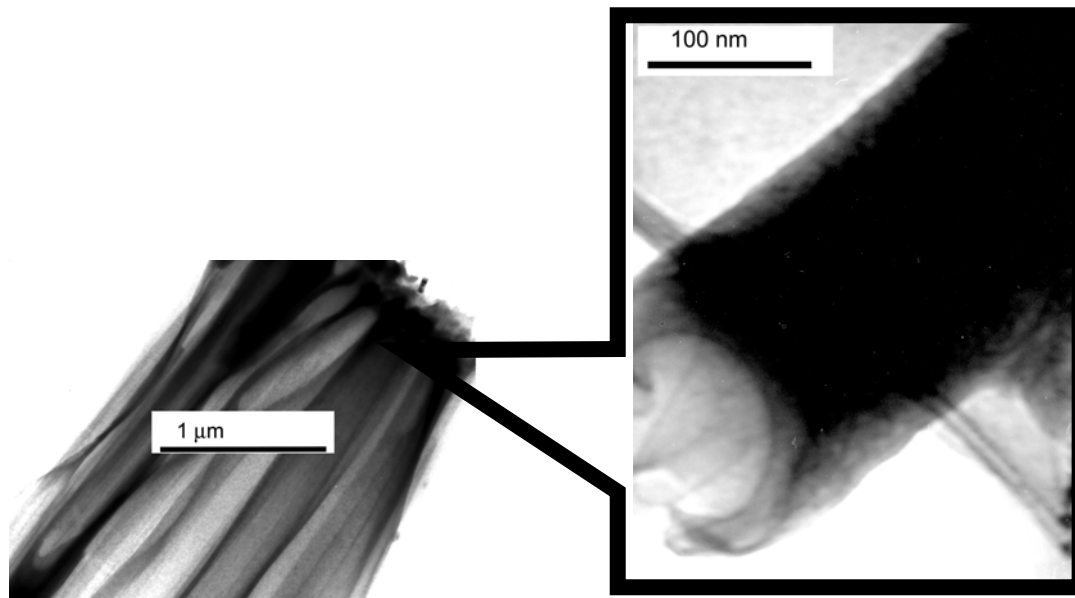
Figure 5.18 (c) TEM of CoNiFe/Cu tubes (6 s alloy layer pulse)

First multilayer tubes were deposited, after which the back of the membrane was re-sputtered with a second layer of Au to induce a subsequent nucleation process. Using the previously deposited dual sputtered membrane, Cu was deposited from the same low efficiency CoNiFeCu electrolyte. Concentric tubes were observed.
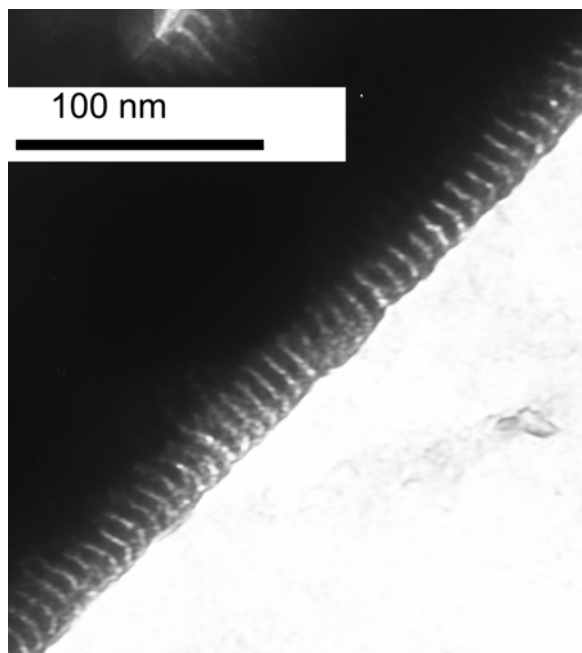
Figure 5.19 (a) TEM of CoNiFe/Cu wires (20 s Cu layer deposition)
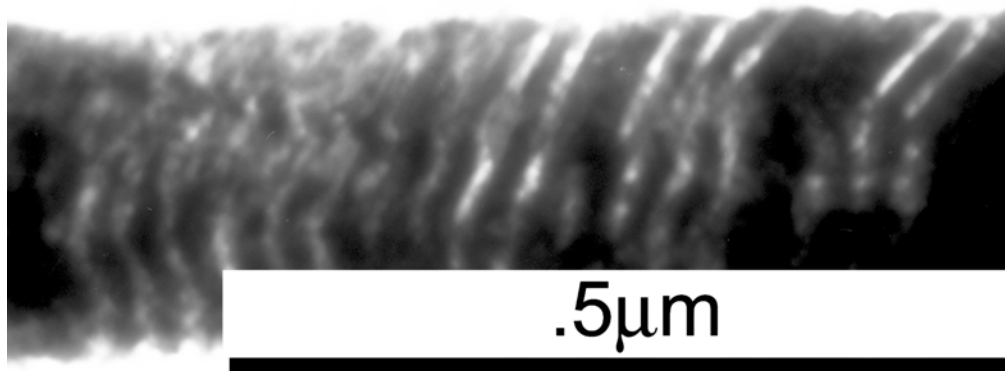
Figure 5.19 (b) TEM of CoNiFe/Cu wires (100 s Cu layer deposition)
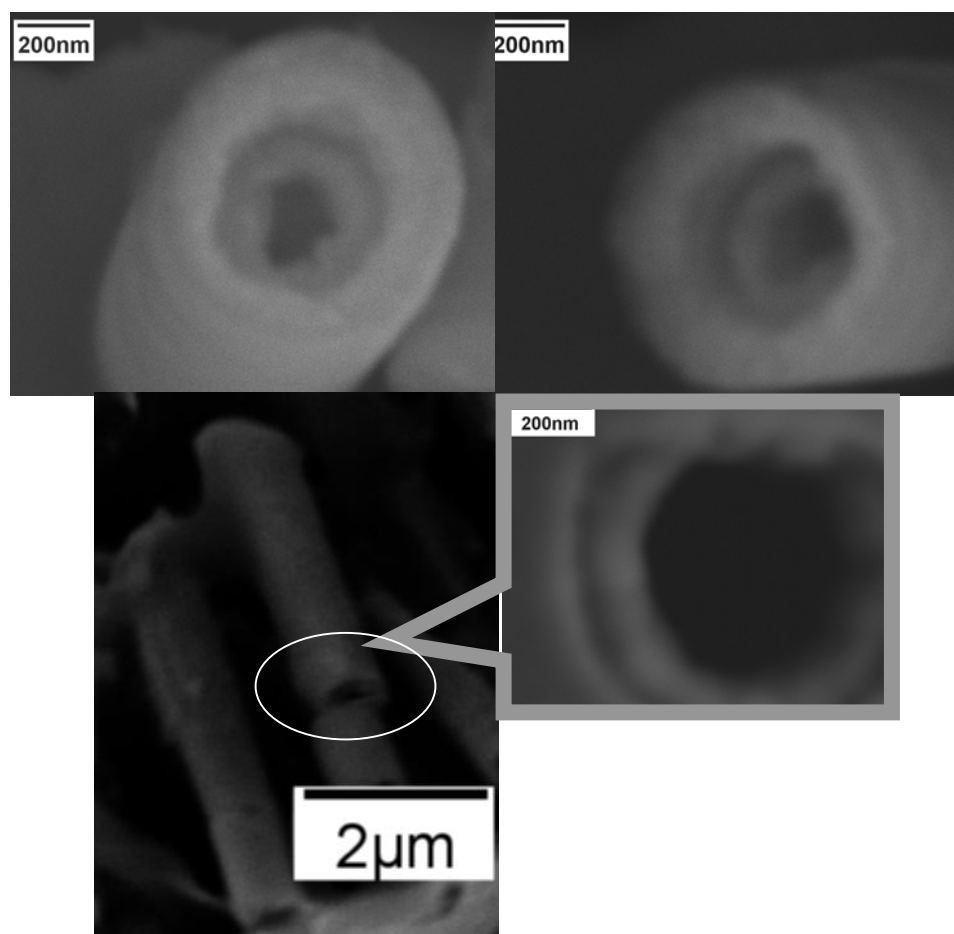
Figure 5.20 SEM of concentric tubes: CoNiFe/Cu exterior-Cu interior

5.4 Summary and Conclusions

Metallic elemental Cu and CoNiCu alloy nanotubes were electrodeposited inside PC and AAO membranes using potentiostatic control. The tubes were obtained from a low-efficiency

electrolyte that was critical for the tube formation. The partial pore coverage on the bottom of the membranes did not influence the tube formation.

Multilayered CoNiFe/Cu nanotubes were electrodeposited in both PC and AAO membranes of different pore sizes using pulsed potential electrodeposition and a single electrolyte. Giant magnetoresistance was shown in multilayered CoNiCu/Cu and CoNiFe/Cu tubes electrodeposited inside 200 nm pore AAO membranes. The tube GMR was observed to be sensitive to the alloy layer deposition potential. Parameters affecting the transition from nanowires to nanotubes were investigated. The membrane pore size dictated whether or not nanotubes were formed keeping other electrodeposition variables constant. Tubes were obtained in the 200 nm and larger pore size membranes. The ferromagnetic alloy layer pulsing time also affected tube vs. wire formation. Keeping the same Cu layer pulsing time and increasing the alloy layer deposition time influenced the tube formation because the transient Cu current was more than 50 % anodic. Varying the Cu pulsing time did not influence the tube formation.

CHAPTER VI TEMPERATURE EFFECT ON NANOSTRUCTURES AND GMR

Various deposition parameters affect the GMR via compositional and nanostructural changes. In the previous chapter it was shown how nanowire GMR is affected by the electrolyte concentration. The electrolyte temperature is another electrochemical deposition parameter that influences the chemical composition of the deposit and consequently the magnetic properties. Recently, Pattanaik *et al.* (Pattanaik, 2003) looked at the effect of both electrolyte temperature and annealing on CoCu thin film GMR. As the bath temperature increased from 20 to 35 ^{0}C, the resulting films showed an increase in magnetoresistance. However, further increasing the bath temperature showed a decrease in the films' GMR. Compositional analysis showed that with an increase in bath temperature from 20 to 35 ^{0}C, the Co concentration in the film decreases by 5 %. Also, further increasing the bath temperature lowered the Co concentration. Their findings imply that suitable control of bath temperature can optimize the Co concentration in the deposit, and thereby maximize MR. Post deposition annealing was also examined in their study and had affected the film magnetoresistance. Pattanaik *et al.* (Pattanaik, 2003) showed that the MR had a peak for a certain annealing temperature. Annealing can promote different granular structure of the films by thermally activating phase separation. In general thermal annealing reduces the structural disorder and modifies the Co particle size distribution.

6.1 Electrolyte Temperature Effect

To the best of the authors' knowledge, there are no studies done on the electrolyte temperature effect on the GMR of CoNi(Fe)/Cu nanowires and nanotubes. Therefore this study is focused on the investigation of the deposition of CoNiFe/Cu nanowires and tubes from electrolytes of different temperatures. Figure 6.1 shows the circulating hot water bath that was
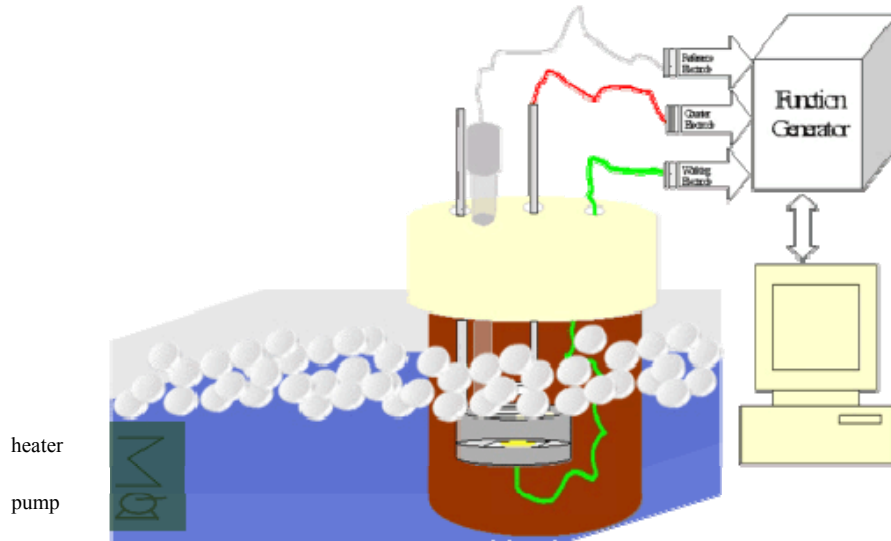
Figure 6-1 Electrolyte temperature control set-up

used to control the electrolyte temperature. The controlled temperature ranged between 25 to 90 °C. The electrodeposition current is affected by the electrolyte temperature. For example, under kinetic control the reaction rate is affected not only by the electrolyte concentration and the applied potential, but also by the electrolyte temperature, as indicated in equation 6-1, where the r_c is the cathodic reaction rate, i_c is the cathodic current, n is the number of electrons transferred, F is Faraday constant, k_c is the kinetic rate constant, C_s is the species surface concentration, p is the reaction order, and $\dfrac{-\alpha_c \cdot F}{R \cdot T}$ or b_k is the Tafel slope, a temperature dependent variable describing the relation between reaction kinetics and potential.

$$-r_c = \frac{i}{n \cdot F} = k_c \cdot \prod_j (C_s)^p = k_{c,0} \cdot \left[\prod_j (C_s)^p \right] \cdot \frac{-\alpha_c \cdot F \cdot E}{R \cdot T} = k_{c,0} \cdot \left[\prod_j (C_s)^p \right] (-b_k \cdot E) \qquad 6\text{-}1$$

The process is in the kinetic regime when the supply of reactants to the electrode surface is sufficient to avoid mass transfer limitations.

The equilibrium reversible potential can be influenced by temperature. Expression 6-2 is the Nernst relation that shows how the reduction potential is influenced by temperature, where

the concentrations of the oxidized and reduced species are C_O and C_R. The reversible potential E_{rev} is a characteristic property of the specific reaction.

$$E_{rev} = E_o + \frac{R \cdot T}{n \cdot F} \cdot \ln \left(\frac{\prod\limits_i C_{O,i}}{\prod\limits_j C_{R,j}} \right) \qquad 6\text{-}2$$

Among the four metals discussed in this study, Cu has a most positive (noble) E_{rev}. Therefore, Cu would be reduced far before the Co, Ni or Fe that have much more negative E_{rev}. The overpotential, η, is defined as the difference between applied potential (E) and the reversible potential, E_{rev}, which is the potential when the total current is zero, equation 6-3.

$$\eta = E - E_{rev} \qquad 6\text{-}3$$

The temperature influence comes together when expressing the electrodeposition current. Equation 6-4 shows the expression of the reduction current in which the temperature term is present twice. The reaction order (p) is equal to 1 in our particular case.

$$i_c = -n \cdot F \cdot k_{c,o} \cdot \exp\left(\frac{-\alpha_c \cdot F \cdot E_{rev}}{R \cdot T} \right) \cdot (C_s)^P \cdot \exp\left(\frac{-\alpha_c \cdot F \cdot \eta}{R \cdot T} \right) \qquad 6\text{-}4$$

When the applied potential is low, the reduction reaction is under kinetic control and the surface concentration of metal ions can be approximated equal to the bulk concentration. In the kinetic controlled regime, the deposition current depends exponentially on the applied potential. When the applied potential is high, then mass transport dominates. When mass transport is significant, the surface concentration is less than the bulk concentration leading to a concentration gradient at the electrode surface. Therefore when the overpotential is high, the reaction rate increases but the surface concentration decreases to zero. At this point the reaction rate is limited by the surface concentration, i.e. by the species diffusion to the electrode surface and at this point the

electrodeposition reached the limiting current (pure mass transport regime). In the electrolyte studied here, the Cu and Fe concentrations are very low and their reduction is limited by the rate of transport to the electrode surface. Since the diffusivities of liquids are rather low (10^5 less than in gases) the Cu and Fe reduction reactions are expected to be under diffusion control. The mass transport limited rate can be increased inducing agitation, increasing concentration of the reactant or increasing the temperature of the electrolyte. Diffusivities are also a function of temperature as shown by Stokes-Einstein relation (6-5).

$$\frac{D_i \cdot \mu}{T} = constant \qquad 6\text{-}5$$

For multicomponent liquid diffusion there are no simple, practical estimation methods for predicting diffusion coefficients. The generalized Stefan-Maxwell equations using binary diffusion coefficients are not easily applicable to liquids. There are many correlations available for diffusion coefficients in the liquid phase than for the gas phase that reflects the much greater complexity of liquids on a molecular level. Gas-phase diffusion exhibits negligible composition effects and deviations from thermodynamic ideality. Liquid-phase diffusion involves volumetric and thermodynamic effects due to composition variations. The Stokes-Einstein equation is the starting point for many correlations. Increasing the electrolyte temperature during deposition would increase the reaction rate constants and therefore the reaction rates. Under diffusion control equation 6-1 is modified to neglect kinetic limitations and becomes equation 6-6.

$$r = \frac{i}{n \cdot F} = -D\nabla C_i \qquad 6\text{-}6$$

Since the cathodic current is directly proportional to the reaction rate (6-1), the electrodeposition current is expected to increase at higher temperatures. Using a MathCAD simulation the

reduction currents were computed for different temperatures. The simulation took into account both the hydrogen and the oxygen reduction currents as well as the water dissolution currents.

6.1.1 Steady State Model for Electrolyte Temperature Effect

When modeling the electrodeposition of the Co-Ni-Fe-Cu quaternary system one has to be aware of the anomalous co-deposition behavior that has been observed and reported in the literature. Anomalous co-deposition is the preferential deposition of the less noble metal in the system. Different mechanisms have been proposed to account for the abnormal electrodeposition phenomenon. Zhuang and Podlaha (Zhuang and Podlaha, 2003) thoroughly studied the anomalous deposition of FeCoNi system and showed that the most noble species reaction rate was inhibited by the least noble species, consistent with the expected behavior of anomalous codeposition introduced by Brenner (1963). Their mathematical model simulated both the inhibiting and the catalytic effects observed during NiCoFe alloy deposition and assumed that the metal deposition occurred in a two-step mechanism. Their study also took into account that intermediates were formed and adsorb at the cathode. Their study showed that the least noble element reaction rate was actually enhanced during the anomalous co-deposition. They found that the inhibition of Ni and the enhancement of Fe were concentration dependent.

Previous studies published by Dahms and Croll (Dahms and Croll, 1965) on the anomalous co-deposition concluded that the inhibition of the more noble element was coming from the ferrous hydroxides blocking the electrode surface. Matlosz *et al.* (Matlosz, 1993) work on the anomalous co-deposition suggested that the metal was reduced in consecutive steps and that the Fe intermediates would cover up most of the electrode area therefore inhibiting the Ni deposition. Sasaki and Talbot suggested two distinct rate-determining steps existing in the reduction of metals during the anomalous co-deposition. Huang and Podlaha (Huang and

94

Podlaha, 2004) developed a non-steady state model for the electrodeposition of CoNiFeCu. The model combined the anomalous kinetic co-deposition with the mass transport considerations to describe the compositional gradients that happen when making multilayers of ferromagnetic and nonmagnetic materials. When the transient effect is considered the composition gradient does not exceed a thickness of 3 nm in the ferromagnetic layer. They also concluded that the copper deposition was affected by the presence of the adsorbed iron intermediates.

This present MathCAD model does not include a mechanism to describe the anomalous codeposition and it is used to predict only behavior. In this model the anomalous reduction of the iron-group metals was assumed to happen in a single step mechanism and the anodic and cathodic reaction components followed the Tafel kinetics shown in equation 6-1. A consequence of not including a kinetic model for the anomalous codeposition is that this simulation cannot be used to predict changes in the electrolyte composition.

Therefore, for a kinetically controlled process the current expression can be expressed in terms of the kinetic constant k, Tafel slope (b_k), species concentration (C) and applied potential (E). In a diffusion-limited case, the electrodeposition current (6-7) is expressed as a function of the concentration gradient (dC/dx) and species diffusivity (D). In equation 6-7 the concentration gradient is approximated as a straight line. Since the electrodeposition happens on the surface, the concentration becomes the surface concentration.

$$\frac{i}{n \cdot F} = D \cdot \frac{C_s - C_b}{\delta} \qquad \text{diffusion controlled current} \qquad 6\text{-}7$$

In a mixed deposition regime, both the kinetic and the diffusive effects contribute to the current density. To get a combined expression, the diffusion expression (6-7) is used to solve for the surface concentration and which is then substituted it into the kinetic expression (6-4).

For instance, the kinetic-diffusion mixed current for one of the electrodeposited species (Cu) at room temperature is shown in Equation (6-8), where δ is the boundary layer thickness, n is the number of transferred electrons and Cb_{Cu} is the bulk concentration of the Cu species. The reversible potential was adjusted for the three different temperatures and also specific kinetic constants were calculated.

$$i_{CuRT} = -k_{Cu} \cdot n \cdot F \cdot \frac{\dfrac{\left(-n \cdot F \cdot D_{CuRT} \cdot Cb_{Cu}\right)}{-\delta}}{k_{Cu} \cdot n \cdot F \cdot \exp\left[-b_{CuRT} \cdot \left(\eta + E_{revCu}\right)\right] - \dfrac{n \cdot F \cdot D_{CuRT}}{-\delta}} \cdot \exp\left[-b_{CuRT} \cdot \left(\eta + E_{revCu}\right)\right] \qquad 6\text{-}8$$

$$\text{where} \qquad E_{rev} = E_0 + \frac{R \cdot T}{n \cdot F} \cdot \ln(Cb)$$

The total steady state electrodeposition current equation (6-9) was found by adding up all the participant species currents and also the side reaction currents, such as the hydrogen evolution current, the water dissociation current and the dissolved oxygen current.

$$i_{Total} = \sum_{j} i_{j} \qquad 6\text{-}9$$

Table 6-1 presents the room temperature diffusion coefficients and kinetic parameters used in the model. The limiting current of each individual species present is calculated in the far right column. The diffusion coefficient was calculated assuming the Nernst diffusion layer expression 6-10, where i_{lim} was the limiting current, δ is the diffusion layer thickness, n are the transferred electrons, F is Faraday's constant and C_b is the bulk concentration. The diffusion coefficient varied with temperature according to Stokes-Einstein equation 6-5. All kinetic parameters such as rate constants and inverse Tafel slopes were taken from a previous study of Zhuang and Podlaha (2003) and Huang and Podlaha (2004).

$$D = \frac{-i_{lim,exp}\delta}{nFC_b} \qquad 6\text{-}10$$

To model the CoNiFeCu partial and total currents the following assumptions were made: (1) double layer charging was negligible (2) enough supporting electrolyte made migration negligible (3) Concentration gradients were unidirectional (4) one step kinetic mechanisms (5) uniform nucleation (6) steady state electrodeposition.

Table 6-1 Simulation kinetic and diffusion constants

species	D_i (cm^2/s)	k (cm/s)	α	C_b (mol/L)	b (V^{-1})	i_{lim} (mA/cm^2)
Fe	3.00E-06	1.00E-20	1.17	1.00E-03	45.26	0.096
Co	2.56E-06	1.80E-12	0.52	5.00E-02	20.116	4.117
Cu	2.56E-06	1.00E-08	1.71	1.00E-03	66.149	0.082
Ni	2.56E-06	9.00E-11	0.415	1.80E-02	16.054	1.482
H$_2$	7.33E-04	1.00E-06	0.39	1.00E-03	15.087	2.357
H$_2$O	5.27E-05	4.50E-11	0.251	1.00E+00	9.71	1.70E+03
O$_2$	2.42E-05	1.00E-17	1.41	2.70E-04	9.71	0.21

The graph in Figure 6.2 shows the modeled total currents of CoNiFeCu at three different temperatures: cold (4 ^{o}C), room temperature (RT) and hot (50 ^{o}C). In the model the side reactions currents were included and simulated for different electrolyte temperatures. Figure 6.3 shows the modeled side reaction currents at different temperatures. In the mixed (kinetic-mass transport) electrodeposition regime the hydrogen current is higher in the cold electrolyte than in the RT or hot electrolyte, as Figure 6.3 (a) illustrates. However, at high overpotentials the hydrogen limiting current behaves oppositely with temperature, increasing in the higher temperature electrolyte and decreasing in the 4 ^{o}C environment. The water dissolution current is shown in Figure 6.3 (b). At higher overpotentials (in the alloy deposition region) the water dissolution current did not seem to be much affected much by the electrolyte temperature, but for smaller overpotentials the water dissolution current is higher in the chilled electrolyte.
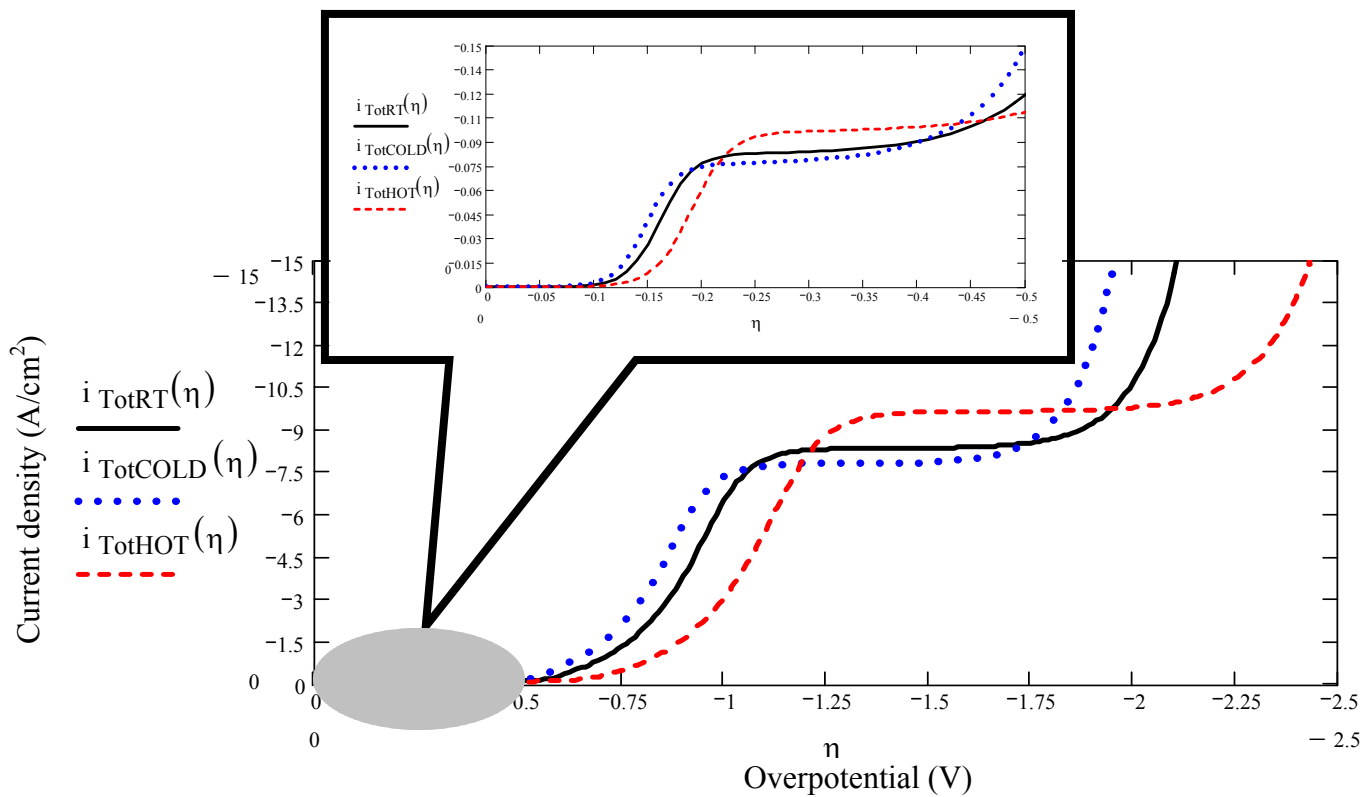
Figure 6-2 Simulated CoNiFeCu total currents at different electrolyte temperatures

Figure 6.3 (c) shows the modeled oxygen current at different temperatures. It is interesting to see that the O_2 current increased at the lower temperature since more O_2 was dissolved in the electrolyte at 4 ^{o}C.

Inspection of the modeled partial current densities of the different metal species involved in the electrodeposition reveals that all elemental electrodeposition currents increased at higher electrolyte temperature. Also the metal reduction potentials shifted to the right, towards the more negative potentials, when the electrolyte temperature increased. Figure 6.4 shows the species partial currents modeled at the three different temperatures. Even though all currents increased similarly with temperature, when the temperature decreased to 4 ^{o}C the Ni and Fe currents showed a small reduction with electrolyte temperature. The current efficiency was modeled for the deposition at different electrolyte temperatures. Current efficiencies were calculated by adding up all the metal currents and dividing the sum by the overall total current.

Figure 6.5 shows the current efficiencies at different electrolyte temperatures. The overall current efficiency reached a maximum of 100 % in the Cu deposition region between at –0.15 V and –0.4 V. The current efficiency drops at the more negative Cu deposition potentials and in the alloy deposition region. For instance, the efficiency drops from 100 % at 0.25 V to 75 % at –0.5 V. In the alloy deposition region the efficiency reaches a maximum of 66 % in the range
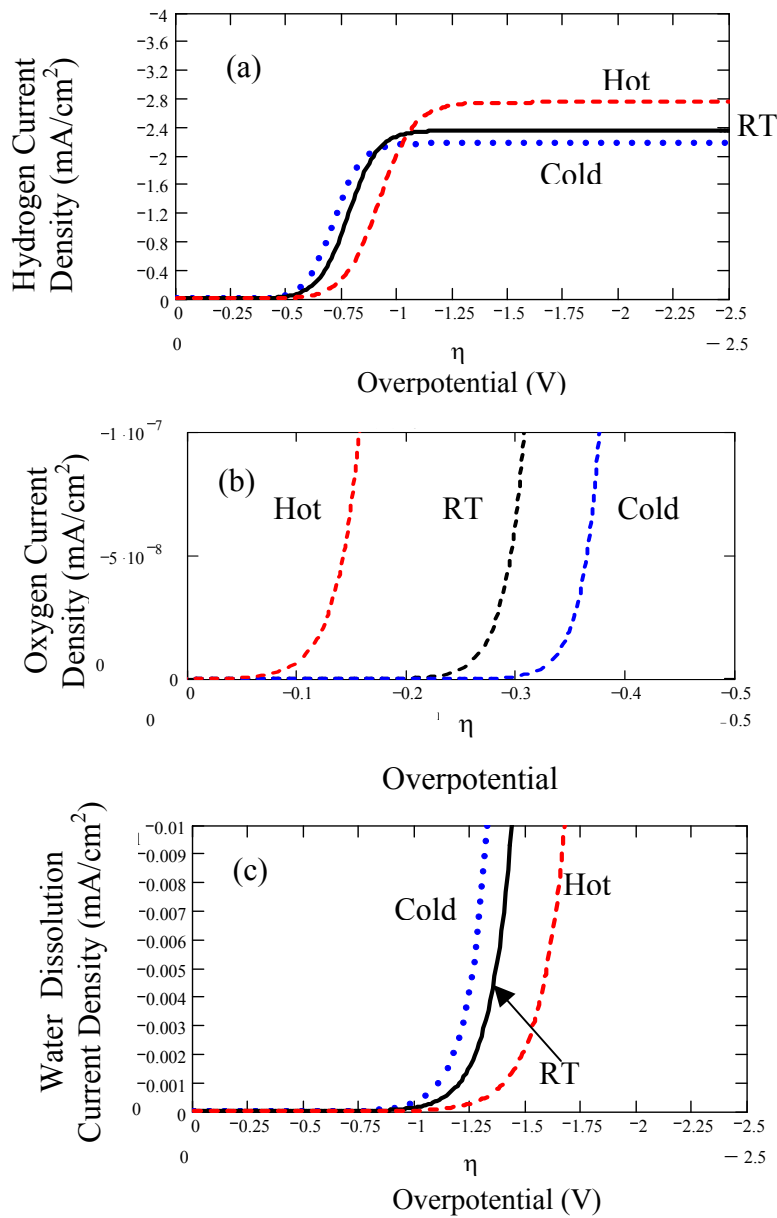
Figure 6.3 Modeled side reactions currents at different temperatures. (a) hydrogen current (b) oxygen current (c) water dissolution current

from −1.2 V to −1.7 V. The alloy efficiency drops to 35 % at higher overpotentials, past −1.7 V.

The model the current efficiency was not affected much by the temperature. The higher

efficiencies were slightly shifted towards the more negative potentials when the electrolyte was

heated and towards the more noble potential when the electrolyte was chilled. At −1.5 V the

alloy current efficiency seems to be the same for the three studied temperature cases. In the Cu

region, -0.25 V seemed to yield the maximum current efficiency for all three electrolyte

temperatures. Next, the simulated reduction currents were compared to the actual deposition

currents.
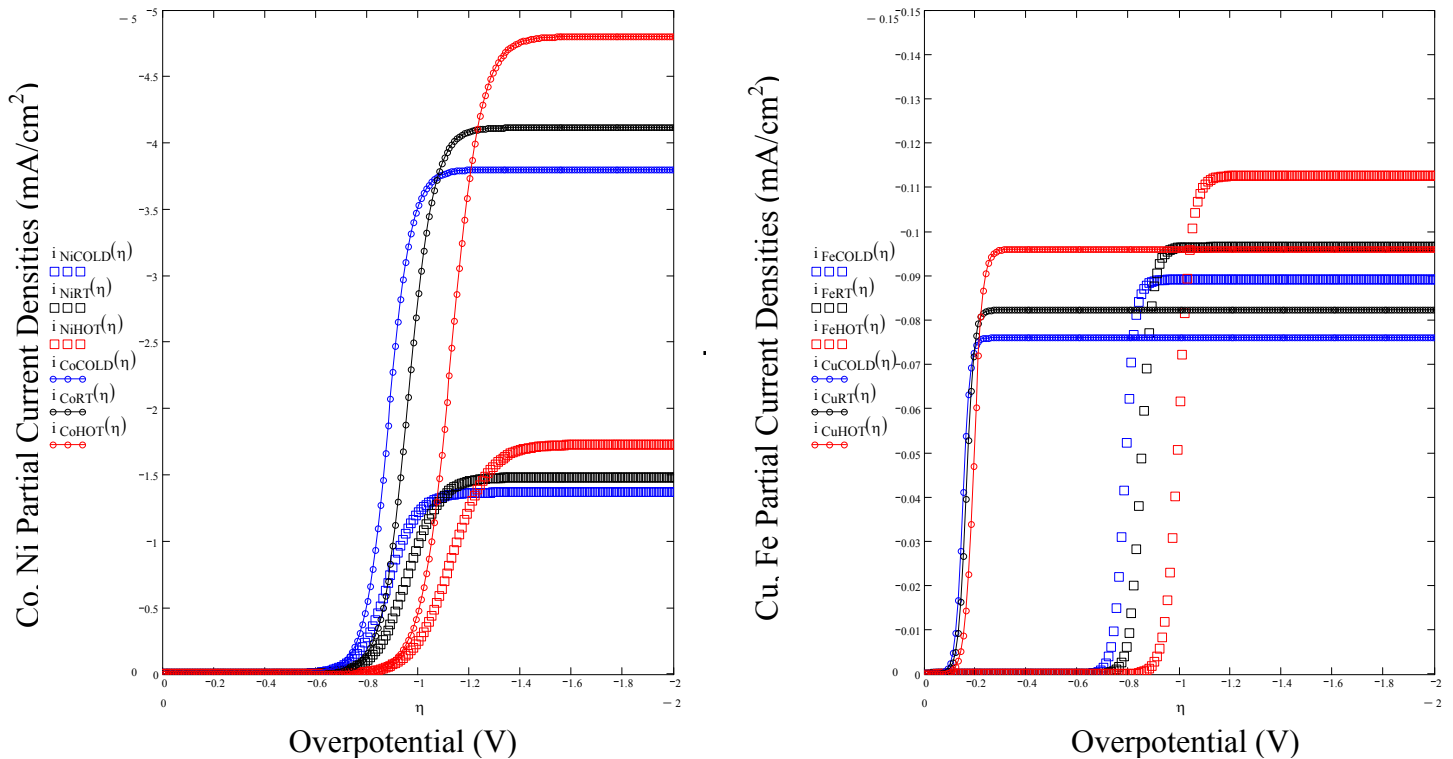
Figure 6.4 Modeled partial current densities at three electrolyte temperatures
(a) Co and Ni (b) Cu and Fe

Figure 6.6 shows the electrolyte behavior for different temperatures when the potential was swept in time at a rate of (25 mV/s). The polarization curves at different temperatures were
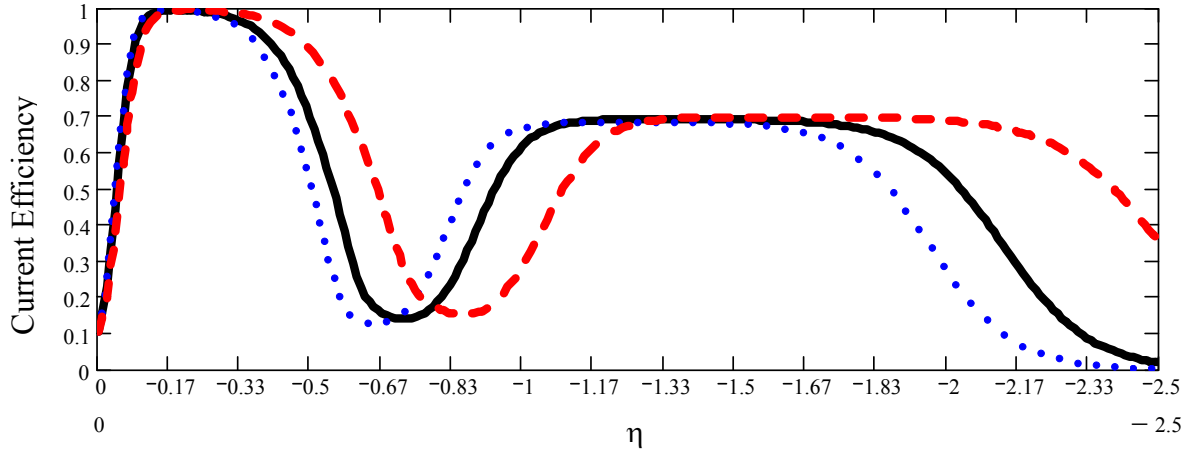
Figure 6.5 Modeled current efficiencies at different temperatures

carried out using the AAO membrane as the cathode.

To understand the different deposition behavior when changing the electrolyte temperature, deposition current was plotted and compared for the three main temperature cases: chilled (4 $^{\circ}$C), room temperature and hot (50 $^{\circ}$C). From the polarization behavior run in the high temperature electrolyte it was observed that the electrolyte temperature affected the current and the current increased with electrolyte temperature as illustrated in Figure 6.6 (a). Figure 6.6 (b) shows the simulated polarization curves at the same three temperatures. When the electrolyte was 50 $^{\circ}$C, the current was considerably higher and it exhibited two peaks related to a transient mass transport effect. The first peak was in the Cu deposition region and the second peak was in the alloy deposition region. At room temperature, the current decreased compared to the 50 $^{\circ}$C case, and both the Cu and alloy peaks were smaller. When the electrolyte is chilled at 4 $^{\circ}$C, the current is significantly reduced, but the Cu peak is still present, however diminished in size.

When comparing the experimental polarization curves performed at different temperatures, Figure 6.6 (a), with the modeled currents, Figure 6.6 (b), it could be observed that

101

the general current behavior was in agreement: the overall current increased at higher temperatures and decreased at the cooler temperature. In the model the alloy deposition current at all three temperatures reaches a limiting current between 9 and 12 mA at a small negative potential of -1.3 V. This behavior is not observed experimentally, since only the 50 ^{o}C alloy current shows a much larger limiting current of 30 mA at a high potential of -2.25 V.

Experimentally, the limiting current is not reached in the alloy deposition region when the electrolyte was chilled at 4 ^{o}C, due to the absence of the peak. Also, at 50 ^{o}C the mass transport region is not as flat as when the current was simulated. Out of the three studied temperature cases, the experimental room temperature current profile was closest in agreement to the modeled case. In general the model does not simulate the peaks observed in the experimental case but captures the change in the total current with temperature. The Cu mass transport peak increased considerable when the electrolyte temperature was 50 ^{o}C, however the model did not reflect it. In both the experimental and simulated scenarios the total reduction current showed an increase with the electrolyte temperature and a decrease when the electrolyte was chilled to 4 ^{o}C. Experimentally, the total current decreased by 5.75 % experimentally when the cold electrolyte was used and increased by 13.5 % when the electrolyte was heated to 50 ^{o}C. Also, the reduction potential shifted by 0.14 V towards the more negative potential when the electrolyte was heated. However, when the electrolyte was chilled the reduction potential shifted to the more noble region by 0.065V. In the alloy deposition region, at 4 ^{o}C the total current was -8 mA compared to -8.5 mA at room temperature and -9.8 mA at 50 ^{o}C.   In the Cu deposition region, in the low temperature electrolyte the current measured -0.079 mA compared to -0.085 mA at room temperature and -0.098 mA at 50 ^{o}C. Therefore when the electrolyte was chilled, the Cu current

decreased more than the alloy current. Moreover, when the electrolyte was heated, the Cu current and the alloy current increased equally.
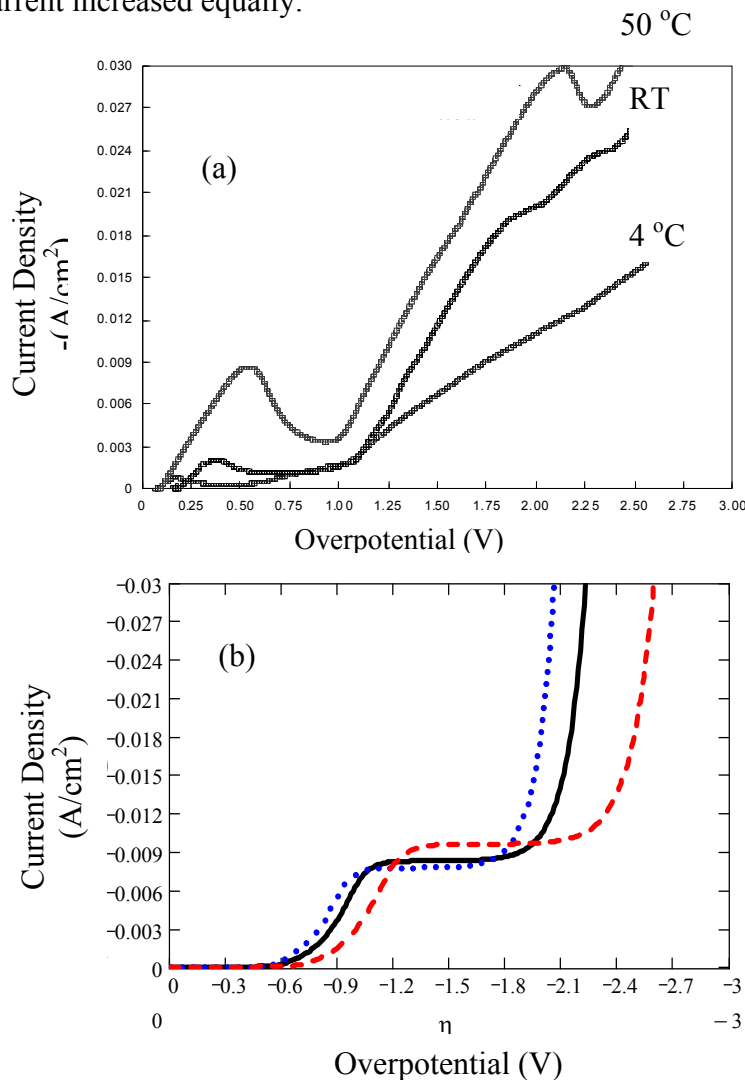
Figure 6.6 CoNiFeCu polarization curves for different electrolyte temperatures
(a) experimental data (50 ^{o}C, RT and 4°C) (b) modeled curves (50 ^{o}C, RT and 4°C)

6.1.2 Non-Steady State Model for Electrolyte Temperature Effect

To get a closer fit model of the nanowire deposition at different temperatures the steady state current assumption had to be altered. The species concentration is not only a function of position (x) but it also changing with time (t). The species concentration expression is shown in equation 6-11.

$$\frac{\partial C}{\partial t} = D\,\frac{\partial^2 C}{\partial x^2} \qquad\qquad 6\text{-}11$$

In order to obtain the surface concentration profile and hence the current density, the 2$^{\text{nd}}$ order PDE (6-11) has to be solved. Laplace transforms were used to convert the 2$^{\text{nd}}$ order PDE into an ODE, by reducing the number of variables to only the dimensional component. To make the integration easier, a dimensionless concentration was defined so that the integration limits would be 0 and 1. The characteristic equation in the Laplace domain is shown in equation 6-12, where C^T is dimensionless concentration in the Laplace domain, D is the species diffusivity, s is the Laplace domain constant, and C1 and C2 are the constants that need be evaluated using the boundary conditions after transforming them into the Laplace domain. Un-transformed boundary conditions are listed in 6-13 and 6-14. Far from the electrode surface where the reaction takes place, the species concentration is assumed to be the same as the bulk concentration, 6-13. Close to the electrode surface, the surface concentration changes according to the diffusion relation shown in equation 6-14.

$$C^T = C1 \cdot e^{\sqrt{\frac{s}{D}} \cdot x} + C2 \cdot e^{-\sqrt{\frac{s}{D}} \cdot x} \qquad\qquad 6\text{-}12$$

$$x = \delta \qquad C = Cb \qquad\qquad 6\text{-}13$$

$$x = 0 \qquad \frac{i}{n \cdot F} = -D \cdot \frac{C_s - C_b}{\delta} \qquad\qquad 6\text{-}14$$

The untransformed PDE characteristic equation constant C2 is solved for, equation 6-15. C1 is a function of C2.

$$C1 = \frac{k_{Cu} \cdot Cs \cdot e^{(-b \cdot E)} + D \cdot C2 \cdot \sqrt{\frac{s}{D}}}{D\sqrt{\frac{s}{D}}} \qquad C2 = \frac{\left(-k_{Cu} \cdot Cs \cdot e^{-b \cdot E}\right)}{D \cdot \left(e^{\sqrt{\frac{s}{D}} \cdot \delta} + e^{-\sqrt{\frac{s}{D}} \cdot \delta}\right) \cdot \sqrt{\frac{s}{D}}} \qquad 6\text{-}15$$

In addition, the potential was not a constant, but it varied with the sweep rate (λ) and it also had to be transformed in the Laplace domain. The x-axis on the polarization curve is the potential range, that actually varied with the sweep rate (λ) and the Laplace form is shown below in 6-16:

$$\frac{dE}{dt} = \lambda$$

$$s \cdot E_{Laplace} - E_0 = \lambda$$

$$E_{Laplace} = \frac{\lambda + E_0}{s} \qquad\qquad 6\text{-}16$$

For example, the Cu surface concentration was transformed back to the time domain using Mathematica. The surface concentration of Cu shown in 6-17 was substituted in the defined dimensionless concentration form and solved. The Cu current profile at room temperature is shown in expression 6-18, after replacing the surface concentration with the expression shown in 6-17.

$$Cs_{CuRT} = \frac{\left[100000 \cdot (D_{CuRT})\right]^{\left(\frac{1}{2}\right)} \cdot Cb_{Cu} \cdot \exp(0.75t)^{0.1}}{100000 \cdot (D_{CuRT})^{\left(\frac{1}{2}\right)} \cdot t^{0.25} + 56419 \cdot Cb_{Cu} \cdot k_{oCuRT} \cdot \exp\left(\frac{-\alpha_{Cu} \cdot Faraday \cdot E_{revCuRT}}{R \cdot T_{RT}}\right) \cdot \exp\left(-1 \cdot b_{CuRT} \cdot \eta\right) \cdot t^{0.25} - 56419 Cb_{Cu} \cdot k_{oCuRT} \cdot \exp\left(\frac{-\alpha_{Cu} \cdot Faraday \cdot E_{revCuRT}}{R \cdot T_{RT}}\right) \cdot \exp\left(-1 \cdot b_{CuRT} \cdot \eta\right) \cdot \exp\left(\frac{-0.15}{0.5 \cdot D_{CuRT}} \cdot \frac{\delta^3}{t^{-3}}\right)} \qquad 6\text{-}17$$

$$i_{CuRT} = -k_{oCuRT} \cdot \exp\left(\frac{-\alpha_{Cu} \cdot Faraday \cdot E_{revCuRT}}{R \cdot T_{RT}}\right) \cdot n \cdot Faraday \cdot Cs_{CuRT} \cdot \exp\left(-b_{CuRT} \cdot \eta\right) \qquad 6\text{-}18$$

Figure 6.7 shows a comparison between the non-steady state modeled Cu current and the experimental polarization curves. In the experimental polarization curves the Cu limiting current peak increases drastically in the high temperature electrolyte and becomes almost flat in the chilled electrolyte. In the modeled case, the Cu limiting current peak does not change drastically with electrolyte temperature, maintaining almost the same shape and size for all three temperatures.
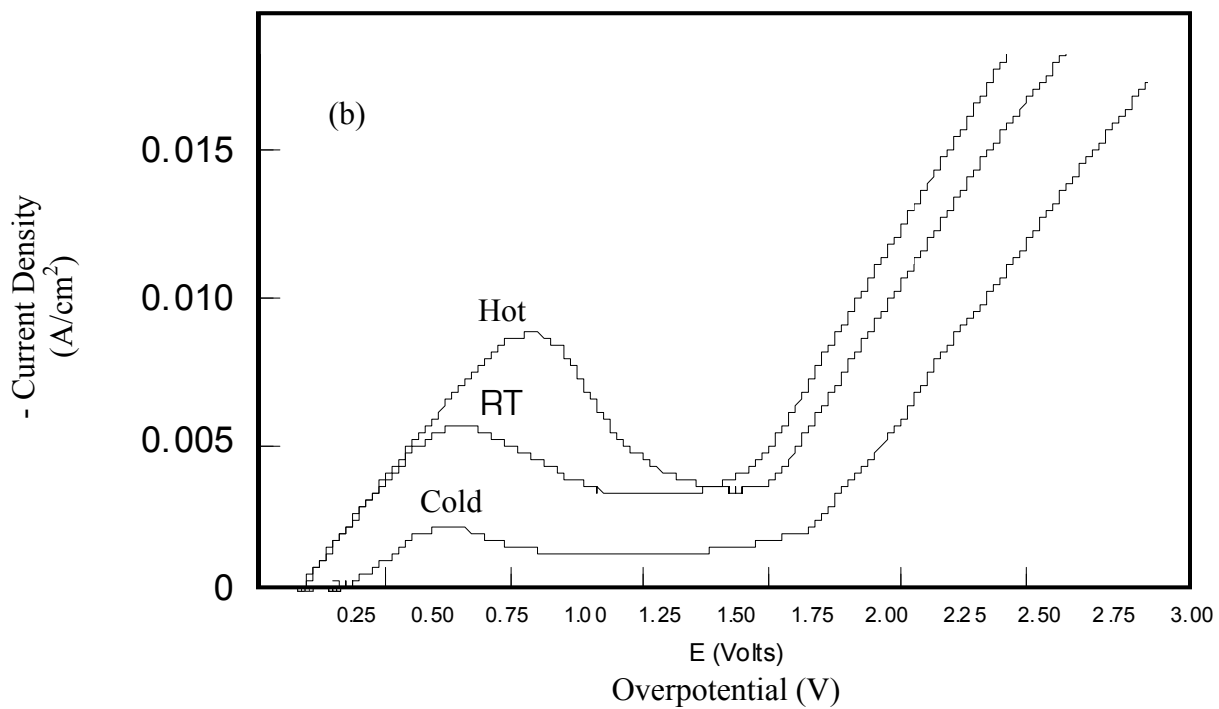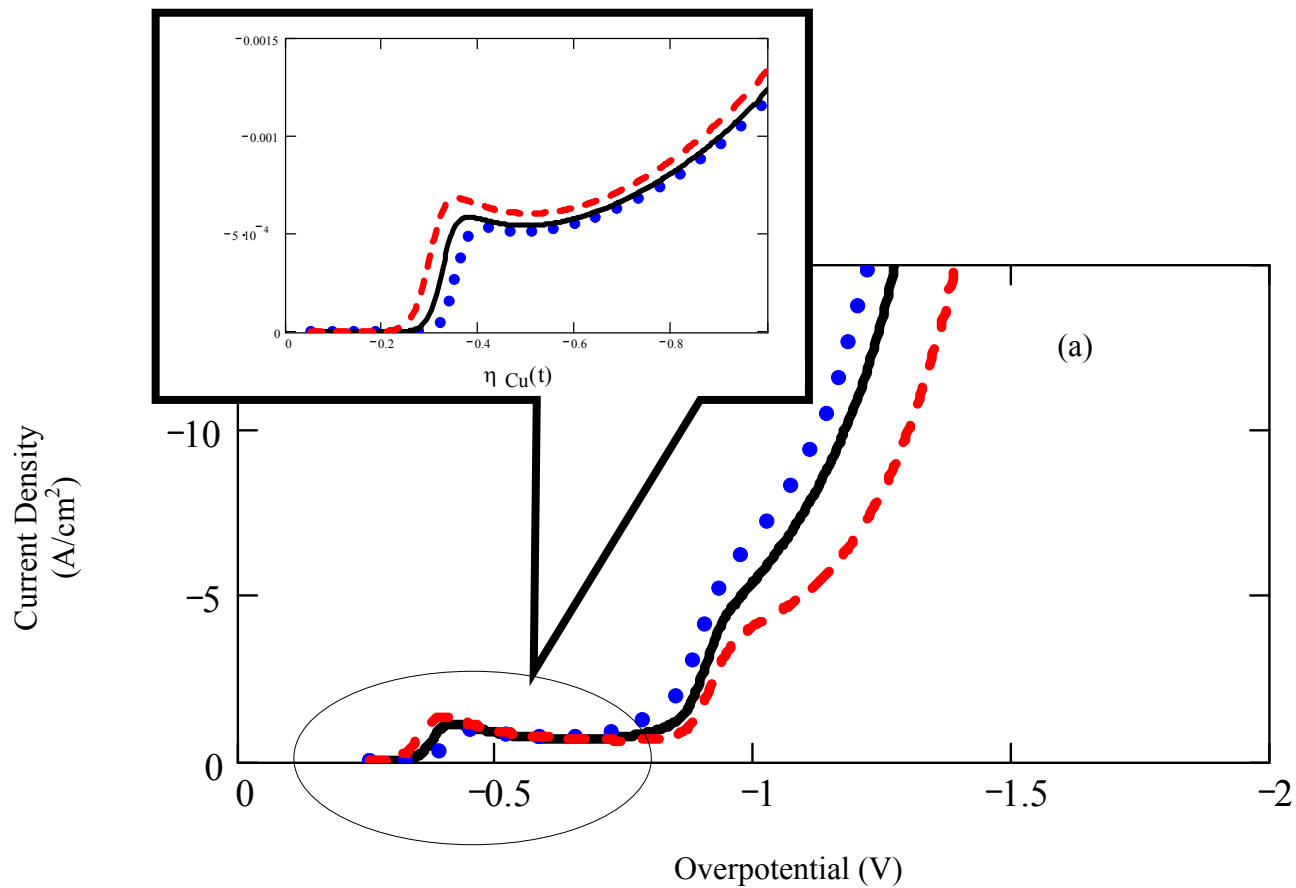
Figure 6.7 Comparison of modeled and experimental Cu currents at different electrolyte temperatures (a) non-steady state model (b) experimental

Since the Cu deposition is under diffusion control it can be inferred that the diffusion constants used in this simulation were not well adjusted for temperature changes. In the current model species diffusivities varied with temperature according to the Stokes-Einstein relation (6-5), which is the general starting point of the more complex, case-by-case experimental correlations found in literature. For a more precise fit of the experimental currents with temperature variations, the diffusion coefficients have to more specifically predicted.

6.1.3 Multilayered Nanowires at Different Electrolyte Temperatures

Figure 6-8 shows the alloy nanowire deposition under potentiostatic control when the electrolyte temperature was varied. The sudden increase in the transient current profile shows when the alloy nanowires reached the top of the membrane and consequently the deposition reached a steady state. In the higher temperature electrolyte the increase in current density is abrupt and it is easier to pinpoint where the nanowires completely filled the AAO membrane.
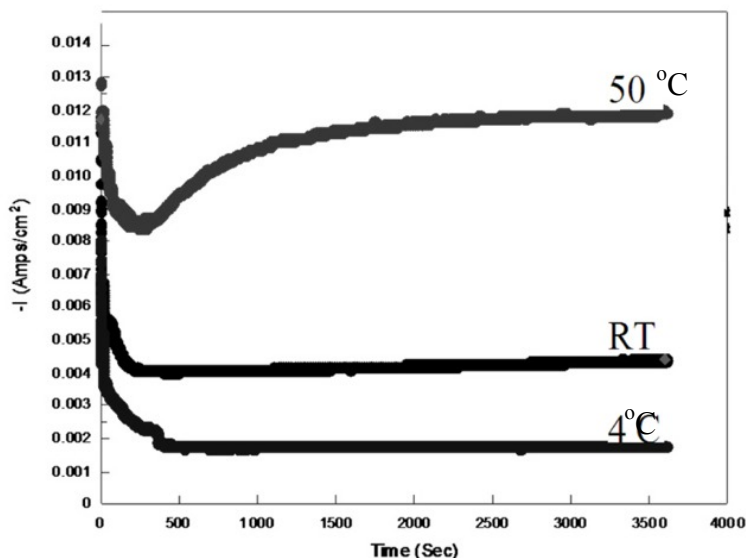
Figure 6.8 Alloy nanowire currents at different electrolyte temperatures

When the electrolyte was hot it took 500 s for the deposition to reach steady state. During the electrodeposition of multilayers, the potential was stepped between the high reduction potential

of the alloy layer (-1.4 V) and the more noble potential of Cu (-0.4 V) as shown in the schematic of Figure 6.9 (a). Multilayers were also electrodeposited at 4°C, room temperature and 50 $^{\circ}$C, and the electrolyte temperature affected the current transients during each layer deposition. The Cu transient currents and the alloy transient currents behaved differently with electrolyte temperature.

Figure 6-8 (b) shows the Cu transient current profiles at different temperatures. When the electrolyte was chilled the Cu current decreased 45 % relative to the room temperature current. When the electrolyte was heated to 50 $^{\circ}$C the Cu current increased 43 % relative to the room temperature Cu current. The high temperature also increased the anodic current that contributes to the loss of the alloy layer through a displacement reaction during the transition from the alloy potential to the Cu.

Figure 6-9 (c) shows the alloy layer current transient profiles when the electrolyte temperature was 4 $^{\circ}$C, room temperature and 50 $^{\circ}$C. The alloy layer current increased 32 % relative to the room temperature current when the electrolyte was heated to 50 $^{\circ}$C, and decreased 48 % relative to the room temperature current when the electrolyte was chilled to 4 $^{\circ}$C.

Figure 6-9 (d) shows the alloy layer transient current for the entire pulsing time at different temperatures. The current behavior differs with temperature. At 4 $^{\circ}$C, in the first 2000 s the current drops almost linearly, which is typical for a diffusion-controlled reaction. After 2500 s the current increases linearly for 300 s and then plateaus up to 12000 s. At 50 $^{\circ}$C, the current behaves oppositely. In the first 2000 s the current increases linearly after which it drops for 300 s, then plateaus up to 8000 s after which it keeps increasing until the deposition was stopped. The cold and hot currents profiles are almost mirror images of each other.
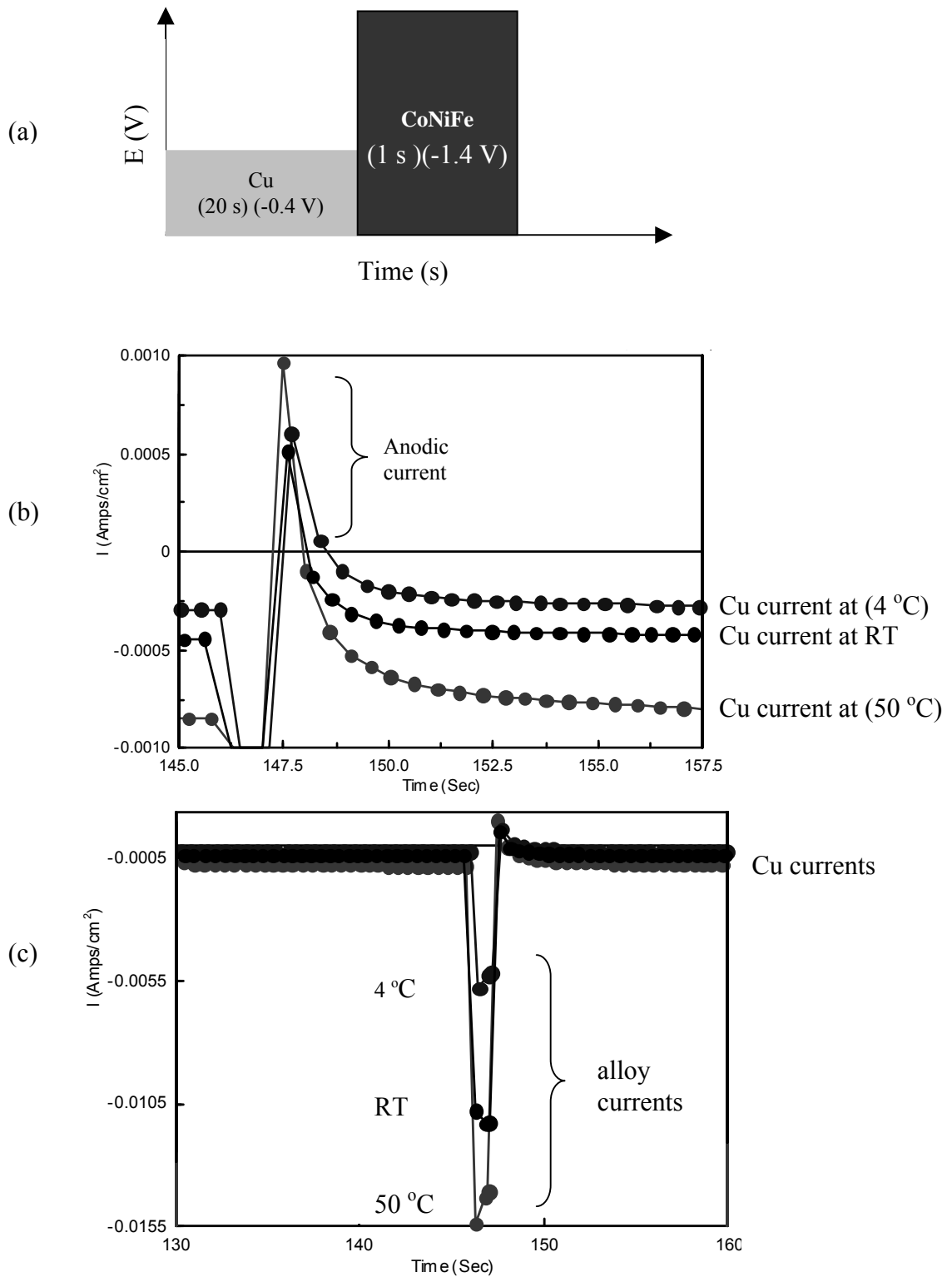
Figure 6-9 Transient currents during pulsed electrodeposition at 4 ^{o}C, RT and 50 ^{o}C (a) potential pulsing schematic (b) Cu layer transient (c) alloy layer transient

Figure 6-9 (e) shows the Cu layer transient current for a long pulsing time at different temperatures. The current behavior is different with temperature. At 50 ^{o}C, the current decreases in the first 5000 s and reaches a semi-steady state after 10000 s. In the room temperature case, the Cu current suddenly increased after 6000 s of deposition. At 4 ^{o}C the Cu current remains almost the same, which could be a sign of a kinetic controlled electrodeposition. The high temperature alloy growth yielded nanowires while from the cold electrolyte the result of electrodeposition was nanotubes. In the first 2500 s of deposition, the current dropped during tube formation and increased during wire growth, which could be explained by changes in the electrodeposition area. In general, when wires are electrodeposited the current increases drastically when the nanowires reach the top of the membrane and the deposition area increases.

The overall sample composition changed with electrolyte temperature. CoNiFeCu alloy was deposited at -1.4 V and different electrolyte temperatures. Table 6-2 shows the WDS composition analysis of the alloy samples deposited at three different temperatures. When the deposition was carried out from the hot electrolyte, the Cu content in the alloy was very large (80 %) while the Co content was much smaller (16.7 %) than obtained from the temperature electrolyte. When the electrolyte was controlled at 4 ^{o}C, the Cu content in the alloy decreased to 26.6 %, while the Co content was much higher (69.4 %) than at 50 ^{o}C. The lowest Cu content (18.8 %) and the highest Co content (76.98 %) were observed from the room temperature deposition.

Current efficiencies at these three temperatures were calculated after weighting the samples and integrating the current. At room temperature the current efficiency was 69.4 % for the alloy deposition. At 50 ^{o}C the current efficiency drops to 51 % compared to the room temperature current efficiency. Interestingly, at the low temperature of 4 ^{o}C the current

(d)
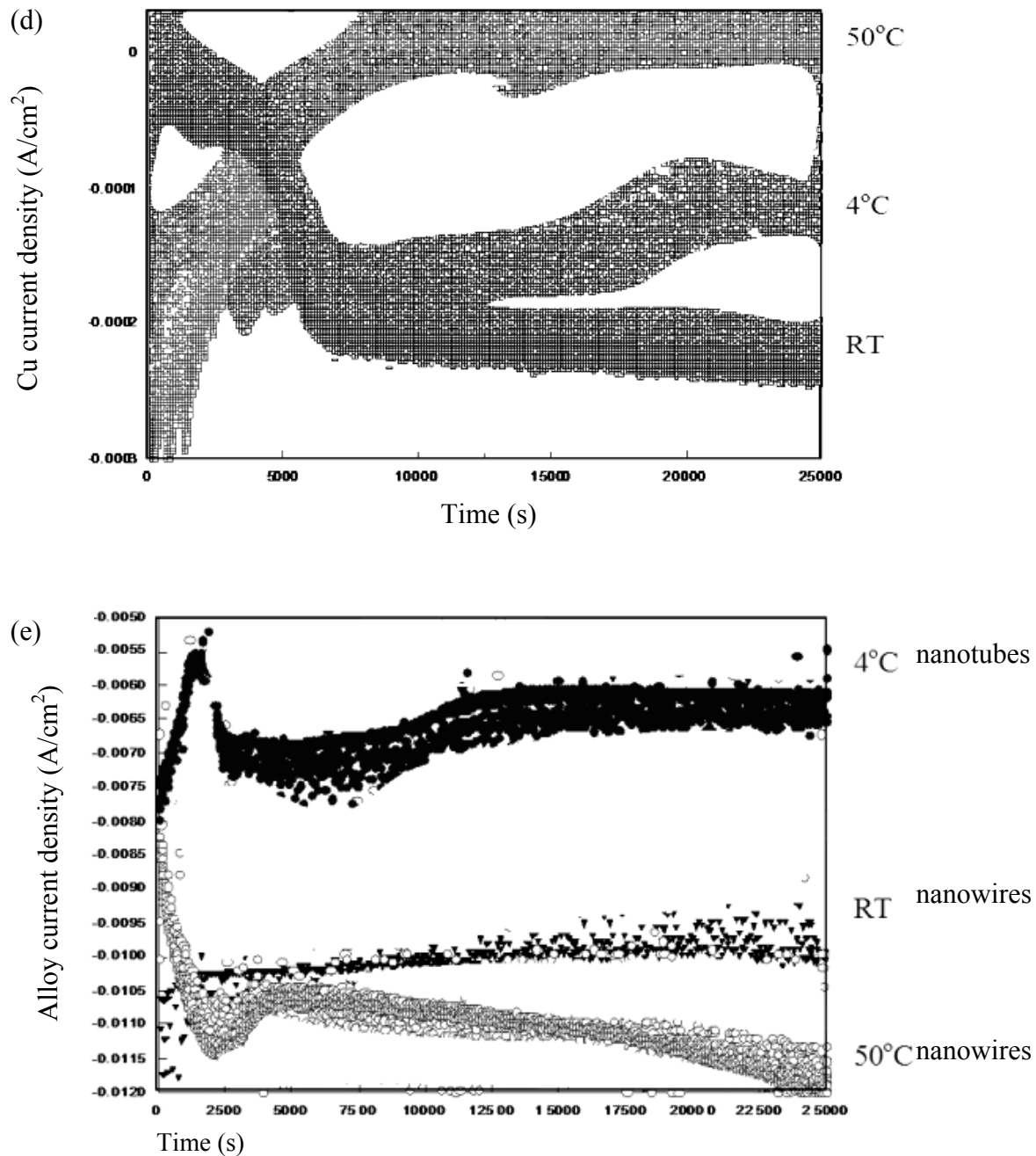
Figure 6.9 Total transient currents at 50°C, RT and 4 °C
(d) Cu layer current (e) alloy layer current

efficiency increased to 95.6 %. Similar behavior was observed for the Cu deposition. At room

temperature, the Cu current efficiency was 68 % and it drops to 55 % when the electrolyte was

heated to 50 °C. The highest Cu current efficiency 89 % was observed when the Cu was

deposited from the 4 °C electrolyte.

Table 6-2. WDS analysis of CoNiFeCu alloy at different temperatures

Electrolyte Temperature (C)	WDS (% composition)			
	Fe	Ni	Cu	Co
50C	0.224	2.846	80.200	16.730
4C	1.400	2.560	26.600	69.440
Room	1.440	2.790	18.790	76.980

The modeled current efficiency at room temperature was 87 % in the Cu deposition region and 67 % in the alloy deposition region. However the Cu current efficiency decreased to 82 % when the electrolyte was chilled and increased to 95 % when the electrolyte was heated. Therefore side reaction currents are higher than what accounted for in the model.

6.2 Electrolyte Temperature Effect on GMR

The electrodeposition conditions that yielded the highest GMR were used to study the effect of electrolyte temperature on the nanowires GMR. The conditions used to obtain the 20 % GMR at room temperature were: 20 nm AAO, CoNiFeCu/Cu wires, 50 mM $CoSO_4$, 25 mM $NiSO_4$, 0.5 mM $FeSO_4$, 1mM $CuSO_4$, 10 mM sulfamic acid and 27 mM Na-K tartrate, Cu layer (-0.4 V for 20 s)/CoNiFe (-1.4 V for 1 s). For this study the electrolyte temperature was controlled using a water bath shown in Figure 6-1.

Figure 6-10 shows the effect of electrolyte temperature on CoNiFe/Cu nanowire GMR. The electrolyte was heated to 25 $^{\circ}$C and 50 $^{\circ}$C during the electrodeposition process. The electrodeposition parameters were kept constant, the Cu layer was deposited at (-0.4 V for 20 s) and the CoNiFe alloy layer at (-1.4 V for 1 s). The GMR was enhanced when the electrodeposition was carried out from a slightly heated (25 $^{\circ}$C) electrolyte. However, when the electrolyte was heated to 50 $^{\circ}$C, the GMR values dropped. The results were repeated several

times to show the variability in the GMR data. The GMR from the hot electrolyte shows a larger variation than the GMR obtained in the nanowires deposited from the 25 ^{o}C electrolyte.
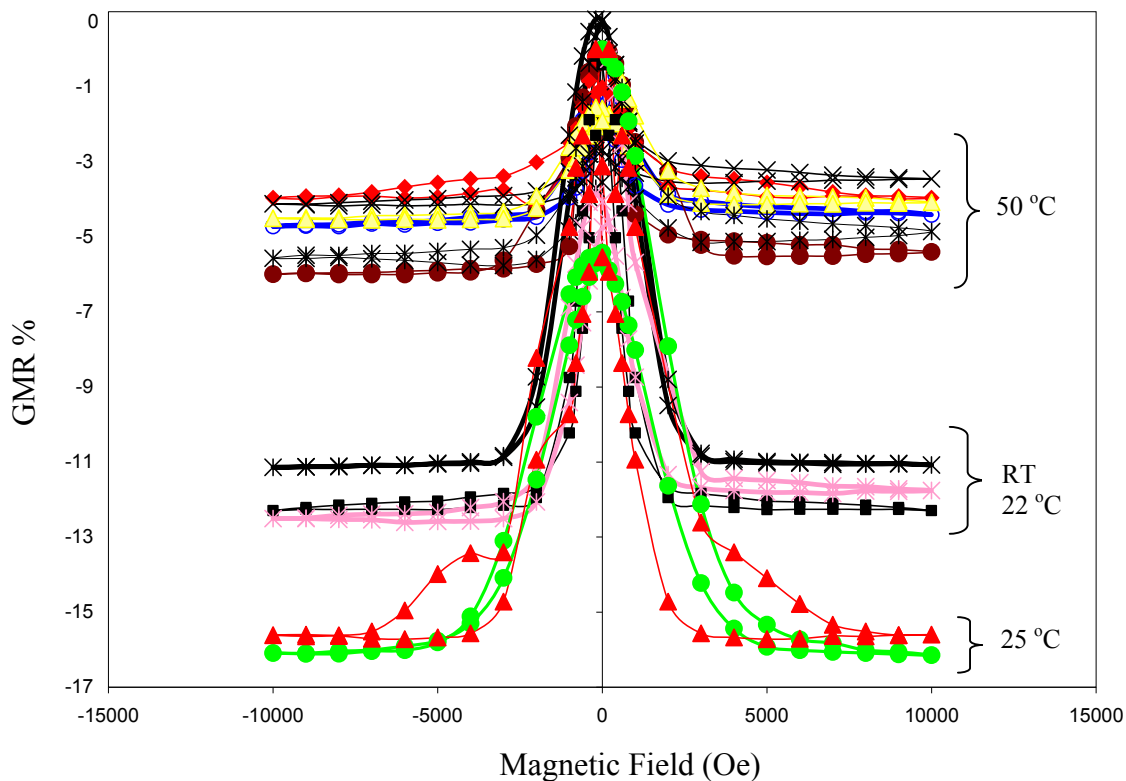
Figure 6.10 Effect of electrolyte temperature on CoNiFe/Cu nanowire GMR

6.2.1 Electrolyte Temperature Effect on Nanowires-Nanotube Transition

Another important aspect of the temperature study is to investigate if the tube formation is influenced by changes in temperature. Starting with the conditions that yielded the highest GMR (20 % at room temperature): [20 nm AAO, CoNiFeCu/Cu wires, 50 mM $CoSO_4$, 25 mM $NiSO_4$, 0.5 mM $FeSO_4$, 1 mM $CuSO_4$, 10 mM sulfamic acid and 27 mM Na-K tartrate, Cu layer (-0.4 V for 20 s)/CoNiFe (-1.4 V for 1 s), the electrolyte temperature was decreased to 4 ^{o}C using an ice bath shown below in Figure 6.11.
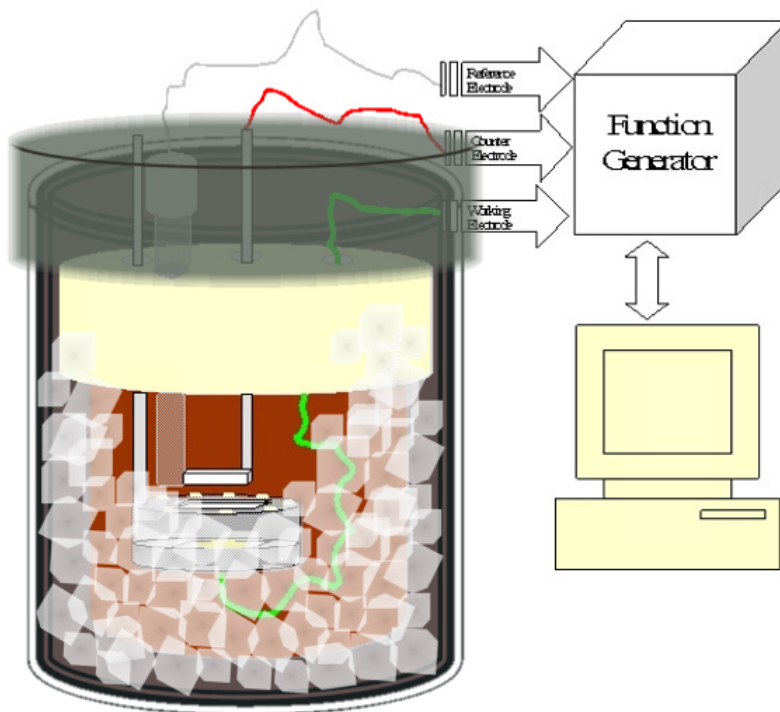
Figure 6.11 Chilled electrolyte set-up

To understand the different deposition behavior when changing the electrolyte temperature, deposition current was plotted and compared for the three temperature cases: chilled (4 °C), room temperature and hot (50 °C). Figure 6.12 shows the electrodeposition current behavior when (a) CoNiFeCu alloy was deposited at a constant potential (-1.4 V) and different electrolyte temperature and when (b) Cu was deposited at different temperatures and constant potential (-0.4 V). To determine the mass transport effect during deposition, the current was plotted against $t^{1/2}$, Figure 6.12 (a) and (b). At low temperature, the Cu current decreases almost linearly with the $t^{1/2}$ which is typical for a diffusion controlled deposition. At 50 °C, the Cu current is not totally linear with $t^{1/2}$. The alloy current does not show as much diffusion limited behavior as the Cu current does, as expected since Co and Ni are kinetically controlled. Figure 6.13 shows that tubes were obtained from the chilled electrolyte when either Cu or alloy was deposited at constant potential. Figure 6.13 (a) shows the SEM picture of large array of Cu nanotubes deposited at (-0.4 V). The tube' diameter is 190 $\pm$ 18 nm. Figure 6.13 (b) shows that alloy tubes were also obtained when the potential was much higher (-1.4 V) in the chilled

electrolyte. When the same sample was repeated from an electrolyte at 50 °C, wires were observed instead of tubes. Figure 6.14 show that when even at higher temperatures (50 °C), the deposition starts off as tubes. The SEM in Figure 6.14 shows the first 100 s of alloy deposition at 50 °C.
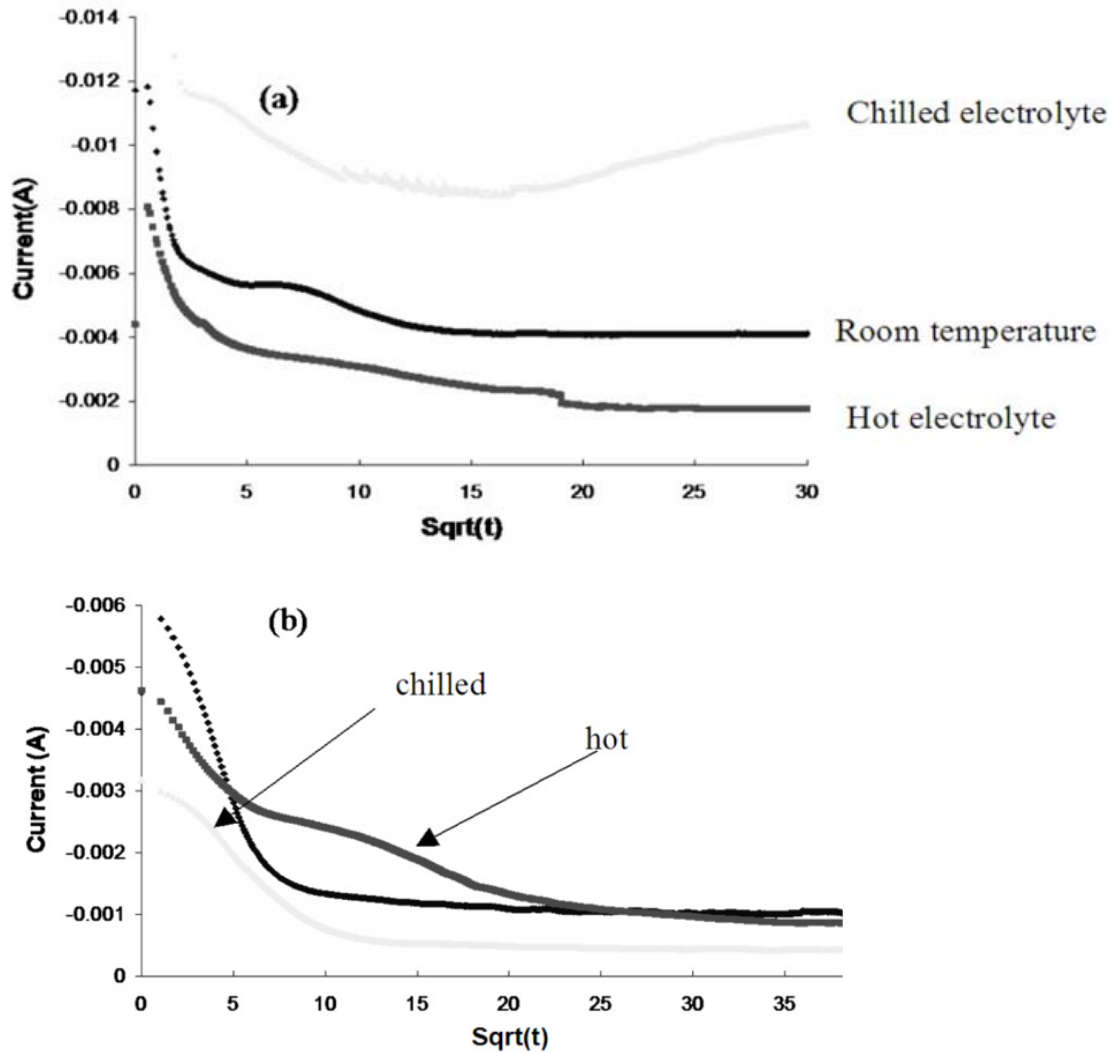
Figure 6.12 CoNiFeCu current profile during deposition at constant potential and different temperature electrolytes (a) alloy current (-1.4 V) vs. time$^{(1/2)}$, (b) Cu current (-0.4 V) vs. time $^{(1/2)}$

Figure 6.15 shows the tube formation from the electrolyte chilled at 4 °C. The same electrolyte used for making wires was chilled to 4 °C during the electrodeposition process. Using

the same deposition parameters (potential, time) for making nanowires, the only parameter altered was the electrolyte temperature. In the 20 nm pore diameter AAO membrane, the Cu layer was deposited at (-0.4 V for 20 s) and the CoNiFe alloy layer at (-1.4 V for 1 s). Figure 6.15 shows that depositing in the chilled conditions nanotubes formed instead of nanowires. In Figure 6.15 (a) an array of tubes from the chilled electrolyte was observed at the TEM.
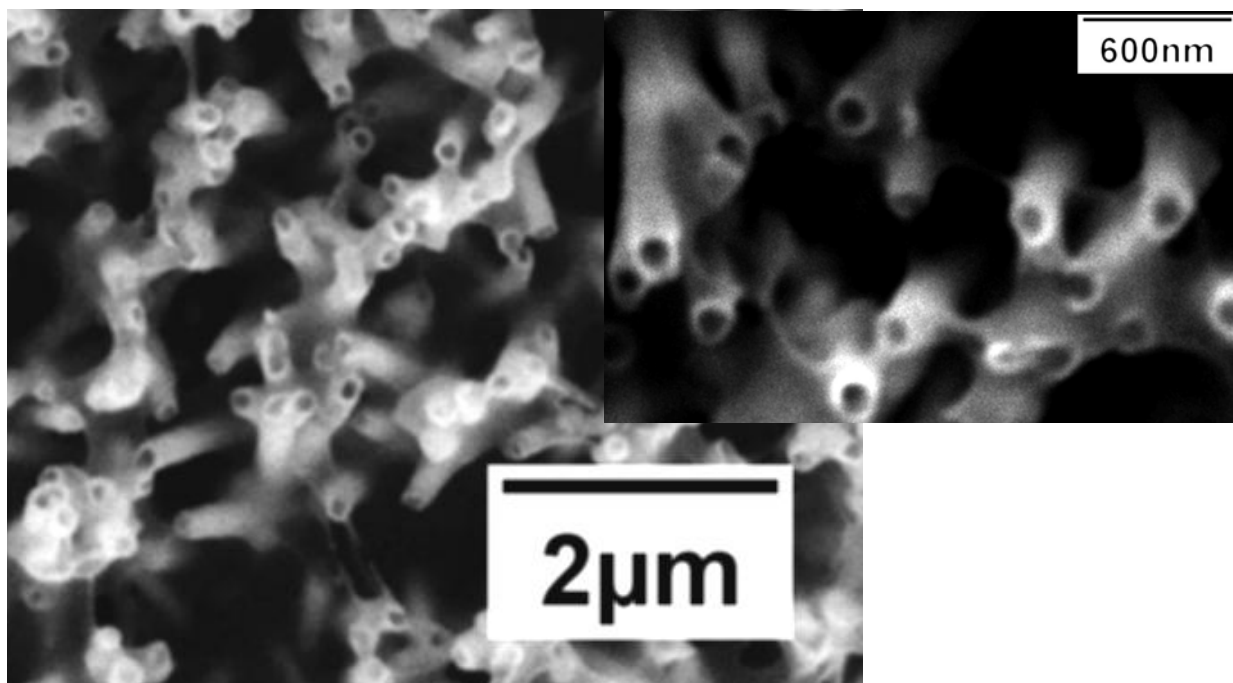
Figure 6.13 (b) SEM of CoNiFe alloy tubes from chilled electrolyte
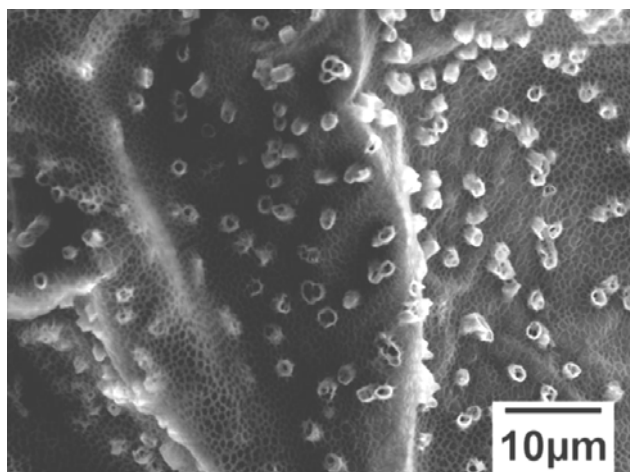
Figure 6.14 SEM of alloy nucleation at 50 ^{o}C

116

At higher magnifications, Figure 6.15 (b) shows multilayer formation at the tube wall. The averaged Cu layer was 1.75 nm while the alloy CoNiFe layer was 2.25 nm.
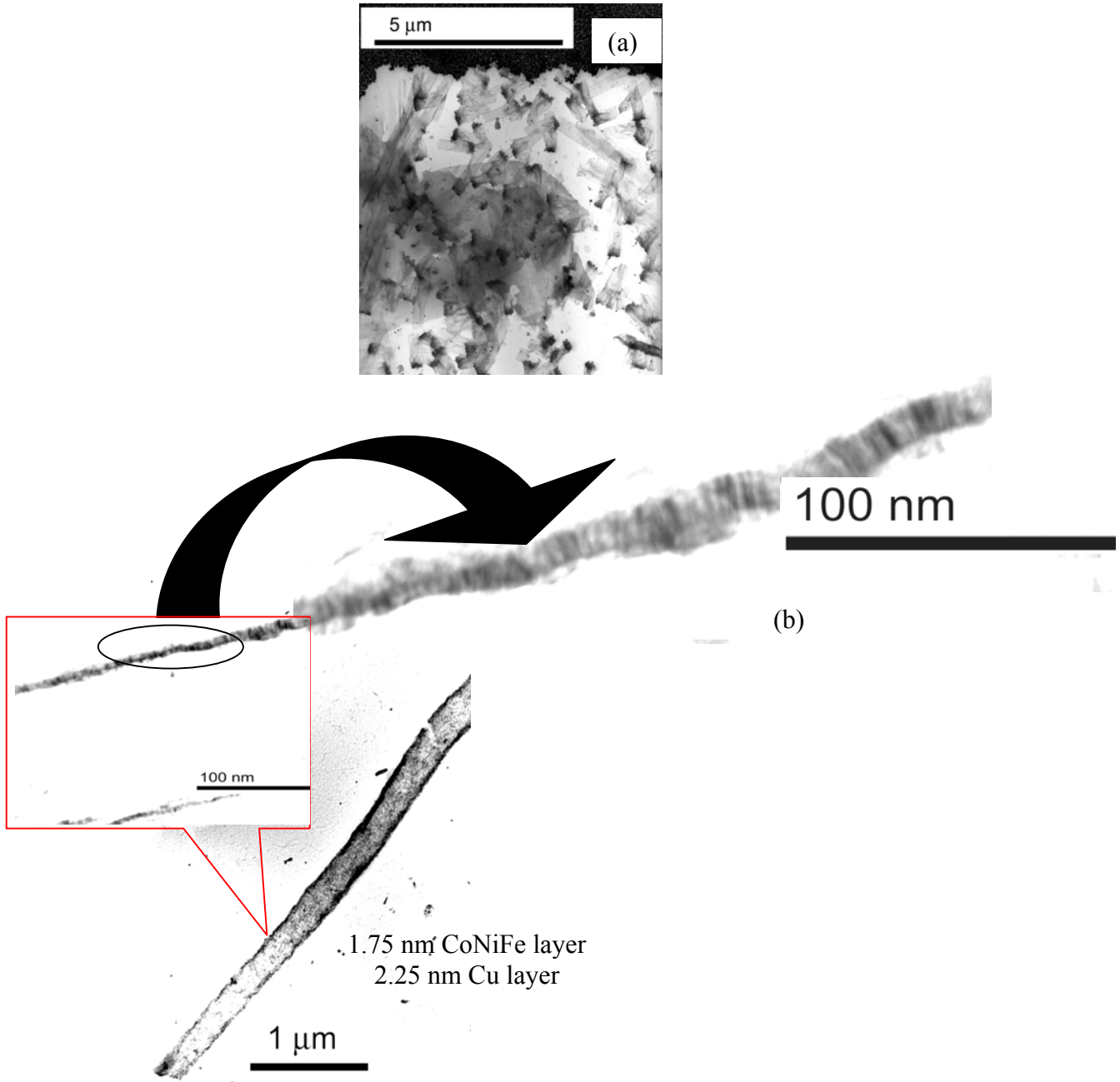
Figure 6.15 TEM of multilayered CoNiFe/Cu nanotubes formed from chilled (4 ^{o}C) electrolyte. (a) Low magnification nanotubes array (b) Higher magnification – multilayer image

GMR was measured in the tubes formed from the chilled electrolyte. Although the GMR value was not large, the magnetic field saturation was smaller that the wires' saturation field. Figure 6.16 shows the GMR profile of the CoNiFe/Cu tubes deposited from the chilled electrolyte that showed the smallest magnetic saturation field (0.04 T) obtained in our lab so far.
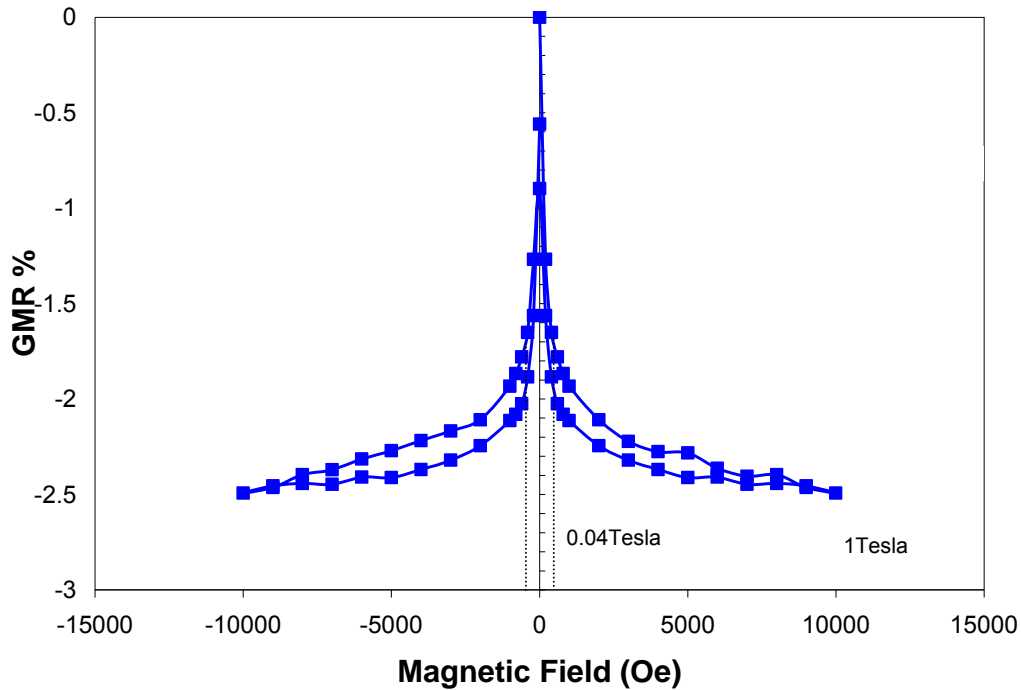
Figure 6.16 Room temperature GMR of CoNiFe/Cu nanotubes from chilled electrolyte

6.3 Nanostructures Annealing Effect

After electrodeposition, heat-treating the deposit could also affect the magnetic properties. There is considerably more literature studies dealing with the effect of temperature on the deposited material. Peter *et al.* (Peter, 2006) recently published a study on the annealing temperature effect of electrodeposited Co-Cu/Cu thin films on their GMR behavior. Their study took into account that the magnetic layers were not entirely ferromagnetic (FM) but also contained superparamagnetic (SPM) regions. In order to reveal the behavior of FM and SPM

with temperature they investigated a range of temperatures (12–300 K), and observed the effect of temperature on the decomposed magnetoresistance contributions. They concluded that the SPM part of the GMR did not depend on temperature. They also concluded that the spin dependent scattering was independent of temperature. The GMR decreased with annealing temperature for electrodeposited thin films. The shape of the MR curves also changed significantly with temperature in the case of Ni-Cu/Cu multilayers, since all the SPM regions become FM regions at the lowest measuring temperature. For the Co-Cu/Cu system, some SPM regions remained in the SPM state. In the case of the Ni-Cu/Cu multilayers, there was a SPM-FM transition at low temperature because the measuring temperature becomes lower than the blocking temperature of some SPM regions. They assumed there was also a possible paramagnetic-ferromagnetic transition of the boundary separating the SPM and FM regions. By comparing the composition dependence of the Curie temperature of the Ni-Cu and Co-Cu alloys, they showed that the Ni-Cu system could undergo a paramagnetic-ferromagnetic transition 2.6 times higher than the Co-Cu system. In the Ni/Cu system, they believed there were high composition variations due to the miscibility of the components. In the case of the Co-Cu system due to limited miscibility, the boundary regions were Cu rich and could not undergo a PM-FM transition at any temperature.

Annealing temperature effect on the GMR of CoFe/Cu multilayered thin film was recently investigated by Rafaja *et al.* (2004). In their study they deposited 20 multilayers by vacuum sputtering technique and then annealed the deposit at various high temperatures. The GMR increased to 23 % from 20 % when the thin film was annealed at a particular temperature (235 ^{o}C). When the film was annealed at a slightly higher temperature of 340 ^{o}C the GMR decreased drastically to 6%. The increase in the GMR value was attributed to a better separation

of the magnetic and non-magnetic layers. However, at higher annealing temperatures, the GMR decreased due to the interface roughness and non-continuous interfaces leading to the short-circuiting of the magnetic layers. Their study also pointed out that annealing had a negligible influence on the layer thickness. They concluded that the quality of the interfaces was affected by intermixing of atomic species, which is caused by the penetration of high-energy atoms into deeper layers. Therefore, in the immiscible system of CoFe-Cu, the soft annealing could influence reverse out-diffusion of the atomic species at the interfaces, which in turn would improve the GMR. Rafaja *et al.* proposed that in the virgin samples the intermixing of atomic species caused by penetration of high energy atoms deeper into layers during layer deposition affected the quality of the interfaces. Annealing at the higher temperatures further increased the interface roughness and therefore lowered the magnetoresistance.

According to Pattanaik *et al.* (Pattanaik, 2003) the increase in the Co/Cu thin film GMR was due the reduction of defects and film stress unpon annealing. The increase in GMR was explained by the segregation of Co fine particles. At the ideal annealing temperature the ferromagnetic particle segregation was complete and the segregated Co particles start growing in size resulting in multidomain ferromagnetic particles reducing the ferromagnetic/nonmagnetic interfacial sites for spin dependent scattering. The thin film GMR improved for a particular annealing temperature and deteriorated for temperatures below or above the ideal annealing temperature. Annealing time played a crucial role as it controls the extent of Co-particle segregation or growth. Their TEM showed that the average grain size doubled upon annealing.

Several studies have shown the negative effect of high temperature treatment on the GMR. However, there are no studies on how the low temperature treatment would affect the nanowire GMR. Evans *et al.* (Evans, 2000) investigated the electrodeposition of CoNiCu/Cu

120

multilayers in aluminum oxide templates and showed that annealing the deposit would reduce the GMR effect due to interdiffusion and recrystallization phenomena.

Li *et al.* (Li, 2005) recently studied the effects of annealing temperature on magnetic properties of CoPt alloy nanowires and they found that a certain annealing temperature (400 °C) can improve the magnetic coercivity and squareness. Under normal conditions the solubility of ferromagnetic and nonmagnetic metals is very low, but under nonequilibrium conditions, like annealing, these metals could form metastable phases that could re-crystallize forming small ferromagnetic particles of single magnetic domain nature. In their study, Liu *et al.* showed that as the annealing temperature increased from 100 to 400 °C, the coercivity and squareness increased due to structural relaxation and defect reduction. They also pointed out that there is a large mismatch between the thermal expansion coefficients of CoPt alloy and AAO, therefore the nanowires expand freely along the wire axis during annealing. As the annealing temperature increased, the Co grains grew larger in size and began to coalesce. Also, annealing at high temperatures (above 400 °C) will increase the AAO internal stress and the pores will be distorted, destroying the wires shape anisotropy. Furthermore, at 600 and 700 °C, the Co became hcp with the easy axis perpendicular to nanowire, which diminished the anisotropy. Also, at high temperature, Co reacted with O_2 in the AAO deteriorating the magnetic properties.

Wang *et al.* (Wang, 2002) looked at the effect of temperature on magnetization for different alloy nanowire systems such as Co-Cu, Fe-Ag and Co-Ag electrodeposited in AAO. Their group found that the perpendicular coercivity increased with annealing temperature, reached a maximum at (500 °C) and then decreased sharply at higher temperatures.

It has been shown that higher GMR was found when the measurements were done at low temperatures. For example, Dubois *et al.* (Dubois, 1999) showed that at 77 K NiFe/Cu nanowires

GMR was 65 %, and at an even lower temperature (4.2 K), the GMR increased to 78 %. Since the CoNiFeCu/Cu nanowires and tubes GMR was only measured at room temperature, the low temperature GMR measurements could yield larger changes in resistance.

In the present study the annealing temperature effect on the GMR of CoNiFe/Cu nanowires and tubes was investigated. In the first case, we used atmosphere annealing ranging from 100 to 400 ^{o}C. Figure 6.17 shows the effect of atmosphere annealing temperature on the same sample of CoNiFe/Cu nanowires GMR. The electrolyte composition was 50 mM $CoSO_4$, 18 mM $NiSO_4$, 1 mM $FeSO_4$, 1 mM $CuSO_4$, 10 mM sulfamic acid and 27 mM Na-K tartrate. Deposition conditions applied for making the sample shown in Figure 6.17 were: Cu layer (-0.4 V for 20 s)/CoNiFe (-2 V for 1 s)]. Annealing not done consecutively, therefore one sample of GMR was broken down into several pieces that were annealed separately at different temperatures and then measured. Out of the investigated temperatures, the best annealing temperature was concluded to be 300 ^{o}C. The nanowires GMR increased by 2 % when the sample was annealed at 300 ^{o}C. Annealing at 100 ^{o}C and 200 ^{o}C resulted in lower GMR.

Annealing the tubes at 300 ^{o}C seemed to have a beneficial effect on GMR. Figure 6.18 (a) shows how the atmosphere annealing affected the nanotubes GMR. The GMR of the tubes formed from a 4 ^{o}C electrolyte doubled when it was annealed at 300 ^{o}C. The electrolyte composition was 50 mM $CoSO_4$, 25 mM $NiSO_4$, 0.5 mM $FeSO_4$, 1 mM $CuSO_4$, 10 mM sulfamic acid and 27 mM Na-K tartrate. Deposition conditions applied for making the chilled tubes shown in Figure 6.18 were: Cu layer (-0.4 V for 20 s)/CoNiFe (-2.25 V for 1 s)] at 4 ^{o}C. Figure 6.18 (b) shows a low resolution TEM the chilled tubes before the air annealing at 300 ^{o}C. It is clear that the tubes diameter differ substantially, the smallest shown being 168 nm and the largest 223 nm. Figure 6.18 (c) shows a higher resolution (250 k) TEM of the chilled nanotubes after

annealing. The layer formation is evident specially looking cross the tube walls: the alloy (darker layer) was 4.4 nm and the Cu layer was slightly thinner, 4.1 nm.
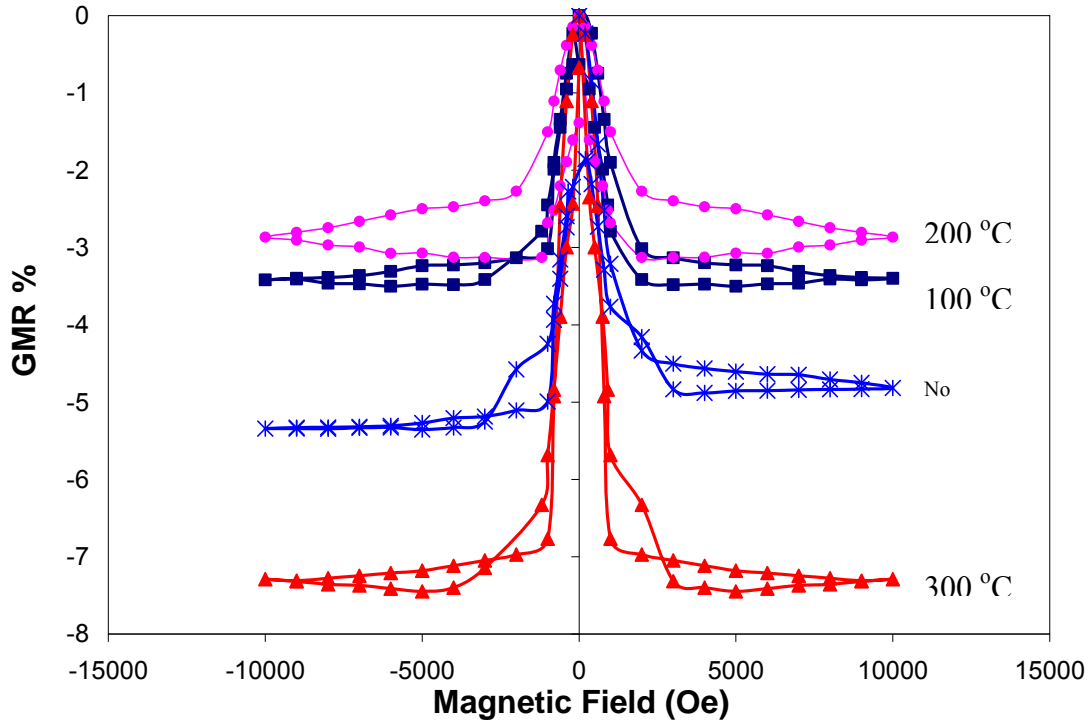
Figure 6.17 Air annealing temperature effect on CoNiFe/Cu nanowires GMR
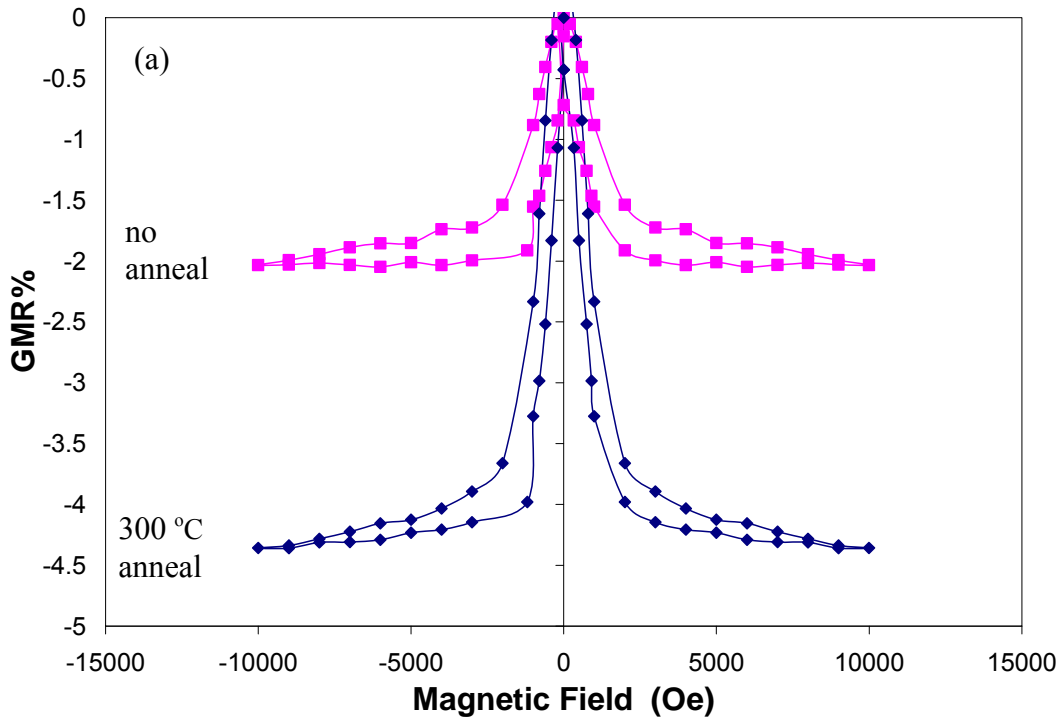
Figure 6.18 (a) Air annealing of CoNiFe/Cu tubes deposited at 4 $^{\circ}$C

The tube diameter after annealing was 181 nm, similar to the diameter of the tube before annealing. The GMR doubled and tripled in some cases when the H_2 was flown during the annealing process. Figure 6.19 (a) shows the CoNiFe/Cu nanowires GMR increase when annealed in a pure H_2 environment. The electrolyte composition was 50 mM $CoSO_4$, 25 mM $NiSO_4$, 0.5 mM $FeSO_4$, 1 mM $CuSO_4$, 10 mM sulfamic acid and 27 mM Na-K tartrate.

(b)

223.7nm

192.3 nm

168.2 nm

0.5 µm
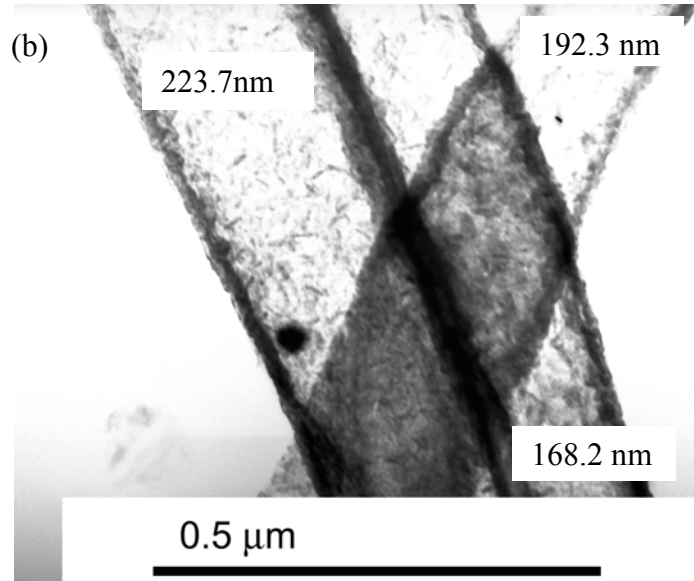
Figure 6.18 (b) TEM of the air annealed CoNiFe/Cu tubes deposited at 4 ^{o}C

(c)

tube diameter = 181.2 nm (5.4 nm SD)
alloy layer = 4.4 nm (0.7 nm SD)
Cu layer = 4.1 nm (0.5 nm SD)

100 nm
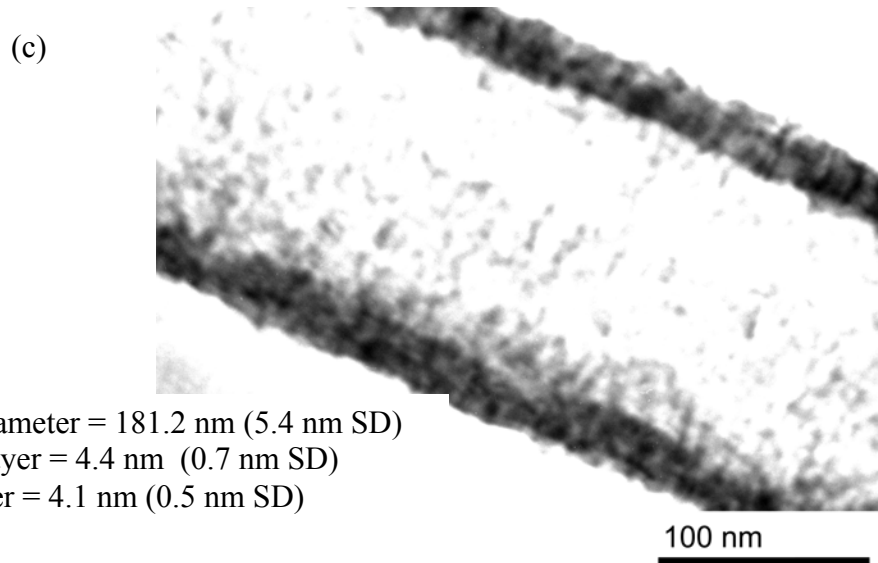
Figure 6.18 (c) TEM of the atmosphere annealed CoNiFe/Cu tubes
(4 ^{o}C deposition)

124

Deposition conditions applied for making the sample shown in Figure 6.19 were: Cu layer (-0.4 V for 20 s)/CoNiFe (-1.5 V for 1 s)]. The CoNiFe/Cu nanowires GMR increased from 12 % (no annealing) to 22 % when it was annealed at 300 ^{o}C in pure H_2 environment. Figure 6.19 (b) shows the entire deposition data for making the multilayer nanowires. Figure 6.19 (c) shows the charge profile during electrodepositing of multilayer.
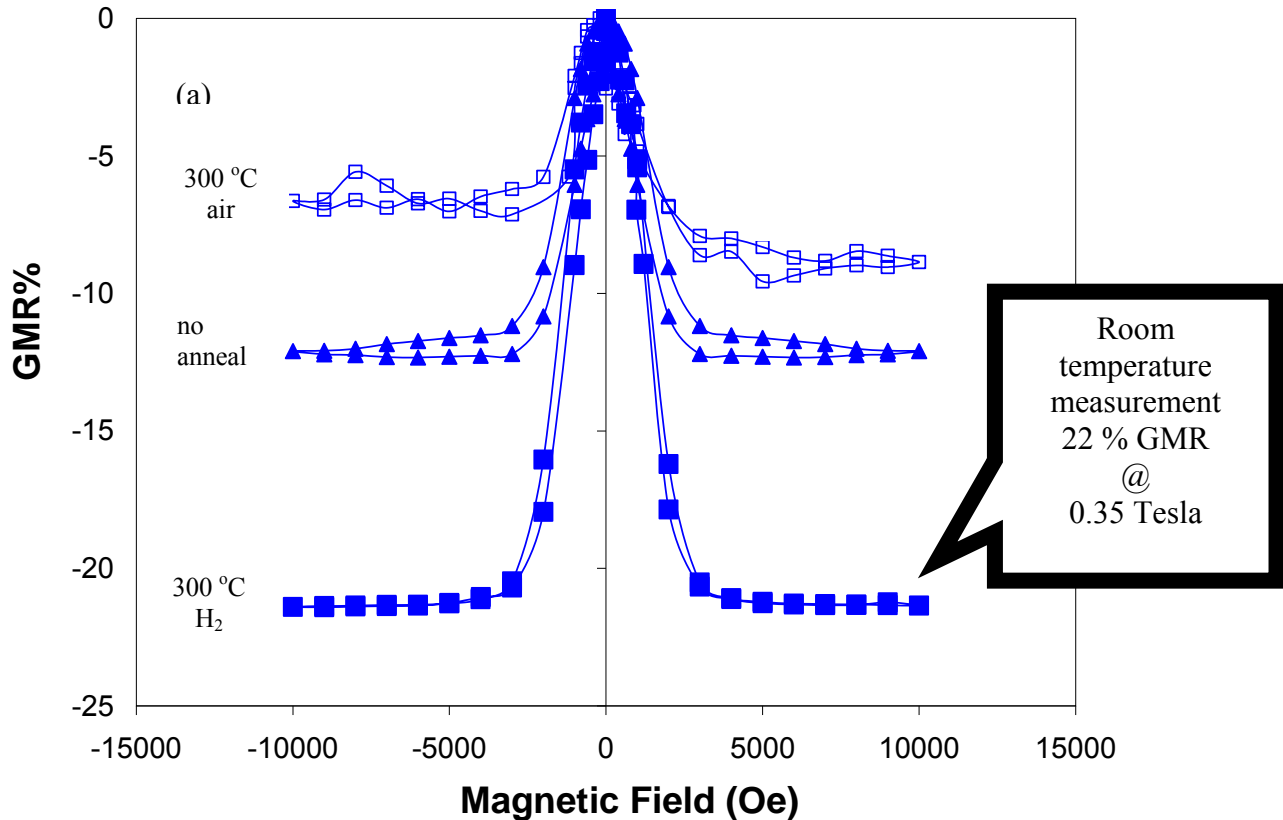
Figure 6.19 (a) CoNiFe/Cu nanowires annealed at 300 ^{o}C in H_2 environment
GMR (room temperature measurement)

Figure 6.20 shows another example of annealing under H_2 when the GMR doubled compared to the sample that was not annealed. The electrolyte composition was 50 mM $CoSO_4$, 25 mM $NiSO_4$, 0.5 mM $FeSO_4$, 1 mM $CuSO_4$, 10 mM sulfamic acid and 27 mM Na-K tartrate. Deposition conditions applied for making the sample shown in Figure 6.20 were: Cu layer (-0.4 V for 20 s)/CoNiFe (-1.7 V for 1 s)]. When the sample was annealed at 300 ^{o}C in pure H_2 the

CoNiFe/Cu nanowires GMR increased from 10 % (no annealing) to 16 %. Therefore annealing in hydrogen at 300 $^\circ$C improved the GMR.
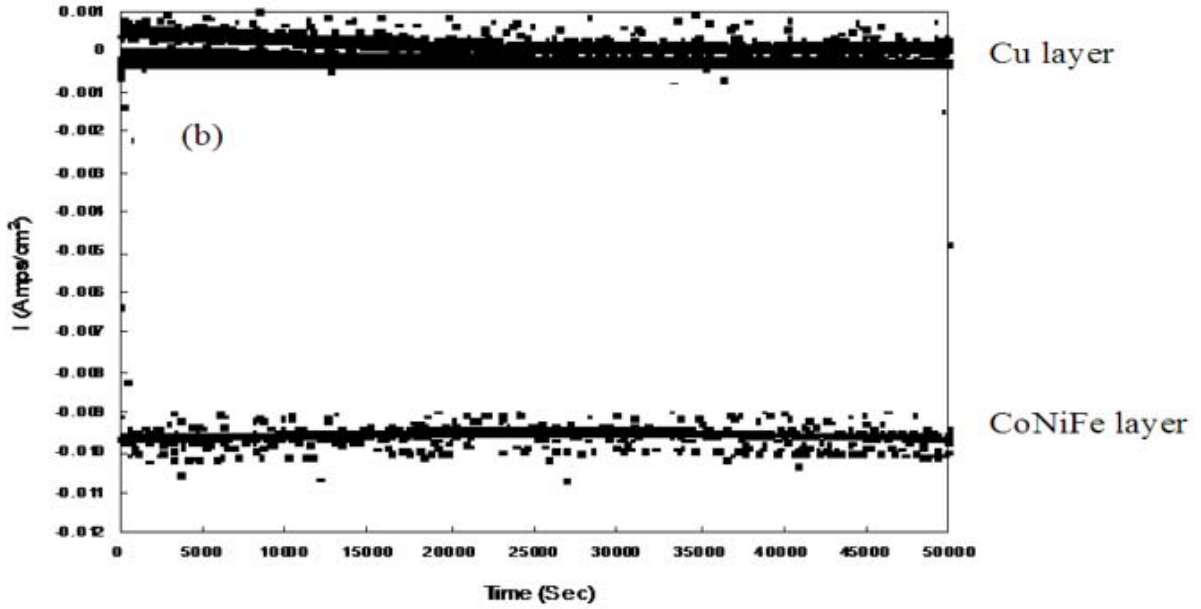
Figure 6.19 (b) CoNiFe/Cu nanowires annealed at 300 $^\circ$C in H$_2$ environment deposition data
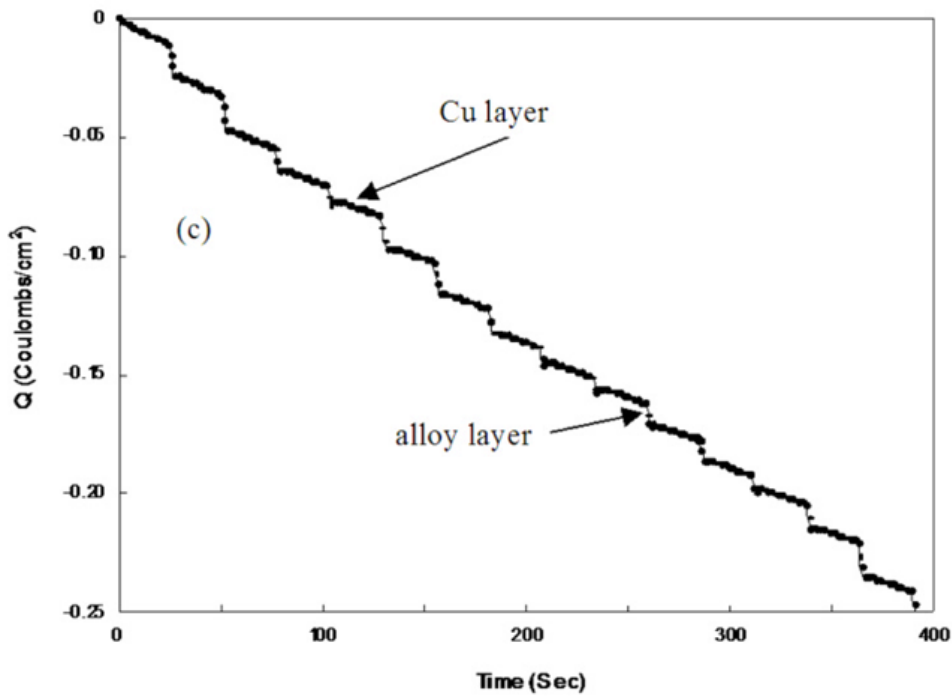
Figure 6.19 (c) CoNiFe/Cu nanowires annealed at 300 $^\circ$C in H$_2$ environment - charge profile

126

Since the H_2 annealing seemed to have a major effect on the nanowires GMR, the highest obtained GMR (20 %) conditions were employed to make more GMR followed by H_2 annealing. The electrolyte composition of the highest obtained GMR of the CoNiFe/Cu nanowires was 50 mM $CoSO_4$, 25 mM $NiSO_4$, 0.5 mM $FeSO_4$, 1 mM $CuSO_4$, 10 mM sulfamic acid and 27 mM Na-K tartrate. Deposition conditions applied for making the best GMR sample were: Cu layer (-0.4 V for 20 s)/CoNiFe (-1.5 V for 1 s)]. Figure 6.21 shows the profile of the reproduced GMR sample. Then, the best sample was reproduced and measured; instead of 20 % at room temperature it had an even higher 24.5 %, even before annealing. The sample was then annealed in flowing H_2 and then re-measured at room temperature. With H_2 annealing, the CoNiFe/Cu nanowire GMR increased from 24.5 % (no annealing) to 30 %.
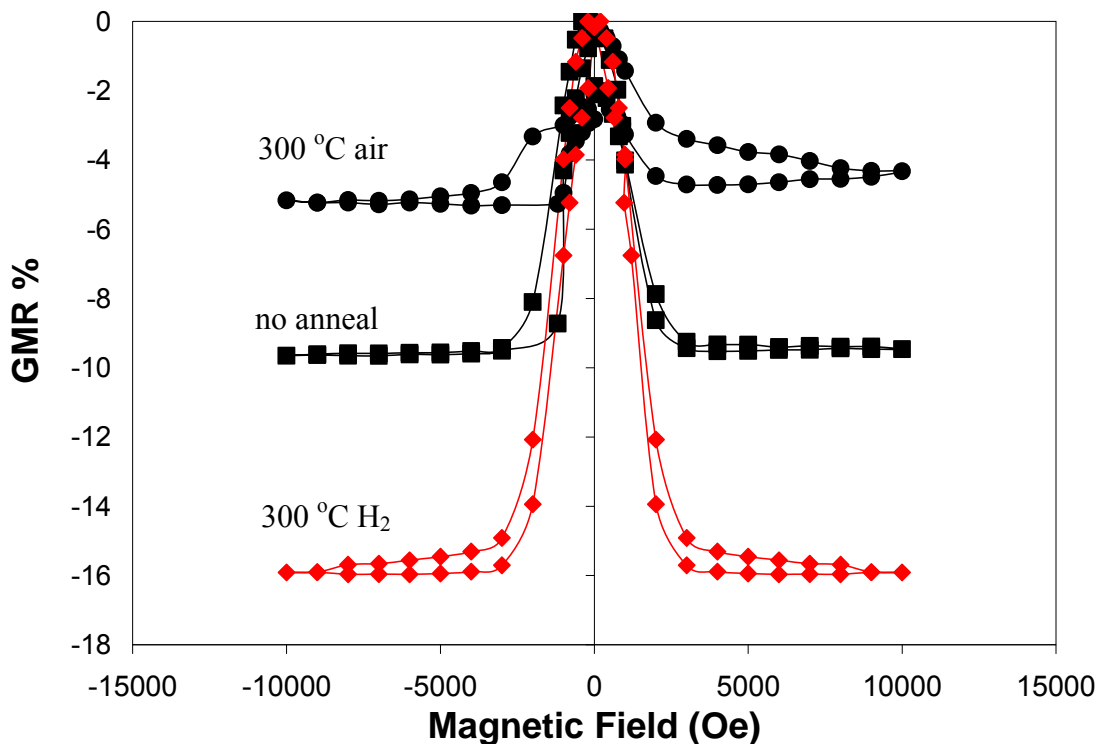
Figure 6.20 Nanowires GMR annealed at 300 ^{o}C in H_2 environment

The same annealed sample was also measured for GMR at a lower temperature, to avoid lattice

vibrations and other quantum interactions that would eventually damage the GMR. When measured at 100 K (above liquid N_2 temperature) the sample showed an increase in GMR up to 38.5 %.
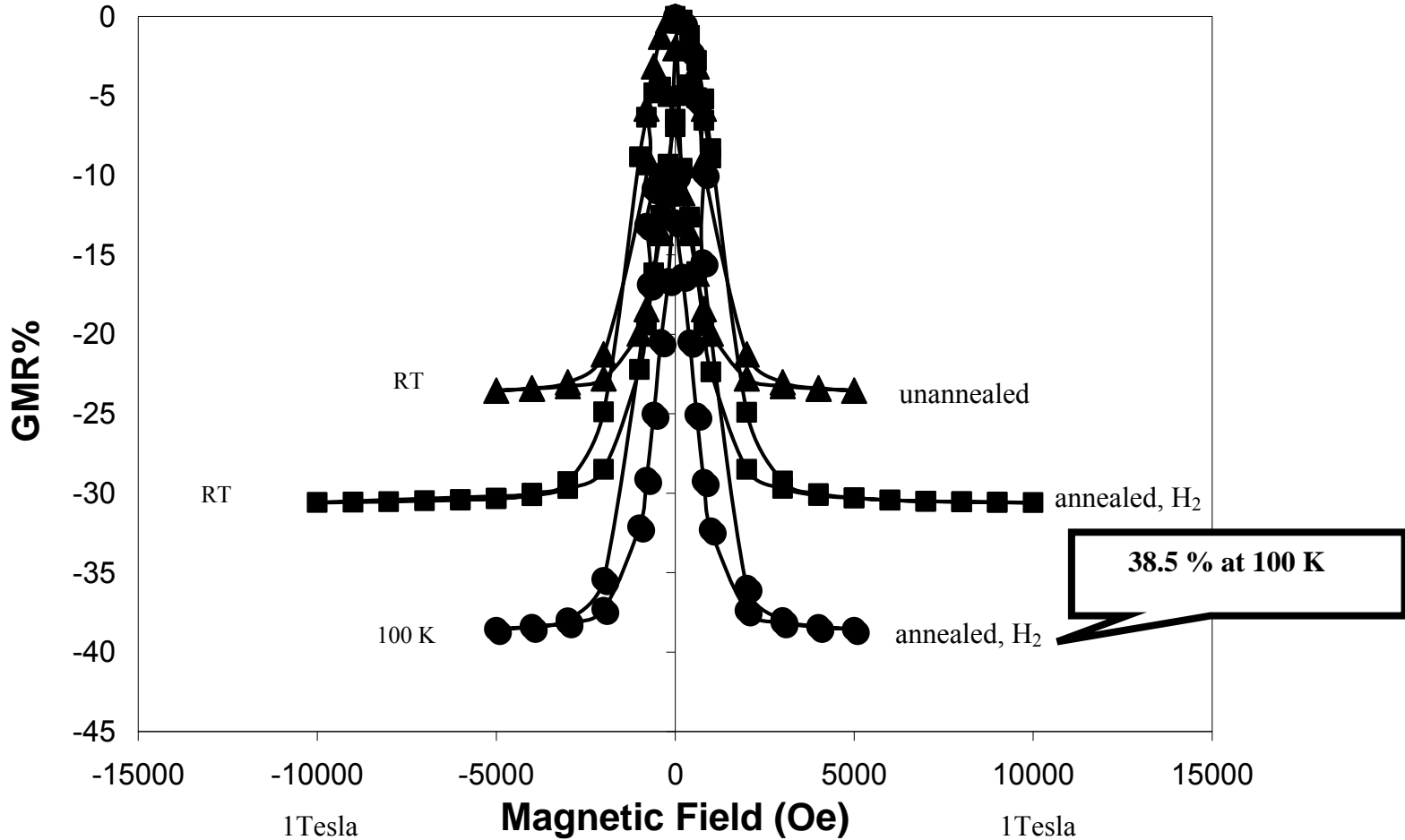
Figure 6.21 Multilayered CoNiFe/Cu nanowires GMR before and after H_2 annealing

Figure 6.22 shows high-resolution TEM micrographs of the CoNiFe/Cu nanowires before and after annealing in H_2. At a magnification of 200 K, Figure 6.22 (a) shows the multilayers before annealing. The dark CoNiFe alloy layer was 2.1 nm with a standard deviation of 1.1 nm and the light Cu layer was 2.6 nm with 0.7 nm in standard deviation. The wire diameter before annealing was 205.8 nm with 13.9 nm in standard deviation. At a magnification of 150 k, Figure 6.22 (b) shows the multilayers after the H_2 annealing at 300 ^{o}C. The dark CoNiFe alloy layer was a little

thicker after annealing 2.4 nm with a standard deviation of 0.7 nm and the light Cu layer was 1.6

nm with 0.5 nm in standard deviation. The wire diameter seemed to be much smaller after

annealing was 99.7 nm with 4.5 nm in standard deviation.

CoNiFe layer = 2.1 nm (1.1 SD)
Cu layer = 2.6 nm (0.7 SD)
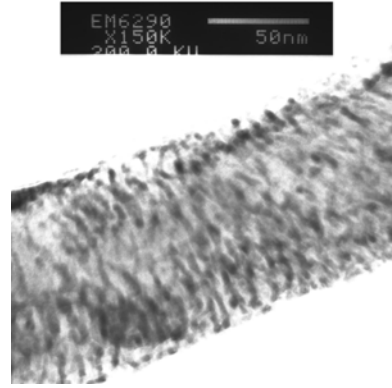
CoNiFe layer = 2.4 nm (0.7 SD)
Cu layer = 1.6 nm (0.5 SD)

Figure 6.21 High resolution TEM multilayered CoNiFe/Cu nanowires before and after H_2 annealing
(a) before annealing (b) after H_2 annealing at 300 ^{o}C

The motivation of the TEM investigation was to examine annealing effect on the

nanostructures. In the previous section it was demonstrate that the annealing temperature

affected the wires and tubes GMR. From the TEM investigation it was observed that annealing

had an effect on the nanostructures diameters, grain sizes and ultimately the layer sizes. Upon

annealing, the grain sizes enlarged, in some cases more than doubled. The best GMR was

observed when the nanowires were annealed in H_2 environment at 300 ^{o}C.

Table 6-3 Wires and tubes annealing TEM observations

Structure	Deposition conditions			membrane pore (nm)	pore diameter		annealing treatment		grain size		wall size		layers				GMR (RT)
	Electrolyte Temperature	layer potential & time											Cu		alloy		
		Cu	alloy		size (nm)	SD (nm)	gas	temperature	size (nm)	SD (nm)	size (nm)	SD (nm)	size (nm)	SD (nm)	size (nm)	SD (nm)	
tube	RT (22 C)	0.4 V (100 s)	1.4 (3 s)	200	126	8.96	No annealing		5.99	2.24	15.74	4.1	3.15	0.49	4.17	1.02	2.5
tube	RT (22 C)	0.4 V (100 s)	1.4 (3 s)	200	171.057	7.226	air	300 C	11.08	3.3	12.26	4.364	4.47	1.467	5.481	1.441	2.75
tube	Chilled (4 C)	0.4 V (20 s)	1.4 (1 s)	20	168.885	16.85	No annealing		4.18	0.88	17.05	4.098	1.631	0.84	1.533	0.34	2.5
tube	Chilled (4 C)	0.4 V (20 s)	1.4 (1 s)	20	159.07	35.01	air	300 C	19.97	5.963	15.26	2.75	4.324	0.79	4.33	0.622	4.25
wire	RT (22 C)	0.4 V (20 s)	1.4 (1 s)	20	175.89	8.263	No annealing		7.11	2.53	NA	NA	2.95	1.19	2.935	1.052	22
wire	RT (22 C)	0.4 V (20 s)	1.4 (1 s)	20	99.53	5.46	H_2	300 C	6.14	2.48	NA	NA	1.27	0.5	2.25	0.27	30
wire	Heated (50 C)	0.4 V (20 s)	1.4 (1 s)	20	185.31	11.11	air	300 C	not distinguished				7.75	1.65	19.8	2.52	8

This form of annealing showed a small decrease in the grain size, however a visible reduction (50 %) of the Cu layer. The wire diameter also shrunk with annealing in flowing H_2. The air annealing promoted grains coalescence that did not necessary improve the GMR. For example in the chilled tubes case the grain size increased four times upon annealing in air. More specifically Table 6-3 shows measurements of the CoNiFe/Cu tubes and wire before and after annealing. The wire diameter was 175 nm before annealing and it increased when after annealing in air. Before the heat treatment the Cu layer was 2.95 nm, the alloy layer was 2.6 nm, the grain size measured 8 nm and the yielded GMR was 22 % at room temperature. When the wires were annealed in air and 300 ^{o}C, annealing did not improve the wires GMR since the wire diameter increased, the Cu layer more than doubled to 7.75 nm and the alloy layer expanded six times (19 m) under the TEM. Noticeable is that the wire diameter shrunk to 99 nm when the wires were annealed in H_2. The Cu layer size reduced to 1.27 nm, the alloy layer also slightly decreased to 2.25 nm and the grain size decreased to 6 nm, which is smaller than the grain sizes measured in the wires before annealing 8 nm.

The GMR increased after the H_2 annealing probably because the layer interfaces improved. The alloy layer maintained the same size while the Cu layer decreased upon annealing in H_2. The room temperature electrolyte tubes also went through changes upon annealing. The tubes were only annealed in air and the annealing did not substantially improve the GMR, even though the grain sizes showed a considerable enlargement with annealing at 300 ^{o}C. The 300 ^{o}C was the only annealing temperature to enhance GMR. The tube wall thickness slightly decreased upon annealing, while both the Cu and the alloy layers slightly increased with annealing. The chilled tubes showed a slight GMR improvement after with air annealing at 300 ^{o}C and it is

noteworthy that both the Cu and the CoNiFe layer thickness visibly doubled and the grain size increased six times after annealing.

6.4 Conclusions

Compared to the room temperature electrodeposition, the Cu current registered a significant decrease when the deposition was performed from the chilled electrolyte, and oppositely, when the electrolyte was heated to 50 $^{\circ}$C, the Cu current increased by the same amount. In the high temperature electrolyte the anodic current increased and lead to a larger loss of the alloy layer. Another hypothesis is that the dissolution of the alloy layer may form metal oxides at the layer interfaces. The alloy layer current was more affected by the low temperature electrolyte than by the hot electrolyte. During pulsing, the alloy layer transient current behavior was opposite in the low and the hot temperature electrolyte: at 4 $^{\circ}$C the current dropped linearly, typical for a diffusion-controlled reaction and at 50 $^{\circ}$C, the current increased almost linearly. The cold and hot current profiles were mirror images of each other. The Cu layer transient current during pulsing did not follow the same profile as the alloy layer current. At 50 $^{\circ}$C, the current decreased in the first 5000 s, while in the 4 $^{\circ}$C electrolyte the copper current remained consistent to a kinetic control electrodeposition.

The overall sample composition changed with electrolyte temperature even when maintaining the same deposition potential. The Cu content in the alloy increased in the when the electrodeposition was carried out from the hot electrolyte. The smallest Cu amount in the alloy deposition was found from the room temperature electrolyte, which coincidently yielded the highest GMR values. The overall current efficiency dropped in the hot electrolyte and increased in the chilled electrolyte.

131

Electrolyte temperature had an effect on the electrodeposition currents and consequently on the GMR. When the electrolyte was heated to 50 ^{o}C, the GMR values dropped significantly since the layer sizes drastically increased and also the Cu content in the alloy layer was higher.

Tubes instead of wires were obtained from the chilled electrolyte and only wires were obtained in the heated electrolyte. However, even though wires were the result of the high temperature electrolyte, the electrodeposition started off in the form of tubes. GMR was measured in the tubes formed from the chilled electrolyte and the smallest magnetic saturation field (0.04 T) was observed. Out of the investigated temperatures, the best annealing temperature was concluded to be 300 ^{o}C. Annealing the tubes at 300 ^{o}C and air seemed to have a positive effect on GMR, but the most dramatic outcome was observed when the nanowires were annealed at 300 ^{o}C with pure H_2 flowing. Hydrogen gas is a reducing agent and it is believed that it may have diffused inside the membrane and reduced the oxides formed on the alloy layers. The GMR doubled and tripled in some cases when the H_2 was flown during the annealing process. The dark CoNiFe alloy layer slightly increased after annealing while the light Cu layer substantially decreased.

In agreement with Pattanaik *et al.* (2003) observations, the distribution of the magnetic grain, their volume fraction and intergranular separation were crucial parameters that affected the GMR behavior. At a particular temperature (300 ^{o}C) annealing lead to a better segregation of Co rich fine particles which in turn lead to increasing ferromagnetic–nonmagnetic interfacial sites for spin-dependent scattering and therefore larger GMR. When annealing past 300 ^{o}C the complete segregated Co rich particles started growing in size resulting in multidomain ferromagnetic particles that reduced the GMR values. Pattanaik's TEM report on the annealing of thin films showed an average grain size of 5–10 nm in as-deposited films that increased to 20–

40 nm upon annealing. In this present work, the same kind of increase in grain sizes was observed but only when the annealing was done in air. Oppositely, when the annealing was preformed in a reducing environment (flowing H_2) the grain sizes slightly decreased. More importantly, the layer sizes decreased significantly after H_2 annealing.

According to Li *et al*. (2005), the annealing treatment led to the formation of smaller Co particles that improved magnetic properties. In agreement with this present work, as annealing temperature increased, the Co rich grains grew larger and led to an increase in the coercivity and past a certain annealing temperature, most of the alloy particles began to coalesce. Li *et al*. (2005) also pointed out that annealing at high temperature (above 300 ^oC) would relieve internal stress but the alumina template pores were distorted and that could explain the loss of GMR. In Li's study, at high annealing temperatures Co rich alloys reacted with O_2 from the AAO deteriorating the squareness and the perpendicular anisotropy of the nanowires, which could also explain the damaged GMR in the present case. In a different study on nanowires annealing, Wang *et al*. (2002) observed that during the annealing process the increase in the saturation magnetization began as the ferromagnetic metal atoms began to cluster, but the coercivity was not affected until the ferromagnetic metal precipitates grew much larger with annealing temperature.

Heat treatment can eliminate defects and dislocations in the metals. The hydrogen provides a protective environment to keep the metals in a zero valence state as opposed to letting them oxidize. This kind of annealing is used in industry for metals processing, however H_2 would be mixed with N_2 for safety reasons. Since there is almost not H_2 and Al_2O_3 interactions especially compared to the metal's ability to chemisorp H_2, alumina plays an important role and is just providing the porous skeleton for H_2 to diffuse to the metal surface. In granular samples

annealing in H_2 promotes sintering effects making particle size more homogenous and in multilayered could make the layers more distinct and uniform while preventing oxidation and even reversing what may have already oxidized. Hydrogen reduction can have a big influence on metal alloy formation and its properties. Hydrogen could help forming a more stable alloy altering the actual atomic ratios of the alloy and the electronic interactions of the metals with each other and maybe promoting better GMR.

CHAPTER VII BISMUTH TELLURIDE NANOTUBES ELECTRODEPOSITION

The thermoelectric effect, also known as the Peltier–Seebeck effect, is the conversion of heat differentials to voltage and vice versa. The thermoelectric materials can generate electrical power from heat or use electricity to heat and cool. The thermo-electric phenomena provides a way to locally control temperature. For instance, at the nano-scale thermo-electric phenomena could be used to control the temperature of individual living cells. Solid thermal and electrical transport properties are affected by dimensionality, and therefore nanometer scaled solids could be a breakthrough in thermoelectric technology.

7.1 Background

Thermoelectricity is a combination of simultaneous thermal and electrical phenomena. The transfer of electrons that results when two dissimilar materials are connected creates a voltage potential across the junction of the two materials in contact. It is observed that the voltage potential changes when the metal junction is cooled or heated. This is the basic concept of a thermocouple. Heating or cooling two dissimilar joined materials causes a flow of electrical current between the joined materials. The schematic in Figure 7.1 illustrates the concept.
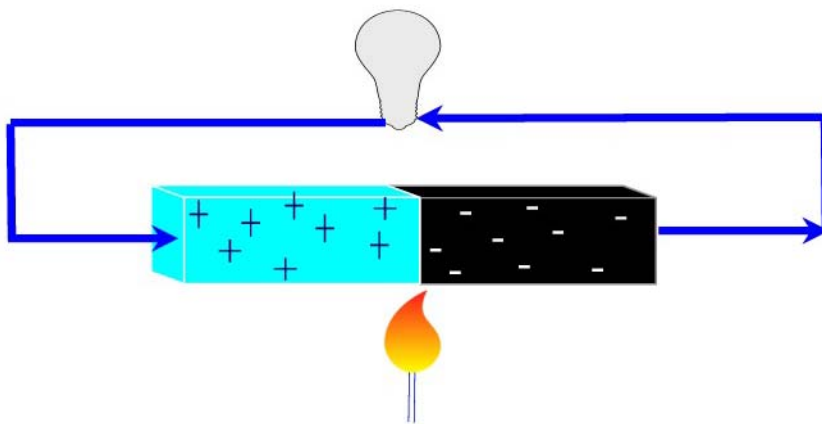
Figure 7.1 Thermoelectricity concept schematic

Temperature measurements using thermocouples are based on the discovery by Seebeck in 1821 that an electric current flows in a continuous circuit of two different metallic wires if the two junctions are at different temperatures. The most common metal pairs used for thermocouples include platinum-rhodium, chromel-alumel, copper-constantan, and iron-constantan. The thermal EMF is a measure of the difference in temperature between T_2 and T_1. In control systems the reference junction is usually located at the Emf-measuring device. The reference junction may be held at constant temperature such as in an ice bath or it may be at ambient temperature but electrically compensated (cold junction-compensated circuit) so that it appears to be held at a constant temperature, Figure 7.2, where A and B are the two metals, and T_1 and T_2 are the temperatures of the junctions.
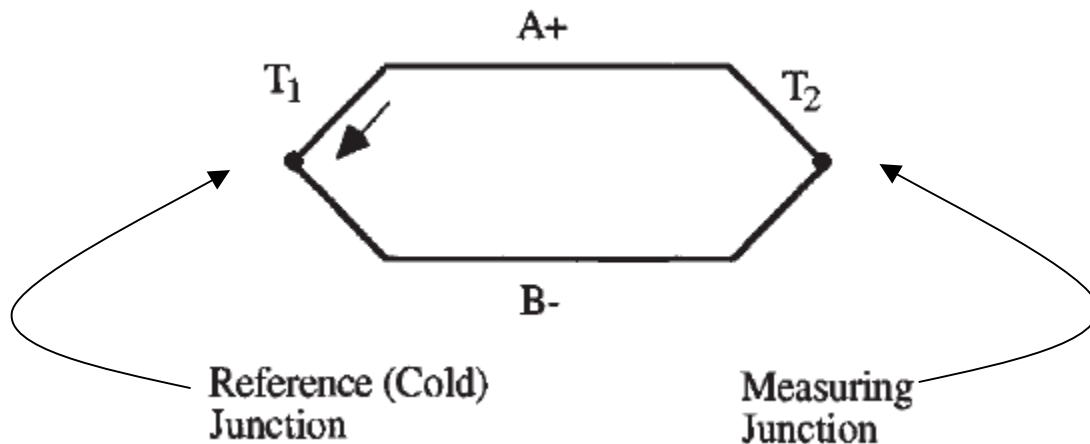
Figure 7.2 Thermal EMF as a measure of the temperature difference

The thermoelectric power of thermocouple materials makes them adequate for use at liquid-air temperatures and above. The level of the temperature measurement (4 K, 20 K, 77 K, or higher) and the temperature range needed are to be considered when selecting the two materials for making a thermocouple. Since platinum has an electrical resistance that goes to zero as the absolute temperature decreases to zero, the lower useful limit of platinum is about 20 K. Below

20 K, semiconductor thermometers are preferred. Semiconductors have just the opposite resistance temperature dependence of metals, their resistance increases as the temperature is lowered, because fewer valence electrons can be promoted into the conduction band at lower temperatures.

Thus, semiconductors are usually chosen for temperatures from about 1 to 20 K. In a semiconductor type of material, both electrons and holes facilitate the movement of charge. Depending on the majority of carrier type, semiconductors can be categorized into two types: n-type (electron carriers) and p-type (holes carriers). One method of inducing a flow of carriers, and consequently obtaining a voltage, is applying a heat flux. The thermoelectric phenomenon is illustrated in three closely related effects: Seebeck, Peltier and Thomson effects. By measuring the Seebeck coefficient, the Peltier and Thomson coefficients can be calculated. The Seebeck effect is the conversion of temperature differences directly into a volatge. Peltier effect is considered the inverse of the Seebeck effect. The Seebeck coefficient is the ratio between the voltage created and the temperature gradient, as shown in equation 7-1, where $\alpha(T)$ is the Seebeck coefficient, $\nabla(T)$ is the temperature gradient and E is the voltage.

$$E = \alpha(T)\ \nabla T \qquad \text{7-1}$$

The Seebeck effect is based on the fact that when a temperature gradient is applied on one end of a conductor, the charge carriers, the electrons or holes, will thermally diffuse from the hot to the cold end of the conductor where charge will build up creating an electric field inside the sample. At a constant temperature, when two different materials are connected, the Peltier effect manifests as the observed electric and thermal current created by the materials' junction. The magnitude and direction of the current is dictated by the Seebeck coefficient. The Peltier effect is the creation of a heat difference from an electric voltage, which is the reverse of the

Seebeck effect. The Peltier coefficient is defined as the ratio of the power generated at the junction to the current flowing through it, equation 7-2, where Π is the Seebeck coefficient, and I is the current flowing though the joined materials.

$$\Pi = Power/I \qquad \text{7-2}$$

When an electrical current is flowing through a material and a temperature gradient is applied, thermal energy is generated or absorbed along the sample. However the Seebeck coefficient varies as a function of temperature along the sample, therefore the sample acts as a series of Peltier junctions. The Peltier effect occurs when a current is passed though two dissimilar metals or between a p-type and an n-type semiconductor. The current drives a transfer of heat: one side cools off and while the other side heats up. This principle is also known as thermoelectric cooling. An interesting consequence of this effect is that the direction of heat transfer is controlled by the polarity of the current. Therefore, reversing the current flow will change the direction of heat absorbed or released. When the current is forced to flow though the circuit, heat is evolved at one junction and absorbed at the other junction. When electrons flow from a region of high density to a region of low density they expand and cool the region.

The Thomson coefficient is the ratio of the power generated per unit volume and the applied current and temperature gradient, equation 7-3.

$$\tau = Power/(I\,\nabla T) \qquad \text{7-3}$$

Where τ is the Thomson coefficient, I is the current flowing though the sample and ∇T is the applied temperature gradient. Equation 7-4 relates the Peltier to the Seebeck coefficient.

$$\Pi = \alpha T \qquad \text{7-4}$$

Equation 7-5 shows the relationship between the Thomson and the Seebeck coefficient.

$$\tau = T \frac{d\alpha}{dT}$$

7-5

Therefore a thermo-electric EMF is created when a temperature difference is applied to a metal or semiconductor. The voltage created is of the order of microvolts per degree difference. In semiconductors the type of charge carriers, electrons or holes, decides the sign of the thermo-power. This phenomenon is based on the principle of charge carrier diffusion. In semiconductors, charge carriers will start diffusing when a temperature gradient is applied at one end of the semiconductor. The hot charge carriers diffuse from the hotter end to the colder end, where there is a lower density of hot carriers. The cold charge carriers diffuse to the hot temperature region where there are less cold charge carriers. The movement of heat through the hot and cold charge carriers is called a heat current.

If both ends of the semiconductor are kept at constant temperatures, a constant heat current flows from one end to the other and there is constant carrier diffusion. If the rate of diffusion of hot and cold carriers in opposite directions is equal there would be not net charge change. If the diffusion charges are scattered by impurities, imperfections or lattice vibrations (phonons) then the diffusion rates would be different, creating a higher density of one type of carriers at one end of the conductor. The difference between the positive and negative charges creates a potential difference. This electric field opposes the uneven scattering of carriers, and equilibrium is reached when the same numbers of carriers are diffusing in opposite direction. This means that the thermo power of a material is largely dependent on impurities, imperfections and structural changes. Lattice vibrations, also known as phonons, also move along the thermal gradient and lose momentum when interacting with electrons and imperfections in the crystals. If

the phonon-electron interaction prevails, phonons will push the electrons to one end of the material and contributes to the thermoelectric effect. This phonon-electron contribution is most important in a certain temperature region close to 1/5 of the Debye temperature (θ_D). At lower temperatures than the one shown in equation 7-6, there are fewer phonons available for drag, while at higher temperatures the phonons-phonons scattering dominates.

$$T \approx \frac{1}{5}\theta_D \qquad\qquad \text{7-6}$$

Currently in the field of cryobiology there is a need to monitor and control the temperature at the cellular level and microscale thermoelectric coolers (µTECs) could be the solution. A TEC can be made of alternating n/p-type semiconductor elements thermally connected in parallel and electrically connected in series, as shown in Figure 7.3. When a current is passed through the device, heat is absorbed at one end and rejected at the other end. When two different semiconductors are in contact, the electrons will diffuse from the n-type where the electrons concentration is higher to the p-type where the electrons concentration is lower.
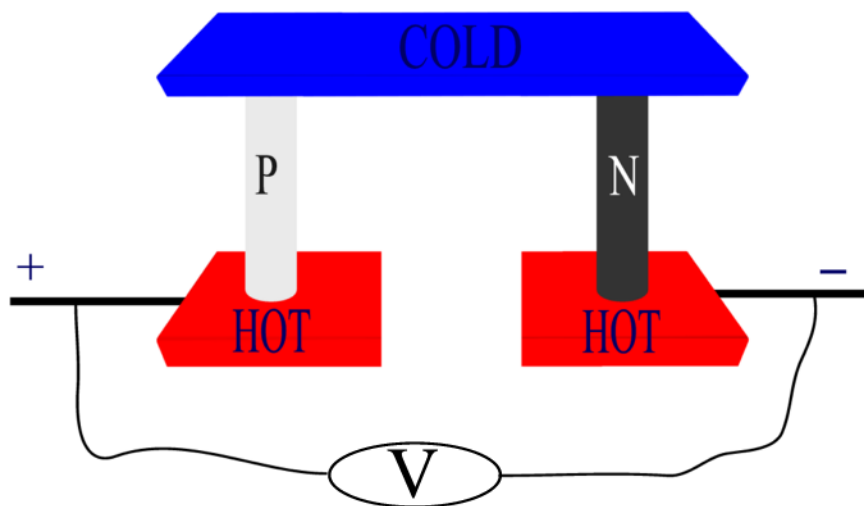
Figure 7.3 Thermoelectric cooler schematic

This diffusion of charge carriers will produces a temperature difference and it is the basic idea behind a thermoelectric cooler. In Figure 7.3 the negative pole attracts the holes in the p-type element while the electrons in the n-type element are attracted by the positive pole of the voltage.

To attain the best thermoelectric performance, it is important to choose materials with the highest figure of merit (Z), which is defined by the equation 7-7, where α is the Seebeck coefficient, K is the thermal conductivity and R is the electrical resistance.

$$Z = \frac{(\alpha_p - \alpha_n)^2}{K_{TE} R} \qquad 7\text{-}7$$

To maximize the figure of merit (Z) and therefore to enhance the TEC performance the material is required to have large Seebeck coefficients (for both the p and n type), and low thermal conductivity and electrical resistance. The alloy of bismuth-telluride satisfies these requirements and up to present is the most efficient TEC material.

Alloys of bismuth telluride (Bi_2Te_3) have been obtained by different fabrication techniques such as sputtering (Goldsmid, 1986, Rowe, 1999, Shafai, 2001, Bottner, 2004), chemical vapor deposition (CVD) (Venkatasubramanian, 1997, Boulouz, 1998), molecular-beam epitaxy (MBE) (Charles, 1988, Boyer and Cisse, 1988), evaporation (Volkein, 1990, Zou, 2001) and electrodeposition (Magri, 1996, Chaouni, 2000, Miyazaki and Kajitani, 2001, Tittes, 2003, Prabhakar, 2004). Electrodeposition offers not only a low cost alternative method but also the ability to control the alloy composition by changing the electrolyte concentration, current density, and applied potential. Using electrodeposition it is possible to modify and control the main carrier type in the alloy, to yield either a n-type or a p-type semiconductor. By adjusting the percentage of tellurium or bismuth in the deposit the obtained alloy can function as an n-type or

p-type semiconductor. When the deposit is tellurium rich the semiconductor behaves as a n-type semiconductor, and when the deposit is bismuth rich the alloy shows a p-type semiconductor behavior.

Manufacturing micro and nano-TECs is in the incipient phase. In the past 5 years only a few studies were performed on the manufacturing of TEC materials by electrodeposition. At the micro scale thermoelectric devices can be utilized as electric generators, coolers and infrared detectors. Bismuth telluride (Bi_2Te_3) alloys have highly desirable qualities such as high electrical conductivity, low thermal conductivity and high Seebeck coefficients, making it one of the most favorable TEC materials.

Bulk and thin film electrodeposition of Bi_2Te_3 has been successfully shown by different research groups such as Takahashi *et al.* (Takahashi, 1993, 2003), Martin-Gonzales *et al.* (Martin-Gonzales, 2002), Miyazaki and Kajitani (Miyazaki and Kajitani, 2001) and Yoo *et al.* (Yoo, 2005). One of the first groups to electrodeposit Bi_2Te_3 and confirm the deposit structure using XRD analysis was Takahashi *et al.* They showed a more systematic investigation of the electrochemical reactions and compositional changes as a function of applied potential in the nitric acid bath and also proposed several intermetallic Bi_2Te_3 compound formation at different potentials. Miyazaki and Kajitani showed that the deposition of either n-type or p-type bismuth telluride could be controlled by controlling the deposition potential. Their study suggested that the compositional shift to the Bi-rich side introduces p-type semiconductor characteristics in Bi_2Te_3. In a more recent study, Takahashi *et al*. used a more complex electrodeposition bath containing EDTA (ethylenediaminetetraacetic acid) and suggested that the formation of bismuth hydroxide $Bi(OH)_3$ could be suppressed by using EDTA as a complexing agent.

Yoo *et al*. used potentiostatic electrodeposition to obtain n-type Bi_xTe_y films and also concluded that the film concentration affected the thermoelectric properties. The highest negative Seebeck coefficient of (−188.5 µV/K) was obtained from a stoichiometric deposited film of Bi_2Te_3 at a deposition potential of −0.170 V. They also found that annealing at 250 ^{o}C in a reducing H_2 atmosphere enhanced the thermoelectric properties and reduced film defects. After annealing, they concluded that the Seebeck coefficient of the electrodeposited n-type Bi_2Te_3 thin films was comparable to the bulk Bi_2Te_3 Seebeck coefficient (220 µV/K).

In a theoretical study, Hicks and Dresselhaus (Hicks and Dresselhaus, 1993) predicted a major increase in the figure of merit of nanostructured thermoelectric materials. For a nanowire of 0.5 nm diameter they estimated a figure of merit of 14, which would be 28 times larger than the bulk Bi_2Te_3 figure of merit of 0.5. Consequently, researching the fabrication and characterization of nanowire structures of thermoelectric materials is receiving much attention due to the possibility of enhancing the figure of merit by reducing the structural dimensions.

The heat transport concept has its base in Boltzmann's theory that relates the amount of heat transported in a solid by individual phonons, electrons and their fluxes that depend on the particles density of states and their group velocity that in turn depends on the scattering mechanisms. Most importantly, dimensionality (the nano-size scale) affects both the density of states and the scattering mechanism. It has been recently demonstrated by Hicks and Dresselhaus (Hicks and Dresselhaus, 1993) that the thermoelectric efficiency of surperlattices can be double that of the conventional solids. The thermoelectric power, or Seebeck coefficient, is more sensitive to the details of the energy band structure and scattering than the electrical conductivity. The Seebeck coefficient relates the temperature gradient and the electric field (E=S∇T) and is an equation of state that does not depend on the path taken by the carrier though

the material. A higher electron density results in a higher electrical conductivity but in a lower Seebeck coefficient . Longer electron mean free paths could improve the electrical conductivity without lowering the Seebeck coefficient. Increasing the electron mean free paths is equivalent to increasing thermal conductivity that is dominated by acoustic phonons. It has already been shown by Bergman and Fel (1999) that the power factor can be enhanced in a mixture though electron energy filtering by size quantization and by the reduction of lattice thermal conduction due to scattering and phonon refraction on the nanoscale physical boundaries.

When controlling the dimensionality at the nanoscale, the goal is to minimize the lattice thermal conductivity while reducing the electrical conductivity, but the disorder and nanoscale defects become more pronounced than in bulk solids. Both electron and phonons mean free paths are on the order of thousands of nanometers, but it is only beneficial that the sample dimension is smaller than the phonon mean free path but not the electron mean free path. Therefore, size quantization effects can increase the Seebeck effect since the density of the electric states is a strong function of dimensionality. The Seebeck coefficient is a function of the density of states energy derivative and it is enhanced when the density of state function peaks sharply, like in the low dimensional crystals. This functionality requires that the characteristic sample dimension, also thought of as the thickness of the quantum well, must be on the order of the electron wavelength. Ashcroft and Mermin (1976) showed that the density of state dependence on the inverse of the electric field potential can result in divergences of the density of state function in the lower dimensions, concluding that nanoscale dimensionality would be particularly favorable for thermoelectric properties.

Another requirement for enhanced thermoelectric phenomena is that the material should be almost free of disorder in order for the band structure to hold. However, the smaller the

quantum wire diameter, the higher the chances that a defect would localize the electron wave function, consequently impeding transport. The band structure does not hold when localized effects that are characterized by phase coherence dominate the conduction.

In general, thermoelectric materials are narrow band gap semiconductors. For a low carrier density, the Seebeck coefficient is large but the conductivity is low and vice versa for a large carrier density. Cutler and Mott (1969) concluded there is an optimal doping level that maximizes the figure of merit. In the same early study they showed that figure of merit would drastically increase in the low dimensionality materials. Experientially, the Dresselhaus group (1993) marked the beginning of the low dimensional thermoelectricity. Simkin and Mahan (2000) showed that the Seebeck coefficient is sensitive to the energy derivative of the conductivity and that the sharp peaks in the energy of state function are a hallmark of the low-dimensional materials and would increase the Seebeck coefficient for a given carrier density and conductivity. However, the same study pointed out that the range of Fermi energies over which the figure of merit increases is much smaller for the low dimensional systems compared to the bulk materials. Therefore, it should be noted that finding the optimal doping level is crucial for the thermoelectric materials at the nanoscale. In a recent study by Humphrey and Linke (2005) the thermoelectric solid materials were modeled with continuous energy bands but with spatially localized spikes in the density of states, arising from quantum dots embedded in the material. The electrons were simulated as diffusing through the material influenced by the thermal gradient. The charge carriers encounter spatial variations in the temperature and potential gradient. Humphrey and Linke (2005) predicted that under the right conditions the figure of merit values would increase as high as 10 at 300 K.

At low temperatures the conductance decreases and this conduction regime is called "weak localization" in which the propagation waves are not blocked by the defects. At low temperatures, the waves can circumvent the defects in the solid by propagating around them through constructive quantum mechanical interference. This constructive quantum mechanical interference can happen only when the waves retain the memory of their relative phase. This is also known as the phase coherence length and it is only a few nanometers in most solids near the liquid helium temperature. In the case of Bi, the spin orbit interactions are dominant and the sign of the temperature dependence is reversed (the conductivity increases with increasing temperature). This phenomenon is called antilocalization. The temperature dependence is both a function of the phase braking mechanism and the system dimensionality. Magnetoresistance is another experimental quantity that identifies the presence of localization. The MR sign is inverted for localization and antilocalization such that when the spin orbit scattering is small (like in Zn) the MR is negative while the MR is positive when the spin orbit scattering dominates like in Bi. (Heremans, 2003) The work published by Prosen and Campbell (2000) concluded that the thermal conductivity is expected to decrease towards the low dimensionality.

Scattering mechanisms can be separated into the intrinsic or extrinsic due to scattering of phonons at the sample boundaries. It has been proven long ago (Peierls, 1929) that a harmonic scattering are not present in 1D phonon systems and especially when dealing with Unklapp processes that dominate the scattering near the Debye temperature. In other words, the extrinsic scattering mechanism dominates the 1D systems, unlike the 3D systems, therefore the temperature dependence of the lattice thermal conductivity in 1D systems should follow that of the specific heat, therefore especially temperature independent above the Debye temperature. This scattering of phonons at the sample boundaries is prevalent in the nanostructures and it is

independent of temperature. Daly *et al.* (2002) ran a molecular dynamic simulation and reported a minimal thermal conductivity of surperlattices in the direction perpendicular to the layers. Interface roughness also minimized the thermal conductivity because it added more resistance to the propagation of acoustic waves between different layers of acoustic properties. It was also concluded that on the nanoscale the lattice thermal conductivity was reduced in comparison to bulk materials.

Thin film multilayers of $(Bi_{1-x}Sb_x)_2/(Se_{1-y}Te_y)_3$ have been recently shown to produce an increase in the thermoelectric figure of merit. Published in Nature, Venkatasubramanian *et al.* (2001) showed an enlarged figure of merit of 2.4 in multilayered thin films of Bi_2Te_3(1nm)/Sb_2Te_3 (5 nm). In essence the explanation of the increase in ZT is the reduction in the thermal conductivity when dealing with very small layers (quantum wells). BiSb nanowires are predicted to have better thermoelectric behavior than bulk Bi and the fabrication techniques involving vapor deposition come of little use since the vapor pressures of Bi and Sb are so different at any given temperature. Electrodeposition would be an ideal candidate for making these kinds of nanostructures.

Other reports of increasing ZT with multilayers were published on systems such as PbTe/PbSeTe and PbTe/PbEuTe for which the room temperature n-type ZT was 1.5 and the p-type ZT was 1.2. Beyer *et al.* (2002) showed that in multilayered thin films of PbTe/PbSrTe would have a ZT of 1 but only when the layers were smaller than 3 nm.

Bismuth is a favorite and promising element for the study of thermoelectric properties on the nanometer scale. The small effective mass of electrons in the material yields a long electron de Broglie wavelength with large mobility and mean free path. Moreover when the material is shaped in the form of nanowires, the quantized band structure of Bi leads to density of state

singularities. Bulk Bi is a semimetal with a conduction band and a valence band that overlap by 38 meV at 4K. Size quantization increases the energies of electron/hole bands. Down to the nanowire size the conduction and valence band overlap decreases and becomes an energy gap in very narrow nanowires (under 50 nm). Therefore there is a size-quantization-driven metal to semiconductor transition. Again, the optimal figure of merit is very sensitive to doping because the enhancement happens when the Fermi energy is located near one of the density of states discontinuities. Doping has to be well controlled because disorder kills the figure of merit. Disorder will smear discontinuities which in turn would decrease the Seebeck coefficient, and the localization effects will compete with the size quantization reducing the electrical conductivity. Wires with diameters between 200 to 70 nm are semimetals. The thermoelectric power of the semiconductor nanowires is very much enhanced compared to the metallic wires, and their thermopower decreases at low temperatures. Heremans and Thrush (1999) pointed out that the alumina matrix conducts most of the heat when the wires are embedded in the AAO template.

The main mechanism for the figure of merit enhancement is caused by the increase of density of states near the Fermi level. The main consequence is that a sufficient density of charge carriers can exist in the solid phase to maintain a high electrical conductivity, but the Fermi energy is narrow, which would enlarge the Seebeck coefficient. Superlattices with controlled phonon thermal conductivity at the interfaces are predicted to have an enhanced figure of merit. Quantum wires in which the electronic density of states have narrow peaks at quantized values of energy are predicted to have larger figure of merit. For thermoelectric applications bismuth is an attractive element, because the electron effective mass is small along certain crystallographic

148

directions and the electron wave functions are large. Even more bismuth lattice thermal conductivity is small which would further increase the figure of merit.

7.2 Experimental

Polycarbonate (PC), Osmonics, Poretics nanoporous membranes and Whatman Anodisc alumina membranes (AAO) were used as templates for electrodeposition of nanostructures. The manufacturer specified pore diameter ranged from 20 nm to 2 microns, while the membrane thickness was 6 microns for the polycarbonate membranes and 60 microns for the AAO membranes. For electrical contact, Au was sputtered on one side of the template.

The Au coated template acted as the working electrode and was fixed inside a polyetheretherketone (PEEK) stationary holder exposing a square area of 2.25 cm^2 of the membrane. The cathode membrane was positioned horizontally opposing a platinum counter electrode. A saturated calomel electrode (SCE) was used as the reference. The electrolyte for nanotube deposition was varied starting with an initial concentration of 0.01 M bismuth oxide and tellurium oxide. In this study, the initial concentration was doubled, quadrupled and the ratios of bismuth oxide and tellurium oxide were varied in order to study the concentration effect on the Seebeck coefficient measurements. The overpotential was controlled versus the open circuit potential (OCP) that ranged between +0.1 V and –0.1 V. All experiments were carried out with a Solatron 1255B/1287 potentiostat/function generator. A scanning electron microscope (SEM) JEOL JSM-840A, operated at 20 kV was utilized to observe the electrodeposited nanotubes after the supporting PC membrane was dissolved in dichloromethane. The Seebeck measurements were taken at room temperature using two nano-voltmeters. Seebeck coefficient measurements were taken for both n-type (Te rich) and p-type (Bi rich) samples. The Seebeck coefficient (S) is measured by mounting the sample on the device shown in Figure 7.4 such that

it would have good electrical contacts between the heater and heat sink. One end of the device

has a Constantan reference sample whose Seebeck coefficient is known to be $S_R = 40 \ \mu V/K$.

Therefore the Seebeck coefficient of the sample to be measured is $S_S = (\Delta E_S / \Delta E_R) * S_R$

where ΔE_S = voltage drop obtained for the sample at a temperature drop of ΔT_R

ΔE_R = voltage drop of the reference at a temperature drop of ΔT_R

S_R = Seebeck coefficient measurement of the reference

S_S = Seebeck coefficient measurement of the sample
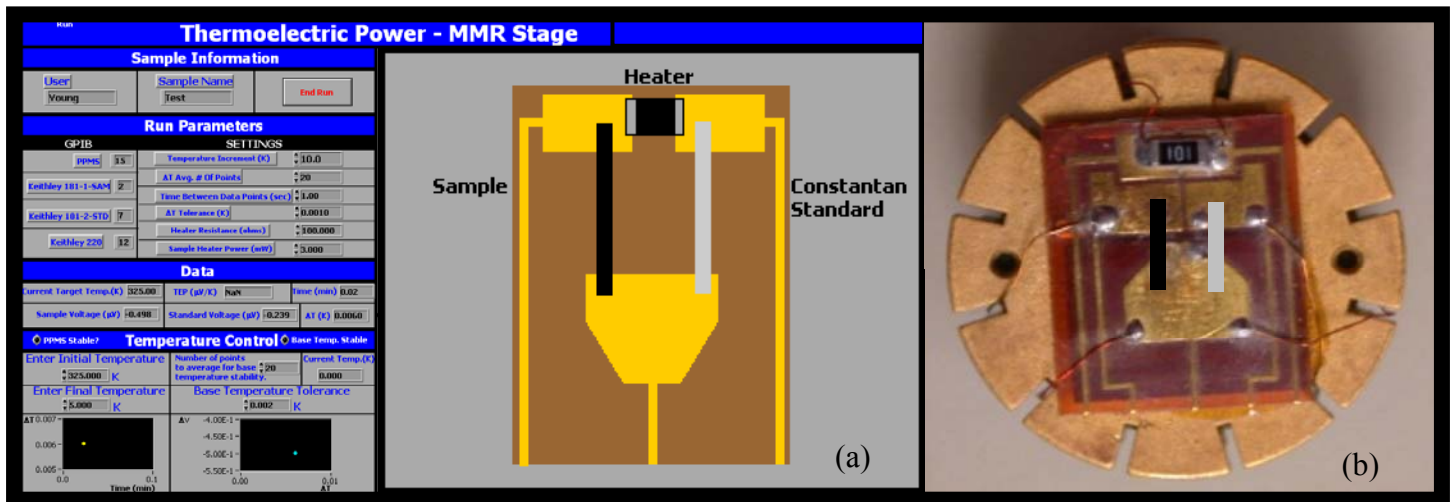
Figure 7.4 Seebeck coefficient measurements (a) schematic (b) actual puck

7.3 Results and Discussion

Figure 7.5 shows a SEM image of bismuth telluride wires obtained by electrodeposition inside

20 nm diameter pores AAO membrane. The electrodeposition was carried out potentiostatically

from a diluted (1X) electrolyte (0.01 M Bi_2O_3 and 0.005 M Te_2O_3). Figure 7.5 (a) shows an

array of Bi_2Te_3 wires obtained at a high overpotential (-0.4 V) = [–0.21 V vs. OCP (-0.19 V vs.

SCE)] for 1 h. The XRF composition analysis of the (-0.4 V) nanowire sample showed 59.8 %

Bi and 40.2% Te. Figure 7.5 (b) shows an array of Bi$_2$Te$_3$ wires obtained at a low overpotential (-0.07 V vs. OCP (-0.09 V vs. SCE)] for 14 h. The XRF composition analysis of the (-0.16 V) nanowire sample had 17.25 % Bi and 82.75 % Te. Figure 7.5 (c) shows the XRF composition analysis as a function of overpotential for bismuth telluride nanowires electrodeposited from the diluted (1X) electrolyte. Figure 7.5 (d) shows the Seebeck coefficients of the bismuth telluride nanowires plotted as a function of the electrodeposition potential. The highest n-type Seebeck coefficient of the nanowires deposited inside the AAO membrane was –25 μV/K. From this type of diluted solution all the p-type Seebeck coefficients came out rather small, with a maximum value of 4 μV/K.
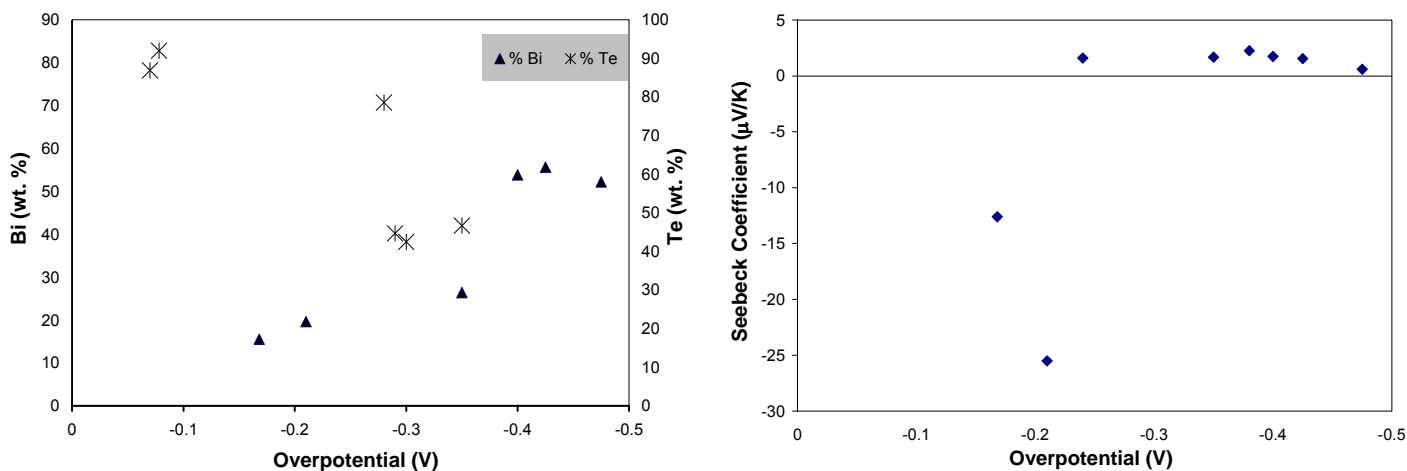
Figure 7.5 (c) Composition function of potential   (d) Seebeck coefficients function potential

Figure 7.6 shows a SEM image of bismuth telluride tubes obtained by electrodeposition inside 400 nm diameter pores PC membrane. The electrodeposition was carried out potentiostatically from a diluted (1X) electrolyte (0.01 M Bi$_2$O$_3$ and 0.005 M Te$_2$O$_3$). Figure 7.6 (a) shows an array of Bi$_2$Te$_3$ tubes obtained at a high overpotential (-0.4 V) = [–0.24 V vs. OCP (-0.16 V vs. SCE)] for 1 h. Figure 7.6 (b) shows an array of Bi$_2$Te$_3$ tubes obtained at a low overpotential (-0.13 V) = [–0.00001 V vs. OCP (-0.13 V vs. SCE)] for 14 h. Clear tubular structures were observed from

151

electrodeposition into the large 400 nm pores membrane. In Figure 7.6(c) the tubes Seebeck coefficients are plotted as a function of overpotential. The positive Seebeck coefficients 'S' suggests that the majority carriers are holes, and a negative 'S' suggests that the majority carriers are electrons-like. For these 1X tubes the highest n-type coefficient was -55 $\mu V/k$ when the electrodeposition overpotential was small, -0.06 V. However, all the p-type Seebeck coefficients were quite small, less than 2 $\mu V/K$.
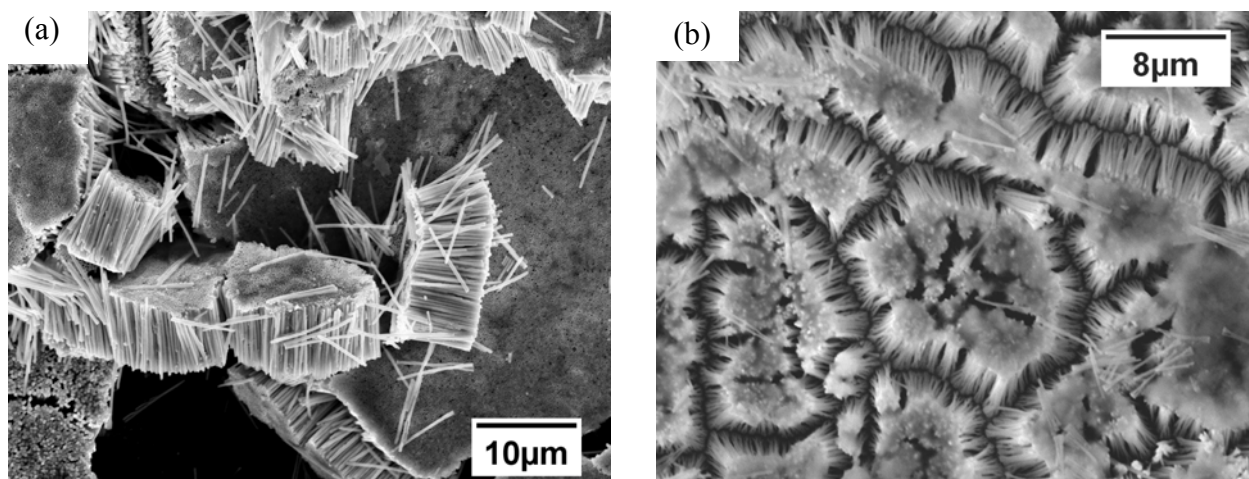
Figure 7.5 SEM of electrodeposited bismuth telluride wires
(a) (-0.4 V vs. SCE) (b) (-0.16 V vs. SCE)

Figure 7.7 shows the Seebeck coefficients of the tubes obtained from a 2X and 4X concentration electrolyte. The results obtained from the 2X electrolyte, Figure 7.7 (a), show that the highest n-type coefficient was -47.2 $\mu V/K$ at a low overpotential of -0.06 V. More importantly, from the 2X electrolyte the highest p-type Seebeck coefficient increased to 13.5 $\mu V/K$ when a lower overpotential -0.16 V was applied. The results from the 4X electrolyte, Figure 7.7 (b) show a higher n-type Seebeck coefficient of -55.7 $\mu V/K$ obtained at -0.06 V

overpotential. However, the p-type Seebeck coefficient from the 4X electrolyte did not improve compared to the 2X electrolyte.

In Figure 7.8, the effect of the pore diameters on the Seebeck coefficient measurements is reported. The electrolyte concentration was maintained constant at 0.04 M (4X solution). Using the larger pore size PC membranes (2000 nm) the Seebeck coefficients of these larger tubes were compared to the 400 nm tubes from the same electrolyte concentration, Figure 7.8 (b). Comparing the 400 nm tubes Seebeck coefficients (Figure 7.7 b) with the 2000 nm tubes Seebeck coefficients (Figure 7.8), it is interesting to note that the pore diameters had a negligible effect on the Seebeck coefficient measurements of both p-type and n-type Bi_2Te_3 nanotubes. When larger pore (2000 nm) diameters were used, the highest Seebeck coefficient values for the n-type and p-type bismuth telluride nanotubes were -56 μV/K at (-0.06 V vs. SCE) and 1.6 μV/K (-0.26 V vs. SCE), respectively. For a 400 nm pore diameter the Seebeck coefficient values for a n-type and p-type bismuth telluride nanotubes were -55.7 μV/K (-0.06 V vs. SCE) and 3 μV/K (-0.35 V vs. SCE), respectively.

Figure 7.9 shows the 400 nm tubes Seebeck coefficients obtained when the ratios of bismuth to tellurium were varied in the 2X (0.02 M) electrolyte. Figure 7.9 (a) presents the effect of increased bismuth content (5 bismuth to 1 tellurium). The highest n-type Seebeck coefficient was –44 μV/K at –0.09 V overpotential, while the highest p-type Seebeck coefficient was 7 μV/K at a higher overpotential of -0.3 V. There was not a significant rise in the Seebeck coefficient measurements when the ratio of bismuth and telluride was 5:1. Figure 7.9 (b) shows the effect of the increased tellurium concentration with respect to bismuth. In this case the ratio of bismuth to tellurium became 3:5, and it is very important to note that the p-type Seebeck coefficient increased significantly to 57 μV/K at a very low overpotential of –0.02 V. However,

153

using this 3:5 ratio the highest n-type Seebeck coefficient −32 μV/K was not as high as the one

obtained from the 3:1 ratio solution.

7.4 Conclusions
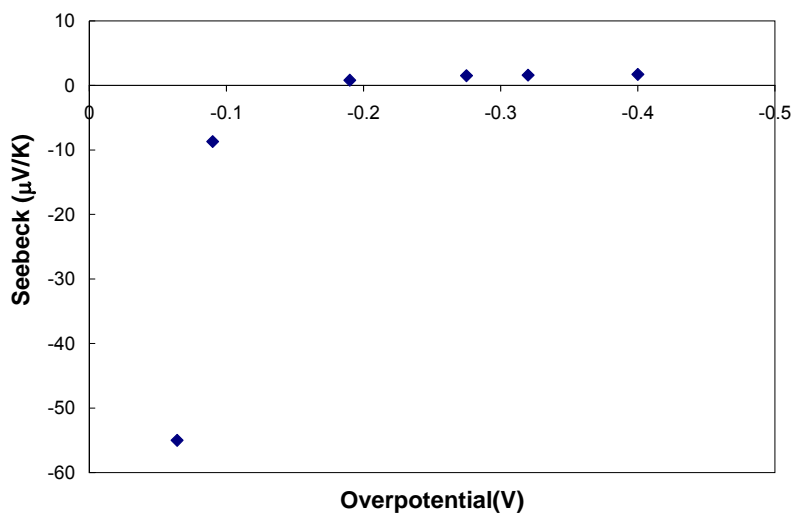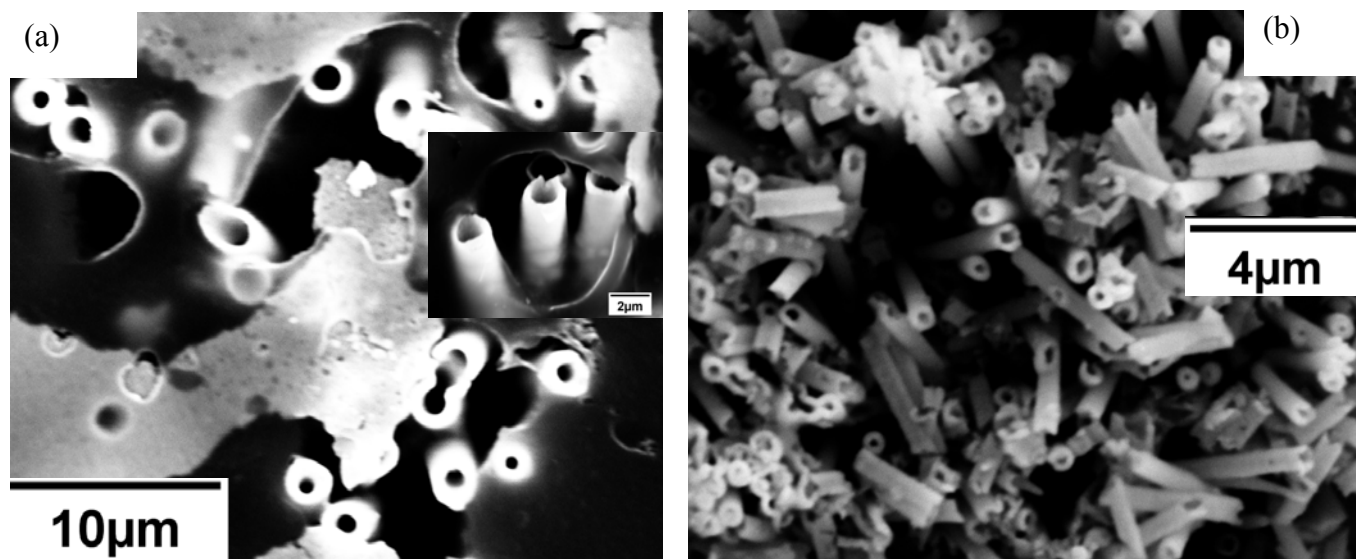
Figure 7.6 SEM of electrodeposited bismuth telluride tubes
(a) high overpotential (-0.4 V vs. SCE) (b) low overpotential (-0.13 V vs. SCE) (c) Seebeck
coefficient for nanotubes from 1X electrolyte

Different electrolyte concentrations were tested in order to optimize the Seebeck coefficients in

nanowires and nanotubes. The highest n-type Seebeck coefficient -56 μV/K was observed in a

400 nm nanotubes structure when the applied overpotential was -0.06 V and the electrolyte concentration was 4X (0.04 M) bismuth-telluride solution.
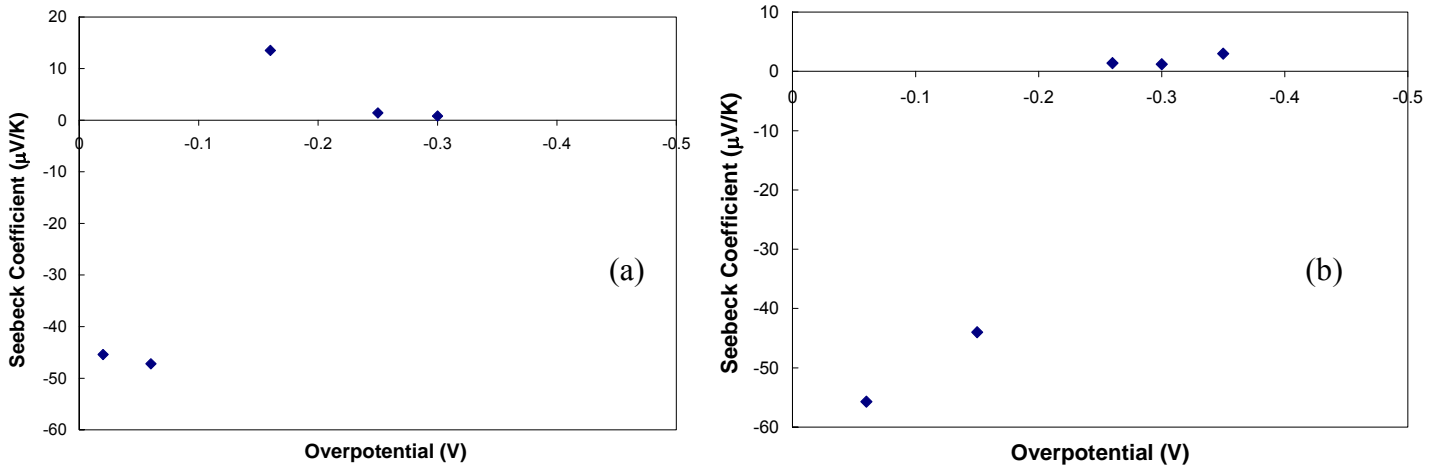
Figure 7.7 Bismuth telluride nanotubes (400 nm pores) Seebeck coefficients as a function of overpotential for different concentration electrolytes (a) 2X concentration (b) 4X concentration
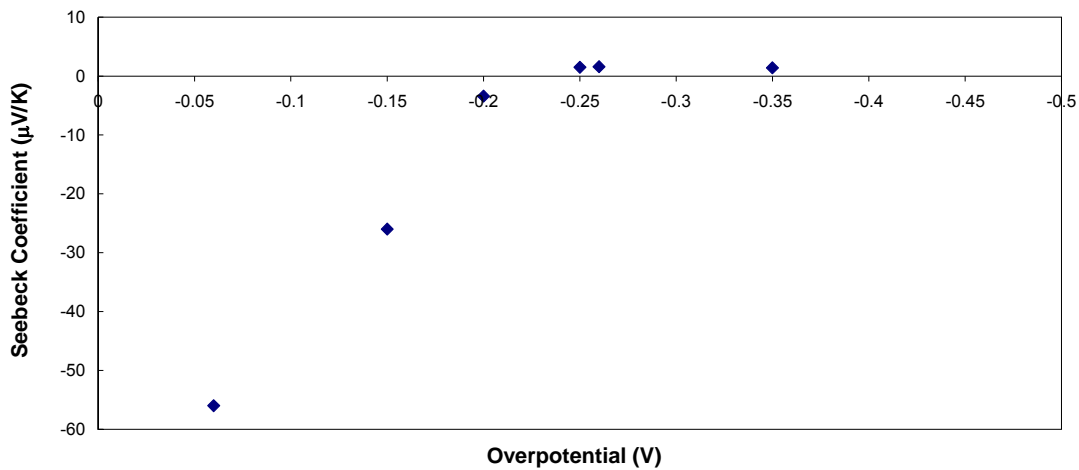
Figure 7.8 Seebeck coefficients of bismuth telluride nanotubes from large pore size (2000 nm) PC membrane and 4X electrolyte

A similar high value of -55 μV/K was also observed from the 1X (0.01 M) electrolyte concentration. Therefore, it was concluded that for the n-type Seebeck coefficients the electrolyte

concentration did not play a crucial role. However, when the same 1X electrolyte was employed to electrodeposit wires in 20 nm pores and then tubes in 400 nm pores, the observed n-type Seebeck coefficients varied dramatically from –25.5 µV/K in the wire geometry to –55 µV/K in the tube geometry. Therefore, for the same type of electrolyte, the Seebeck coefficients of the nanotubes were higher that the wires.

The real interesting observation is the jump in the value of the p-type bismuth telluride nanotubes when the ratio of bismuth and telluride was 3:5. The best Seebeck coefficient value obtained for p-type nanotubes was 57 µV/K, obtained at a very low overpotential of -0.02 V.
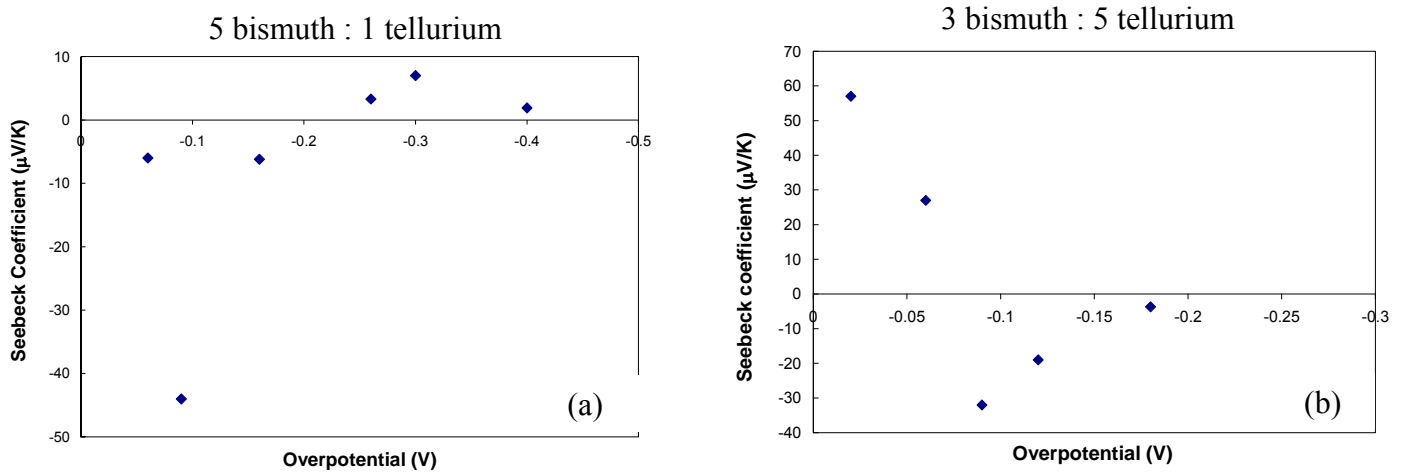
Figure 7.9 Seebeck coefficients of different bismuth to tellurium ratio nanotubes (a) larger bismuth content (5:1) (b) larger tellurium content (3:5)

The bismuth telluride electrodeposition project was carried on in collaboration with D. Pinisetty form the Mechanical Engineering department at LSU.

CHAPTER VIII CONCLUSIONS

The current perpendicular to the plane giant magneto-resistance (CPP)-(GMR) effect makes multilayered nanowires of huge interest as magnetic sensor materials. Electrodeposition is the most efficient method for fabricating high aspect ratio nanostructures. In this dissertation, the CoNiFeCu alloy system was more rigorously investigated in order to electrodeposit multilayered nanowires and nanotubes and optimize the GMR effect.

Electrolyte composition influenced GMR by affecting the alloy layer composition and thickness. With the addition of $FeSO_4$ to the electrolyte the GMR tended to decrease, although the saturation magnetization field was improved. A large amount of $FeSO_4$ (4 mM) or $CoSO_4$ did not have a positive effect on GMR. Hydrogen annealing of CoNiFe/Cu nanowires had a great impact on the GMR. After annealing in flowing H_2, the largest CoNiFe/Cu GMR value observed at room temperature was 30 % and almost 40 % at 100 K measurement.

Both a steady state and a non steady state MathCAD simulation were used to predict the current behavior as a function of the electrolyte temperature. The steady state model captured the main trend of the current with temperature, but it did not reflect the mass transport peak in the Cu deposition region. To get better deposition current simulation with temperatures a non steady state scenario was considered, in which species concentration are changing in time. The mass transport peak showed up in the non steady state model but the overall simulation did not completely agree with the experimental observations. Not including a kinetic model for the anomalous codeposition at different temperature is one of the shortcomings of this model that could explain why this simulation cannot be used to predict changes in the electrolyte composition. Experimentally, the Cu current registered a significant decrease when the deposition was performed from the chilled electrolyte, and oppositely, when the electrolyte was

heated to 50 ^{o}C, the Cu current increased by the same amount. In the high temperature electrolyte the anodic current, observed during alloy layer deposition, increased and lead to a larger loss of the alloy layer. Electrolyte temperature had an effect on the electrodeposition currents and consequently on the GMR. When the electrolyte was heated to 50 ^{o}C, the GMR values dropped significantly since the layer sizes were not the optimal thickness and the Cu content in the alloy layer was much higher.

Microfluidic nanoparticle sensors based on GMR nanowires were fabricated for the first time. The fabrication process involved stamping of a micro-channel pattern onto PDMS. The sensor testing results showed a high signal-to-noise ratio, good reproducibility and sensitivity.

Higher signal-to-noise ratios and better GMR sensitivity make multilayered nanotubes fabricated by electrodeposition an attractive and cost efficient material for their potential use in magnetic sensing applications. Multilayered CoNiFeCu/Cu tubes were electrodeposited inside commercially available nanoporous membranes from a single bath electrolyte. The nanotubes exhibited GMR at room temperature and at low magnetic saturation fields (less than 0.5 Tesla). Electrolyte temperature affected the tube vs. wire formation. Smaller diameter tubes were obtained from a 4 ^{o}C electrolyte. Multilayered CoNiFeCu/Cu nanotubes showed room temperature GMR at low magnetic field (0.04 Tesla).

Bismuth Telluride nanotubes were deposited inside commercially available membranes. The highest Seebeck coefficient for a p-type Bi_2Te_3 nanotubes was 57 μV/K, at a concentration of 0.02 M and at a potential of -0.02 V vs. SCE when the ratio of bismuth to telluride was 3:5. The electrolyte concentration affected the tube formation and the Seebeck coefficient results.

REFERENCES

- D. Almawlawi, N. Coombs and M. Moskovits, *Journal of Applied Physics*, **70**, 4421 (1991).

- Bai and C.C. Hu, *Electrochemistry Communications*, **5**, 78-82 (2003).

- J. Bao, C. Tie, Z. Xu, Q. Zhou, D. Shen and Q. Ma, *Advanced Materials*, **13**, 1631 (2001).

- M.N. Baibich, J.M. Broto, A. Fert, F. Nguyen Van Dau, F. Petroff, P. Etienne, G. Creuzet, A. Friederich and J. Chazelas, *Physical Review Letters,* **61,** 2472 (1988).

- D. R. Baselt, G. U. Lee, M. Natesan, S.W. Metzger, P. E. Sheehan and R. J. Colton, *Biosensors & Bioelectronics* **13**, 731-739 (1998).

- G. Binasch, P. Grünberg, F. Saurenbach and W. Zinn, *Physics Review B*, **39,** 4828 (1989).

- Blondel, J. Meier, B. Doudin and J. Ansermet, *Applied Physics Letters*, **65,** 3019 (1994).

- Blondel, J. Meier, B. Doudin and J.Ph. Ansermet, K. Attenborough, P. Evans, R. Hart, G. Nabiyouni and W. Schwarzacher, *Journal of Magnetism and Magnetic Materials,* **148,** 317 (1995).

- Blondel, B. Doudin and J.Ph. Ansermet, *Journal of Magnetism and Magnetic Materials*, **165,** 34 (1997).

- H.J. Blythe, V.M. Fedfosyuk, W. Schwarzacher and O.I. Kasyutich, *Journal of Magnetism and Magnetic Materials*, **208,** 251-254 (2000).

- O. Chene and D. Landolt, *Journal of Applied Electrochemistry*, **19,** 188 (1989).

- D. Davis and E.J. Podlaha, **"CoFeNiCu/Cu Nanowires and Tubes"**, 205th Meeting of the Electrochemical Society, San Antonio, TX May 9, (2004).

- D. Davis and E.J. Podlaha, *Electrochemical and Solid State Letters,* **8,** D1 (2005).

- D. Davis, M. Moldovan, D. P. Young, E. J. Podlaha, *ECS Transactions,* 208th Meeting of the Electrochemical Society, Los Angeles, CA, (2005).

- T.E. Dinan, M. Matlosz and D. Landolt, *Journal of Electrochemical Society*, **138,** 2947 (1991).

- Q. D. Huan, P. Yong, W. Cheng-Wei and L. Hu-Lin, *Acta Physica Sinica*, **50,** 144 (2001).

- S. Dubois, J.M. Beuken, L. Piraux, J.L. Duvail, A. Fert, J.M. George, and J.L. Maurice, *Journal of Magnetism and Magnetic Materials*, **165,** 30 (1997).

- S. Dubois, E. Chassaing, J.L. Duvail, L. Piraux and M.G. Waals, *Journal of Chimie Physique,* **96,** 1316 (1999).

- P.R. Evans, G. Yi and W. Schwarzacher, *Applied Physics Letters, 76,* 481 (2000).

- V.M. Fedfosyuk, W. Schwarzacher, O.I. Kasyutich and G. Yi, *Physics of Low Dimensional Structures,* **11/12,** 61 (1999).

- P.S. Fodor, G.M. Tsoi and L.E. Wenger, *Journal of Applied Physics*, **91,** 8186 (2002).

- Fert, Bartheleny, P. Paltier, P. Holody, R. Loloee, F. Petroff, P.A. Schroeder, L.B. Steren, and T. Valet, *Material Science and Engineering*, **B 31,** 1 (1995).

- Y. Fukunaka, M. Motoyama, Y. Konishi, and R. Ishii, *Electrochemical and Solid State Letters,* **9**, C62 (2006).

- J.M. Garcia, A. Asenjo, J. Velazquez, D. Garcia and M. Vazquez, *Journal of Applied Physics*, **85,** 5480 (1999).

- J.M. Garcia, A. Thiaville and J. Miltat, *Journal of Magnetism and Magnetic Materials*, **249,** 163 (2002).

- R. Gasparac, P. Kohli, M.O. Mota, L. Trofin and C.R. Martin, *NanoLetters*, **4,** 513 (2004).

- S. Ge, C. Li, X. Ma, W. Li, L. Xi and C.X. Li, *Journal of Applied Physics*, **90,** 509 (2000).

- D.L. Graham, H.A. Ferreira, P.P. Freitas, and J.M.S. Cabral, *Biosensors and Bioelectronics*, **18,** 483 (2003).

- G.P. Heydon, R.S. Hoon, A.N. Farley, S. L. Tomlinson, M.S. Valera, K. Attenborough and W. Schwarzacher, *Journal of Physics D: Applied Physics,* **30,** 1084 (1997).

- S. Hou, C. Harell, L. Trofin, P. Kohli and C.R. Martin, *Journal of the American Chemical Society*, **126,** 5674 (2004).

- Q. Huang, D.P. Young, J.Y. Chan, J. Jiang and E.J. Podlaha, *Journal of the Electrochemical Society*, **149,** C349 (2002).

- Q. Huang and E.J. Podlaha, *Journal of Electrochemical Society*, **151,** C119-C126 (2004).

- Q. Huang, D. Davis and E. J. Podlaha, "Electrodeposition of FeCoNi/Cu Nanowires", *Journal of Applied Electrochemistry*, in press (2005).

- J. C. Hulteen, K. B. Jirage, and C. R. Martin, *Journal of American Chemical Society,* **120**, 6603 (1998).

- M. Jimbo, T. Kanda, S. Goto, S. Tsunashima and S. Uchiyama, *Japanese Journal of Applied Physics*, **31,** L1349 (1992).

- K. B. Jirage, J. C. Hulteen, and C. R. Martin, *Science,* **278**, 655 (1997).

- K. B. Jirage, J. C. Hulteen, and C. R. Martin, *Analytical Chemistry,* **71**, 4913 (1999).

- W. Kautek, S. Reetz and S. Pentzien, *Electrochimica Acta,* **40,** 1461(1995).

- Y. Katsumi, R. Gasparac and C. R. Martin, *Journal of the Electrochemical Society*, **151**, E14-E19 (2004).

- H.R. Khan and K. Petrikowski, *Journal of Magnetism and Magnetic Materials*, **249,** 458 (2002).

- H.R. Khan and K. Petrikowski, *Materials Science and Engineering C*, **19,** 345 (2002).

- J. D. Klein, R. D. Herrick, D. Palmer, M. J Sailor, C. J Brumlik and C. R. Martin, *Chemistry of Materials,* **5**, 902 (1993).

- J.R. Ku, R.Vidu, R. Talroze and P. Stroeve, *Journal of American Chemical Society*, **126**, 15022 (2004).

- B.B. Lakshmi, C.J. Patrissi and C.R. Martin, *Chemistry of Materials*, **9,** 2544 (1997).

- S. B. Lee and C. R. Martin, *Journal of American Chemical Society,* **124,** 11850 (2002).

- S. F. Lee, W. P. Pratt, Q. Yang, P. Holody, R. Loloee, P. A. Schroeder and J. Bass, *Journal of Magnetism and Magnetic Materials*, **118,** 1 (1993).

- W. Lee, M. Alexe, K. Nielsch, and U. Gosele, *Chemistry of Materials*, **7**, 3325 (2005).

- W. Lee, R. Scholz, K. Nielsch, and G. Ulrich, *Angewandte Chemie,* **44**, 6050 (2005).

- W. J. Lee and W. H. Smyrl, *Electrochemical and Solid State Letters,* **8**, B7-B9 (2005).

- S.K.J. Lenczowski, C. Schönenberger, M.A.M. Gijs and W.J.M. de Jonge, *Journal of Magnetism and Magnetic Materials,* **148,** 456 (1995).

- K. Liu, K. Nagodawithana, P. Searson and C. Chien, *Physical Review B*, **51,** 7381 (1995).

- C.R. Martin, *Science*, **266,** 5193 (1994).

- C.R. Martin, M. Nixhizawa, K. Jirage and M. Kang, *Journal of Physical Chemistry B*, **105,** 1925 (2001).

- T.R. McGueire and R.I. Potter, *IEEE Transactions on Magnetics,* **11,** 1018 (1975).

- R. L. Millen, T. Kawaguchi, M. C. Granger and M. D. Porter, *Journal of Analytical Chemistry*, **77**, 6581-6587 (2005).

- S.A. Miller, V.Y. Young and C.R. Martin, *Journal of American Chemical Soc*iety, **123,** 12335 (2001).

- N.F. Mott, *Advanced Physics*, **13,** 325 (1964).

- Y. Mu, R. Wang, K. Wu, D. Xu and G. Guo, *Advanced Materials,* **16**, 1550 (2004).

- M. Nishizawa, V. P. Menon and C. R. Martin, *Science*, **268**, 700 (1995).

- K. Ounadjela, R. Ferre, L. Louail, J.M. George, J.L. Maurice, L. Piraux and S. Dubois, *Journal of Applied Physics*, **8,** 5455 (1997).

- P. Parkin, *Annual Review,* **25,** 357 (1995).

- N. Pekas, M. D. Porter, M. Tondra, A. Popple, and A. Jander, *Applied Physics Letters*, **85,** 4785 (2004).

- D.J. Pena, B. Razavi, P.A. Smith, J.K. Mbindyo, M.J. Natan, T.S. Mayer, T.E. Mallouk and C.D. Keating, *Materials Research Society Symposium*, **636,** D4.6.1 (2001).

- L. Piraux, J.M. George, J.F. Despres, C. Leroy, E. Ferain, R. Legras, K. Ounadjela and A. Fert, *Applied Physics Letter*s, **65,** 2484 (1994).

- L. Piraux, S. Dubois and A. Fert, *Journal of Magnetism and Magnetic Materials,* **159,** 287-292 (1996).

- L. Piraux, S. Dubois, J. L. Duvail, K. Ounadjela and A. Fert, *Journal of Magnetism and Magnetic Materials*, **175,** 127 (1997).

- K. R. Pirota, M. Provencio, K. L. Garcia, R. E. Galindo, Z. P. Mendoza, M. H. Velez, and M. Vazquez, *Journal of Magnetism and Magnetic Materials***, 68,** 290 (2005).

- W.P. Pratt, S.F. Lee, G.M. Slaughter, R. Loloee, P.A. Schroeder and J. Bass, *Physics Review Letters*, **66,** 3060 (1991).

- G. R. Pattanaik, D. K. Pandya and S. C. Kashyap, *Thin Solid Films,* **433,** 247–251 (2003).

- L. Péter, Z. Rolik, L. F. Kiss, J. Tóth, V. Weihnacht, C. M. Schneider and I. Bakonyi, *Physical Review B*, **73,** 174410 (2006).

- L. Pu, X. Bao, J. Zou, and D. Feng, <u>*Angewandte Chemie International Edition,*</u> **40,** 1490 (2001).

- D.H. Qin, C.W. Wang, Q.Y. Sun and H.L. Li, *Applied Physics A*, **74,** 761 (2002).

- D. Rafaja, J. Ebert, G. Miehe, N. Martz, M. Knapp, B. Stahl, M. Ghafari, H. Hahn, H. Fuess, P. Schmollngruber, P. Farber and H. Siegle, *Thin Solid Films*, **460**, 256-263 (2004).

- C.A. Ross, *Annual Review of Material Science,* **24,** 159 (1994).

- C.A. Ross, M. Hwang, M. Shima, H.I. Smith, M. Farhoud, T.A Savas, W. Schwarzacher, J. Parrochon, W. Escoffier, H.N. Bertram, F.B. Humphrey and M. Redjdal, *Journal of Magnetism and Magnetic Materials*, **249,** 200 (2002).

- H. Schwanbeck and U. Schmidt, *Electrochimica Acta,* **45,** 4389 (2000).

- W. Schwarzacher and D.S. Lashmore, *IEEE Transactions on Magnetics,* **32,** 3133 (1996).

- W. Schwarzacher, K. Attenborough, A. Michel, G. Nabiyouni and J.P. Meier, *Journal of Magnetism and Magnetic Materials*, **165,** 23 (1997).

- W. Schwarzacher, O.I. Kasyutich, P.R. Evans, M.G. Darbyshire, Ge Yi, V.M. Fedosyuk, F. Rousseaux, E. Cambril and D. Decanini, *Journal of Magnetism and Magnetic Materials*, **198-199,** 185 (1999).

- D.J. Sellmyer, M. Zheng and R. Skomski, *Journal of Physics: Condensed Matter*, **13,** R433-460 (2001).

- Y.C. Sui, R. Skomski, K.D. Sorge and D.J. Sellmyer, *Journal of Applied Physics*, **95,** 7151 (2004).

- T. Thurn-Albrecht, J. Schotter, G.A. Kastle, N. Emley, T.Shibauchi, L. Krusin-Elbaum, K. Guarini, C.T. Black, M.T. Tuominen and T.P. Russell, *Science*, **290,** 2127 (2000).

- M. Tondra, M. D. Porter and R. Lipert, *Journal of Vacuum Science Technology A,* **18,** 4 (2000).

- M. Tondra, A. Popple, A. Jander, R. L. Millen, N. Pekas and M. D. Porter, *Journal of Magnetism and Magnetic Materials,* **293,** 725–730 (2005).

- Y. Ueda, N. Hataya and H. Zaman, *Journal of Magnetism and Magnetic Materials,* **156,** 350 (1996).

- R. Vaidyanathan, J.L. Stickney, S.M. Cox, S.P. Compton and U. Happek**,** *Journal of Electroanalytical Chemistry*, **559,** 55 (2003).

- T. Valet and A. Fert, *Physical Review B*, **48,** 7099 (1993).

- S. Valizadeh, J. George, P. Leisner and L. Hultman, *Electrochimica Acta,* **47,** 865-874 (2001).

- R. Vaidyanathan, J. L. Stickney, S. M. Cox, S. P. Compton and U. Happek, *Journal of. Electroanalytical Chemistry***, 559,** 55 (2003).

- S. Vankrunkelsven, D. Clicq, K. Pappaert, G.V. Baron and G. Desmet, *Analytical Chemistry*, **76,** 3005 (2004).

- L. Vila, J.M. George, G. Faini, A. Popa, U. Ebels, K. Ounadjela and L. Piraux, *IEEE Transactions on Magnetics*, **38,** 2578 (2002).

- C.Z. Wang, G.W. Meng, Q.Q. Fang, X.S. Peng, Y.W. Wang, Q. Fang and L.D. Zhang, *Journal of Physics D: Applied Physics*, **35,** 738 (2002).

- J.B. Wang, Q.F. Liu, D.S Xue, Y. Peng, X.Z Cao and F.S. Li, *Journal of Physics D: Applied Physics*, **34,** 3442 (2001).

- L. Wang, K.Y. Zhang, A. Metrot, P. Bonhomme and M. Troyon, *Thin Solid Films*, **288,** 86 (1996).

- Y.W. Wang, G.Z. Wang, S.X. Wang, T. Gao, H. Sang and L.D. Zhang, *Applied Physics A*, **74,** 577 (2002).

- Y.W. Wang, L.D. Zhang, G.W. Meng, X.S. Peng, Y.X. Jin and J. Zhang, *Journal Physical Chemistry B*, **106,** 2502 (2002).

- K. Yamada, R. Gasparac, C.R. Martin, *Journal of Electrochemical Society*, **151,** E14 (2004).

- W.C. Yoo and J-K. Lee, *Advanced Materials*, **16,** 1097 (2004).

- S. Yu, S. B. Lee, and C. R. Martin, *Analytical Chemistry,* **75**, 1239 (2003).

- H. Zhu, S. Yang, G. Ni, D. Yu and Y. Du, *Scripta Materialia*, **44,** 2291 (2001).

- H. Zhu, S. Yang, G. Ni, D. Yu and Y. Du, *Journal of Magnetism and Magnetic Materials*, **234,** 454 (2001).

- L. Wang, K. Zhang, A. Metrot, P. Bonhomme and M. Troyon, *Thin Solid Films*, **288,** 86 (1996).

- Y. Wang, C. Ye, F. Changhui, Z. Xiaosheng, and L. Zhang, *Chemistry Letters,* **33**, 166-167 (2004).

- M. T. Wu, I. C. Leu, J. H. Yen, and M. H. Hon, *Journal of Physical Chemistry B*, **109**, 9575-9580 (2005).

- Z. L. Xiao, C. Y. Han, U. Welp, H. H. Wang, W. K. Kwok, G. A. Willing, J. M. Hiller, R. E. Cook, D. J. Miller, and G. W. Crabtree, *Nano Letters*, **2**, 1293 (2002).

Steady state Cu currents at different electrolyte temperatures

$$E_{revCuRT} := E_{0Cu} + \frac{R \cdot T_{RT}}{n \cdot Faraday} \cdot \ln\left(Cb_{Cu} \cdot \frac{L}{mol}\right)$$

$$E_{revCuCOLD} := E_{0Cu} + \frac{R \cdot T_{COLD}}{n \cdot Faraday} \cdot \ln\left(Cb_{Cu} \cdot \frac{L}{mol}\right)$$

$$E_{revCuHOT} := E_{0Cu} + \frac{R \cdot T_{HOT}}{n \cdot Faraday} \cdot \ln\left(Cb_{Cu} \cdot \frac{L}{mol}\right)$$

$$E_{revCuRT} = 0.251 \text{ V}$$

$$E_{revCuCOLD} = 0.258 \text{ V}$$

$$E_{revCuHOT} = 0.236 \text{ V}$$

$$k_{oCuRT} := \frac{k_{Cu}}{\exp\left(\dfrac{-\alpha_{Cu} \cdot Faraday \cdot E_{revCuRT}}{R \cdot T_{RT}}\right)}$$

$$k_{oCuCOLD} := \frac{k_{Cu}}{\exp\left(\dfrac{-\alpha_{Cu} \cdot Faraday \cdot E_{revCuRT}}{R \cdot T_{RT}}\right)}$$

$$k_{oCuHOT} := \frac{k_{Cu}}{\exp\left(\dfrac{-\alpha_{Cu} \cdot Faraday \cdot E_{revCuRT}}{R \cdot T_{RT}}\right)}$$

$$i_{CuRT}(\eta) := -k_{oCuRT} \cdot \exp\left(\frac{-\alpha_{Cu} \cdot Faraday \cdot E_{revCuRT}}{R \cdot T_{RT}}\right) \cdot n \cdot Faraday \cdot \frac{\dfrac{(-n \cdot Faraday \cdot D_{CuRT} \cdot Cb_{Cu})}{-\delta}}{k_{oCuRT} \cdot \exp\left(\dfrac{-\alpha_{Cu} \cdot Faraday \cdot E_{revCuRT}}{R \cdot T_{RT}}\right) \cdot n \cdot Faraday \cdot \exp(-b_{CuRT} \cdot E(\eta)) - \dfrac{n \cdot Faraday \cdot D_{CuRT}}{-\delta}} \cdot \exp(-b_{CuRT} \cdot E(\eta))$$

$$i_{CuCOLD}(\eta) := -k_{oCuCOLD} \cdot \exp\left(\frac{-\alpha_{Cu} \cdot Faraday \cdot E_{revCuCOLD}}{R \cdot T_{COLD}}\right) \cdot n \cdot Faraday \cdot \frac{\dfrac{(-n \cdot Faraday \cdot D_{CuCOLD} \cdot Cb_{Cu})}{-\delta}}{k_{oCuCOLD} \cdot \exp\left(\dfrac{-\alpha_{Cu} \cdot Faraday \cdot E_{revCuCOLD}}{R \cdot T_{COLD}}\right) \cdot n \cdot Faraday \cdot \exp(-b_{CuCOLD} \cdot E(\eta)) - \dfrac{n \cdot Faraday \cdot D_{CuCOLD}}{-\delta}} \cdot \exp(-b_{CuCOLD} \cdot E(\eta))$$

$$i_{CuHOT}(\eta) := -k_{oCuHOT} \cdot \exp\left(\frac{-\alpha_{Cu} \cdot Faraday \cdot E_{revCuHOT}}{R \cdot T_{HOT}}\right) \cdot n \cdot Faraday \cdot \frac{\dfrac{(-n \cdot Faraday \cdot D_{CuHOT} \cdot Cb_{Cu})}{-\delta}}{k_{oCuHOT} \cdot \exp\left(\dfrac{-\alpha_{Cu} \cdot Faraday \cdot E_{revCuHOT}}{R \cdot T_{HOT}}\right) \cdot n \cdot Faraday \cdot \exp(-b_{CuHOT} \cdot E(\eta)) - \dfrac{n \cdot Faraday \cdot D_{CuHOT}}{-\delta}} \cdot \exp(-b_{CuHOT} \cdot E(\eta))$$

Figure A1: Steady state modeled Cu partial current at different electrolyte temperatures

Steady state Co currents at different electrolyte temperatures

$$E_{revCoRT} := E_{0Co} + \frac{R \cdot T_{RT}}{n \cdot Faraday} \cdot \ln\left(Cb_{Co} \cdot \frac{L}{mol}\right)$$

$$E_{revCoCOLD} := E_{0Co} + \frac{R \cdot T_{COLD}}{n \cdot Faraday} \cdot \ln\left(Cb_{Co} \cdot \frac{L}{mol}\right)$$

$$E_{revCoHOT} := E_{0Co} + \frac{R \cdot T_{HOT}}{n \cdot Faraday} \cdot \ln\left(Cb_{Co} \cdot \frac{L}{mol}\right)$$

$$E_{revCoRT} = -0.319 \text{ V}$$

$$E_{revCoCOLD} = -0.316 \text{ V}$$

$$E_{revCoHOT} = -0.325 \text{ V}$$

$$k_{oCoRT} := \frac{k_{Co}}{\exp\left(\dfrac{-\alpha_{Co} \cdot Faraday \cdot E_{revCoRT}}{R \cdot T_{RT}}\right)}$$

$$k_{oCoCOLD} := \frac{k_{Co}}{\exp\left(\dfrac{-\alpha_{Co} \cdot Faraday \cdot E_{revCoRT}}{R \cdot T_{RT}}\right)}$$

$$k_{oCoHOT} := \frac{k_{Co}}{\exp\left(\dfrac{-\alpha_{Co} \cdot Faraday \cdot E_{revCoRT}}{R \cdot T_{RT}}\right)}$$

$$i_{CoRT}(\eta) := -k_{oCoRT} \cdot \exp\left(\frac{-\alpha_{Co} \cdot Faraday \cdot E_{revCoRT}}{R \cdot T_{RT}}\right) \cdot n \cdot Faraday \cdot \frac{\frac{(-n \cdot Faraday \cdot D_{CoRT} \cdot Cb_{Co})}{-\delta}}{k_{oCoRT} \cdot \exp\left(\frac{-\alpha_{Co} \cdot Faraday \cdot E_{revCoRT}}{R \cdot T_{RT}}\right) \cdot n \cdot Faraday \cdot \exp(-b_{CoRT} \cdot E(\eta)) - \frac{n \cdot Faraday \cdot D_{CoRT}}{-\delta}} \cdot \exp(-b_{CoRT} \cdot E(\eta))$$

$$i_{CoCOLD}(\eta) := -k_{oCoCOLD} \cdot \exp\left(\frac{-\alpha_{Co} \cdot Faraday \cdot E_{revCoCOLD}}{R \cdot T_{COLD}}\right) \cdot n \cdot Faraday \cdot \frac{\frac{(-n \cdot Faraday \cdot D_{CoCOLD} \cdot Cb_{Co})}{-\delta}}{k_{oCoCOLD} \cdot \exp\left(\frac{-\alpha_{Co} \cdot Faraday \cdot E_{revCoCOLD}}{R \cdot T_{COLD}}\right) \cdot n \cdot Faraday \cdot \exp(-b_{CoCOLD} \cdot E(\eta)) - \frac{n \cdot Faraday \cdot D_{CoCOLD}}{-\delta}} \cdot \exp(-b_{CoCOLD} \cdot E(\eta))$$

$$i_{CoHOT}(\eta) := -k_{oCoHOT} \cdot \exp\left(\frac{-\alpha_{Co} \cdot Faraday \cdot E_{revCoHOT}}{R \cdot T_{HOT}}\right) \cdot n \cdot Faraday \cdot \frac{\frac{(-n \cdot Faraday \cdot D_{CoHOT} \cdot Cb_{Co})}{-\delta}}{k_{oCoHOT} \cdot \exp\left(\frac{-\alpha_{Co} \cdot Faraday \cdot E_{revCoHOT}}{R \cdot T_{HOT}}\right) \cdot n \cdot Faraday \cdot \exp(-b_{CoHOT} \cdot E(\eta)) - \frac{n \cdot Faraday \cdot D_{CoHOT}}{-\delta}} \cdot \exp(-b_{CoHOT} \cdot E(\eta))$$
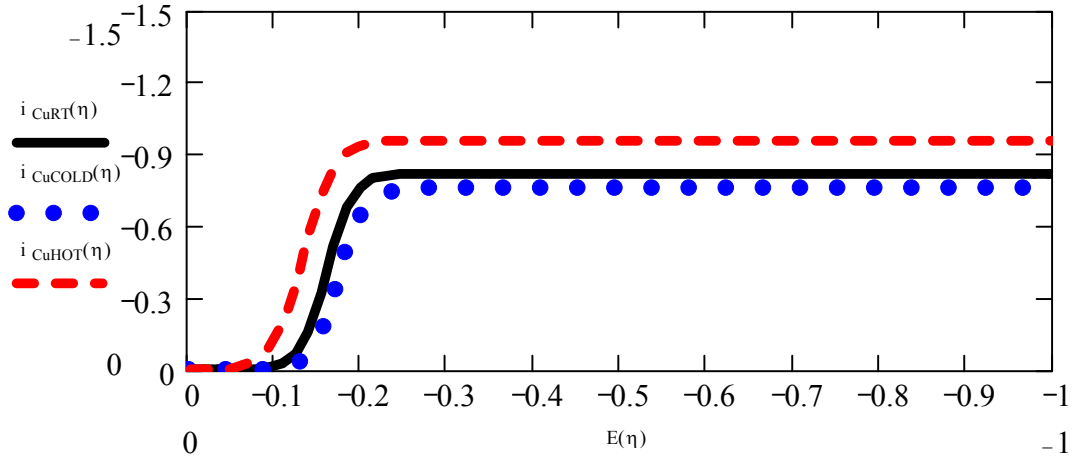

Figure A2: Steady state modeled Co partial current at different electrolyte temperatures

Steady state Fe currents at different electrolyte temperatures

$$E_{revFeRT} := E_{0Fe} + \frac{R \cdot T_{RT}}{n \cdot Faraday} \cdot \ln\left(Cb_{Fe} \cdot \frac{L}{mol}\right) \qquad E_{revFeCOLD} := E_{0Fe} + \frac{R \cdot T_{COLD}}{n \cdot Faraday} \cdot \ln\left(Cb_{Fe} \cdot \frac{L}{mol}\right) \qquad E_{revFeHOT} := E_{0Fe} + \frac{R \cdot T_{HOT}}{n \cdot Faraday} \cdot \ln\left(Cb_{Fe} \cdot \frac{L}{mol}\right)$$

$$E_{revFeRT} = -0.536\,V \qquad E_{revFeCOLD} = -0.529\,V \qquad E_{revFeHOT} = -0.551\,V$$

$$k_{oFeRT} := \frac{k_{Fe}}{\exp\left(\frac{-\alpha_{Fe} \cdot Faraday \cdot E_{revFeRT}}{R \cdot T_{RT}}\right)} \qquad k_{oFeCOLD} := \frac{k_{Fe}}{\exp\left(\frac{-\alpha_{Fe} \cdot Faraday \cdot E_{revFeRT}}{R \cdot T_{RT}}\right)} \qquad k_{oFeHOT} := \frac{k_{Fe}}{\exp\left(\frac{-\alpha_{Fe} \cdot Faraday \cdot E_{revFeRT}}{R \cdot T_{RT}}\right)}$$

$$i_{FeRT}(\eta) := -k_{oFeRT} \cdot \exp\left(\frac{-\alpha_{Fe} \cdot Faraday \cdot E_{revFeRT}}{R \cdot T_{RT}}\right) \cdot n \cdot Faraday \cdot \frac{\frac{(-n \cdot Faraday \cdot D_{FeRT} \cdot Cb_{Fe})}{-\delta}}{k_{oFeRT} \cdot \exp\left(\frac{-\alpha_{Fe} \cdot Faraday \cdot E_{revFeRT}}{R \cdot T_{RT}}\right) \cdot n \cdot Faraday \cdot \exp(-b_{FeRT} \cdot E(\eta)) - \frac{n \cdot Faraday \cdot D_{FeRT}}{-\delta}} \cdot \exp(-b_{FeRT} \cdot E(\eta))$$

$$i_{FeCOLD}(\eta) := -k_{oFeCOLD} \cdot \exp\left(\frac{-\alpha_{Fe} \cdot Faraday \cdot E_{revFeCOLD}}{R \cdot T_{COLD}}\right) \cdot n \cdot Faraday \cdot \frac{\frac{(-n \cdot Faraday \cdot D_{FeCOLD} \cdot Cb_{Fe})}{-\delta}}{k_{oFeCOLD} \cdot \exp\left(\frac{-\alpha_{Fe} \cdot Faraday \cdot E_{revFeCOLD}}{R \cdot T_{COLD}}\right) \cdot n \cdot Faraday \cdot \exp(-b_{FeCOLD} \cdot E(\eta)) - \frac{n \cdot Faraday \cdot D_{FeCOLD}}{-\delta}} \cdot \exp(-b_{FeCOLD} \cdot E(\eta))$$

$$i_{FeHOT}(\eta) := -k_{oFeHOT} \cdot \exp\left(\frac{-\alpha_{Fe} \cdot Faraday \cdot E_{revFeHOT}}{R \cdot T_{HOT}}\right) \cdot n \cdot Faraday \cdot \frac{\frac{(-n \cdot Faraday \cdot D_{FeHOT} \cdot Cb_{Fe})}{-\delta}}{k_{oFeHOT} \cdot \exp\left(\frac{-\alpha_{Fe} \cdot Faraday \cdot E_{revFeHOT}}{R \cdot T_{HOT}}\right) \cdot n \cdot Faraday \cdot \exp(-b_{FeHOT} \cdot E(\eta)) - \frac{n \cdot Faraday \cdot D_{FeHOT}}{-\delta}} \cdot \exp(-b_{FeHOT} \cdot E(\eta))$$
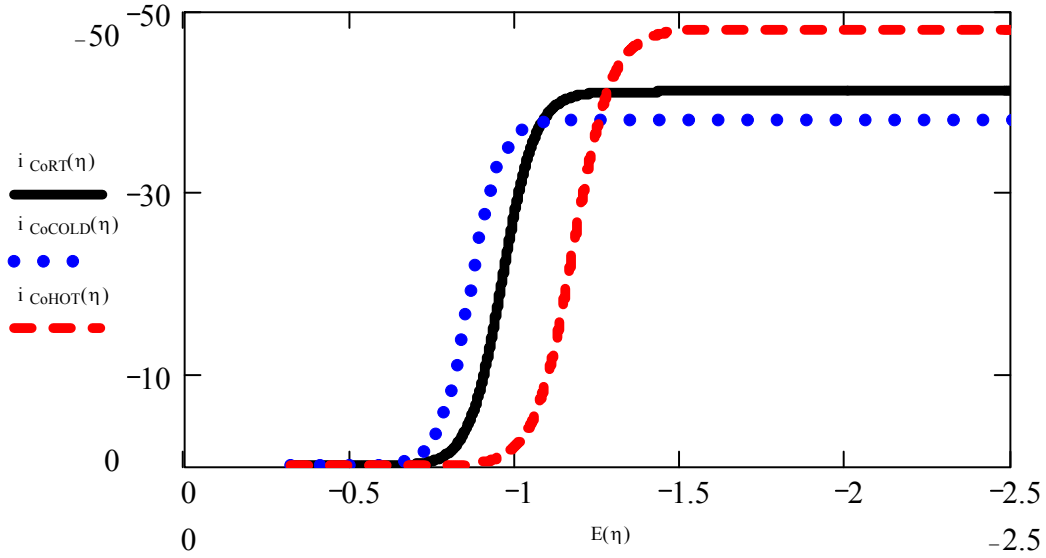
Figure A3: Steady state modeled Fe partial current at different electrolyte temperatures

Steady state Ni currents at different electrolyte temperatures

$$E_{revNiRT} := E_{0Ni} + \frac{R \cdot T_{RT}}{n \cdot Faraday} \cdot \ln\left(Cb_{Ni} \cdot \frac{L}{mol}\right)$$

$$E_{revNiCOLD} := E_{0Ni} + \frac{R \cdot T_{COLD}}{n \cdot Faraday} \cdot \ln\left(Cb_{Ni} \cdot \frac{L}{mol}\right)$$

$$E_{revNiHOT} := E_{0Ni} + \frac{R \cdot T_{HOT}}{n \cdot Faraday} \cdot \ln\left(Cb_{Ni} \cdot \frac{L}{mol}\right)$$

$$E_{revNiRT} = -0.309\,V$$

$$E_{revNiCOLD} = -0.305\,V$$

$$E_{revNiHOT} = -0.318\,V$$

$$k_{oNiRT} := \frac{k_{Ni}}{\exp\left(\dfrac{-\alpha_{Ni} \cdot Faraday \cdot E_{revNiRT}}{R \cdot T_{RT}}\right)}$$

$$k_{oNiCOLD} := \frac{k_{Ni}}{\exp\left(\dfrac{-\alpha_{Ni} \cdot Faraday \cdot E_{revNiRT}}{R \cdot T_{RT}}\right)}$$

$$k_{oNiHOT} := \frac{k_{Ni}}{\exp\left(\dfrac{-\alpha_{Ni} \cdot Faraday \cdot E_{revNiRT}}{R \cdot T_{RT}}\right)}$$

$$i_{NiRT}(\eta) := -k_{oNiRT} \cdot \exp\left(\frac{-\alpha_{Ni} \cdot Faraday \cdot E_{revNiRT}}{R \cdot T_{RT}}\right) \cdot n \cdot Faraday \cdot \frac{\frac{\left(-n \cdot Faraday \cdot D_{NiRT} \cdot Cb_{Ni}\right)}{-\delta}}{k_{oNiRT} \cdot \exp\left(\frac{-\alpha_{Ni} \cdot Faraday \cdot E_{revNiRT}}{R \cdot T_{RT}}\right) \cdot n \cdot Faraday \cdot \exp\left(-b_{NiRT} \cdot E(\eta)\right) - \frac{n \cdot Faraday \cdot D_{NiRT}}{-\delta}} \cdot \exp\left(-b_{NiRT} \cdot E(\eta)\right)$$

$$i_{NiCOLD}(\eta) := -k_{oNiCOLD} \cdot \exp\left(\frac{-\alpha_{Ni} \cdot Faraday \cdot E_{revNiCOLD}}{R \cdot T_{COLD}}\right) \cdot n \cdot Faraday \cdot \frac{\frac{\left(-n \cdot Faraday \cdot D_{NiCOLD} \cdot Cb_{Ni}\right)}{-\delta}}{k_{oNiCOLD} \cdot \exp\left(\frac{-\alpha_{Ni} \cdot Faraday \cdot E_{revNiCOLD}}{R \cdot T_{COLD}}\right) \cdot n \cdot Faraday \cdot \exp\left(-b_{NiCOLD} \cdot E(\eta)\right) - \frac{n \cdot Faraday \cdot D_{NiCOLD}}{-\delta}} \cdot \exp\left(-b_{NiCOLD} \cdot E(\eta)\right)$$

$$i_{NiHOT}(\eta) := -k_{oNiHOT} \cdot \exp\left(\frac{-\alpha_{Ni} \cdot Faraday \cdot E_{revNiHOT}}{R \cdot T_{HOT}}\right) \cdot n \cdot Faraday \cdot \frac{\frac{\left(-n \cdot Faraday \cdot D_{NiHOT} \cdot Cb_{Ni}\right)}{-\delta}}{k_{oNiHOT} \cdot \exp\left(\frac{-\alpha_{Ni} \cdot Faraday \cdot E_{revNiHOT}}{R \cdot T_{HOT}}\right) \cdot n \cdot Faraday \cdot \exp\left(-b_{NiHOT} \cdot E(\eta)\right) - \frac{n \cdot Faraday \cdot D_{NiHOT}}{-\delta}} \cdot \exp\left(-b_{NiHOT} \cdot E(\eta)\right)$$
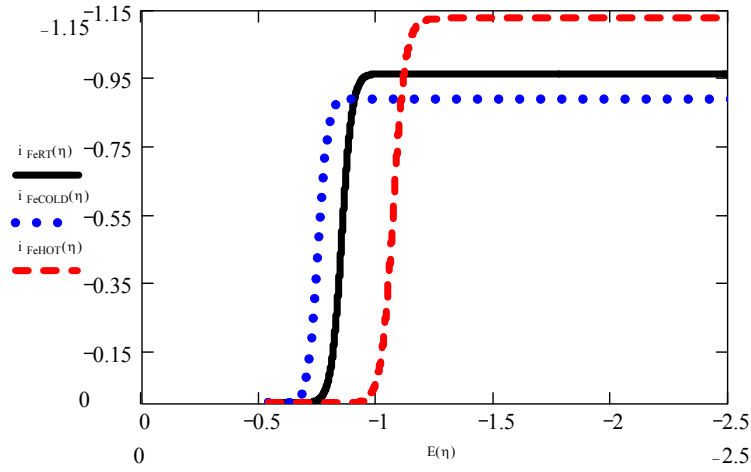

Figure A4: Steady state modeled Ni partial current at different electrolyte temperatures

Steady state H₂ currents at different electrolyte temperatures

$$E_{revHRT} := E_{0H} + \frac{R \cdot T_{RT}}{n \cdot Faraday} \cdot \ln\left(Cb_H \cdot \frac{L}{mol}\right)$$

$$E_{revHCOLD} := E_{0H} + \frac{R \cdot T_{COLD}}{n \cdot Faraday} \cdot \ln\left(Cb_H \cdot \frac{L}{mol}\right)$$

$$E_{revHHOT} := E_{0H} + \frac{R \cdot T_{HOT}}{n \cdot Faraday} \cdot \ln\left(Cb_H \cdot \frac{L}{mol}\right)$$

$$E_{revHRT} = -0.119\,V$$

$$E_{revHCOLD} = -0.11\,V$$

$$E_{revHHOT} = -0.139\,V$$

$$k_{oHRT} := \frac{k_H}{\exp\left(\dfrac{-\alpha_H \cdot Faraday \cdot E_{revHRT}}{R \cdot T_{RT}}\right)}$$

$$k_{oHCOLD} := \frac{k_H}{\exp\left(\dfrac{-\alpha_H \cdot Faraday \cdot E_{revHRT}}{R \cdot T_{RT}}\right)}$$

$$k_{oHHOT} := \frac{k_H}{\exp\left(\dfrac{-\alpha_H \cdot Faraday \cdot E_{revHRT}}{R \cdot T_{RT}}\right)}$$

$$i_{HRT}(\eta) := -k_{oHRT} \cdot \exp\left(\frac{-\alpha_H \cdot Faraday \cdot E_{revHRT}}{R \cdot T_{RT}}\right) \cdot n \cdot Faraday \cdot \frac{\dfrac{(-n \cdot Faraday \cdot D_{HRT} \cdot Cb_H)}{-\delta}}{k_{oHRT} \cdot \exp\left(\dfrac{-\alpha_H \cdot Faraday \cdot E_{revHRT}}{R \cdot T_{RT}}\right) \cdot n \cdot Faraday \cdot \exp(-b_{HRT} \cdot E(\eta)) - \dfrac{n \cdot Faraday \cdot D_{HRT}}{-\delta}} \cdot \exp(-b_{HRT} \cdot E(\eta))$$

$$i_{HCOLD}(\eta) := -k_{oHCOLD} \cdot \exp\left(\frac{-\alpha_H \cdot Faraday \cdot E_{revHCOLD}}{R \cdot T_{COLD}}\right) \cdot n \cdot Faraday \cdot \frac{\dfrac{(-n \cdot Faraday \cdot D_{HCOLD} \cdot Cb_H)}{-\delta}}{k_{oHCOLD} \cdot \exp\left(\dfrac{-\alpha_H \cdot Faraday \cdot E_{revHCOLD}}{R \cdot T_{COLD}}\right) \cdot n \cdot Faraday \cdot \exp(-b_{HCOLD} \cdot E(\eta)) - \dfrac{n \cdot Faraday \cdot D_{HCOLD}}{-\delta}} \cdot \exp(-b_{HCOLD} \cdot E(\eta))$$

$$i_{HHOT}(\eta) := -k_{oHHOT} \cdot \exp\left(\frac{-\alpha_H \cdot Faraday \cdot E_{revHHOT}}{R \cdot T_{HOT}}\right) \cdot n \cdot Faraday \cdot \frac{\dfrac{(-n \cdot Faraday \cdot D_{HHOT} \cdot Cb_H)}{-\delta}}{k_{oHHOT} \cdot \exp\left(\dfrac{-\alpha_H \cdot Faraday \cdot E_{revHHOT}}{R \cdot T_{HOT}}\right) \cdot n \cdot Faraday \cdot \exp(-b_{HHOT} \cdot E(\eta)) - \dfrac{n \cdot Faraday \cdot D_{HHOT}}{-\delta}} \cdot \exp(-b_{HHOT} \cdot E(\eta))$$
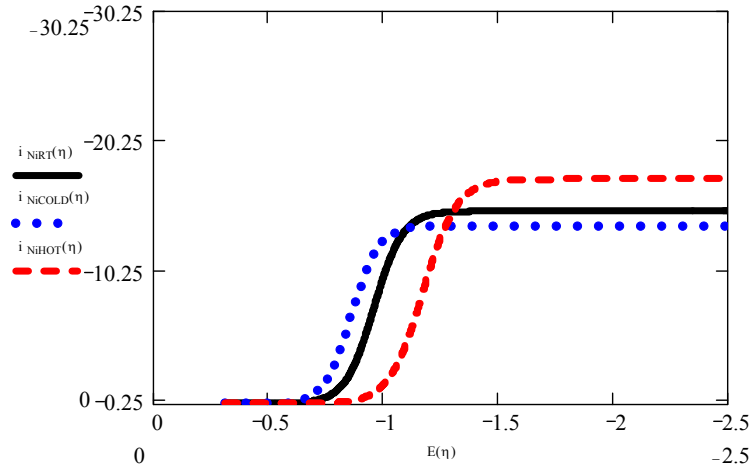

Figure A5: Steady state modeled H₂ partial current at different electrolyte temperatures

Steady state H₂O currents at different electrolyte temperatures

$$E_{revHOHRT} := E_{0HOH} + \frac{R \cdot T_{RT}}{n \cdot Faraday} \cdot \ln\left(Cb_{HOH} \cdot \frac{L}{mol}\right)$$

$$E_{revHOHCOLD} := E_{0HOH} + \frac{R \cdot T_{COLD}}{n \cdot Faraday} \cdot \ln\left(Cb_{HOH} \cdot \frac{L}{mol}\right)$$

$$E_{revHOHHOT} := E_{0HOH} + \frac{R \cdot T_{HOT}}{n \cdot Faraday} \cdot \ln\left(Cb_{HOH} \cdot \frac{L}{mol}\right)$$

$$E_{revHOHRT} = -0.83\,V$$

$$E_{revHOHCOLD} = -0.83\,V$$

$$E_{revHOHHOT} = -0.83\,V$$

$$k_{oHOHRT} := \frac{k_{HOH}}{\exp\left(\dfrac{-\alpha_{HOH} \cdot Faraday \cdot E_{revHOHRT}}{R \cdot T_{RT}}\right)}$$

$$k_{oHOHCOLD} := \frac{k_{HOH}}{\exp\left(\dfrac{-\alpha_{HOH} \cdot Faraday \cdot E_{revHOHRT}}{R \cdot T_{RT}}\right)}$$

$$k_{oHOHHOT} := \frac{k_{HOH}}{\exp\left(\dfrac{-\alpha_{HOH} \cdot Faraday \cdot E_{revHOHRT}}{R \cdot T_{RT}}\right)}$$

$$i_{HOHRT}(\eta) := -k_{oHOHRT} \cdot \exp\left(\frac{-\alpha_{HOH} \cdot Faraday \cdot E_{revHOHRT}}{R \cdot T_{RT}}\right) \cdot n \cdot Faraday \cdot \frac{\dfrac{(-n \cdot Faraday \cdot D_{HOHRT} \cdot Cb_{HOH})}{-\delta}}{k_{oHOHRT} \cdot \exp\left(\dfrac{-\alpha_{HOH} \cdot Faraday \cdot E_{revHOHRT}}{R \cdot T_{RT}}\right) \cdot n \cdot Faraday \cdot \exp(-b_{HOHRT} \cdot E(\eta)) - \dfrac{n \cdot Faraday \cdot D_{HOHRT}}{-\delta}} \cdot \exp(-b_{HOHRT} \cdot E(\eta))$$

$$i_{HOHCOLD}(\eta) := -k_{oHOHCOLD} \cdot \exp\left(\frac{-\alpha_{HOH} \cdot Faraday \cdot E_{revHOHCOLD}}{R \cdot T_{COLD}}\right) \cdot n \cdot Faraday \cdot \frac{\dfrac{(-n \cdot Faraday \cdot D_{HOHCOLD} \cdot Cb_{HOH})}{-\delta}}{k_{oHOHCOLD} \cdot \exp\left(\dfrac{-\alpha_{HOH} \cdot Faraday \cdot E_{revHOHCOLD}}{R \cdot T_{COLD}}\right) \cdot n \cdot Faraday \cdot \exp(-b_{HOHCOLD} \cdot E(\eta)) - \dfrac{n \cdot Faraday \cdot D_{HOHCOLD}}{-\delta}} \cdot \exp(-b_{HOHCOLD} \cdot E(\eta))$$

$$i_{HOHHOT}(\eta) := -k_{oHOHHOT} \cdot \exp\left(\frac{-\alpha_{HOH} \cdot Faraday \cdot E_{revHOHHOT}}{R \cdot T_{HOT}}\right) \cdot n \cdot Faraday \cdot \frac{\dfrac{(-n \cdot Faraday \cdot D_{HOHHOT} \cdot Cb_{HOH})}{-\delta}}{k_{oHOHHOT} \cdot \exp\left(\dfrac{-\alpha_{HOH} \cdot Faraday \cdot E_{revHOHHOT}}{R \cdot T_{HOT}}\right) \cdot n \cdot Faraday \cdot \exp(-b_{HOHHOT} \cdot E(\eta)) - \dfrac{n \cdot Faraday \cdot D_{HOHHOT}}{-\delta}} \cdot \exp(-b_{HOHHOT} \cdot E(\eta))$$

Steady state O₂ currents at different electrolyte temperatures

$$E_{revORT} := E_{0O} + \frac{R \cdot T_{RT}}{n \cdot Faraday} \cdot \ln\left(Cb_{ORT} \cdot Cb_{proton} \cdot \frac{4}{mol^5} \cdot \frac{L^5}{5}\right)$$

$$E_{revOHOT} := E_{0O} + \frac{R \cdot T_{HOT}}{n \cdot Faraday} \cdot \ln\left(Cb_{OHot} \cdot Cb_{proton} \cdot \frac{4}{mol^5} \cdot \frac{L^5}{5}\right)$$

$$E_{revOCOLD} := E_{0O} + \frac{R \cdot T_{COLD}}{n \cdot Faraday} \cdot \ln\left(Cb_{OCold} \cdot Cb_{proton} \cdot \frac{4}{mol^5} \cdot \frac{L^5}{5}\right)$$

$$E_{revORT} = 0.647\,V \qquad E_{revOHOT} = 0.543\,V \qquad E_{revOCOLD} = 0.696\,V$$

$$k_{oORT} := \frac{k_O}{\exp\left(\frac{-\alpha_O \cdot Faraday \cdot E_{revORT}}{R \cdot T_{RT}}\right)}$$

$$k_{oOCOLD} := \frac{k_O}{\exp\left(\frac{-\alpha_O \cdot Faraday \cdot E_{revORT}}{R \cdot T_{RT}}\right)}$$

$$k_{oOHOT} := \frac{k_O}{\exp\left(\frac{-\alpha_O \cdot Faraday \cdot E_{revORT}}{R \cdot T_{RT}}\right)}$$

$$i_{ORT}(\eta) := -k_{oORT} \cdot \exp\left(\frac{-\alpha_O \cdot Faraday \cdot E_{revORT}}{R \cdot T_{RT}}\right) \cdot n \cdot Faraday \cdot \frac{\frac{(-n \cdot Faraday \cdot D_{ORT} \cdot Cb_{ORT})}{-\delta}}{k_{oORT} \cdot \exp\left(\frac{-\alpha_O \cdot Faraday \cdot E_{revORT}}{R \cdot T_{RT}}\right) \cdot n \cdot Faraday \cdot \exp(-b_{ORT} \cdot E(\eta)) - \frac{n \cdot Faraday \cdot D_{ORT}}{-\delta}} \cdot \exp(-b_{ORT} \cdot E(\eta))$$

$$i_{OCOLD}(\eta) := -k_{oOCOLD} \cdot \exp\left(\frac{-\alpha_O \cdot Faraday \cdot E_{revOCOLD}}{R \cdot T_{COLD}}\right) \cdot n \cdot Faraday \cdot \frac{\frac{(-n \cdot Faraday \cdot D_{OCOLD} \cdot Cb_{OCold})}{-\delta}}{k_{oOCOLD} \cdot \exp\left(\frac{-\alpha_O \cdot Faraday \cdot E_{revOCOLD}}{R \cdot T_{COLD}}\right) \cdot n \cdot Faraday \cdot \exp(-b_{OCOLD} \cdot E(\eta)) - \frac{n \cdot Faraday \cdot D_{OCOLD}}{-\delta}} \cdot \exp(-b_{OCOLD} \cdot E(\eta))$$

$$i_{OHOT}(\eta) := -k_{oOHOT} \cdot \exp\left(\frac{-\alpha_O \cdot Faraday \cdot E_{revOHOT}}{R \cdot T_{HOT}}\right) \cdot n \cdot Faraday \cdot \frac{\frac{(-n \cdot Faraday \cdot D_{OHOT} \cdot Cb_{OHot})}{-\delta}}{k_{oOHOT} \cdot \exp\left(\frac{-\alpha_O \cdot Faraday \cdot E_{revOHOT}}{R \cdot T_{HOT}}\right) \cdot n \cdot Faraday \cdot \exp(-b_{OHOT} \cdot E(\eta)) - \frac{n \cdot Faraday \cdot D_{OHOT}}{-\delta}} \cdot \exp(-b_{OHOT} \cdot E(\eta))$$
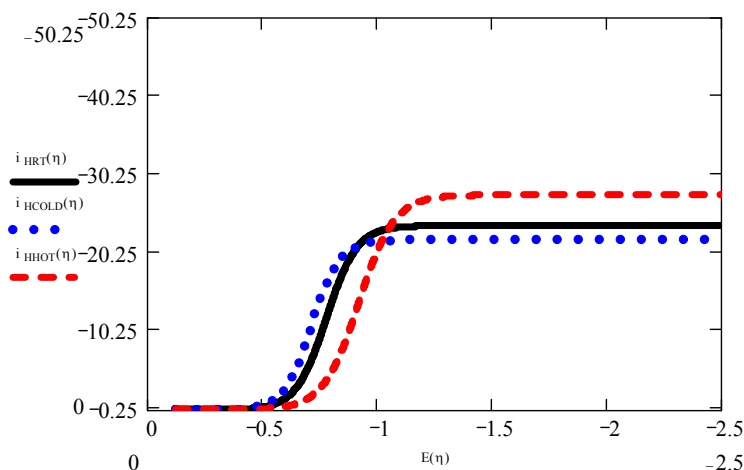

Figure A6: Steady state modeled O₂ partial current at different electrolyte temperatures

Non steady state Cu currents at different electrolyte temperatures

$$Cs_{CuRT}(t,\eta) := \left[\left[100000 \cdot (D_{CuRT})\right]^{\left(\frac{1}{2}\right)} \cdot Cb_{Cu}\right] \cdot \frac{(0.00025t)^{-0.5} \cdot \exp(0.75t)^{0.1}}{\left[100000 \cdot (D_{CuRT})\right]^{\left(\frac{1}{2}\right)} \cdot t^{0.25} + 56419 \cdot Cb_{Cu} \cdot k_{oCuRT} \cdot \exp\left(\frac{-\alpha_{Cu} \cdot Faraday \cdot E_{revCuRT}}{R \cdot T_{RT}}\right) \cdot \exp(-1 \cdot b_{CuRT} \cdot \eta(t)) \cdot t^{0.25} - 56419 Cb_{Cu} \cdot \left(k_{oCuRT} \cdot \exp\left(\frac{-\alpha_{Cu} \cdot Faraday \cdot E_{revCuRT}}{R \cdot T_{RT}}\right)\right) \cdot \exp(-1 \cdot b_{CuRT} \cdot \eta(t)) \cdot \exp\left(\frac{-0.15}{0.5 \cdot D_{CuRT}} \cdot \frac{\delta^3}{t^{-3}}\right)}$$

$$i_{CuRT}(t,\eta) := -k_{oCuRT} \cdot \exp\left(\frac{-\alpha_{Cu} \cdot Faraday \cdot E_{revCuRT}}{R \cdot T_{RT}}\right) \cdot n \cdot Faraday \cdot Cs_{CuRT}(t,\eta) \cdot \exp(-b_{CuRT} \cdot \eta(t))$$

$$Cs_{CuHOT}(t,\eta) := \left[\left[100000 \cdot (D_{CuHOT})\right]^{\left(\frac{1}{2}\right)} \cdot Cb_{Cu}\right] \cdot \frac{(0.00025t)^{-0.5} \cdot \exp(0.75t)^{0.1}}{\left[100000 \cdot (D_{CuHOT})\right]^{\left(\frac{1}{2}\right)} \cdot t^{0.25} + 56419 \cdot Cb_{Cu} \cdot \left(k_{oCuRT} \cdot \exp\left(\frac{-\alpha_{Cu} \cdot Faraday \cdot E_{revCuRT}}{R \cdot T_{HOT}}\right)\right) \cdot \exp(-1 \cdot b_{CuHOT} \cdot \eta(t)) \cdot t^{0.25} - 56419 Cb_{Cu} \cdot \left(k_{oCuRT} \cdot \exp\left(\frac{-\alpha_{Cu} \cdot Faraday \cdot E_{revCuRT}}{R \cdot T_{HOT}}\right)\right) \cdot \exp(-1 \cdot b_{CuHOT} \cdot \eta(t)) \cdot \exp\left(\frac{-0.15}{0.5 \cdot D_{CuHOT}} \cdot \frac{\delta^3}{t^{-3}}\right)}$$

$$i_{CuHOT}(t,\eta) := -k_{oCuHOT} \cdot \exp\left(\frac{-\alpha_{Cu} \cdot Faraday \cdot E_{revCuRT}}{R \cdot T_{HOT}}\right) \cdot n \cdot Faraday \cdot Cs_{CuHOT}(t,\eta) \cdot \exp(-b_{CuHOT} \cdot \eta(t))$$

$$Cs_{CuCOLD}(t,\eta) := \left[100000(D_{CuCOLD})\right]^{\left(\frac{1}{2}\right)} \cdot Cb_{Cu}\right] \cdot \frac{(0.00025t)^{-0.5} \cdot \exp(0.75t)^{0.1}}{\left[1000000(D_{CuCOLD})\right]^{\left(\frac{1}{2}\right)} \cdot t^{0.25} + 56419 \cdot Cb_{Cu} \cdot \left(k_{oCuRT} \cdot \exp\left(\frac{-\alpha_{Cu} \cdot Faraday \cdot E_{revCuRT}}{R \cdot T_{COLD}}\right)\right) \cdot \exp(-1 \cdot b_{CuCOLD} \cdot \eta(t)) \cdot t^{0.25} - 56419 Cb_{Cu} \cdot \left(k_{oCuRT} \cdot \exp\left(\frac{-\alpha_{Cu} \cdot Faraday \cdot E_{revCuRT}}{R \cdot T_{COLD}}\right)\right) \cdot \exp(-1 \cdot b_{CuCOLD} \cdot \eta(t)) \cdot \exp\left(\frac{-0.15}{0.5 \cdot D_{CuCOLD}} \cdot \frac{\delta^3}{t^{-3}}\right)}$$

$$i_{CuCOLD}(t,\eta) := -k_{oCuRT} \cdot \exp\left(\frac{-\alpha_{Cu} \cdot Faraday \cdot E_{revCuRT}}{R \cdot T_{COLD}}\right) \cdot n \cdot Faraday \cdot Cs_{CuCOLD}(t,\eta) \cdot \exp(-b_{CuCOLD} \cdot \eta(t))$$

Figure A7: Non-steady state modeled Cu partial current at different electrolyte temperatures

Non steady state Co currents at different electrolyte temperatures

$$Cs_{CoRT}(t,\eta) := \left[\left[100000 \cdot (D_{CoRT})\right]^{\left(\frac{1}{2}\right)} \cdot Cb_{Co}\right] \cdot \frac{(0.00025t)^{-0.5} \cdot \exp(0.75t)^{0.1}}{\left[100000 \cdot (D_{CoRT})\right]^{\left(\frac{1}{2}\right)} \cdot t^{0.25} + 56419 \cdot Cb_{Co} \cdot k_{oCoRT} \cdot \exp\left(\frac{-\alpha_{Co} \cdot Faraday \cdot E_{revCoRT}}{R \cdot T_{RT}}\right) \cdot \exp(-1 \cdot b_{CoRT} \cdot \eta(t)) \cdot t^{0.25} - 56419Cb_{Co} \cdot \left(k_{oCoRT} \cdot \exp\left(\frac{-\alpha_{Co} \cdot Faraday \cdot E_{revCoRT}}{R \cdot T_{RT}}\right)\right) \cdot \exp(-1 \cdot b_{CoRT} \cdot \eta(t)) \cdot \exp\left(\frac{-0.15}{0.5 \cdot D_{CoRT}} \cdot \frac{\delta^3}{t^{-3}}\right)}$$

$$i_{CoRT}(t,\eta) := -k_{oCoRT} \cdot \exp\left(\frac{-\alpha_{Co} \cdot Faraday \cdot E_{revCoRT}}{R \cdot T_{RT}}\right) \cdot n \cdot Faraday \cdot Cs_{CoRT}(t,\eta) \cdot \exp(-b_{CoRT} \cdot \eta(t))$$

$$Cs_{CoHOT}(t,\eta) := \left[\left[100000 \cdot (D_{CoHOT})\right]^{\left(\frac{1}{2}\right)} \cdot Cb_{Co}\right] \cdot \frac{(0.00025t)^{-0.5} \cdot \exp(0.75t)^{0.1}}{\left[100000 \cdot (D_{CoHOT})\right]^{\left(\frac{1}{2}\right)} \cdot t^{0.25} + 56419 \cdot Cb_{Co} \cdot k_{oCoRT} \cdot \exp\left(\frac{-\alpha_{Co} \cdot Faraday \cdot E_{revCoRT}}{R \cdot T_{HOT}}\right) \cdot \exp(-1 \cdot b_{CoHOT} \cdot \eta(t)) \cdot t^{0.25} - 56419Cb_{Co} \cdot \left(k_{oCoRT} \cdot \exp\left(\frac{-\alpha_{Co} \cdot Faraday \cdot E_{revCoRT}}{R \cdot T_{HOT}}\right)\right) \cdot \exp(-1 \cdot b_{CoHOT} \cdot \eta(t)) \cdot \exp\left(\frac{-0.15}{0.5 \cdot D_{CoHOT}} \cdot \frac{\delta^3}{t^{-3}}\right)}$$

$$i_{CoHOT}(t,\eta) := -k_{oCoRT} \cdot \exp\left(\frac{-\alpha_{Co} \cdot Faraday \cdot E_{revCoRT}}{R \cdot T_{HOT}}\right) \cdot n \cdot Faraday \cdot Cs_{CoHOT}(t,\eta) \cdot \exp(-b_{CoHOT} \cdot \eta(t))$$

$$Cs_{CoCOLD}(t,\eta) := \left[\left[100000 \cdot (D_{CoCOLD})\right]^{\left(\frac{1}{2}\right)} \cdot Cb_{Co}\right] \cdot \frac{(0.00025t)^{-0.5} \cdot \exp(0.75t)^{0.1}}{\left[100000 \cdot (D_{CoCOLD})\right]^{\left(\frac{1}{2}\right)} \cdot t^{0.25} + 56419 \cdot Cb_{Co} \cdot k_{oCoRT} \cdot \exp\left(\frac{-\alpha_{Co} \cdot Faraday \cdot E_{revCoRT}}{R \cdot T_{COLD}}\right) \cdot \exp(-1 \cdot b_{CoCOLD} \cdot \eta(t)) \cdot t^{0.25} - 56419Cb_{Co} \cdot \left(k_{oCoRT} \cdot \exp\left(\frac{-\alpha_{Co} \cdot Faraday \cdot E_{revCoRT}}{R \cdot T_{COLD}}\right)\right) \cdot \exp(-1 \cdot b_{CoCOLD} \cdot \eta(t)) \cdot \exp\left(\frac{-0.15}{0.5 \cdot D_{CoCOLD}} \cdot \frac{\delta^3}{t^{-3}}\right)}$$

$$i_{CoCOLD}(t,\eta) := -k_{oCoRT} \cdot \exp\left(\frac{-\alpha_{Co} \cdot Faraday \cdot E_{revCoRT}}{R \cdot T_{COLD}}\right) \cdot n \cdot Faraday \cdot Cs_{CoCOLD}(t,\eta) \cdot \exp(-b_{CoCOLD} \cdot \eta(t))$$
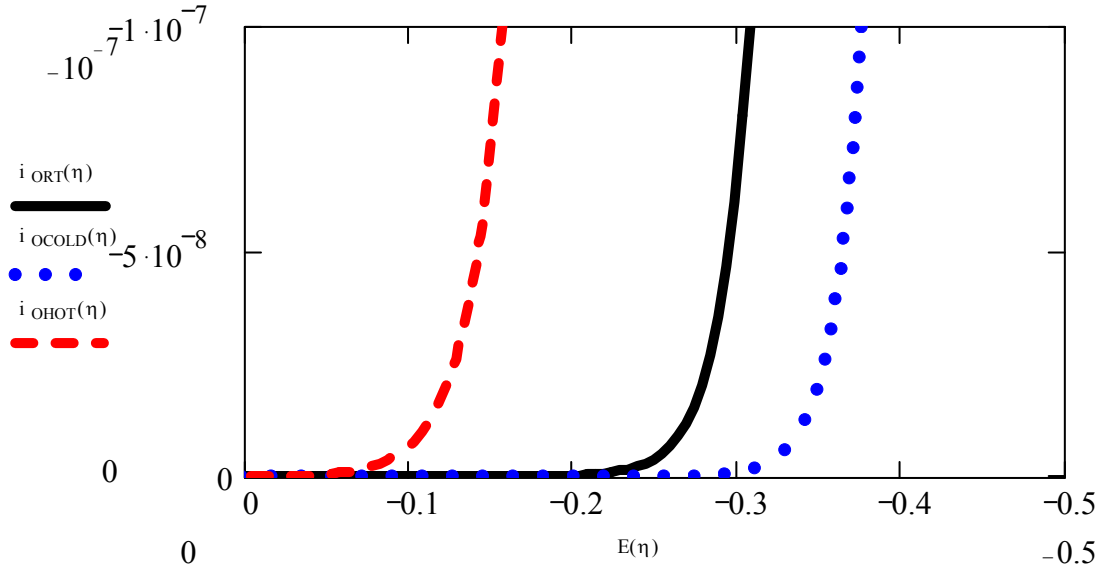

Figure A8: Non-steady state modeled Co partial current at different electrolyte temperatures

Non steady state Fe currents at different electrolyte temperatures

$$Cs_{FeRT}(t,\eta) := \left[100000 \cdot (D_{FeRT})\right]^{\left(\frac{1}{2}\right)} \cdot Cb_{Fe}\right] \cdot \frac{(0.00025t)^{-0.5} \cdot \exp(0.75t)^{0.1}}{\left[100000 \cdot (D_{FeRT})\right]^{\left(\frac{1}{2}\right)} \cdot t^{0.25} + 56419 \cdot Cb_{Co} \cdot k_{oFeRT} \cdot \exp\left(\frac{-\alpha_{Fe} \cdot Faraday \cdot E_{revFeRT}}{R \cdot T_{RT}}\right) \cdot \exp\left(-1 \cdot b_{FeRT} \cdot \eta(t)\right) \cdot t^{0.25} - 56419 Cb_{Fe} \cdot \left(k_{oFeRT} \cdot \exp\left(\frac{-\alpha_{Fe} \cdot Faraday \cdot E_{revFeRT}}{R \cdot T_{RT}}\right)\right) \cdot \exp\left(-1 \cdot b_{FeRT} \cdot \eta(t)\right) \cdot \exp\left(\frac{-0.15}{0.5 \cdot D_{FeRT}} \cdot \frac{\delta^3}{t^{-3}}\right)}$$

$$i_{FeRT}(t,\eta) := -k_{oFeRT} \cdot \exp\left(\frac{-\alpha_{Fe} \cdot Faraday \cdot E_{revFeRT}}{R \cdot T_{RT}}\right) \cdot n \cdot Faraday \cdot Cs_{FeRT}(t,\eta) \cdot \exp\left(-b_{FeRT} \cdot \eta(t)\right)$$

$$Cs_{FeCOLD}(t,\eta) := \left[100000 \cdot (D_{FeCOLD})\right]^{\left(\frac{1}{2}\right)} \cdot Cb_{Fe}\right] \cdot \frac{(0.00025t)^{-0.5} \cdot \exp(0.75t)^{0.1}}{\left[100000 \cdot (D_{FeCOLD})\right]^{\left(\frac{1}{2}\right)} \cdot t^{0.25} + 56419 \cdot Cb_{Co} \cdot k_{oFeRT} \cdot \exp\left(\frac{-\alpha_{Fe} \cdot Faraday \cdot E_{revFeRT}}{R \cdot T_{COLD}}\right) \cdot \exp\left(-1 \cdot b_{FeCOLD} \cdot \eta(t)\right) \cdot t^{0.25} - 56419 Cb_{Fe} \cdot \left(k_{oFeRT} \cdot \exp\left(\frac{-\alpha_{Fe} \cdot Faraday \cdot E_{revFeRT}}{R \cdot T_{COLD}}\right)\right) \cdot \exp\left(-1 \cdot b_{FeCOLD} \cdot \eta(t)\right) \cdot \exp\left(\frac{-0.15}{0.5 \cdot D_{FeCOLD}} \cdot \frac{\delta^3}{t^{-3}}\right)}$$

$$i_{FeCOLD}(t,\eta) := -k_{oFeRT} \cdot \exp\left(\frac{-\alpha_{Fe} \cdot Faraday \cdot E_{revFeRT}}{R \cdot T_{COLD}}\right) \cdot n \cdot Faraday \cdot Cs_{FeCOLD}(t,\eta) \cdot \exp\left(-b_{FeCOLD} \cdot \eta(t)\right)$$

$$Cs_{FeHOT}(t,\eta) := \left[100000 \cdot (D_{FeHOT})\right]^{\left(\frac{1}{2}\right)} \cdot Cb_{Fe}\right] \cdot \frac{(0.00025t)^{-0.5} \cdot \exp(0.75t)^{0.1}}{\left[100000 \cdot (D_{FeHOT})\right]^{\left(\frac{1}{2}\right)} \cdot t^{0.25} + 56419 \cdot Cb_{Co} \cdot k_{oFeRT} \cdot \exp\left(\frac{-\alpha_{Fe} \cdot Faraday \cdot E_{revFeRT}}{R \cdot T_{HOT}}\right) \cdot \exp\left(-1 \cdot b_{FeHOT} \cdot \eta(t)\right) \cdot t^{0.25} - 56419 Cb_{Fe} \cdot \left(k_{oFeRT} \cdot \exp\left(\frac{-\alpha_{Fe} \cdot Faraday \cdot E_{revFeRT}}{R \cdot T_{HOT}}\right)\right) \cdot \exp\left(-1 \cdot b_{FeHOT} \cdot \eta(t)\right) \cdot \exp\left(\frac{-0.15}{0.5 \cdot D_{FeHOT}} \cdot \frac{\delta^3}{t^{-3}}\right)}$$

$$i_{FeHOT}(t,\eta) := -k_{oFeRT} \cdot \exp\left(\frac{-\alpha_{Fe} \cdot Faraday \cdot E_{revFeRT}}{R \cdot T_{HOT}}\right) \cdot n \cdot Faraday \cdot Cs_{FeHOT}(t,\eta) \cdot \exp\left(-b_{FeHOT} \cdot \eta(t)\right)$$
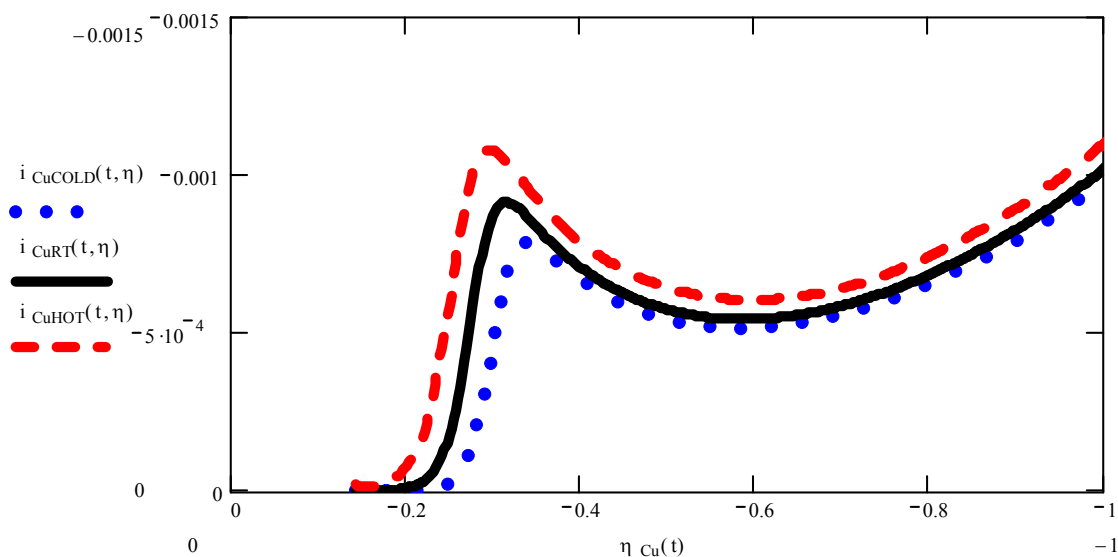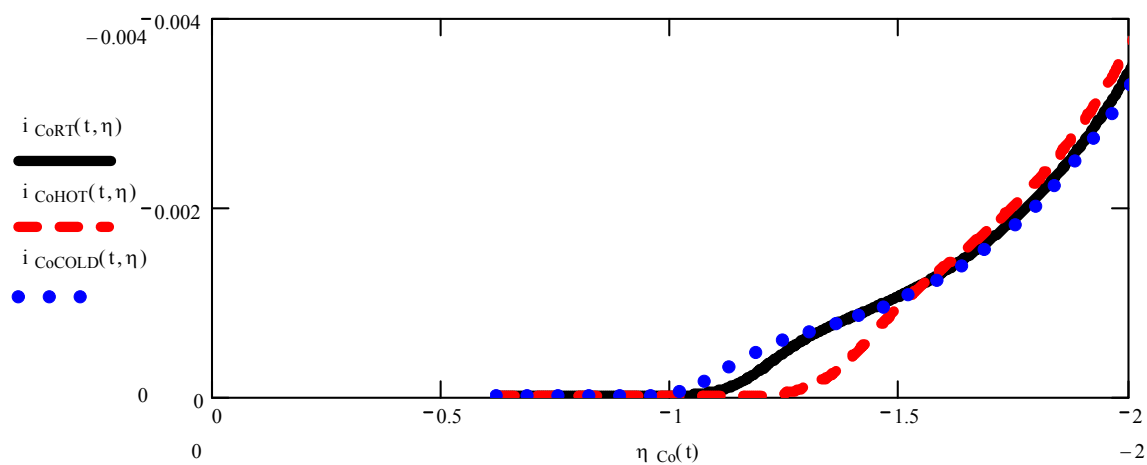

Figure A9: Non-steady state modeled Fe partial current at different electrolyte temperatures

Non steady state Ni currents at different electrolyte temperatures

$$Cs_{NiRT}(t,\eta) := \left[100000 \cdot (D_{NiRT})\right]^{\left(\frac{1}{2}\right)} \cdot Cb_{Ni}\right] \cdot \frac{(0.00025t)^{-0.5} \cdot \exp(0.75t)^{0.1}}{\left[100000 \cdot (D_{NiRT})\right]^{\left(\frac{1}{2}\right)} \cdot t^{0.25} + 56419 \cdot Cb_{Ni} \cdot k_{oNiRT} \cdot \exp\left(\frac{-\alpha_{Ni} \cdot Faraday \cdot E_{revNiRT}}{R \cdot T_{RT}}\right) \cdot \exp\left(-1 \cdot b_{NiRT} \cdot \eta(t)\right) \cdot t^{0.25} - 56419 Cb_{Ni} \cdot \left(k_{oNiRT} \cdot \exp\left(\frac{-\alpha_{Ni} \cdot Faraday \cdot E_{revNiRT}}{R \cdot T_{RT}}\right)\right) \cdot \exp\left(-1 \cdot b_{NiRT} \cdot \eta(t)\right) \cdot \exp\left(\frac{-0.15}{0.5 \cdot D_{NiRT}} \cdot \frac{\delta^3}{t^{-3}}\right)}$$

$$i_{NiRT}(t,\eta) := -k_{oNiRT} \cdot \exp\left(\frac{-\alpha_{Ni} \cdot Faraday \cdot E_{revNiRT}}{R \cdot T_{RT}}\right) \cdot n \cdot Faraday \cdot Cs_{NiRT}(t,\eta) \cdot \exp\left(-b_{NiRT} \cdot \eta(t)\right)$$

$$Cs_{NiCOLD}(t,\eta) := \left[100000 \cdot (D_{NiCOLD})\right]^{\left(\frac{1}{2}\right)} \cdot Cb_{Ni}\right] \cdot \frac{(0.00025t)^{-0.5} \cdot \exp(0.75t)^{0.1}}{\left[100000 \cdot (D_{NiCOLD})\right]^{\left(\frac{1}{2}\right)} \cdot t^{0.25} + 56419 \cdot Cb_{Ni} \cdot k_{oNiRT} \cdot \exp\left(\frac{-\alpha_{Ni} \cdot Faraday \cdot E_{revNiRT}}{R \cdot T_{COLD}}\right) \cdot \exp\left(-1 \cdot b_{NiCOLD} \cdot \eta(t)\right) \cdot t^{0.25} - 56419 Cb_{Ni} \cdot \left(k_{oNiRT} \cdot \exp\left(\frac{-\alpha_{Ni} \cdot Faraday \cdot E_{revNiRT}}{R \cdot T_{COLD}}\right)\right) \cdot \exp\left(-1 \cdot b_{NiCOLD} \cdot \eta(t)\right) \cdot \exp\left(\frac{-0.15}{0.5 \cdot D_{NiCOLD}} \cdot \frac{\delta^3}{t^{-3}}\right)}$$

$$i_{NiCOLD}(t,\eta) := -k_{oNiRT} \cdot \exp\left(\frac{-\alpha_{Ni} \cdot Faraday \cdot E_{revNiRT}}{R \cdot T_{COLD}}\right) \cdot n \cdot Faraday \cdot Cs_{NiCOLD}(t,\eta) \cdot \exp\left(-b_{NiCOLD} \cdot \eta(t)\right)$$

$$Cs_{NiHOT}(t,\eta) := \left[100000 \cdot (D_{NiHOT})\right]^{\left(\frac{1}{2}\right)} \cdot Cb_{Ni}\right] \cdot \frac{(0.00025t)^{-0.5} \cdot \exp(0.75t)^{0.1}}{\left[100000 \cdot (D_{NiHOT})\right]^{\left(\frac{1}{2}\right)} \cdot t^{0.25} + 56419 \cdot Cb_{Ni} \cdot k_{oNiRT} \cdot \exp\left(\frac{-\alpha_{Ni} \cdot Faraday \cdot E_{revNiRT}}{R \cdot T_{HOT}}\right) \cdot \exp\left(-1 \cdot b_{NiHOT} \cdot \eta(t)\right) \cdot t^{0.25} - 56419 Cb_{Ni} \cdot \left(k_{oNiRT} \cdot \exp\left(\frac{-\alpha_{Ni} \cdot Faraday \cdot E_{revNiRT}}{R \cdot T_{HOT}}\right)\right) \cdot \exp\left(-1 \cdot b_{NiHOT} \cdot \eta(t)\right) \cdot \exp\left(\frac{-0.15}{0.5 \cdot D_{NiHOT}} \cdot \frac{\delta^3}{t^{-3}}\right)}$$

$$i_{NiHOT}(t,\eta) := -k_{oNiRT} \cdot \exp\left(\frac{-\alpha_{Ni} \cdot Faraday \cdot E_{revNiRT}}{R \cdot T_{HOT}}\right) \cdot n \cdot Faraday \cdot Cs_{NiHOT}(t,\eta) \cdot \exp\left(-b_{NiHOT} \cdot \eta(t)\right)$$

Figure A10: Non-steady state modeled Ni partial current at different electrolyte temperatures

Non steady state H_2 currents at different electrolyte temperatures

$$Cs_{HRT}(t,\eta) := \left[\left[100000\cdot\left(D_{HRT}\right)\right]^{\left(\frac{1}{2}\right)}\cdot Cb_H\right]\cdot \frac{(0.00025t)^{-0.5}\cdot \exp(0.75t)^{0.1}}{\left[100000\cdot\left(D_{HRT}\right)\right]^{\left(\frac{1}{2}\right)}\cdot t^{0.25} + 56419\cdot Cb_H\cdot k_{oHRT}\cdot \exp\left(\frac{-\alpha_H\cdot Faraday\cdot E_{revHRT}}{R\cdot T_{RT}}\right)\cdot \exp\left(-1\cdot b_{HRT}\cdot \eta(t)\right)\cdot t^{0.25} - 56419 Cb_H\cdot\left(k_{oHRT}\cdot \exp\left(\frac{-\alpha_H\cdot Faraday\cdot E_{revHRT}}{R\cdot T_{RT}}\right)\right)\cdot \exp\left(-1\cdot b_{HRT}\cdot \eta(t)\right)\cdot \exp\left(\frac{-0.15}{0.5\cdot D_{HRT}}\cdot\frac{\delta^3}{t^{-3}}\right)}$$

$$i_{HRT}(t,\eta) := -k_{oHRT}\cdot \exp\left(\frac{-\alpha_H\cdot Faraday\cdot E_{revHRT}}{R\cdot T_{RT}}\right)\cdot n\cdot Faraday\cdot Cs_{HRT}(t,\eta)\cdot \exp\left(-b_{HRT}\cdot \eta(t)\right)$$

$$Cs_{HCOLD}(t,\eta) := \left[\left[100000\cdot\left(D_{HCOLD}\right)\right]^{\left(\frac{1}{2}\right)}\cdot Cb_H\right]\cdot \frac{(0.00025t)^{-0.5}\cdot \exp(0.75t)^{0.1}}{\left[100000\cdot\left(D_{HCOLD}\right)\right]^{\left(\frac{1}{2}\right)}\cdot t^{0.25} + 56419\cdot Cb_H\cdot k_{oHRT}\cdot \exp\left(\frac{-\alpha_H\cdot Faraday\cdot E_{revHRT}}{R\cdot T_{COLD}}\right)\cdot \exp\left(-1\cdot b_{HCOLD}\cdot \eta(t)\right)\cdot t^{0.25} - 56419 Cb_H\cdot\left(k_{oHRT}\cdot \exp\left(\frac{-\alpha_H\cdot Faraday\cdot E_{revHRT}}{R\cdot T_{COLD}}\right)\right)\cdot \exp\left(-1\cdot b_{HCOLD}\cdot \eta(t)\right)\cdot \exp\left(\frac{-0.15}{0.5\cdot D_{HCOLD}}\cdot\frac{\delta^3}{t^{-3}}\right)}$$

$$i_{HCOLD}(t,\eta) := -k_{oHRT}\cdot \exp\left(\frac{-\alpha_H\cdot Faraday\cdot E_{revHRT}}{R\cdot T_{COLD}}\right)\cdot n\cdot Faraday\cdot Cs_{HCOLD}(t,\eta)\cdot \exp\left(-b_{HCOLD}\cdot \eta(t)\right)$$

$$Cs_{HHOT}(t,\eta) := \left[\left[100000\cdot\left(D_{HHOT}\right)\right]^{\left(\frac{1}{2}\right)}\cdot Cb_H\right]\cdot \frac{(0.00025t)^{-0.5}\cdot \exp(0.75t)^{0.1}}{\left[100000\cdot\left(D_{HHOT}\right)\right]^{\left(\frac{1}{2}\right)}\cdot t^{0.25} + 56419\cdot Cb_H\cdot k_{oHRT}\cdot \exp\left(\frac{-\alpha_H\cdot Faraday\cdot E_{revHRT}}{R\cdot T_{HOT}}\right)\cdot \exp\left(-1\cdot b_{HHOT}\cdot \eta(t)\right)\cdot t^{0.25} - 56419 Cb_H\cdot\left(k_{oHRT}\cdot \exp\left(\frac{-\alpha_H\cdot Faraday\cdot E_{revHRT}}{R\cdot T_{HOT}}\right)\right)\cdot \exp\left(-1\cdot b_{HHOT}\cdot \eta(t)\right)\cdot \exp\left(\frac{-0.15}{0.5\cdot D_{HHOT}}\cdot\frac{\delta^3}{t^{-3}}\right)}$$

$$i_{HHOT}(t,\eta) := -k_{oHRT}\cdot \exp\left(\frac{-\alpha_H\cdot Faraday\cdot E_{revHRT}}{R\cdot T_{HOT}}\right)\cdot n\cdot Faraday\cdot Cs_{HHOT}(t,\eta)\cdot \exp\left(-b_{HHOT}\cdot \eta(t)\right)$$
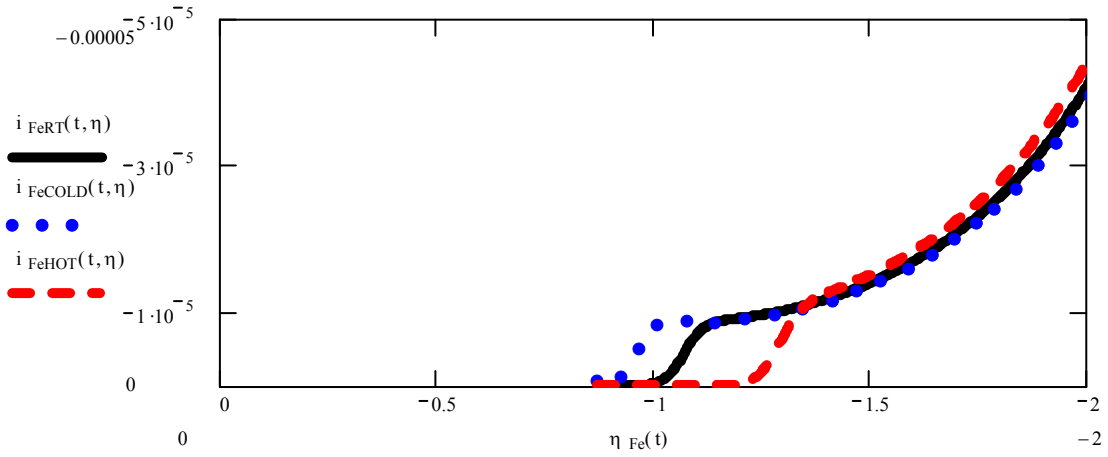

Figure A11: Non-steady state modeled H_2 partial current at different electrolyte temperatures

Non steady state H$_2$O currents at different electrolyte temperatures

$$Cs_{HOHRT}(t,\eta) := \left[\left[100000\cdot(D_{HOHRT})\right]^{\left(\frac{1}{2}\right)}\cdot Cb_{HOH}\right]\cdot \frac{(0.00025t)^{-0.5}\cdot \exp(0.75t)^{0.1}}{\left[100000\cdot(D_{HOHRT})\right]^{\left(\frac{1}{2}\right)}\cdot t^{0.25} + 56419\cdot Cb_{HOH}\cdot k_{oHOHRT}\cdot \exp\left(\frac{-\alpha_{HOH}\cdot Faraday\cdot E_{revHOHRT}}{R\cdot T_{RT}}\right)\cdot \exp\left(-1\cdot b_{HOHRT}\cdot \eta(t)\right)\cdot t^{0.25} - 56419Cb_{HOH}\left(k_{oHOHRT}\cdot \exp\left(\frac{-\alpha_{HOH}\cdot Faraday\cdot E_{revHOHRT}}{R\cdot T_{RT}}\right)\right)\cdot \exp\left(-1\cdot b_{HOHRT}\cdot \eta(t)\right)\cdot \exp\left(\frac{-0.15}{0.5D_{HOHRT}}\cdot \frac{\delta^3}{t^{-3}}\right)}$$

$$i_{HOHRT}(t,\eta) := -k_{oHOHRT}\cdot \exp\left(\frac{-\alpha_{HOH}\cdot Faraday\cdot E_{revHOHRT}}{R\cdot T_{RT}}\right)\cdot n\cdot Faraday\cdot Cs_{HOHRT}(t,\eta)\cdot \exp\left(-b_{HOHRT}\cdot \eta(t)\right)$$

$$Cs_{HOHCOLD}(t,\eta) := \left[\left[100000\cdot(D_{HOHCOLD})\right]^{\left(\frac{1}{2}\right)}\cdot Cb_{HOH}\right]\cdot \frac{(0.00025t)^{-0.5}\cdot \exp(0.75t)^{0.1}}{\left[100000\cdot(D_{HOHCOLD})\right]^{\left(\frac{1}{2}\right)}\cdot t^{0.25} + 56419\cdot Cb_{HOH}\cdot k_{oHOHRT}\cdot \exp\left(\frac{-\alpha_{HOH}\cdot Faraday\cdot E_{revHOHRT}}{R\cdot T_{COLD}}\right)\cdot \exp\left(-1\cdot b_{HOHCOLD}\cdot \eta(t)\right)\cdot t^{0.25} - 56419Cb_{HOH}\left(k_{oHOHRT}\cdot \exp\left(\frac{-\alpha_{HOH}\cdot Faraday\cdot E_{revHOHRT}}{R\cdot T_{COLD}}\right)\right)\cdot \exp\left(-1\cdot b_{HOHCOLD}\cdot \eta(t)\right)\cdot \exp\left(\frac{-0.15}{0.5D_{HOHCOLD}}\cdot \frac{\delta^3}{t^{-3}}\right)}$$

$$i_{HOHCOLD}(t,\eta) := -k_{oHOHRT}\cdot \exp\left(\frac{-\alpha_{HOH}\cdot Faraday\cdot E_{revHOHRT}}{R\cdot T_{COLD}}\right)\cdot n\cdot Faraday\cdot Cs_{HOHCOLD}(t,\eta)\cdot \exp\left(-b_{HOHCOLD}\cdot \eta(t)\right)$$

$$Cs_{HOHHOT}(t,\eta) := \left[\left[100000\cdot(D_{HOHHOT})\right]^{\left(\frac{1}{2}\right)}\cdot Cb_{HOH}\right]\cdot \frac{(0.00025t)^{-0.5}\cdot \exp(0.75t)^{0.1}}{\left[100000\cdot(D_{HOHHOT})\right]^{\left(\frac{1}{2}\right)}\cdot t^{0.25} + 56419\cdot Cb_{HOH}\cdot k_{oHOHRT}\cdot \exp\left(\frac{-\alpha_{HOH}\cdot Faraday\cdot E_{revHOHRT}}{R\cdot T_{HOT}}\right)\cdot \exp\left(-1\cdot b_{HOHHOT}\cdot \eta(t)\right)\cdot t^{0.25} - 56419Cb_{HOH}\left(k_{oHOHRT}\cdot \exp\left(\frac{-\alpha_{HOH}\cdot Faraday\cdot E_{revHOHRT}}{R\cdot T_{HOT}}\right)\right)\cdot \exp\left(-1\cdot b_{HOHHOT}\cdot \eta(t)\right)\cdot \exp\left(\frac{-0.15}{0.5D_{HOHHOT}}\cdot \frac{\delta^3}{t^{-3}}\right)}$$

$$i_{HOHHOT}(t,\eta) := -k_{oHOHRT}\cdot \exp\left(\frac{-\alpha_{HOH}\cdot Faraday\cdot E_{revHOHRT}}{R\cdot T_{HOT}}\right)\cdot n\cdot Faraday\cdot Cs_{HOHHOT}(t,\eta)\cdot \exp\left(-b_{HOHHOT}\cdot \eta(t)\right)\cdot$$

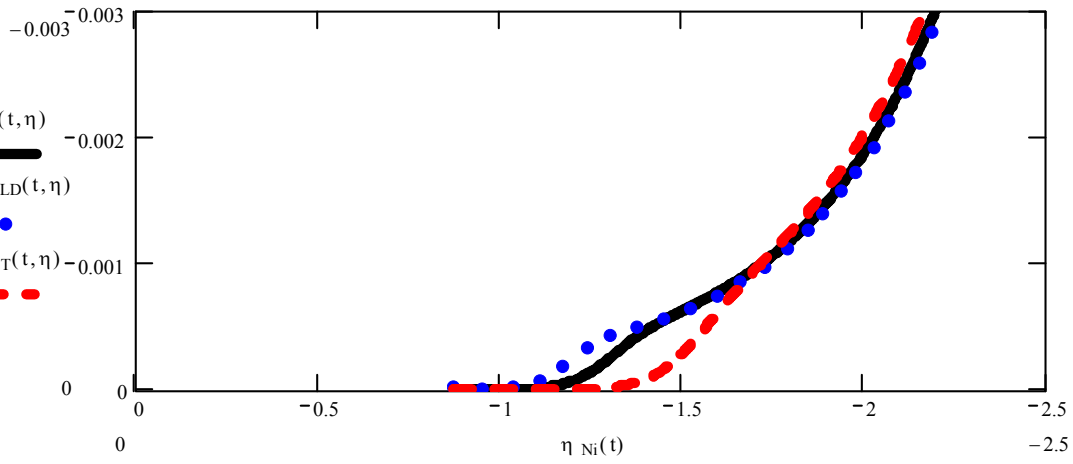Figure A12: Non-steady state modeled H$_2$O partial current at different electrolyte

Non steady state O$_2$ currents at different electrolyte temperatures

$$Cs_{ORT}(t,\eta) := \left[\left[100000\cdot(D_{ORT})\right]^{\left(\frac{1}{2}\right)}\cdot Cb_{ORT}\right]\cdot \frac{(0.00025t)^{-0.5}\cdot \exp(0.75t)^{0.1}}{\left[100000\cdot(D_{ORT})\right]^{\left(\frac{1}{2}\right)}\cdot t^{0.25} + 56419\cdot Cb_{ORT}\cdot k_{oORT}\cdot \exp\left(\frac{-\alpha_{O}\cdot Faraday\cdot E_{revORT}}{R\cdot T_{RT}}\right)\cdot \exp\left(-1\cdot b_{ORT}\cdot \eta(t)\right)\cdot t^{0.25} - 56419Cb_{ORT}\left(k_{oORT}\cdot \exp\left(\frac{-\alpha_{O}\cdot Faraday\cdot E_{revORT}}{R\cdot T_{RT}}\right)\right)\cdot \exp\left(-1\cdot b_{ORT}\cdot \eta(t)\right)\cdot \exp\left(\frac{-0.15}{0.5D_{ORT}}\cdot \frac{\delta^3}{t^{-3}}\right)}$$

$$i_{ORT}(t,\eta) := -k_{oORT}\cdot \exp\left(\frac{-\alpha_{O}\cdot Faraday\cdot E_{revORT}}{R\cdot T_{RT}}\right)\cdot n\cdot Faraday\cdot Cs_{ORT}(t,\eta)\cdot \exp\left(-b_{ORT}\cdot \eta(t)\right)$$

$$Cs_{OCOLD}(t,\eta) := \left[\left[100000\cdot(D_{OCOLD})\right]^{\left(\frac{1}{2}\right)}\cdot Cb_{OCold}\right]\cdot \frac{(0.00025t)^{-0.5}\cdot \exp(0.75t)^{0.1}}{\left[100000\cdot(D_{OCOLD})\right]^{\left(\frac{1}{2}\right)}\cdot t^{0.25} + 56419\cdot Cb_{OCold}\cdot k_{oORT}\cdot \exp\left(\frac{-\alpha_{O}\cdot Faraday\cdot E_{revORT}}{R\cdot T_{COLD}}\right)\cdot \exp\left(-1\cdot b_{OCOLD}\cdot \eta(t)\right)\cdot t^{0.25} - 56419Cb_{OCold}\left(k_{oORT}\cdot \exp\left(\frac{-\alpha_{O}\cdot Faraday\cdot E_{revORT}}{R\cdot T_{COLD}}\right)\right)\cdot \exp\left(-1\cdot b_{OCOLD}\cdot \eta(t)\right)\cdot \exp\left(\frac{-0.15}{0.5D_{OCOLD}}\cdot \frac{\delta^3}{t^{-3}}\right)}$$

$$i_{OCOLD}(t,\eta) := -k_{oORT}\cdot \exp\left(\frac{-\alpha_{O}\cdot Faraday\cdot E_{revORT}}{R\cdot T_{COLD}}\right)\cdot n\cdot Faraday\cdot Cs_{OCOLD}(t,\eta)\cdot \exp\left(-b_{OCOLD}\cdot \eta(t)\right)$$

$$Cs_{OHOT}(t,\eta) := \left[\left[100000\cdot(D_{OHOT})\right]^{\left(\frac{1}{2}\right)}\cdot Cb_{OHot}\right]\cdot \frac{(0.00025t)^{-0.5}\cdot \exp(0.75t)^{0.1}}{\left[100000\cdot(D_{OHOT})\right]^{\left(\frac{1}{2}\right)}\cdot t^{0.25} + 56419\cdot Cb_{OHot}\cdot k_{oORT}\cdot \exp\left(\frac{-\alpha_{O}\cdot Faraday\cdot E_{revORT}}{R\cdot T_{HOT}}\right)\cdot \exp\left(-1\cdot b_{OHOT}\cdot \eta(t)\right)\cdot t^{0.25} - 56419Cb_{OHot}\left(k_{oORT}\cdot \exp\left(\frac{-\alpha_{O}\cdot Faraday\cdot E_{revORT}}{R\cdot T_{HOT}}\right)\right)\cdot \exp\left(-1\cdot b_{OHOT}\cdot \eta(t)\right)\cdot \exp\left(\frac{-0.15}{0.5D_{OHOT}}\cdot \frac{\delta^3}{t^{-3}}\right)}$$

$$i_{OHOT}(t,\eta) := -k_{oORT}\cdot \exp\left(\frac{-\alpha_{O}\cdot Faraday\cdot E_{revORT}}{R\cdot T_{HOT}}\right)\cdot n\cdot Faraday\cdot Cs_{OHOT}(t,\eta)\cdot \exp\left(-b_{OHOT}\cdot \eta(t)\right)$$
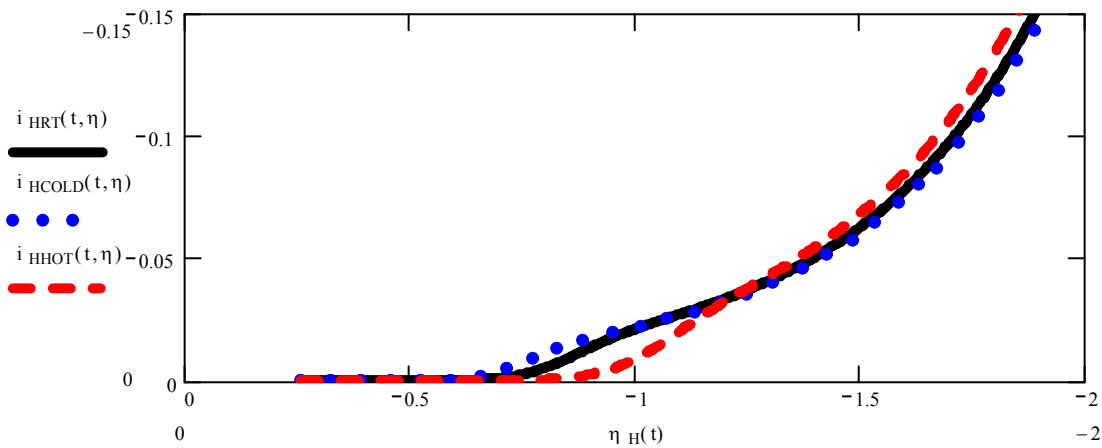
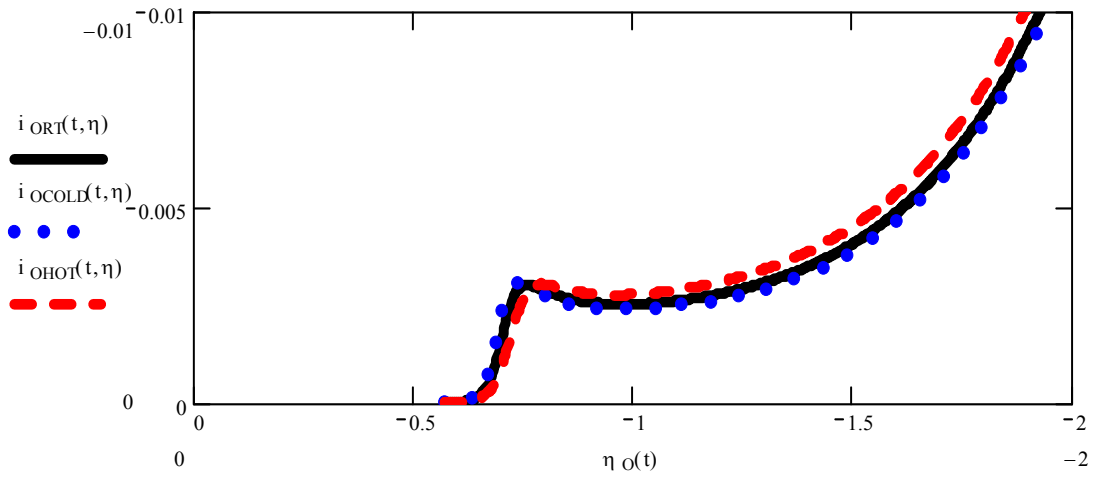Figure A13: Non-steady state modeled O$_2$ partial current at different electrolyte

Steady State Total Currents

$$i_{TotRT}(\eta) := i_{FeRT}(\eta) + i_{CuRT}(\eta) + i_{NiRT}(\eta) + i_{CoRT}(\eta) + i_{HRT}(\eta) + i_{HOHRT}(\eta) + i_{ORT}(\eta)$$

$$i_{TotCOLD}(\eta) := i_{FeCOLD}(\eta) + i_{CuCOLD}(\eta) + i_{NiCOLD}(\eta) + i_{CoCOLD}(\eta) + i_{HCOLD}(\eta) + i_{HOHCOLD}(\eta) + i_{OCOLD}(\eta)$$

$$i_{TotHOT}(\eta) := i_{FeHOT}(\eta) + i_{CuHOT}(\eta) + i_{NiHOT}(\eta) + i_{CoHOT}(\eta) + i_{HHOT}(\eta) + i_{HOHHOT}(\eta) + i_{OHOT}(\eta)$$

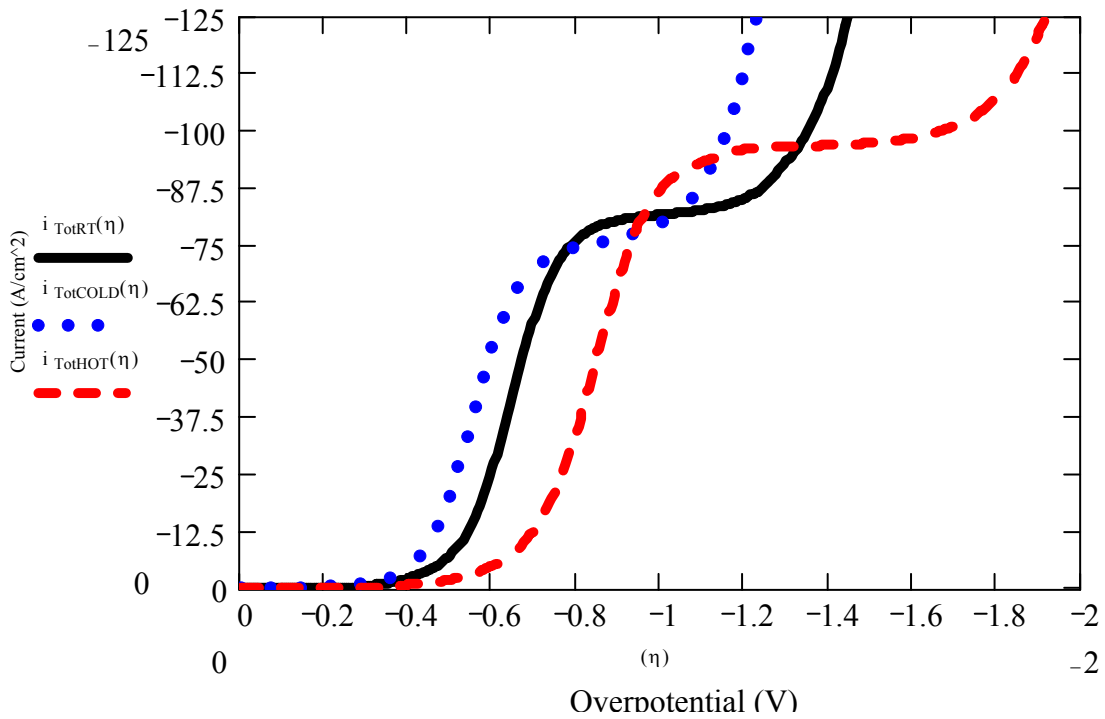

Figure A14: Steady state modeled total currents at different electrolyte temperatures

Non-Steady State Total Currents

$$i_{TotRT}(t,\eta) := \left(i_{FeRT}(t,\eta) + i_{CuRT}(t,\eta) + i_{NiRT}(t,\eta) + i_{CoRT}(t,\eta) + i_{HRT}(t,\eta) + i_{HOHRT}(t,\eta) + i_{ORT}(t,\eta)\right)$$

$$i_{TotCOLD}(t,\eta) := \left(i_{FeCOLD}(t,\eta) + i_{CuCOLD}(t,\eta) + i_{NiCOLD}(t,\eta) + i_{CoCOLD}(t,\eta) + i_{HCOLD}(t,\eta) + i_{HOHCOLD}(t,\eta) + i_{OCOLD}(t,\eta)\right)$$

$$i_{TotHOT}(t,\eta) := \left(i_{FeHOT}(t,\eta) + i_{CuHOT}(t,\eta) + i_{NiHOT}(t,\eta) + i_{CoHOT}(t,\eta) + i_{HHOT}(t,\eta) + i_{HOHHOT}(t,\eta) + i_{OHOT}(t,\eta)\right)$$
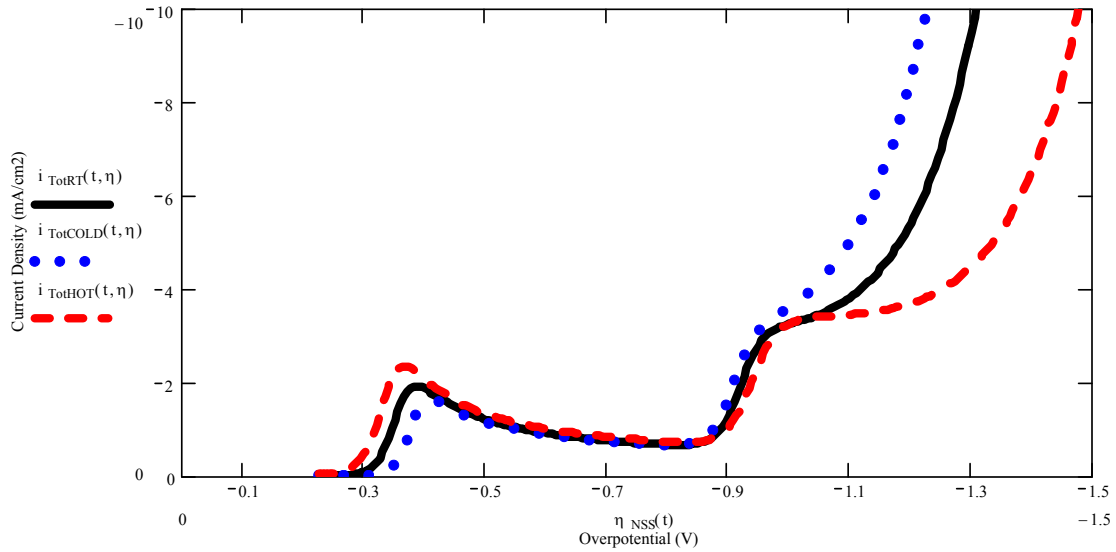

Figure A15: Non-steady state modeled total currents at different electrolyte temperatures

VITA

Mrs. Despina Mehedintu Davis was born in March 1978, in Ploiesti, World War II oil supplier in central Europe, Romania. She came to USA for her bachelor degree and graduated in May 2002 from Texas Tech University with a dual degree in chemical engineering and chemistry. In the fall of 2002, she came to Louisiana State University where she enrolled in graduate studies in the Department of Chemical Engineering. The degree Master of Science in chemical engineering was conferred in May 2005. She will be granted the Doctoral degree in engineering science in May 2007. Upon graduation, she accepted a faculty position in the Engineering Department at Louisiana Tech University in Ruston. A list of publications and presentations include:

- D. Davis, M. Moldovan, M. Henk, X. Xie, D. Young and E.J. Podlaha "GMR in CoNiFe/Cu Multilayered Nanotubes" *Electrochemical and Solid State Letters,* 9(9) (2006)

- D. Davis, M. Moldovan, D. P. Young, E. J. Podlaha, "GMR in Multilayered CoNiFeCu/Cu Nanowires and Nanotubes", "*Electrodeposition of Nano-Engineered Materials-ECS Transactions*, 1 (71) (2006)

- D. Davis, F. R. Fronczek, J. A. Schuerman, J. Selbin and S. F. Watkins, (2,4,6-Trimethyldithiobenzoato-S,S) bis(triphenylphosphine-P)gold(I) [Au($C_{10}H_8S_2$)($C_{18}H_{15}P$)$_2$] Structure, *Acta Crystallographica Section E,* E62 (m1526) (2006)

- D. Davis and E.J. Podlaha, "CoNiCu and Cu Nanotubes Electrodeposition" *Electrochemical and Solid State Letters,* 8(2) D1-D4 (2005)

- Book Chapter: E. J. Podlaha, Y. Li, J. Zhang, Q. Huang, A. Panda, A. Losano-Morales, D. Davis, Z. Guo: *Handbook of Nanomaterials,* ISBN 0849323088, (2005)

- Q. Huang, D. Davis and E. J. Podlaha, "Electrodeposition of FeCoNi/Cu Nanowires", *Journal of Applied Electrochemistry*, 32 871(2006)

- D. Davis, M. Moldovan, D. Young and E.J. Podlaha "Multilayered CoNiFe/Cu Nanowires for GMR Sensing", *Journal of Electrochemical Society* (in preparation)

- D. Davis and E. Podlaha, "*Electrodeposited CoNi(Fe)/Cu Multilayered Nanowires and Tubes for GMR Sensing*", *Gordon Research Conference,* New England, NH, July 2006

- D. Davis, M. Moldovan, D. Young and E. J. Podlaha, *Peaks Conference on Electrochemical Processing for Microelectronics*, Montana, June 2006

- D. Davis, R. Mishra, N. McBride, V. George, M. Moldovan, D. Young and E. J. Podlaha Nanowire GMR based Microfluidic Bio-Sensor, *Center for Bio-Modular Multi-Scale Systems (CBM²) Colloquium*, July 7, 2006

- D. Davis, M. Moldovan, D. Young, and E.J. Podlaha "Nanotubes and Nanowires Electrodeposition" *208th Meeting of the Electrochemical Society*, Los Angeles, Oct. 2005

- D. Davis, M. Moldovan, D. Young, and E.J. Podlaha "Multilayered Nanotubes Magnetic Properties" *Red Tech Conference*, Shanghai-China, May 2005

- D. Davis, M. Moldovan, D. Young, and E.J. Podlaha "Nanotubes and Nanowires Electrodeposition in Polymeric Membranes" *NSF-IGERT Panel Review*, Ian 2005

- E. J. Podlaha, Q. Huang, J. Zhang, Y. Li, D. Davis and M. Guan, "Electrodeposition of Iron-group Multilayer Thin Films and Nanowires", *206th Meeting of the Electrochemical Society*, Hawaii, Oct 2004

- J. Zhang, D. Davis, T. W. Eyster, M. Moldovan, D. Young and E. Podlaha, "Electrodeposited CoNi/Cu Multilayers and Multilayered Nanowires", *Gordon Research Conference,* New England, NH, Aug. 2004

- D. Davis and E.J. Podlaha, "CoFeNiCu/Cu Nanowires and Tubes", *205th Meeting of the Electrochemical Society,* San Antonio, TX, May 9, 2004